Characterisation and Ionisation Modelling of Matrices in MALDI Mass Spectrometry

being a Thesis submitted for the Degree of

Doctor of Philosophy

in the University of Hull

by

Daniel Anthony Allwood, BSc

April 1998

For

Kenneth Gostage,

in memory.

ABSTRACT

Experimental investigation of several matrix molecules commonly used in matrix-assisted laser desorption/ionisation (MALDI) mass spectrometry has provided the basis for modelling matrix ionisation within MALDI. Improvements in sample preparation, and in particular the formation of optically thin matrix films by sublimation-deposition, have made possible the optical characterisation of MALDI matrix molecules. These investigations have yielded estimates of several molecular photophysical parameters relevant to MALDI, e.g. ground state absorption coefficient, α, fluorescence decay rates and fluorescence quantum efficiencies. Furthermore, the strong relationship between α and the degree of matrix ionisation observed due to pulsed laser irradiation has been demonstrated. Based on this information an excited-state ionisation model has been developed wherein a two-photon excited state of the molecule draws upon its vibrational energy to undergo thermal ionisation. Ionisation is assumed to occur within the laser-desorbed gas-phase plume, which provides rapid (ps) thermal equilibration of vibrational energy, and within the laser pulse duration itself. Predictions of this model show excellent agreement with experiment both in terms of the strong power scaling with laser fluence F ($\sim F^{10}$) and in the total ion yield ($\geq 10^{-6}$) and suggests this ionisation route as a plausible alternative to multiple photon ionisation. It is hoped that the matrix photophysical data and ionisation modelling will enable further theoretical treatment of various aspects of MALDI and that the better understanding lent to the subject will ultimately result in improved experimental practise.

ACKNOWLEDGEMENTS

I would like to offer my deepest thanks to my PhD supervisor, Prof. Pete Dyer, who has throughout been a consistent support in providing insightful direction and advice whilst also encouraging learning through independent work. To Prof. Russ Dreyfus I am particularly appreciative for the refreshing perspective he brought to the MALDI work. However, I would also like to thank Prof. Dyer and Prof. Dreyfus for the many unwritten lessons they have, perhaps unknowingly, given me regarding approaches to new problems; I only hope to learn these lessons one day as fully as they have. Dr. Kith Perera is gratefully acknowledged for the invaluable advice and understanding of MALDI he provided me with during the first year of my PhD. Prof. A. Vertes and Prof. F. Hillenkamp are thanked for helpful discussions, particularly regarding the modelling work. Not only for superb technical support, but also for their ideas and many suggestions, I would like to offer sincerest thanks to Paul Monk and Brian Tait, without whom the experimental sections of this thesis would have looked remarkably slimmer. A. Sinclair and G. Robinson are acknowledged for assistance with the SEM, as are Prof. Paul Fletcher and Dr. Klaus Suhling for providing access to spectrophotometers. Thanks also go to Judy and Margaret for secretarial support, particularly whenever I tried to fax anything. For the many other 'colleagues' within the department, I would like to thank them for their suggestions and encouragement, but perhaps more than that for providing outlets of conversation away from physics. In particular, I thank Dimitris for restaurant recommendations, Raj for the football, Rose for laughing at most of my jokes, Rob for always giving a new angle on a topic, Howard for some of the best stories I now tell, James for all the red wine and Franz for whom the sun always seems to shine.

To Mum, Dad, Roy and Marita, my brothers and sisters Amy, Richard, Laurence and Sarah, and the rest of my family go many, many thanks for support, concern and well received distractions from work over the years. The friendships of Chris and Dave (S) as 'kindred spirits' have always been greatly appreciated, as have those of Geoff Mills, whose laugh remains deeply satisfying, Geoff Waring (the only difference between men and boys is the price of their toys...), Cathy, for ice-cream at the cinema (the films weren't bad either), Donna, for her clear and considered opinions on all subjects, Ian Massey, for a description of the rotary wankle engine, and Dan, for proven friendship. Thanks must also go to John, Hannah, Miles and Paul whom I shared houses with in Hull at various points of my PhD. Finally, from my more recent time in Oxford, I would like to thank Dave (G) and Caroline for opening up their house to me as they have done and Ellen for providing such new perspectives.

TABLE OF CONTENTS

1. INTRODUCTION

Over the past ten years, matrix-assisted laser desorption/ionisation (MALDI) has emerged as a powerful analytical tool in supporting the production of intact gas phase ions of large (> 10 kDa) biological and synthetic molecules before mass spectrometric analysis. MALDI is an attractive technique since a wide range of different molecules have been successfully analysed including mixtures of different analyte species, only very small amounts of analyte are required (routinely fmol - pmol), analyte fragmentation is minimal, there exists a relatively high tolerance to contaminants and the time required for preparation and analysis is short (typically < 1 hour).

Although initially confined to a research environment, the potential of MALDI to provide an accurate and rapid method of high mass analysis quickly led to the technique assuming commercial importance and is now commonplace in many biochemistry and chemistry laboratories. Furthermore, the particular suitability of MALDI to time-of-flight (TOF) mass spectrometers led to great improvements being made in TOF instrumentation and a concomitant improvement in MALDI analysis. These improvements have allowed MALDI-TOF mass spectrometry to compete, in terms of mass resolution, with other techniques capable of high mass analysis, chiefly electrospray ionisation with a Fourier transform ion cyclotron resonance mass spectrometer for analysis.

Briefly, 'MALDI' describes the processes resulting from pulsed laser irradiation of a 'matrix' crystal containing analyte molecules. Matrix molecules are generally, but not always, aromatic molecules of molecular weight between 150 - 250 Da and are chosen to absorb the (usually UV) laser radiation. Analyte molecules are most commonly embedded within the matrix crystal structure by co-crystallisation of the respective solutions. Laser irradiation causes desorption and ionisation of both matrix and analyte molecules, usually into an evacuated source region of a mass spectrometer. However, in the absence of a suitable matrix molecule, the production of high mass ions (> 10 kDa) cannot be supported.

An improved understanding of the main processes in MALDI has been gained since its introduction. For example, it is now thought that matrix desorption results directly from absorption of laser light but that analyte molecules become entrained in the expanding matrix plume and thus are carried into the gas phase. Furthermore, the desorption step in MALDI has been treated with some success, most notably by molecular modelling. In terms of ionisation, one of the proposed routes suggests that matrix ionisation proceeds as electron loss within the laser pulse, forming the m^+ ion, followed by hydrogen transfer with other matrices to form $[m+H]^+$. It is then the $[m+H]^+$ ions that undergoes collisional charge transfer reactions with gas phase analyte molecules. However, the absence of a mathematical description of the ionisation step has been conspicuous and is principally due to a lack of data on matrix molecules. One might argue, though, that a better understanding of ionisation mechanisms can only lead to improved performance of MALDI as a whole.

In essence, the work described herein has been aimed at alleviating to some extent this deficiency in the understanding of MALDI, through improved sample preparations allowing data pertaining to matrix molecules to be obtained and culminating in modelling of matrix ionisation. The initial ionisation step to form m^+ is selected as the specific ionisation step to model since all other subsequent ions depend directly on the numbers of m^+ produced. This thesis, therefore, is structured in the following way:

Chapter 2 contains a review of the literature on MALDI, from its introduction to the current level of performance. Little space is given to the different types of molecule analysed, rather the understanding of the mechanisms involved in MALDI is focussed upon with attention also being given to experimental and instrumental considerations.

Chapter 3 describes an experimental study of different sample preparations, principally of matrices, performed with a view to improving MALDI performance and, more importantly, producing samples of sufficiently high uniformity to be useful in quantitative optical measurements. Refrigeration drying of matrix solutions and subsequent mechanical crushing of the resulting crystals yielded samples that displayed a lower threshold fluence for the observation of ions in a TOF mass spectrometer than standard samples. Furthermore, these samples were up to 60 μm thick and covered

several mm^2, displaying excellent surface flatness over this area. Vacuum sublimation-deposition of matrices onto fused silica or glass substrates was also investigated and allowed optically thin films consisting of sub-micron sized crystallites and covering several cm^2 to be grown in a controlled manner. A detailed description of the mass spectrometer used throughout this work is also given, and an isolated study of protein clustering conducted on this instrument is described in Appendix A.

Chapter 4 provides details of the first quantitative optical absorption measurements on solid state matrices which were made possible by the improvements in sample preparation described in Chapter 3. Furthermore, ion production in MALDI was found to depend very strongly on the solid state matrix absorption coefficient, α, at the laser wavelength. Indeed, 3,4,5-trihydroxybenzoic acid, previously thought to be a poor example of a MALDI matrix, has been demonstrated to support the effective desorption and ionisation of a protein species by changing the irradiating laser wavelength to increase α.

Chapter 5 describes an extensive study of the fluorescence of matrix solid films and solutions. Various analytical techniques were employed in order to determine several matrix parameters important to the modelling of matrix ionisation, including: fluorescence quantum efficiencies, singlet-ground decay rates and the 0-0 ground-singlet transition energy. The chapter concludes with an analysis of previously published fluorescence data to provide an estimate of the singlet-singlet interaction rate constant which describes interaction between photoexcited matrix molecules.

In Chapter 6 a new model based on excited state thermal ionisation (ESTI) is proposed to account for matrix ionisation caused by the incident UV laser energy. Essentially, a gas phase matrix molecule is assumed to absorb two laser photons to become highly excited. Interaction between the molecule's vibrational and electronic wavefunctions (*vibronic* interaction) allows the photoexcited electron to draw upon the (thermal) energy within vibrational modes and be ejected. Singlet state populations were initially calculated analytically for a square-shaped temporal laser pulse, with the ionisation step being modelled numerically. The predicted ESTI ion yield dependence on laser fluence shows good agreement with experiment, unlike photoionisation modelling

assuming the step-wise absorption of three photons. The model calculations were then developed to become wholly numerical, allowing ESTI ion yields to be calculated for more realistic temporal laser pulse shapes. It is also shown that the ESTI step occurs on a shorter timescale than the laser pulse, thus preserving the capacity for good mass resolution.

Chapter 7 initially focusses on the inclusion of several matrix processes that were for simplicity neglected in the modelling in Chapter 6. Temperature-dependent heat capacity, triplet states and excited state interactions all affected the level of matrix ionisation significantly, whereas electron-ion recombination, thermionic cooling and 'fluorescence heating' were shown to have a negligible contributory effect. These effects were then included within the model and the ESTI yield dependence on several parameters assessed. Perhaps most notably, this modelling of ESTI indicated that the ion yield will go through a maximum at a certain laser pulse length before starting to reduce again. This is due to the conflicting needs of obtaining a sufficiently high population density of the high lying electronic state, from where thermal ionisation may take place, and a sufficiently high matrix temperature, which is governed largely by the singlet-ground relaxation rate. The former is increased by high irradiance, short laser pulses whereas the latter tends to increase for low irradiance, long laser pulses. Other comparisons made with experiment, particularly where changes in laser wavelength or pulse length have been made, lend further support to ESTI being the dominant initial form of ionisation within MALDI.

Chapter 8 contains a summary of the main features of this thesis before commenting on possible future research activity. The publications that have resulted from this work are listed in Appendix C for convenience.

2 LITERATURE REVIEW

2.1 General Overview

From its introduction in 1988 [1], matrix-assisted laser desorption/ionisation (MALDI) showed great potential as a technique for producing intact gas-phase ions of large (> 10 kDa) naturally occuring and synthetic polymers. Frequency quadrupled Nd:YAG (λ = 266 nm) pulsed laser irradiation of a nicotinic acid (matrix) crystal containing dilute quantities of analyte molecules (100:1 matrix:analyte molar ratio) yielded positively-charged intact analyte ions of molecular weight (M.W.) up to ~ 67 kDa (bovine serum albumin, BSA), detected on a time-of-flight mass spectrometer (TOF-MS). Almost simultaneously, Tanaka *et al.* [2] observed similar results for proteins and synthetic polymers by using N_2 laser radiation (λ = 337 nm) and a matrix mixture of glycerol and fine (300Å) cobalt powder. These observations were of immediate interest in mass spectrometry since the practical mass limit for the production of intact laser desorbed ions had previously been ~ 1 kDa for biopolymers and 9 kDa for synthetic polymers [3]. However, nicotinic acid initially allowed an analyte sensitivity three orders of magnitude greater than with the glycerol/cobalt matrix (pmol rather than nmol) and thus superseded the latter technique. Following its announcement, rapid developments in MALDI occured, including: detection of proteins of M.W. ~ 150 kDa (bovine immunoglobulin G, IgG) [4] and protein clusters of M.W. ~ 200 kDa (BSA trimer) [5], negative ion spectra [4,6], analysis of synthetic polymers [7], mass resolutions $(m/\delta m)_{FWHM} \approx 500$ for M.W. < 20 kDa [6] and a 0.01% mass assignment accuracy using TOF-MS [8]. Furthermore, the short (< 1 hour) time for sample preparation and analysis, the relative insensitivity of MALDI to impurities and contaminants [8], the introduction of matrices effective at the N_2 laser wavelength [9-12] and the subsequent femtomole analyte sensitivity attained [12] quickly led to MALDI becoming a commercially available tool for chemists and biologists.

Analysis of MALDI products with magnetic sector [13,14], quadrupole ion trap [15] and, most notably, Fourier transform ion cyclotron resonance (FTICR) [16-22] instruments improved the mass resolution and accuracy compared to standard TOF-MS;

for example, MALDI FTICR analysis has achieved $(m/\delta m)_{FWHM} \approx 90\ 000$ for bovine insulin (M.W. = 5733.5 Da) [18, 22] and $(m/\delta m)_{FWHM} \approx 1\ 500\ 000$ for bradykinin (M.W. $\approx$ 1060 Da) [19], sub-femtomole sensitivity [23] and a mass assignment accuracy of better than 12 ppm [24,25]. Electrospray ionisation (ESI) [26,27] has emerged as a complementary, or perhaps rival, technique to MALDI in providing an expedient and efficient method of producing intact high mass ions. ESI is generally better suited to the above (non-pulsed) mass spectrometers but suffers from producing very many multiply charged ions of each analyte species rendering analysis of mixed analyte samples highly complex [28].

However, more recent developments in MALDI TOF-MS have seen the technique attain attomole sensitivity [29], a mass limit of ~ 1 MDa [30,31], a mass assignment accuracy of better than 10 ppm [32] and $(m/\delta m)_{FWHM} \approx 12\ 500$ for bovine insulin [33] using delayed ion extraction (see § 2.5). Furthermore, the different samples analysed with MALDI now include: low molecular weight molecules (e.g. monosaccharides and amino acids) [34-36], DNA [37-48], RNA [49], oligodeoxynucleotides [50], synthetic polymers [51-63], fossil fuels [64-68], vitamins [69], oligosaccharides [70-73], peptides [74-78] as well as a range of globular [1,4,5], fibrillary [79], enzymatic [1,4-6,80], odorant binding [81] and highly glycosylated [80,82]. Naturally occuring protein and peptide mixtures have also been analysed including those present in milk [83-85], bacteria [86], vitreous humuor [87] and neurons [88].

2.2 Sample Preparation

The simplest method of MALDI sample preparation is the original *dried droplet* technique [1,3-5]. A premixed solution containing both matrix and analyte molecules is deposited onto a substrate (alternatively, matrix and analyte solutions can be mixed on the substrate) and is allowed to crystallise, usually in air at room temperature [1,3-6] but sometimes under a stream of dry nitrogen [89] or hot air [90]. Typical solution concentrations are 10 g.litre^{-1} for matrices and between 0.1 - 1 g.litre^{-1} for analytes, with the solutions being mixed equivolumetrically. Samples can further be washed with

purified water [6] to remove surface contaminants such as alkali metals, inorganic salts, detergents and involatile liquids. The substrates are usually metallic (e.g. Ag [3,4], Al [3], Pt [8], stainless steel [6]) plates, foil or pins, depending on the mass spectrometer although non-metallic substrates have been used [91-95] as ion-exchange media in order to increase detection sensitivity and tolerance to impurities. Solvents used are typically a mixture of water and an organic solvent (e.g. acetonitrile, methanol, ethanol), often with a small addition (0.1 % vol.) of trifluoroacetic acid (TFA; CF_3COOH) to improve matrix solubility. The choice of solvent for each matrix can influence the efficiency of MALDI [95] although care should be taken that analyte molecules are not fragmented or modified in solution.

The crystals produced using the dried-droplet method are often highly heterogeneous in nature and thus reduce the spot-to-spot reproducibility of MALDI signals. Attempts to improve the sample homogeneity have included: spin-coated samples [96], recrystallising dried samples by depositing further solvent [96], growing of protein-doped matrix single crystals [97], air-brushing [98] or electrospraying [99,100] a premix solution onto the substrate and the formation of matrix thin films. Thin films have been produced by rapid solvent evaporation (acetone) [101] and by smearing matrix crystals with a glass slide [102]. Analyte molecules are incorporated into the matrix by subsequent deposition of a premix solution, with the original matrix film acting as a growth template. In this case the samples display a greater degree of homogeneity than is observed with simple dried-droplet preparation. This bears similarities to the method of drying a pure matrix solution and then depositing analyte solution for the case of analyte insolubility in water [103]. Introduction of a premix solution to the mass spectrometer in aerosol form [104-106] eliminates the need for a substrate and a greater degree of homogeneity can be achieved by controlling the size of aerosols. Alternatively, signal reproducibility from dried-droplet samples can be improved by using relatively large laser spot sizes [107].

2.3 Physical Processes

Over the past ten years, a general picture of the basic steps in MALDI has emerged, albeit highly qualitative in form. The current understanding of the physical processes involved in MALDI is now briefly described:

2.3.1 Crystal Structure

Solution grown matrix crystals can be up to 1 cm in length and are of non-uniform thickness and distribution on the substrate [96,97], although their appearance varies from compound to compound. An important facet of MALDI matrices is the ability to incorporate analyte molecules within their crystal structure. Spectrophotometry of single crystals formed from a mixed solution of the matrix 2,5-dihydroxybenzoic acid (2,5-DHB) and horse heart cytochrome c (M.W. 12 360 Da) [12] showed the solid matrix:analyte ratio to be approximately that of the original solution, although at higher analyte solution concentrations the crystal matrix:analyte ratio tended to saturate. Mass spectrometric analysis of the crystals suggested the analyte molecules to be homogeneously distributed throughout the matrix crystal whilst X-ray analysis showed the 2,5-DHB crystal structure to be largely undisturbed at large matrix:analyte mass ratios ($\sim 10^4$) [12]. Another matrix, sinapinic acid, was shown to incorporate proteins preferentially into one crystal plane [108], an observation later noted for 2,5-DHB [109]. This has been attributed to matrix dimers forming planar structures held to each other by hydrogen bonding [108-110]. Hydrophobic molecules such as proteins can then be incorporated between these matrix sheets as other directions have stronger hydrophilic reactions [108]. This incorporation and isolation of proteins is in preference to the inclusion of contaminants to the MALDI process [97,102], the proteins crystallising before the more soluble contaminants e.g. inorganic salts [107]. As the deposited matrix:analyte ratio decreases, pure analyte crystals form on the substrate [90,111] in addition to the analyte-doped matrix crystals, consistent with the observation of analyte concentration saturation in matrix crystals, mentioned above.

2.3.2 Energy Absorption

It is assumed that most of the laser energy incident on a MALDI sample is absorbed in matrix molecules since analyte absorption is usually very weak at the exciting wavelength (by design). For UV wavelengths, absorption is observed as a vibronic transition in matrix molecules. The lack of samples of uniform, sub-micron thickness possessing large areal coverage (~ 1 cm^2) suitable for measuring solid state matrix absorption coefficients, α, has led to the use of arbitrary units rather than absolute values for α [109]. Solution phase absorption measurements [108,109,112-114] have been used to estimate α for modelling purposes [115] and suggest the solid phase absorption depth, at the wavelengths of interest, to be a few hundred nanometres. However, it is known that molecular crystals often have modified optical spectra as compared to their solutions [109] and hence estimates of α from solution measurements may be subject to considerable uncertainty. Furthermore, the maximum matrix absorption cross-section may change (usually increase) in a transition from the solid to the gas-phase in the MALDI desorption step [116].

Following the absorption of a UV photon, molecules will relax to the lowest available vibrational level in the lowest excited electronic singlet state, S_1, on a picosecond timescale [117]. Molecules may then either undergo intersystem crossing to the triplet manifold or relax to the ground state, S_0, by radiative (fluorescence) or non-radiative (internal conversion) mechanisms (see Chapter 5 for details). Matrix fluorescence quantum efficiencies have been estimated to be between 0.11 - 0.20 and the total decay lifetime of S_1 to be between 3 - 5 ns [109,118] (see Chapter 5 for details). Internal conversion processes will lead to heating of the matrix molecules. Matrix absorption from S_1 or triplet states could possibly lead to cyclic non-radiative relaxation resulting in the rapid heating of matrices (cf. ref 119 for polymers under intense UV illumination).

Changes in laser wavelength have been used to tune to the maximum in matrix UV absorption and hence lower the threshold fluence for the observation of ions [113]. However, tuning IR laser wavelengths across an absorption band was reported as having

little effect on the MALDI process [120]. In one study it has even been suggested that absorptivity has little influence on MALDI as a whole, although in that study several other molecular parameters also changed [121].

Due to the lack of analyte fragmentation in MALDI, it is thought that the temperature of analyte molecules remains relatively low throughout the desorption process. The energy transfer within an analyte-doped matrix crystal undergoing desorption has been modelled with the rate of transfer from matrix to analyte molecules being a slow (non-resonant) process compared with fast matrix-matrix and matrix-lattice interactions [115]. The result was a 'bottleneck' in the temperature of the analyte molecules, this rising by only ~ 100 K in 100 ns compared to a rapid rise in the matrix temperature of ~ 500 K in less than 20 ns.

2.3.3 Desorption and Ionisation

Although desorption and ionisation both deserve independent treatment, many experiments and models are presented in terms of *ion yield*, i.e. dependent on both desorption and ionisation, hence their combination into one section here. As a note on terminology, within the mass spectrometry community the term *desorption* describes the production of intact gas-phase molecules, regardless of the mechanism [122], and not simply the opposite process to surface adsorption.

Desorption is thought to commence promptly, taking place within the (ns) laser pulse [123]. Several measurements of initial velocity [98,124-127] and angular distributions [109,128] of desorbed MALDI species have been made. Motion is directed away from the substrate and matrix ions display a bi-modal axial velocity, having a fast mode velocity of between 1000 - 1500 $m.s^{-1}$ [109,124] and a slow mode velocity of between 300 - 800 $m.s^{-1}$ [98,99,124], depending on the experimental conditions and the particular matrix used [129]. Such a distribution bears a close similarity with that of directly desorbed C_{60} [130], the slow mode having a translational temperature close to the sample surface temperature. Analyte ions, despite their much larger mass, possess velocities matching those of the slower matrix mode [98,99,124] and, interestingly, the slow mode matrix ion signal is reduced when analyte molecules are present in the sample

[99]. The angular distribution of ion velocities does not follow a $cos\theta$ law, expected for a thermal emission process, but instead a $cos^{2.4}\theta$ law has been reported [99] highlighting the directed nature of the desorbed plume (although, the plume is directed slightly towards the direction of laser incidence and not normal to the substrate [99,131]). Furthermore, samples with a greater surface coverage, thus giving a larger desorption yield, provide plumes with less radial divergence and a greater axial velocity [132].

It is therefore thought that desorbed matrix molecules undergo a jet-like expansion with analyte molecules becoming entrained in the slower matrix mode [98,99,124-128]. The jet expansion, which supports rapid (< 10 ps) intermolecular (matrix) energy redistribution [133], serves to vibrationally cool molecules thus largely preventing analyte molecules from fragmenting. This has been modelled by giving matrix molecules in an analyte-doped crystal a stepwise increase in temperature to simulate absorption of laser energy [134]; a higher matrix temperature rise actually gave a lower analyte temperature rise since desorption was more complete and an analyte molecule underwent fewer collisions with 'hot' matrix molecules. This is in contrast to original proposals that analyte molecules with several attached matrix molecules are desorbed and that subsequent evaporation of the matrices from these clusters provides the cooling mechanism [5].

In terms of desorption mechanisms, Vertes and Gijbels [133] present phase explosion and pressure pulse ejection as plausible models for desorption, with phonon avalanche, electronic transitions and stress-induced cracking regarded as unlikely contributory processes. Johnson [135] details quasi-thermal evaporation, layer-by-layer ejection and a pressure pulse model as possible desorption mechanisms. Quasi-thermal evaporation is argued to display a strong power law dependence upon laser fluence whilst layer-by-layer ejection (with negligible solid-phase thermal transport) is suggested to display a threshold fluence that is dependent on the laser beam angle of incidence. Johnson suggests that desorption might commence as quasi-thermal evaporation at low fluences with either layer-by-layer or volume (pressure pulse) ejection becoming dominant at higher fluences.

Molecular dynamics simulations have been performed to model MALDI desorption [136,137]. Zhigilei *et al* [136] used a *breathing sphere* model for molecules to allow photochemical fragmentation and approximate internal degrees of freedom. The modelled desorbed plume possessed axially oriented kinetic energy due to laser induced pressure expansion with molecules gaining a maximum velocity of between 600 - 1500 $m.s^{-1}$, dependent on fluence. At low fluences, intense surface vaporisation of single gas-phase molecules appeared to dominate. At higher fluences, an additional process of collective ejection (ablation) of molecules and clusters was observed, producing higher plume velocities than for sublimation. These (modelled) observations are in good agreement with experiment and lend weight to the suggestion that MALDI desorption evolves from two different mechanisms, as outlined above.

Analyte ionisation can take place over several hundreds of nanoseconds [5,126]. This usually takes the forms of protonation ($[M+H]^+$, where M represents an analyte molecule) or cationisation ($[M+Na]^+$ or $[M+K]^+$) for positive ions and deprotonation ($[M-H]^-$) for negative ions [5,133,138], although the radical molecular ion (M^+) has been observed for synthetic polymer analytes [139]. Interestingly, it has been commented that positively charged analyte ions undergo a greater degree of fragmentation than negative ions [140]. Another common observation is that of matrix adduction to analyte ions (e.g. $[M+m]^+$, where m represents a matrix molecule) [8], a feature of matrices that is considered undesirable since it may limit resolution of analyte peaks. Also, analyte ions are commonly observed to contain more than one charge (e.g. $[M+2H]^{2+}$; see refs. 1-5). Cationisation usually diminishes with successive irradiation of a sample region since Na^+ and K^+ ions are situated close to the surface of matrix crystals [107] but was shown to be greatly enhanced by desorbing analyte molecules into a Na^+ rich environment and delaying the extraction field by a few hundred nanoseconds [141]. This, coupled with the long analyte ionisation times (see above), led to gas-phase reactions being considered the most likely analyte ionisation route [141]. Although special cases have shown analyte ions to exist in matrix crystals [142-144], generally analyte ions do not appear until many neutral molecules have been desorbed (e.g. ref. 145), in support of gas-phase analyte ionisation.

Matrix ion suppression [90,146,147] at the expense of the formation of analyte ions clearly shows analyte protonation to arise from matrix-analyte collisional reactions. This is supported by the kinetic overlap between desorbed analyte molecules and the slow matrix mode, described above. In terms of the formation of $[M+H]^+$ analyte ions for UV-MALDI, the proton donor is considered to be either a matrix ion (usually $[m+H]^+$) [109,138,148] or an excited matrix molecule (m^*) [121,147,149,150]. For the former process, radical molecular matrix ions (m^+) are often assumed to be precursor ions [109,138,148] from which photochemical reactions create ions with different numbers of protons, characteristic to each matrix (e.g. $[m+H]^+$) [138]. m^+ ions are formed early in the incident laser pulse [118] and are proposed to result from collisional interactions between two photoexcited matrix molecules [138]. Usually, both m^+ and $[m+H]^+$ ions are observed in MALDI mass spectra [151] although matrices at room temperature that fail to yield m^+ ions can do so if cooled to 77 K prior to irradiation [149], supporting the hypothesis of precursor ions. Furthermore, thermalisation of laser energy by rear-side desorption [152] yielded no m^+ or $[M+H]^+$ ions, suggesting photoexcitation is a pre-requisite to their formation. For the alternative case of excited-state matrix-analyte proton transfer, matrix and analyte ion formation are considered as competitive rather than consecutive. Heavy atom substitution into matrices [121] increases the rate of intersystem crossing to the triplet manifold, thus increasing the lifetime of excited matrices. This was accompanied by an increase in the number of ions observed and was presented as evidence in favour of excited-state proton transfer.

Typically 10^3 - 10^4 matrix molecules are desorbed before ionisation takes place [125,153], although neutrals may be photoionised by a second (VUV) laser (e.g. refs. 98,145).

The variation of MALDI signals with laser fluence (F) or irradiance (I) is often expressed in terms of a power law relationship. The analyte ion signal is observed to rise steeply upon first being detected, reach a maximum level and then slowly decreasing with increasing fluence [122]. The neutral ***matrix*** desorption yield has been observed to scale as $\sim I^{1-3}$ [153], matrix ions as $\sim I^{2-4}$ [153] and analyte ions as $\sim I^{4-6}$ [125]. However, more rigorous measurements with a 3 ns (FWHM) N_2 laser showed neutral matrix desorption to vary as $\sim F^6$ before saturating at fluences where matrix m^+ ions appeared,

the ion signal increasing as ~ $F^{10.5}$ before reaching a plateau [145]. Analyte ions showed an identical fluence dependence to matrix ions. Furthermore, the neutral matrix yield showed a square dependence upon the laser spot area (A) whilst that of matrix ions varied with A^3. The strong dependence of the matrix ion yield on fluence was explained in terms of Johnson's quasi-thermal sublimation desorption model [135], described above. Interestingly, repetition of these experiments with a 0.55 ns (FWHM) N_2 laser [154] showed neutral and ionised matrix signals to appear at fluences higher than for 3 ns irradiation, despite the irradiance being almost a factor of 6 times greater for the short laser pulse.

A phenomenological model [116] has been used to replicate the analyte ion dependence on irradiance given by Ens *et al* (~ I^{4-6}; see above) [125] and from varying laser focal spot diameters by changing the distance between sample and lens [155]; a Gaussian laser irradiance profile is assumed with local sample regions that receive greater than the thereshold energy emitting a fixed number of gas-phase ions. However, this is in contradiction to later experiments described above where the ion yield is truly shown to be a function of fluence by using an imaged laser beam [145,154].

Laser thresholds have been given both in terms of irradiance (e.g. refs. 122 and 125) and fluence (e.g. refs. 155 and 156) although Beavis [116] hinted at neither irradiance or fluence being the governing parameter but rather a combination of the two, i.e. sufficient energy over a sufficiently short length of time. The threshold laser irradiance, I_{th}, and fluence, F_{th}, have been defined in many different ways but Dreisewerd *et al* [147] noted that they will tend to be specific for the onset of the detection of ions in a particular mass spectrometer.

I_{th} for analyte ions using typical laser pulse lengths (3 - 20 ns) appears to be in the 1 - 2 $MW.cm^{-2}$ region [98,122,125] but reported values of F_{th} have a much larger range of 1 - 50 $mJ.cm^{-2}$ [135,145,155,157,158]. Reports of matrix and analyte thresholds have disagreed in showing them to be equal [145] or different (matrix F_{th} < analyte F_{th}) [98,128,158] although the increase in F_{th} with analyte mass [156] and the existence of a matrix:analyte ratio giving a minimum analyte F_{th} [157] support the likelihood of unequal threshold values. F_{th} decreases when irradiating single crystals rather than dried-droplet

samples [12] and liquid rather than solid matrices [158] but remains constant for both positive and negative ions [158]. F_{th} was observed to have a $cos\theta$ relationship with the laser angle of incidence [156] and was thus argued to support Johnson's pressure-pulse model of desorption [135] (see above), although the experimental data do not separate desorption from ionisation. F_{th} was determined to be approximately equal for 3 ns and 560 fs pulse length lasers [160] and fluence was therefore argued to be of more importance than irradiance. However, the ion yield - fluence relationships were markedly different for the two pulse lengths and so different desorption or ionisation mechanisms may be involved. Interestingly, two collinear sub-threshold laser pulses (each 0.6 F_{th}) were used for MALDI [161] and an optimum delay time between the pulses observed. Repeated irradiation of a dried-droplet sample reduces the ion yield and increases F_{th} [128,158], possibly due to photochemical changes in the matrix molecules or that F_{th} depends on local crystal size. However, these sample exposure effects are not reported for single crystal samples [12].

2.3.4 Post-source Decay

Post-source decay (PSD), or metastable decay, describes the post-acceleration fragmentation of molecules, i.e. in the field-free flight tube for TOF-MS. The degree of analyte PSD generally increases with laser fluence [109], although exceptions to this rule have been reported [127]. Analyte PSD is observed to decrease with repeated irradiation of a sample region [158] and is dependent on the matrix. For example, α-cyano-4-hydroxycinnamic acid (α-CHC) can promote analyte PSD strongly [162,163] due to its low proton affinity [82,150,164] and (consequent) high enthalpy of formation of $[m+H]^+$ [165]. PSD was regarded as a drawback in MALDI for several years [1,3,5,115] but more recent analysis using reflectron-TOF-MS [126] with delayed ion extraction (see §2.5) [166], has allowed sequence specific cleavages in carbohydrates, oligosaccharides, oligonucleotides and peptides to be observed [35,71,78,167-170]. PSD therefore provides a MALDI sequencing technique complementary to collisionally induced dissociation (CID) [69,172-177] and chemical pre-treatment [36,44,77].

2.3.5 Clustering

Analyte molecules in MALDI have a tendency to self-associate and form clusters [1,4,5,37], although it is not clear whether clustering takes place in solution, during crystallisation or in the gas-phase desorbed plume. Studies have shown that solution [177] or gas-phase [178] aggregation are both possible, although clustering has also been observed only for the first laser pulse incident on a given sample position [179]. Clusters of up to the 26-mer of bovine insulin (M.W. ~ 149 kDa) [180], the 15-mer of chicken egg lysozyme (M.W. ~ 215 kDa) [181] and the 8-mer of BSA (M.W. > 500 kDa) [181] have been observed without any special preparative procedures. Increasing laser fluence [180], increasing analyte concentration [182], utilising matrices with a relatively high proton affinity, e.g. sinapinic acid [182], and the use of a conductive substrate [182] all enhance cluster formation. However, low proton affinity matrices, e.g. α-CHC (see §2.3.4), or a non-conductive substrate increase the number of charges available and thus promote mutliple charging of analytes rather than clustering [182]. Multiply charged analyte clusters are readily observed though, e.g. the doubly charged carbonic anhydrase trimer [20].

2.4 Matrices and Lasers

Useful MALDI matrices tend to be organic molecules in the 150 - 250 Da mass range. Qualities of matrices that enhance their performance in MALDI can be derived from the previous sections in this chapter and may be summarised as:

- Strong absorption at laser wavelength
- Low sublimation temperature
- Non-discriminatory inclusion of analyte molecules into their crystal structure
- Insensitivity to contaminants
- Support desorption of analyte molecules
- Efficiently ionise analyte molecules
- Display a low degree of adduction to analyte ions

The 'trial and error' basis upon which matrix screening has been based is a result of this wide range of criteria and that no chemical group is essential in matrix compounds [6,149,183].

Commonly used matrices for UV-MALDI include ferulic acid [9,10], sinapinic acid [9,10], 2,5-DHB [12] and 2-(4-hydroxyphenylazo)benzoic acid (HABA) [7] for general (high M.W.) analysis [12] and α-CHC [11], picolinic acid [49], 3-aminopicolinic acid [38] and 3-hydroxypicolinic acid [39] for analysis of low mass proteins, peptides and DNA. Less common UV matrices include basic molecules for acid sensitive species [184], liquids [160], laser dyes [185,186] and many others for specific analyte analysis [8,56,74,75,112,114,187-189]. IR matrices include the more common UV matrices as well as urea and several carboxylic acids e.g. glycerol and triethanolamine [190]. Furthermore, the use of two or more compounds to form a *co-matrix* can improve analyte sensitivity and mass resolution [8,110,178,191-195].

Originally, 266 nm radiation was used in MALDI, either from a frequency quadrupled Nd:YAG laser [1,5,6] or a frequency doubled excimer-pumped dye laser [4], although the early matrices supported the use of 248 nm (KrF excimer laser) radiation [111]. The discovery of matrices suitable for different wavelengths allowed the use of XeCl (308 nm) [125], N_2 (337 nm) [138], p-terphenyl dye (343 nm) [146], XeF (353 nm) [26,196] and frequency tripled Nd:YAG (355 nm) [9,10] lasers in the UV. Furthermore, Er:YAG (2.94 μm) [190], CO_2 (10.6 μm) [197], and free-electron [198] lasers and a Cr:LiSAF-pumped optical parametric oscillator (2.65 - 3.2 μm) [120] have been used for IR irradiation, whilst a frequency doubled Nd:YAG laser (532 nm) [186] has provided a visible wavelength source.

2.5 Time-of-flight Mass Spectrometers

MALDI and TOF-MS complement each other well since MALDI is a pulsed technique (a pre-requisite for TOF-MS), creating mainly singly charged monomer ions of M.W. ~ 10^5 Da or greater, and TOF-MS is highly sensitive and has a theoretically unlimited mass detection limit.

The simplest TOF-MS consists of an ion source region with an applied DC extraction field (typically 15 - 30 kV over 1 cm) that accelerates ions, and a field-free flight tube, at the termination of which the ion is detected and its time of arrival recorded. Both regions are evacuated to increase the mean free path between collisions. Cotter [199] gives a mathematical treatment of simple TOF-MS, providing an expression for the highest attainable mass resolution and highighting the quadratic relationship between the mass to charge ratio of an ion (m/z) and its flight time (t). This relationship leads the simplest form of TOF-MS calibration [8]:

$$\frac{m}{z} = At^2 + B \qquad 2.1$$

where A and B are calibration coefficients. Calibration can be achieved by using the arrival time of two peaks of known mass, either as part of the spectrum to be calibrated (internal calibration [8,80,122]) or in a separate reference spectrum (external calibration [87]), and solving eqn. 2.1. However, changes in laser fluence and matrix can affect the calibration [87] due to variation in the initial velocity distribution of desorbed species. The relative mass independence of initial analyte velocities [98,109,124] (see §2.3.3) can create inaccuracies if calibrating using eqn. 2.1 although this can be alleviated by using calibration schemes that include initial ion velocities [200,201]. For synthetic polymers with a regular repeat unit, self-calibration based upon the mass difference between successive peaks can be applied [53,54].

Improvements to simple TOF-MS, for example, post-source focussing [202], pulsed extraction [203] and, more importantly, delayed extraction [32,33,204-210], have allowed the mass resolution to be improved greatly as described in §2.1 above. Typical delayed extraction times are of between 350 - 1 000 ns [33,204] although much longer 6 - 7 μs delays have been used [205].

A wire ion guide, along the central axis of the flight tube and held at a low potential (~100 V), improves the transmission efficiency of ions by focussing their trajectories and also improves the mass resolution [211]. A bipolar pulse placed onto a

wire ion guide can have the added effect of reducing the number of fast, low mass (matrix) ions that strike the detector [212]. This is also achieved by employing XY deflection plates, located immediately following the source chamber, with a pulsed monopolar potential [80]. Reflectrons (ion mirrors) are often used either to improve the mass resolution by compensating for the velocity spread in each ion species [1,33], or for the analysis of PSD [35,71,78,167,213-215] and CID [174,214] fragments. Curved field reflectrons, carefully operated, offer further improvements in mass resolution and fragment analysis [175,214,216-218]. Other modifications include an rf-ion trap source to act as a CID cell [171,219-222] and orthogonal desorption of ions into the extraction field to minimise velocity distribution effects [223].

Ions are most usually detected by using a hybrid multichannel plate (MCP) / electron multiplier arrangement (e.g. ref. 224). These detectors do, however, suffer from an electron or secondary ion emission yield that varies with the mass and kinetic energy of the incident species [224-227], leading to mass discrimination effects [225,228]. Despite this, and the varying efficiencies for different species, it has been shown to be possible to conduct quantitative MALDI analysis [229,230]. Alternative detectors have included a 'Faraday cup' ion-collector [231,232], an inductive detector [233], a superconducting tunnel junction detector [234] and a quartz crystal microbalance for detection of all desorbed molecules [128].

3 SAMPLE PREPARATION

3.1 Introduction

As described in §2.2, the samples produced for MALDI mass spectrometric analysis are highly non-uniform in appearance causing quantitative experiments to be subject to a considerable degree of uncertainty. This chapter describes efforts to reproducibly improve the controlled growth and uniformity of matrix samples. A brief description of instrumentation used is followed by an assessment of different preparative procedures.

3.2 Instrumentation

All MALDI mass analysis was performed using a Vestec Researchtec time-of-flight (TOF) mass spectrometer (VESTEC Corp., Houston, TX), shown schematically in fig. 3.1. Up to 24 stainless steel sample pins, tapered to 2 mm in diameter at each end to support samples, could be loaded into a carousel holder that allowed each target pin to be rotated about its long axis ensuring accessibility of the desorbing laser beam to all sample regions. With the carousel in place within the ion source chamber, a CCD camera / monitor link allowed an approximately x 100 magnified view of the selected sample tip. The target area was irradiated using either a N_2 laser (337 nm wavelength, 3 ns pulse width; type VSL - 337ND; Laser Sciences Inc., Cambridge, MA) or a XeCl excimer laser (308 nm wavelength, 10 ns pulse width; model 1030; Questek Inc., Bedford, MA), both operated at ~ 1 Hz with a measured ± 10 % fluctuation in pulse-to-pulse energy. Laser beams were attenuated using either a stepper motor driven fused silica wedge attenuator (935-5-OPT; Newport, Fountain Valley, CA) or filters made from aluminium-coated fused silica slides. The 45° angle made between the focussed laser beam and the sample surface gave laser spot sizes of typically 200 x 300 μm^2 (area based on measurements of laser spots on undeveloped Ilford FP4 [Ilford Ltd., Cheshire, UK] black and white photographic film). Either positively or negatively charged desorbed ions were then accelerated by typically 25 keV throught a two-stage extraction geometry (12 mm

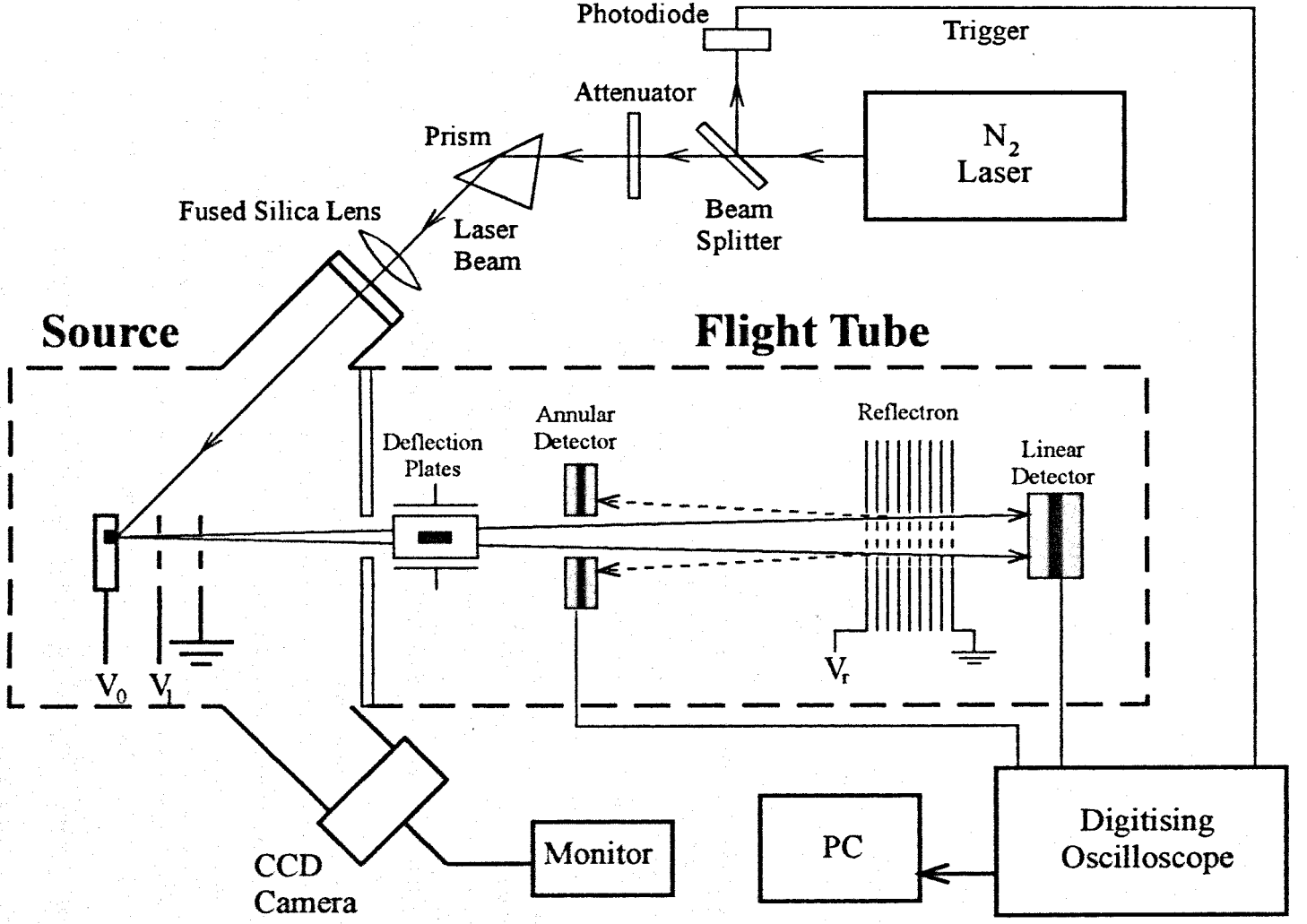

Figure 3.1. Schematic diagram of a Vestec Researchtec time-of-flight mass spectrometer.

total length) before entering a field-free flight tube of length 1.2 m. The ion source chamber and the flight tube were differentially pumped with turbo-molecular pumps to pressures of ~ 10^{-6} torr and ~ 5×10^{-9} torr respectively. Ion detection at the termination of the flight tube was achieved by using a hybrid microchannel plate (MCP; 1390-2500; Galileo Electro-optics Corp., Sturbridge, MA) - dynode electron multiplier (R2362; Hammamatsu Corp., Middlesex, NJ) system, optimised for sensitivity by application of a 3.6 kV accelerating potential. A 500 MHz TDS 520 Tektronix oscilloscope (Tektronix Inc., Beaverton, OR), triggered by the arrival of the laser beam, digitised the ion detector output and enabled averaging of the spectra resulting from successive laser pulses. Transfer of data to a PC and subsequent analysis using GRAMS software (Galactic Industries Corporation, Salem, NH) enabled conversion from time-of-flight to mass spectra. The reflectron (ion mirror) and XY deflection plates on the mass spectrometer were not used in the present work.

Scanning electron microscopy (SEM; Stereoscan 360, Cambridge Instruments, Cambridge, UK and Stereoscan 200, Leica, Cambridge, UK) of samples sputter-coated with a 200 - 300 Å gold layer was performed at an electron acceleration potential of 15 kV and a variable working distance.

Thickness measurements of samples deposited from solution were performed on a high resolution metallurgical optical microscope (Olympus BHM, ± 2 μm depth resolution; Olympus Optical Co. Ltd., Tokyo, Japan). Sublimed film thicknesses were estimated using a Dektak ^{3}ST profiler (Sloan Technical Division, Veeco Co. Inc., Santa Barbara, CA) with a 2.5 μm diameter stylus.

3.3 Standard Methodologies

Six matrices were chosen for study: ferulic acid (3-methoxy-4-hydroxycinnamic acid), sinapinic acid (3,5-dimethoxy-4-hydroxycinamic acid), 2,5-dihydroxybenzoic acid (2,5-DHB), α-cyano-4-hydroxycinnamic acid (α-CHC), coumarin 120 (7-amino-4-methylcoumarin) and nicotinic acid (pyridine-3-carboxylic acid), and the chemical structures of four of these compounds are shown in fig. 3.2. The proteins bovine insulin (M.W. = 5733.5 Da) and chicken egg lysozyme (M.W. = 14 306 Da) were used as analytes in the assessment of preparation techniques. All samples were obtained from Aldrich Chemical Company Ltd. (Gillingham, UK) with the exception coumarin 120 which was supplied by Lambda Physik (Göttingen, Germany). All compounds were used as supplied (stated purity 97 - 99.5 %) without any further purification.

The most common form of sample preparation for MALDI samples is the *dried-droplet* method from solutions, described briefly in §2.2. Ferulic acid, sinapinic acid and α-CHC (cinammic acid derivatives) were dissolved in 30% acetonitrile (ACN; aq) with 0.1% trifluoroacetic acid (TFA) added to the mixed solution, 2,5-DHB in 10% ethanol (aq) + 0.1% TFA, coumarin 120 in 50:50 ACN:methanol + 0.1% TFA and nicotinic acid in H_2O + 0.1% TFA. Proteins were dissolved in 30% ACN (aq) + 0.1% TFA when used with a cinnamic acid derivative matrix or H_2O + 0.1% TFA for all other matrices. Typical solution concentrations were 10 g.litre^{-1} for matrices and 1 g.litre^{-1} for proteins. All solutions were placed in an ultrasonic bath for between 5 - 10 minutes to ensure the removal of all solid material into solution. Standard dried-droplet samples were prepared by the deposition onto TOF pin substrates of either 1.5 μlitre matrix solution and 1.5 μlitre analyte solution or 3 μlitre of a pre-mixed (equivolume) matrix-analyte solution followed by air-drying at room temperature.

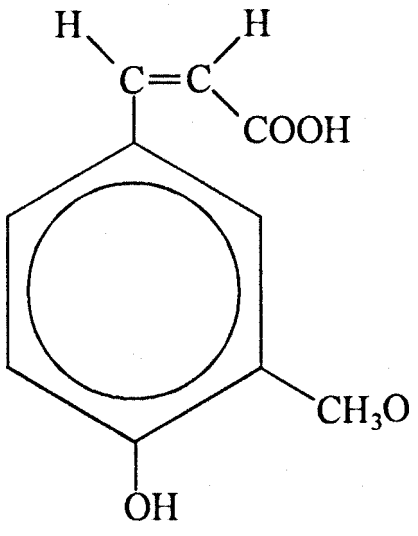

Ferulic Acid

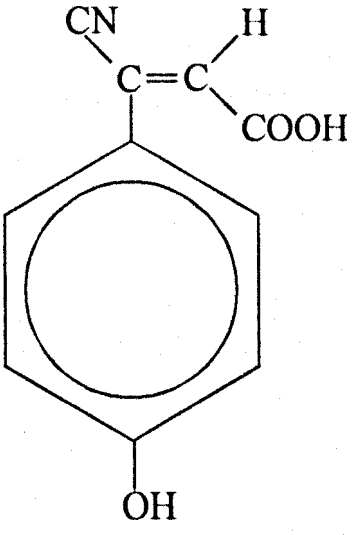

α-Cyano-4-hydroxycinnamic Acid (α-CHC)

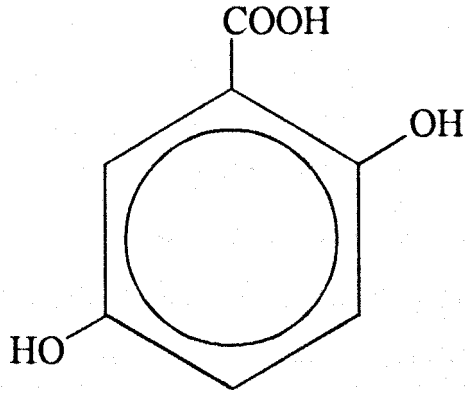

2,5-Dihydroxybenzoic Acid (2,5-DHB)

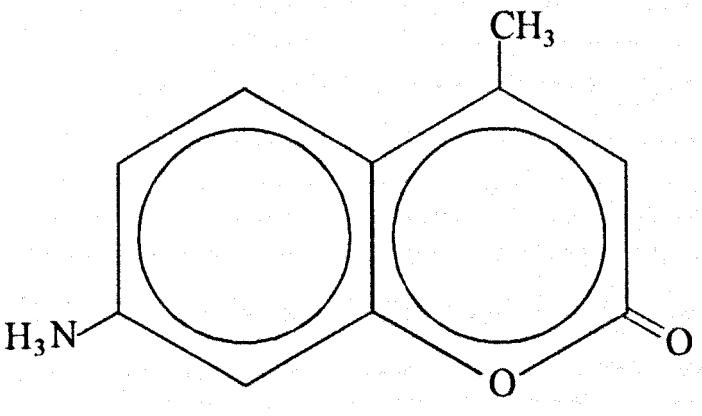

Coumarin 120

Figure 3.2. Chemical structures of several common MALDI matrices

3.4 Solution-based Samples

3.4.1 Preparation

In addition to the 10 g.litre^{-1} matrix solutions for standard dried-droplet samples, 15 g.litre^{-1} and 30 g.litre^{-1} solutions were used, although the latter concentration was often above the saturation point of the solvent; the saturated solutions were, therefore, centrifuged and the supernatant liquid removed with a pipette. When using 30 g.litre^{-1} based matrix solutions, proteins were dissolved to a concentration of 2 g.litre^{-1} in the saturated solution. Mixed matrix-analyte samples were deposited as described in §3.3 whereas pure matrix samples were formed by depositing 2 µlitre of matrix solution onto a TOF pin substrate before air-drying.

Samples based on either the 10 or 15 g.litre^{-1} matrix solutions were prepared for mass spectrometric or SEM analysis in one of the following ways:

i. standard dried-droplet;
ii. spin-coating: air-dried at room temperature at ~ 300 r.p.m.;
iii. refrigeration: air-dried at ~ 2.25°C;
iv. crushed: air-dried at room temperature and crushed;
v. refrigeration and crushing (RC): air-dried at ~ 2.25°C and crushed;
vi. refrigeration, crushing and recrystallisation (recrystallised-RC): as v. followed by application of 1 µlitre solvent and air-dried at ~ 2.25°C.

Saturated solutions were deposited in one of four ways:

i. 2 µlitre deposited on pin substrate, air-dried at room temperature; procedure repeated; crushed;
ii. 2 µlitre deposited on pin substrate, air-dried at room temperature, crushed; whole procedure repeated;
iii. 100 µlitre deposited on 12.7 mm diameter, 6 mm thick soda lima glass disc, air-dried at room temperature; procedure repeated; crushed;

iv. 100 µlitre deposited on 12.7 mm diameter, 6 mm thick soda lima glass disc, air-dried at room temperature, crushed; whole procedure repeated.

The stainless steel pins used in SEM analysis were ground with 240 grit metallographic grinding paper to remove their tapered end and give a diameter of approximately 2.2 mm. A few pins were polished with 1000 grit metallographic grinding paper and 60 µm lapping paper to give a much reduced surface roughness. Sample crushing was achieved using a polished aluminium plate with force being exerted manually through an elastic rod [102]. A little lateral rotation of the aluminium during crushing enhanced the quality of the samples but care had to be taken that the film was not destroyed by excessive movement of the aluminium.

3.4.2 Morphology

As noted in the Introduction (§3.1), dried-droplet samples suffer from poor homogeneity. The crystals in such samples vary in their size, orientation, phase and distribution across the substrate. Even isolated crystals may be highly heterogeneous, as can be seen from the SEM micrograph in fig. 3.3 which shows an α-CHC dendritic phase crystal. This crystal phase for the α-CHC matrix was sometimes quite prevalent within the standard dried-droplet samples, its dendritic structure being an artifact of fast solvent evaporation leading to an inefficient diffusion of released latent heat energy.

Refrigerated drying increased the drying time of 2 µlitre samples on tapered pins from approximately 15 minutes at room temperature to approximately 25 minutes. The effects of refrigeration on sample morphology can be seen in fig. 3.4, showing micrographs of both refrigerated and room temperature dried-droplet samples of ferulic acid and α-CHC. The slower drying in a refrigerated atmosphere induces a more homogeneous crystal growth with a greater level of macroscopic uniformity than for room temperature evaporation. In particular, when compared to room temperature drying, the refrigerated ferulic acid needle-like crystals display a greater radial directionality on the circularly tipped pins (fig. 3.4b) and refrigerated α-CHC samples show a more even distribution of crystals across the substrate (fig. 3.4d). Furthermore,

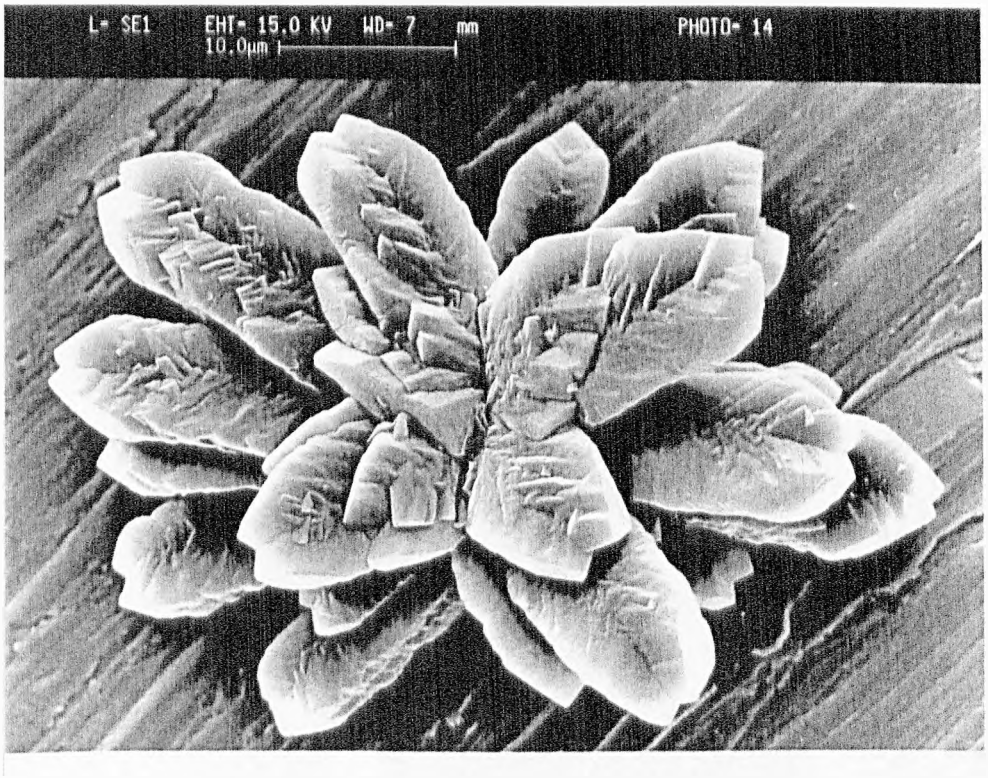

Figure 3.3. Scanning electron micrograph of a dendritic phase α-cyano-4-hydroxycinnamic acid crystal.

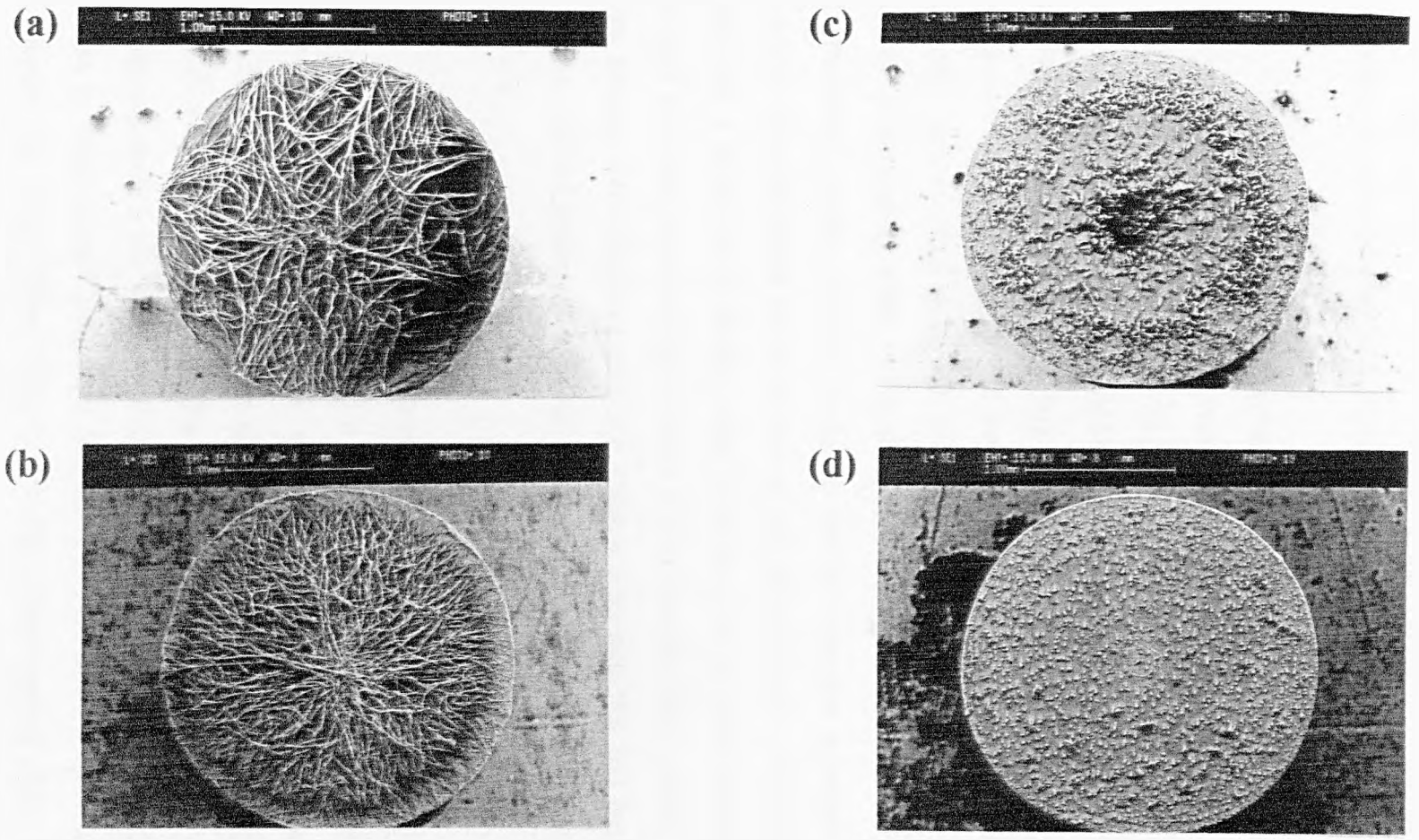

Figure 3.4. SEM micrographs illustrating the macroscopic effect of refrigerated drying on MALDI samples (10 g.litre^{-1}); ferulic acid: (a) room temperature dried-droplet, (b) refrigerated evaporation; α-cyano-4-hydroxycinnamic acid: (c) room temperature dried-droplet, (d) refrigerated evaporation.

the dendritic phase α-CHC crystal observed in samples dried at room temperature (figs. 3.3 and 3.4c) were found in a much reduced abundance within refrigerated samples. The size of the crystals remained largely unaffected by the increased drying time, with ferulic acid crystals retaining a long axis length of ~ 1 mm and α-CHC crystal dimensions remaining at approximately 30 x 40 μm^2.

Crushing samples with aluminium produced films of the material on the substrate, as reported for glass [102]. However, these films were formed over a wider area when crushing with aluminium than with glass, presumably because the metal is a softer material than glass (Mohs scale of hardness: aluminium ≈ 2-3, glass ≈ 4.5-6.5) and its resultant deformation allows a larger effective 'contact' area. Thus aluminium will compensate more for the almost certainly non-parallel contact between substrate and crushing material than glass will. Indeed, a depression in the aluminium surface was visible after crushing which corresponded to deformative contact with the substrate. Furthermore, greater pressure could be exerted onto the substrate with aluminium without incurring failure due to fracture as was often the case with glass. Brass, stainless steel and a single crystal silicon wafer were also used to crush samples but aluminium proved to be the better material in terms of film reproducibility, quality and coverage. A few samples were deposited onto the stainless steel pins that had been highly polished but these lacked cohesivity with the substrate and were removed almost completely by crushing.

Due to an insufficient amount of deposited material, the 10 $g.litre^{-1}$ matrix based samples never completely covered a sample substrate although it should be noted that after crushing, a little deposited material was observed to be smeared onto the aluminium. Figure 3.5 shows micrographs of crushed ferulic acid (figs. 3.5b-d) with a dried-droplet ferulic acid sample (fig. 3.5a) for comparison. A region of crushed matrix of approximately 1 mm^2 is visible (fig. 3.5b), having a thickness of up to 25 μm, and the extent to which sample uniformity is improved over dried-droplet samples is evident (compare fig. 3.5a). When viewed at higher magnifications (figs. 3.5c and d), the somewhat granular appearance of the samples, with dimensions from hundreds of nanometres to one micrometre, suggests that crushing standard MALDI matrices creates

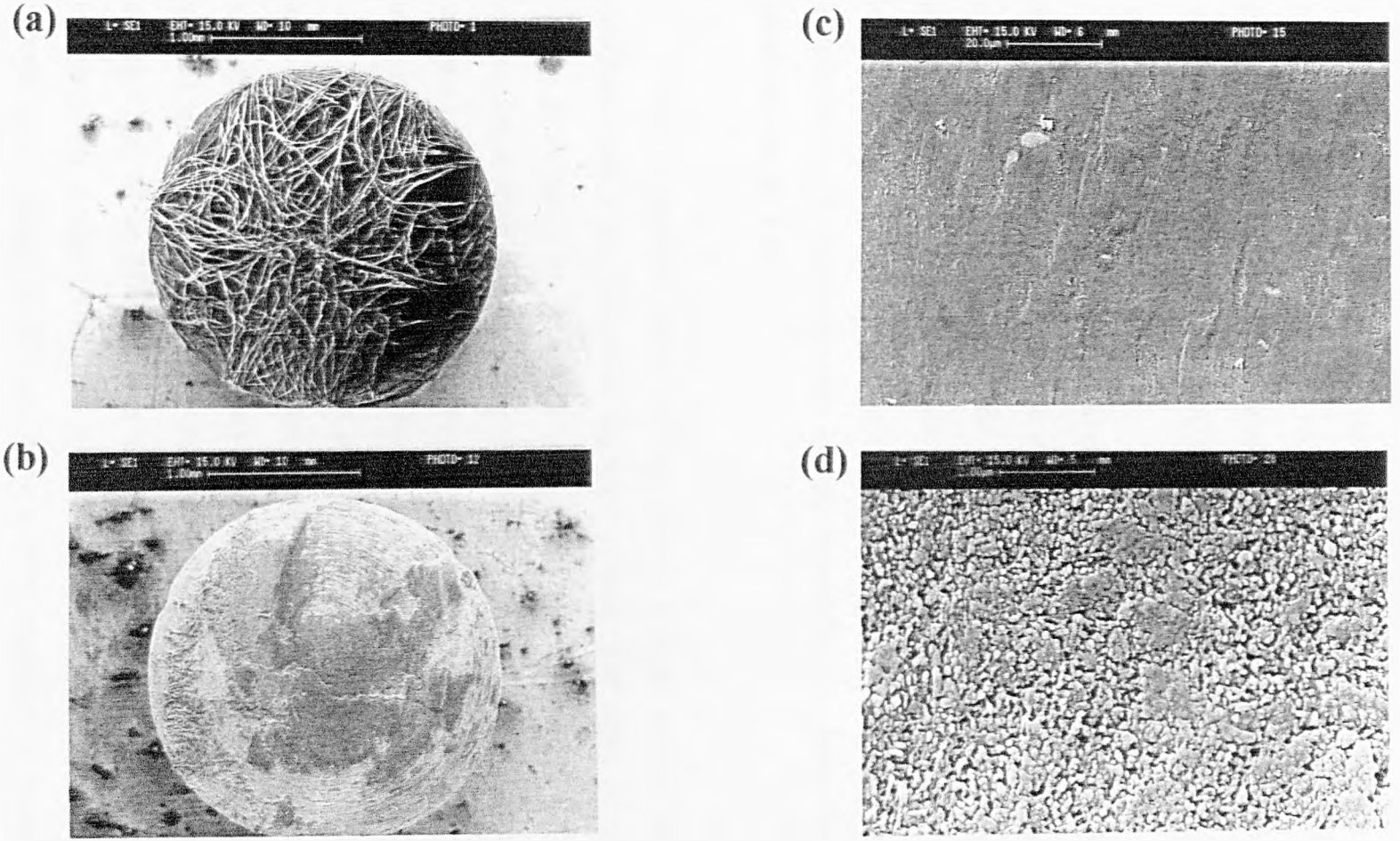

Figure 3.5. SEM micrographs of (a) ferulic acid dried-droplet sample, (b) crushed ferulic acid sample and (c) - (d) a crushed ferulic acid film at higher magnifications, all from 10 g.litre^{-1} samples.

a highly polycrystalline thin film with the larger dried-droplet crystals having been broken down mechanically. In general, crushed sinapinic acid samples showed substrate coverage similar to ferulic acid (fig. 3.5b), α-CHC and coumarin 120 showed evenly distributed but incomplete substrate coverage and 2,5-DHB samples were mainly concentrated around the edges of the substrate. Highly magnified SEM observations showed the different matrices to be remarkably similar in appearance, all displaying the sub-micron granularity described above. The inclusion of analyte protein molecules did not have any visible effect on the sample morphology.

With recrystallisation of samples being achieved by the application of 1 μlitre of solvent to a crushed sample, 15 g.litre^{-1} ferulic acid crushed and recrystallised-crushed samples are shown in fig. 3.6 a and b, respectively. Recrystallisation of ferulic acid appears to produce a large number of small crystals with a long axis length of approximately 10 μm. Presumably, the crushed polycrystalline film provides a growth environment rich in nucleation sites for any recrystallisation, hence the array of small crystals seen in fig. 3.6b.

Using a saturated matrix solution allowed a larger amount of material to be crystallised onto a pin from each deposited volume. The effect of this, upon either crushing procedure (i or ii), was to produce films of between 12 - 30 μm thickness covering larger areas of sample pins than for the 10 g.litre^{-1} based samples. However, small areas of the substrate again remained uncovered due to the removal of the sample onto the aluminium. Figure 3.7, showing a micrograph of a crushed saturated sinapinic acid / chicken egg lysozyme sample, demonstrates the existence of two morphological phases within the crushed film. Principally it is composed of a highly polycrystalline layer, with feature sizes ≤ 100 nm, and small (≤ 500 nm diameter) crystallites protruding from the surface. It is noteworthy that the magnification in fig. 3.7 approaches the resolution limit of the SEM for these samples and yet the granular nature of the film is only marginally evident. This limit is set by the back-scatter of electrons from the sputtered gold coating on the samples (a coating necessary to ensure the electrical conductivity of the surfaces) which displays large atomic number contrast to that of the low atomic mass elements in the matrices, and the inherently low resolution with which

(a)

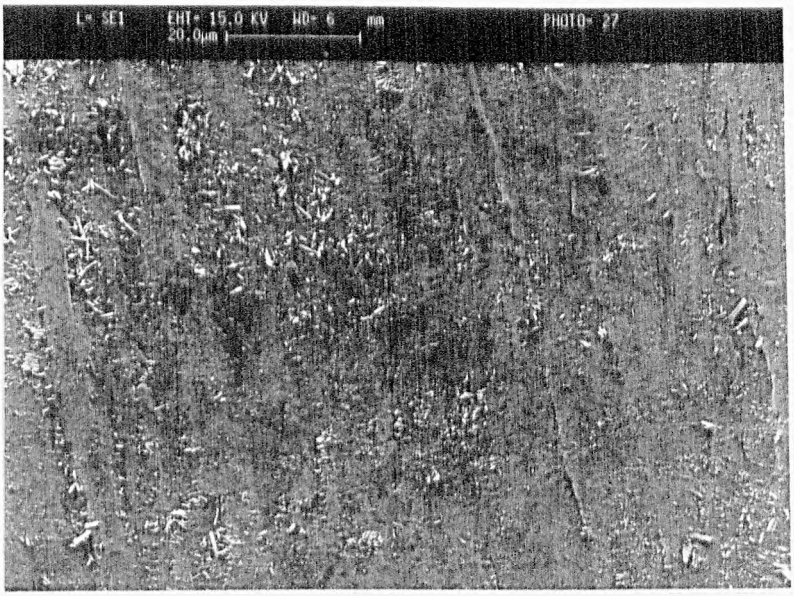

(b)

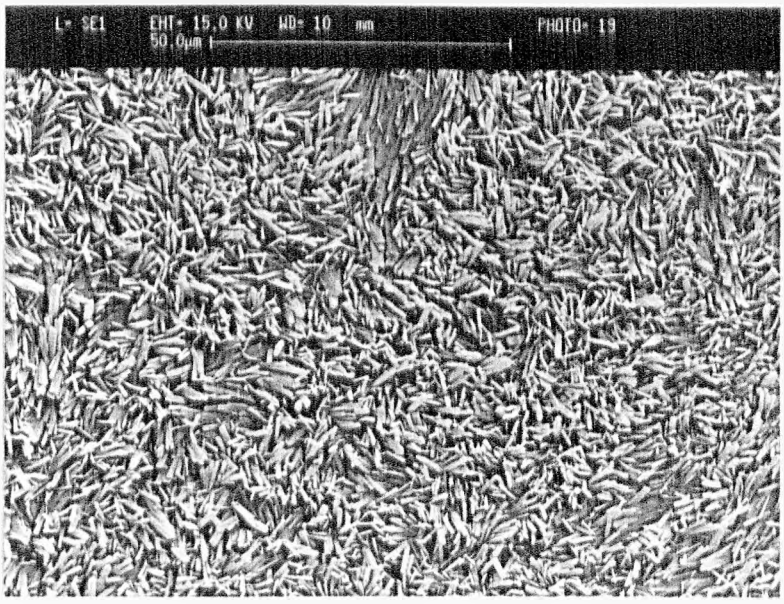

Figure 3.6. Micrographs of (a) 15 g.litre^{-1} crushed ferulic acid and (b) 15 g.litre^{-1} crushed ferulic acid, recrystallised by the application of 1 µlitre of solvent.

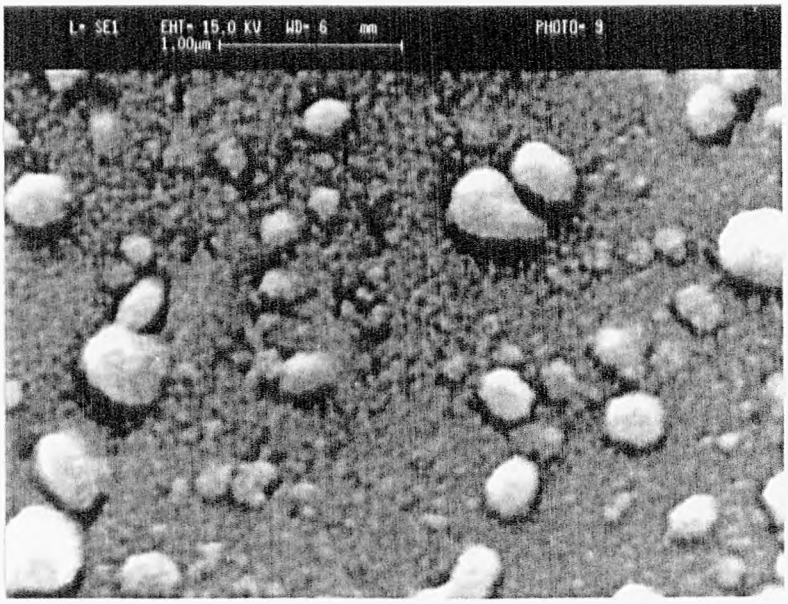

Figure 3.7. Micrograph of a crushed sample comprising sinapinic acid (30 g.litre^{-1}) and chicken egg lysozyme.

features are observed when relying upon topographical differences. Figure 3.7 does, however, represent the averaging of several scans to improve the image sharpness. The dimensions and morphology described above are typical for all of the matrices used, regardless of whether or not a larger 'analyte' molecule was included in the sample preparation.

Depositing and crushing dried concentrated solutions on glass disc substrates proved to further enhance the quality of the films, both in terms of areal coverage and surface morphology, as illustrated in the micrographs in fig. 3.8. The dimensions of the film displayed are approximately 4 x 2 mm^2 in area (fig. 3.8a) and between 45 - 60 μm thick, the film appearing to be highly uniform across the entire region. Higher magnification observations (figs. 3.8b - d) showed a vast improvement in the surface roughness of the films over dried-droplet and crushed samples prepared on stainless steel pins. As the magnification approaches the resolution limit of the SEM (fig. 3.8d), the two morphological phases noted above are again evident. However, the granularity of the polycrystalline film is reduced in dimensions compared to that for samples prepared on stainless steel pins and the number-density of small crystallites protruding from the films is lower than previously observed.

The reproducibility of films formed from saturated solutions was such that approximately half of the samples achieved in excess of 70 % substrate coverage.

3.4.3 Threshold Fluences

There have been numerous methods of defining the 'threshold fluence' or 'threshold irradiance' for desorbed ions [128,145,155,158,159,235] in MALDI and because of this it is impossible to rigorously compare data from different sources. Nonetheless, individual experiments are of value in terms of the comparison they provide within themselves. In the present study using the mass spectrometer, the average molecular ion intensity was plotted as a function of fluence on logarithmic axes, the intersection of the linear fit of these points and the signal-to-noise (S/N) = 2 line being defined as the threshold fluence for ion detection, F_{th}. This procedure is illustrated in fig. 3.9. Each point was found by averaging the molecular ion intensity from between 4 - 8

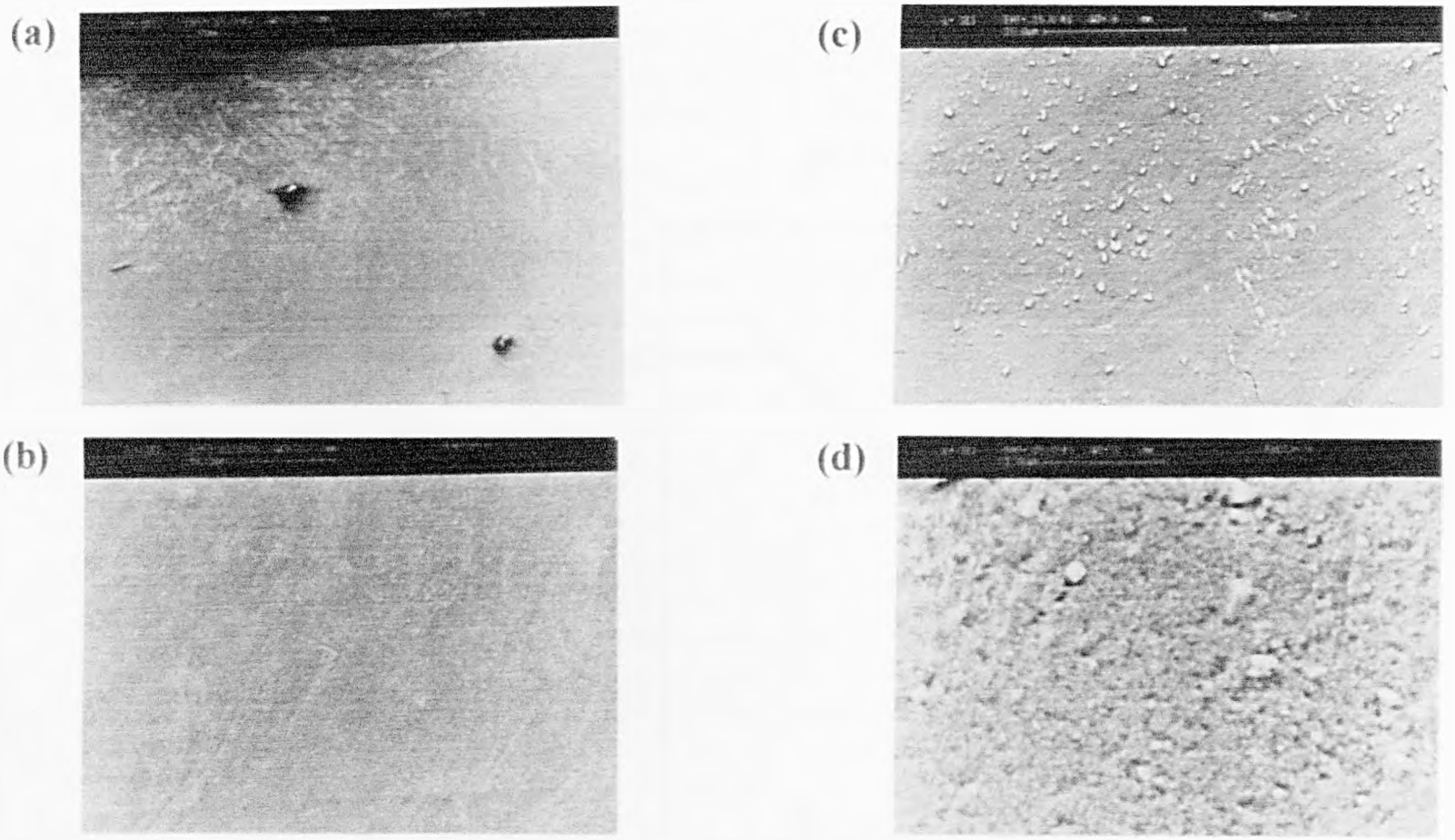

Figure 3.8. SEM micrographs of crushed ferulic acid, fabricated from a 30 g.litre^{-1} solution deposited on a soda lime glass substrate. Micrograph (a) displays the general uniformity of the sample, (b) - (c) show the surface in more detail, and (d) taken at high magnification, illustrates the both the reduced dimensions of the film granularity and the reduced number density of small crystallites present in samples crushed on glass rather than stainless steel

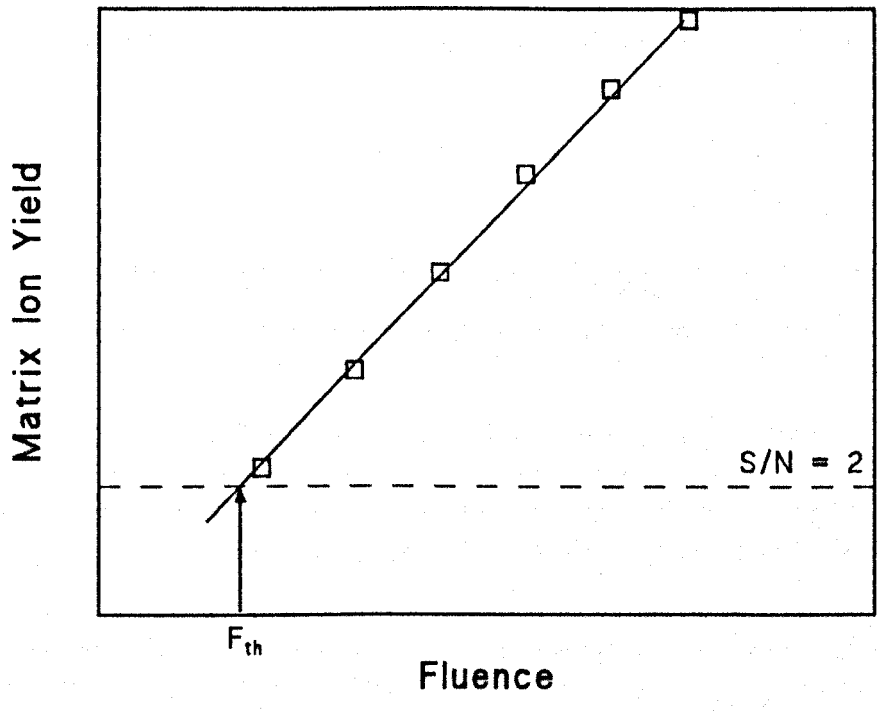

Figure 3.9. Example plot for determination of matrix threshold fluence for ion detection, F_{th}.

spectra, each of 4 - 6 shots and taken from different sample spots under nominally identical experimental conditions.

The measured peak signal intensity at different fluences for crushed and dried-droplet preparations of ferulic acid are shown in fig. 3.10. The error bar indicates one standard deviation of error in the ion data and is representative of all of the points. However, the fluctuation in laser fluence has been omitted from fig. 3.10. Obviously, the analysis of an increased number of spectra will reduce statistical errors in the data, although the detected matrix ion signals do initially show close agreement with a power law dependence on fluence before tending to saturate. The values of these power dependencies are approximately 9.7 and 10.5 for the crushed and dried-droplet samples respectively, in keeping with the high ion-fluence power law relationships that have been reported previously [125,145]. Values of F_{th}, as defined above, for samples prepared using the two techniques are designated in fig. 3.10 using arrows.

Table 3.1 summarises the results of different preparation techniques for the matrices studied. 2 μlitre aliquots of 10 g.litre^{-1} matrix solutions were used throughout with the exception of coumarin 120 where only 1 μlitre was deposited due to the lower viscosity of the solvent used. Pure matrix samples were investigated, rather than those incorporating proteins, to allow results to be more readily interpreted. The most striking observation is the drop in F_{th} for crushed samples from the standard dried-droplet samples, the decrease being ~ 15% for ferulic acid, 2,5-DHB and α-CHC. The recrystallised-RC samples, characterised by microcrystal formation, show F_{th} to lie between the crushed and dried-droplet values. Refrigeration-dried and spin-coated ferulic acid samples show a negligible change in F_{th} from that of dried-droplet samples.

One explanation for the reduced threshold fluence of a smooth, crushed sample might be found in terms of the lower effective surface area this presents to the incoming laser beam. We postulate that the desorption ion yield, Y, is a function of the mean laser energy deposited per unit volume of the sample, $\langle\Gamma\rangle$, of the form:

$$Y = A\left(\langle\Gamma\rangle\right)^m \qquad 3.1$$

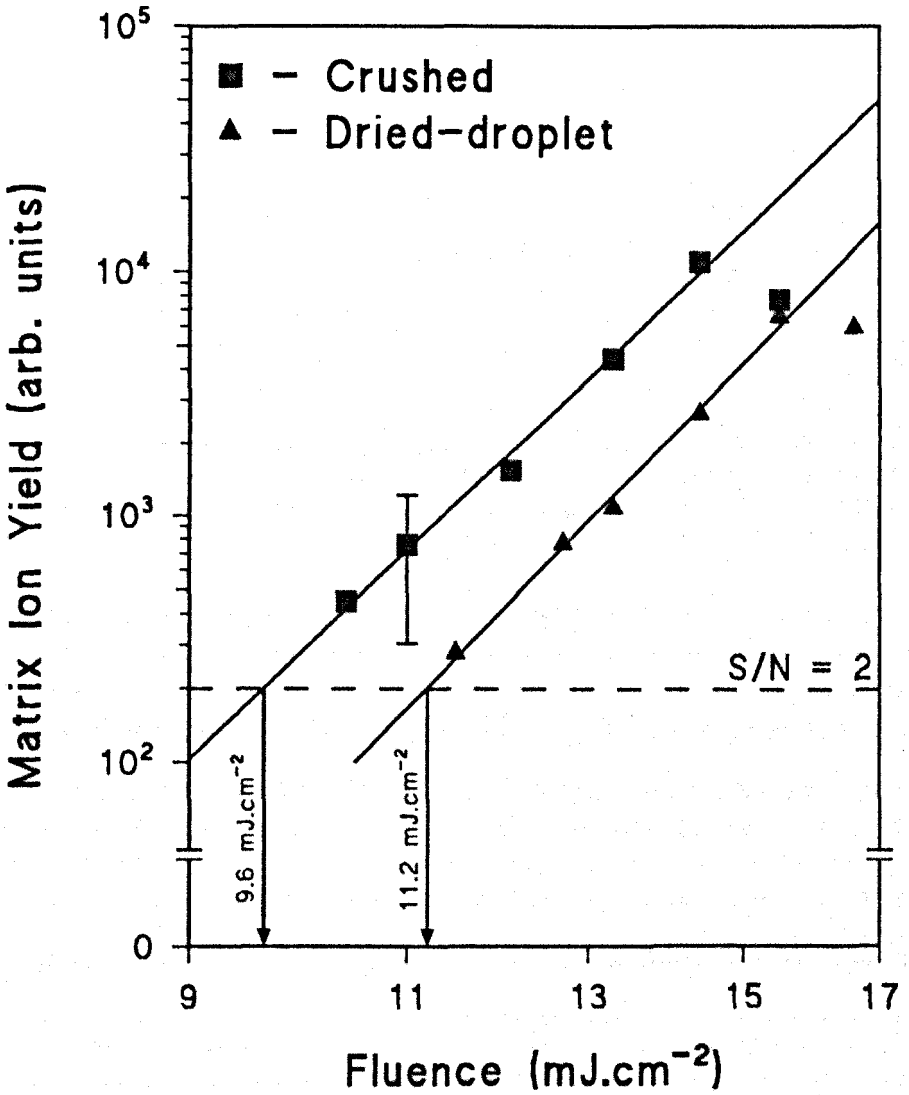

Figure 3.10. Determination of threshold fluence for detection of ferulic acid ions using crushed and dried-droplet preparations.

	SAMPLE PREPARATION					
	Dried-droplet	Spin-coated	Refrigerated (R)	Crushed (C)	RC	RC-recrystallised
MATRIX	FLUENCE ($mJ.cm^{-2}$)	PERCENTAGE DECREASE IN THRESHOLD FLUENCE COMPARED WITH DRIED-SROPLET PREPARATION				
Ferulic Acid	11.2	3 %	2 %	14 %	14 %	13 %
DHB	17.1	1 %	–	–	15 %	9 %
Sinapinic Acid	11.6	–	–	–	8 %	–
α-CHC	4.9	–	–	–	16 %	–
Coumarin 120	7.1	–	–	–	3 %	–

Table 3.1. Threshold fluence, F_{th}, for the observation of molecular ions of five different matrices from room temperature dried-droplet samples and the percentage decrease in F_{th} for various other sample preparations.

where A is a constant for a fixed laser spot size. To describe different surface roughnesses, ξ, we assume that this can be expressed in terms of a ripple amplitude, ξ_0, and characteristic spatial period, Λ, (fig. 3.11) such that $\xi=\xi_0 cos 2\pi x/\Lambda$. For a material exhibiting a complex refractive index $\bar{n} = n + ik$ ($n \sim 1.5$, $k \sim 0.1$ for MALDI matrices [115]) with $k^2 << 1$ such that the real form for Snell's law is approximately valid [236], the spatially averaged $\langle \Gamma \rangle$ is found to be:

$$\langle \Gamma \rangle = \{1 - R(\theta)\} F_0 \alpha \cos\theta \left[\frac{\sin^2\theta + 2n^2}{2n^2} \right] \left(1 - z\chi^2\right) \quad (\chi << 1) \qquad 3.2$$

where $z = \left[2\left(3\sin^2\theta - \cos^2\theta\right) + 2n^2\right] / \left(\sin^2\theta + 2n^2\right)$, $\chi=\xi_0\pi/\Lambda$ and $\alpha=4\pi k/\lambda$ is the absorption coefficient with λ being the laser vacuum wavelength. F_0 is the fluence of the incoming beam normal to its propagation direction, θ is the angle of incidence made with the (mean) surface (see fig. 3.11) and $R(\theta)$ the surface reflection loss.

If the threshold for desorption and ionisation is taken to be defined by some minimum ion signal, Y_{min}, (instrumentally defined), then from equations 3.1 and 3.2 the threshold fluence for a given sample at a fixed angle of incidence is

$$F_{th} = F_0 \cos\theta = B\left(Y_{min}\right)^{1/m} \left(1 - z\chi^2\right)^{-1} \qquad 3.3$$

where

$$B = \left(\frac{1}{A}\right)^{1/m} \frac{1}{(1-R)\alpha} \frac{2n}{\left(2n^2 + \sin^2\theta\right)} \qquad 3.4$$

There is thus a reduction in F_{th} if the surface roughness, characterised by the parameter χ, decreases; this arises because of the lower effective area of the smooth sample.

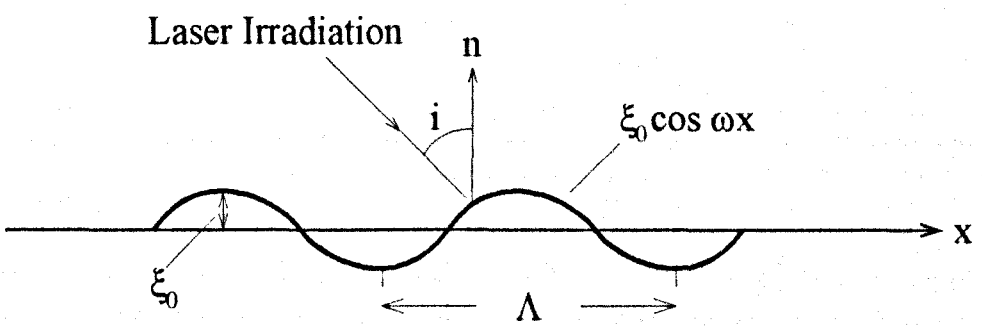

Figure 3.11. Surface roughness characterised by a ripple amplitude ξ and period Λ of the form $\xi = \xi_0 \cos \frac{2\pi x}{\Lambda}$. The incidence angle of the incoming beam to the (mean) surface is *i*.

3.4.4 Sample Performance

The standard (10 g.litre^{-1} matrix : 1 g.litre^{-1} analyte) RC (refrigerated and crushed) samples for mass spectrometry proved to have good pulse-to-pulse and spot-to-spot reproducibility for the analyte ion yield and it was very unusual for a fresh site not to yield signals. For example, at a fluence approximately 30 % greater than that required to observe an analyte ion, an insulin monomer peak from a ferulic acid matrix could be seen consistently and reproducibly for up to 15 consecutive shots at a single spot although such a peak was only seen for a maximum of 50 shots from any one irradiated site. Dried-droplet samples, however, have been reported on many occasions to yield analyte ions consistently for several hundred shots (see, for example, reference 128). That crushing MALDI samples lowers the maximum number of shots that each give rise to a detectable analyte ion signal from a single desorption site is consistent with the suggestions made by the Uppsala group [128] that smaller crystals yield analyte ions at lower fluences than larger crystals and are therefore depleted of the analyte molecules over successive laser pulses more quickly.

Figure 3.12 shows a positive ion time-of-flight mass spectrum of bovine insulin, prepared in a RC ferulic acid matrix. The spectrum is displayed having been smoothed to a minimal extent in order to improve the S/N ratio of the peaks and was obtained at a fluence approximately 30 % above the threshold for observation of an analyte monomer ion. The singly charged insulin signal ($[M+H]^+$) is shown with a measured peak width (FWHM) of ~ 5.6 Da, giving a mass resolution (m/δm) of ~1020; such a resolution is reproducible with RC samples and represents a good degree of accuracy for a linear TOF instrument with a DC accelerating field and an improvement in the resolution obtainable compared to standard dried-droplet samples when utilising such an instrument. As the fluence was decreased, the ion signal intensity was reduced, as expected, and spectra could be obtained with peak-widths even lower than that observed in fig. 3.12. However, such high resolution spectra are probably a result of only a few (<10) analyte ions striking the high gain dynode detector. It is unlikely that a realistic analyte isotopic mass distribution will be provided by such a small number of ions, the peak-widths measured being more representative of the instrumental response time.

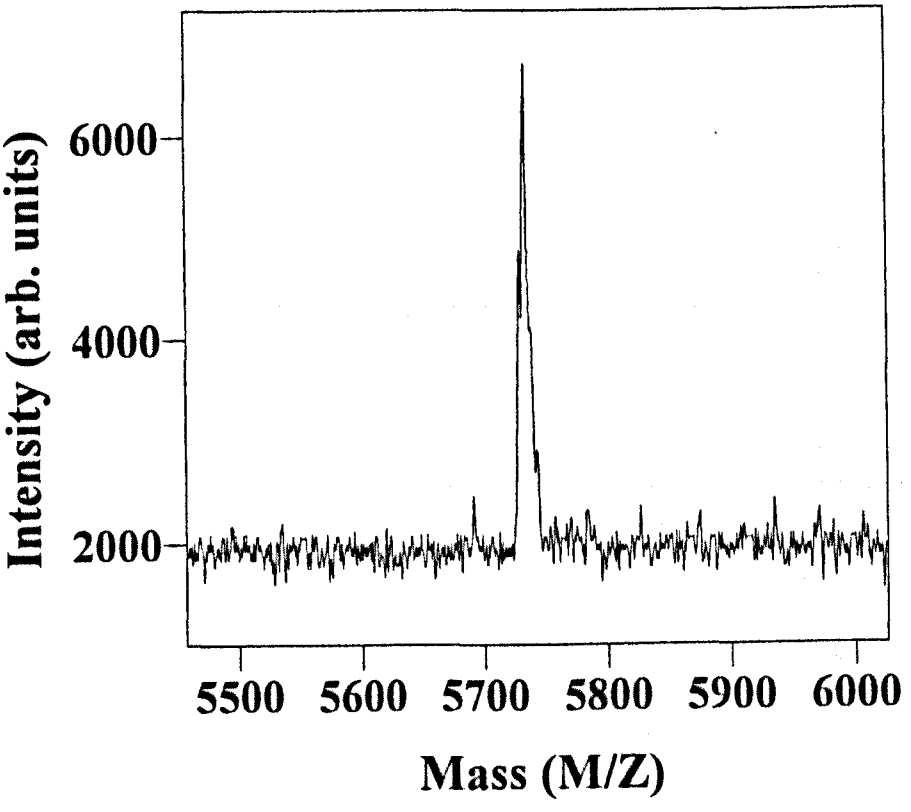

Figure 3.12. Single shot positive ion time-of-flight mass spectrum of bovine insulin from a refrigeration dried, crushed ferulic acid matrix, dislayed with minimal smoothening to improve the signal-to-noise ratio of the peaks. The peak shown represents the insulin monomer ion and was obtained at a fluence ~ 30 % above threshold.

RC samples prepared from saturated matrix solutions generally gave a higher proportion of matrix and impurity adduction to analyte molecular ions. For this reason they were regarded as inferior to the 10 g.litre^{-1} based RC samples for the purposes of mass analysis since a greater degree of adduction will decrease the resolution of the associated signal peaks. The mass resolution displayed in fig. 3.12 was not achieved by crushing samples alone; refrigeration of the samples appeared to positively influence the quality of the spectra obtained. Since refrigerated drying increased the time taken for complete solvent evaporation, a few samples (10 g.litre^{-1} matrix solutions, 1 g.litre^{-1} analyte solutions) were dried in a slight overpressure of the solvent to further increase the drying time, again at ~ 2.25°C. Mass spectra from these samples showed analyte molecular ion peaks with a slowly decaying tail on the high mass side due to severe, non-resolved adduction.

Similar spectra to that shown in fig. 3.12 were achieved for RC samples containing substance P (M.W. = 1347.6 Da), bison heart cytochrome c (M.W. = 12,327 Da) and chicken egg lysozyme (M.W. = 14,306 Da) although the high resolutions could not be repeated for the proteins bovine serum albumin (M.W. ~ 67,000) and bovine immunoglobulin G (M.W. ~ 150,000 Da). Peaks with a high mass resolution continued to have a low S/N ratio.

3.5 Sublimed Films

Although the crushed samples described in the previous section have shown dramatic improvements in surface uniformity compared with dried-droplet samples, there still exists a lack of control over substrate coverage and film thicknesses. Furthermore, the films formed by crushing are far too thick (12 - 60 μm) to allow UV transmission spectroscopy. Despite the crushed films displaying a lower value of F_{th} and improved analyte mass resolutions than dried-droplet samples, further improvements were sought so that meaningful characterisation of solid matrices could be carried out.

To this end, samples formed by sublimation-deposition onto fused silica microscope slides at room temperature (see fig. 3.13) were investigated. The sublimation

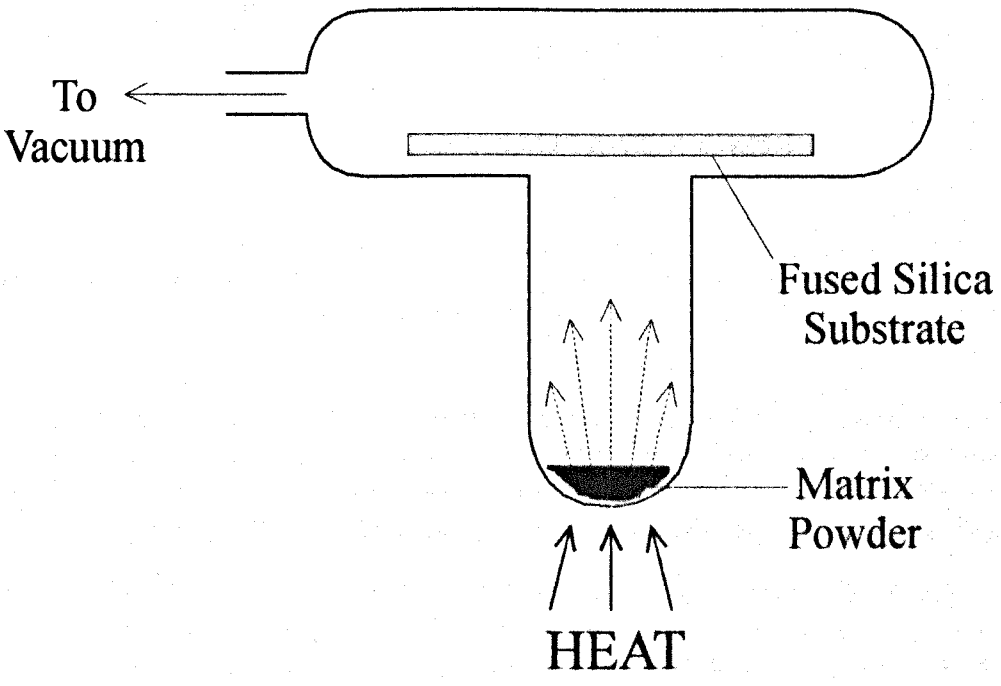

Figure 3.13. Sublimation cell for preparation of matrix thin films.

vessel was fabricated in Pyrex (Corning Corp., Corning, NY) and the source-substrate distance was either 8 or 10 cm. By control of the source temperature (70-100°C) and deposition time (≤ 20 mins), films of thickness in the range 50 - 600 nm could be grown. The deposition rate (≤ 1 nm/s) varied strongly between the various materials sublimed because of differences in their temperature-vapour pressure relationships. The flight path for deposition was maintained at a technical vacuum of $\sim 10^{-5}$ torr, the major contribution to this pressure being sublimed material (the compounds investigated commonly have finite vapour pressures even at room temperature).

The resultant films were transparent, nearly colourless and displayed negligible optical scattering, although optical interference fringes could be observed during the film growth. Optical microscopic inspection of coumarin 120 films showed them to be finely polycrystalline on a micron or sub-micron scale. When examined at higher magnifications by SEM analysis, this micron sized structure appeared to be the exposed facets of a dense layer of ~ 0.3 μm (= 300nm) diameter crystallites lying at random angles (fig. 3.14). 2,5-DHB films were observed to be very similar to sublimed coumarin 120, but ferulic acid samples retained some similarity of appearance to samples formed from dried solutions, consisting of coalescent needle-like features (fig. 3.15).

The ability to measure film thicknesses accurately is critical for quantitative absorption measurements. Prior to stylus-profiling, small areas of the films were removed either with a focused UV laser (~1 mm^2) or mechanical scoring (lines ~ 1 μm wide); the objective was to produce an observable step in thickness within the same area as had been earlier utilized for optical transmission measurement (see Chapter 4). The influence of the profilometer stylus load on the measured compacted mass thickness was investigated using 2,5-DHB as the test film. The results (fig. 3.16a) showed the effective thickness to decrease steadily with increasing load, and above 10-20 mg reached an approximately constant value of ~ 70% that for minimal loading. In obtaining profile traces (see fig. 3.16b) for the measurement of film thicknesses a stylus load of 10 mg was thus chosen. Loads less than this presumably gave larger effective values of thickness due to the stylus following the surface roughness and incomplete compression of the slightly porous sample. Stylus loads much greater than 10 mg, however, appeared to

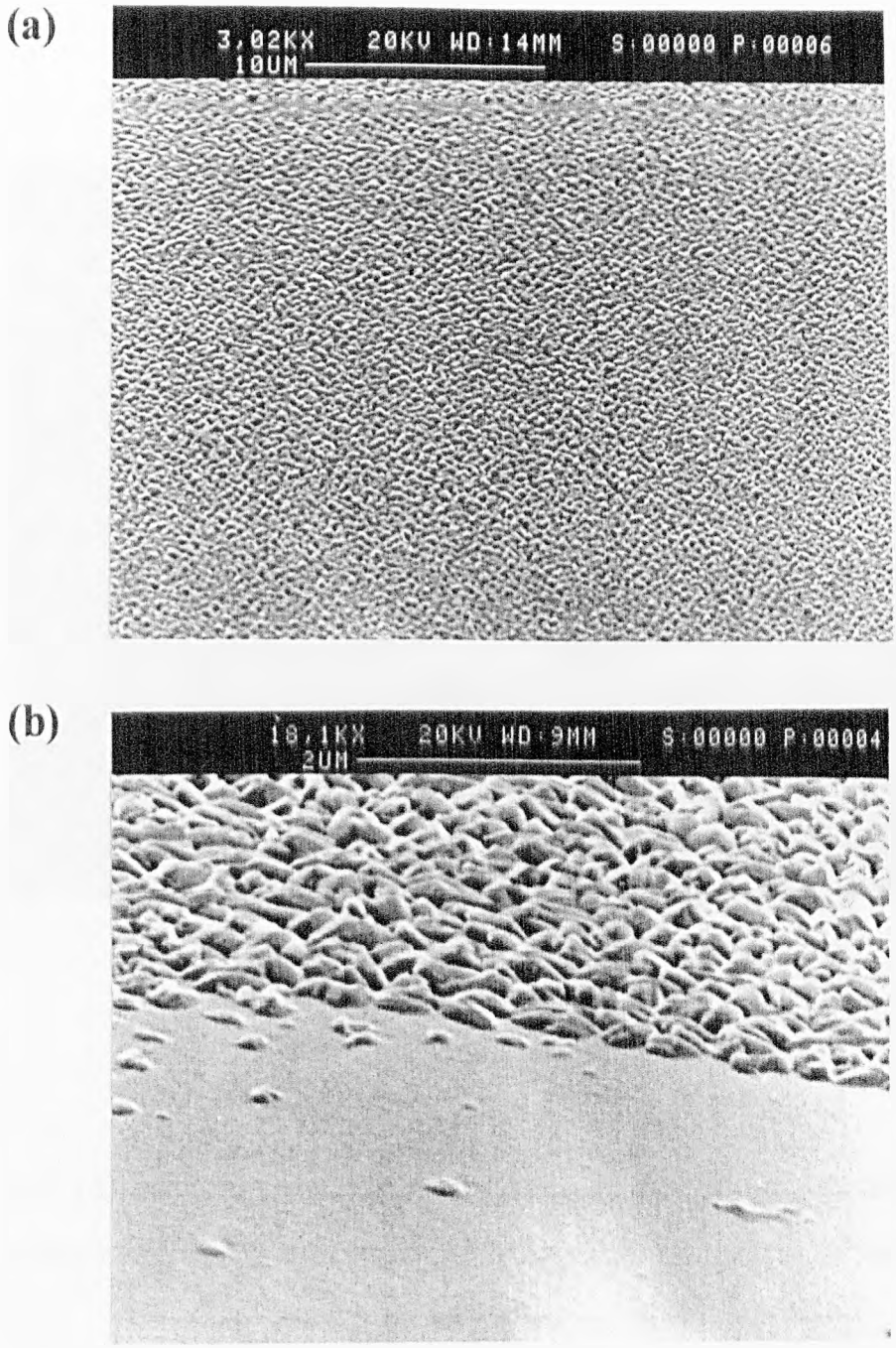

Figure 3.14. Micrographs of a sublimed coumarin 120 film on microscope-slide glass. (a) Sub-micron structure evident (b) higher magnification micrograph showing ~ 0.3 μm sized crystallites.

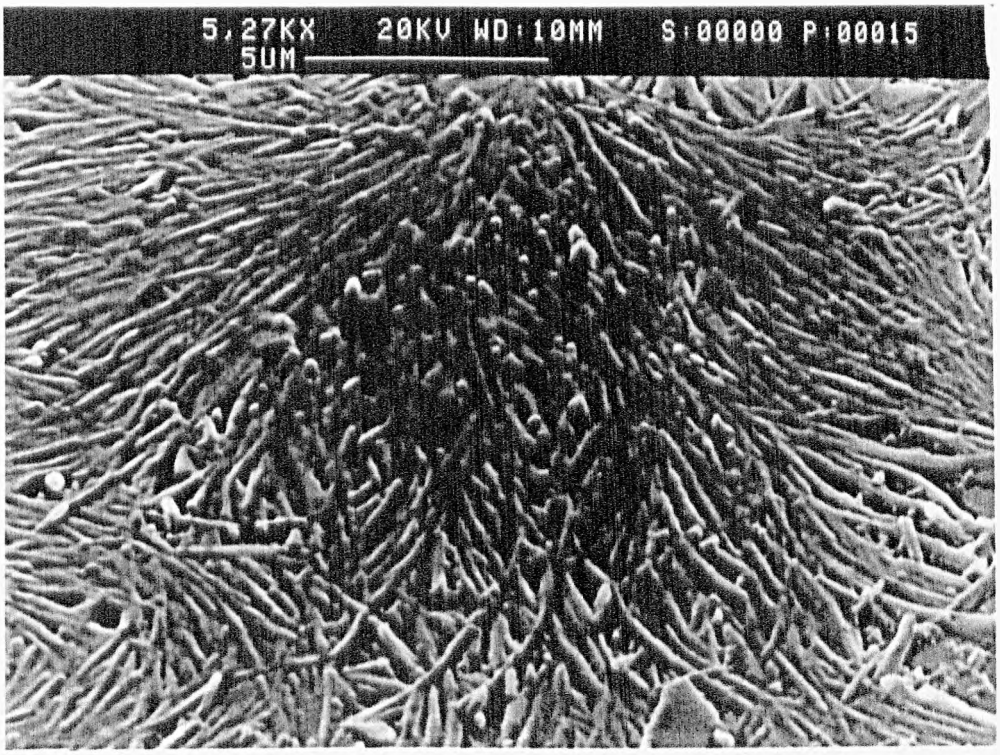

Figure 3.15. Scanning electron micrograph of a ferulic acid sublimed film. Note the needle-like structure visible, also characteristic of ferulic acid crystal growth from solution.

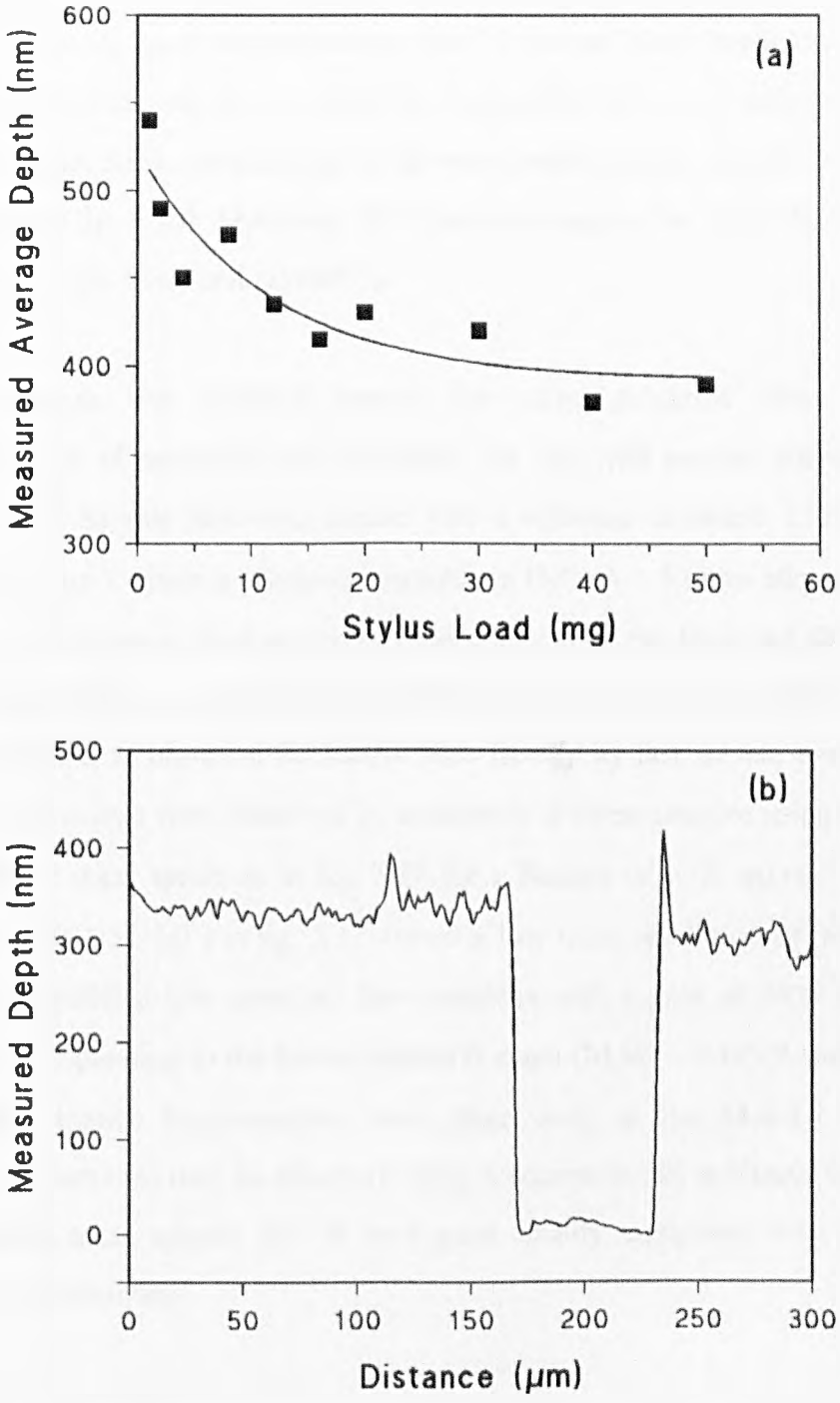

Figure 3.16. Profilometer measurements of a 2,5-dihydroxybenzoic acid film: (a) average depth as a function of stylus load and (b) profilometer trace (10 mg stylus load) of area mechanically cleared of deposited film.

scratch into a film's surface thus reducing the measured thickness. The instrumental accuracy of the thickness measurements was < 1 nm and hence negligibly small. No local irregularities in thickness were recorded by the profiler in the area adjacent to the cleared spots other than debris material due to the mechanical scoring, as seen on the right hand trough edge in fig. 3.16b. However, SEM pictures suggest the stylus diameter must have rested on the tops of several crystallites.

Although the principal reason for using sublimed films was for the characterisation of matrices, their suitability for use with protein analytes was briefly assessed. TOF sample pins were coated with a sublimed coumarin 120 film (estimated thickness ~ 1 μm) which is relatively insoluble in H_2O. A 1.5 μlitre aliquot of 0.5 g.litre^{-1} bovine insulin aqueous solution was then deposited onto the films and allowed to air-dry at room temperature, possibly allowing diffusion of the analyte molecules into the matrix crystal structure, as observed for matrix films formed by fast solvent evaporation [101]. Positive analyte ions were observed by irradiation of these samples using the N_2 laser, as shown by the mass spectrum in fig. 3.17 for a fluence of ~ 40 mJ.cm^{-2}. However, the monomer peak ($[M+H]^+$) in fig. 3.17 shows a low mass resolution of $(m/\delta m)_{FWHM} \sim 30$ and has a significant low mass tail that coincides with a peak at 3429 Da ($[M_B+H]^+$), possibly corresponding to the bovine insulin B chain (M.W. = 3495.9 Da). This suggests that severe analyte fragmentation takes place early in the MALDI process. Thus, although protein ions may be observed using a coumarin 120 sublimed film as a matrix, the resulting mass spectra are of very poor quality compared with other available preparation techniques.

3.6 Conclusions

Different sample preparations of MALDI matrices have been investigated. Refrigerated drying of matrix solutions improved the uniformity of crystal distribution across the substrate. Crushing crystals dried from solution with polished aluminium created polycrystalline (< 1 μm feature size) films of thicknesses between 12 - 60 μm possessing a much improved morphological uniformity over dried-droplet samples, particularly when using saturated matrix solutions and soda lime glass disc substrates.

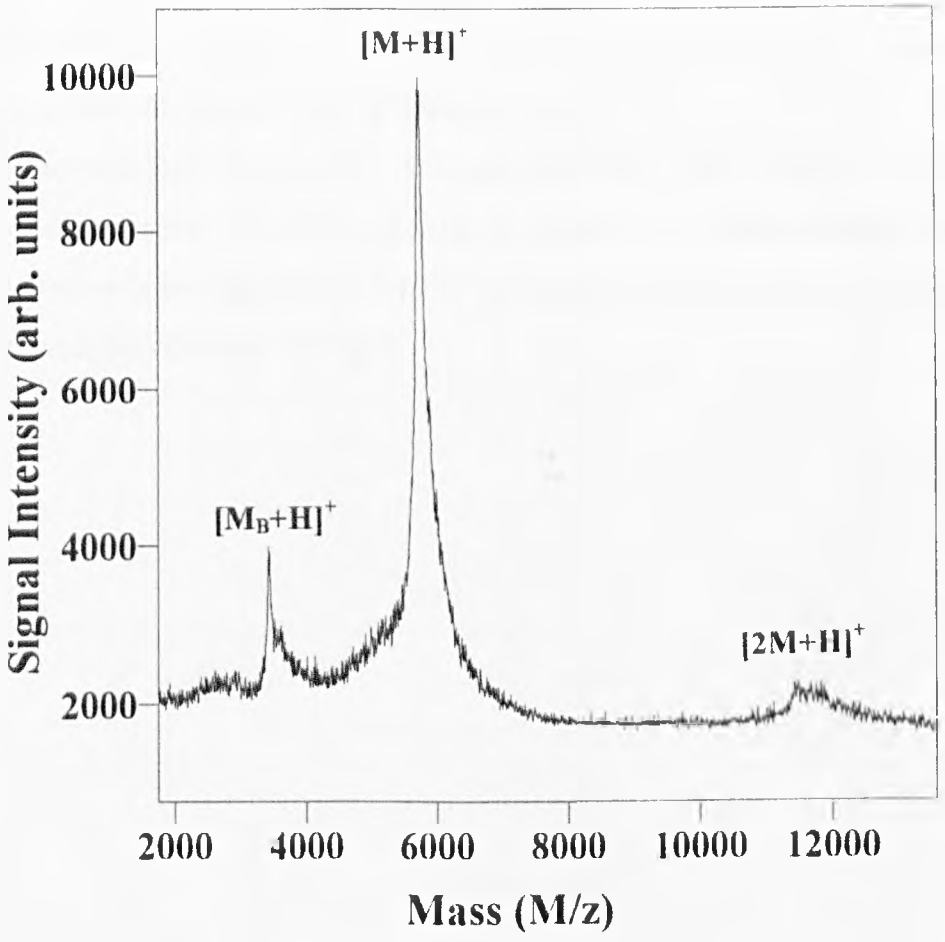

Figure 3.17. Positive ion time-of-flight mass spectrum of bovine insulin, deposited on a coumarin 120 sublimed film. Note the low mass resolution of the monomer ($[M+H]^+$) peak, $(m/\delta m)_{FWHM} \sim 30$, and the presence of the insulin dimer ($[2M+H]^+$) and the insulin B chain monomer ($[M_B+H]^+$).

Films of some matrices displayed a ~ 15% reduction in the threshold fluence for the observation of ions over dried-droplet samples, a result attributed to the lower effective area that the (smooth) crushed film presents. Refrigerated drying and crushing standard dried-droplet films both contributed to an increase in the achievable mass resolution of proteins analysed in the mass spectrometer.

Sublimation-deposition of matrices onto fused silica substrates allowed the controllable growth of uniform films of thickness between 50 nm and > 1 μm, with large areal substrate coverage (several cm^2). Although these films were shown to support the desorption and ionisation of protein molecules to provide (low resolution) mass spectra, their chief purpose is envisaged to be for UV spectroscopy of matrices since they can be grown thin enough to transmit UV light.

4 ABSORPTION

4.1 Introduction

It appears reasonable to assume that the strength of matrix absorption of laser radiation will be of fundamental importance to MALDI as this represents the main process by which energy is coupled into the matrix-analyte system. An accurate estimate of the solid phase absorption coefficient, α, is required for quantitative modelling of desorption and ionisation. However, as described in §2.3.2, for reasons of sample homogeneity, the best estimates of α are derived from solution measurements [108,109,112-114] despite absorption spectra from solid crystals being modified when compared with those of solutions [109]. This chapter capitalises upon the improved sample preparation offered by sublimation-deposition (see Chapter 3) by describing the determination of α for several common MALDI matrices in the solid state. The importance of achieving strong optical absorption in the matrix at the irradiating wavelength for successful operation of the MALDI process is then demonstrated.

4.2 Experimental

The principal matrices investigated were ferulic acid (3-methoxy-4-hydroxycinnamic acid), sinapinic acid (3,5-dimethoxy-4-hydroxycinnamic acid), α-cyano-4-hydroxycinnamic acid (α-CHC), 2,5-dihydroxybenzoic acid (2,5-DHB), coumarin 120 (7-amino-4-methylcoumarin) and nicotinic acid (pyridine-3-carboxylic acid; see §3.3 for details of suppliers). Additionally, the benzoic acid derivatives 2,3-DHB, 2,4-DHB and 3,4,5-trihydroxybenzoic acid (THB) were used to investigate the influence of α on the MALDI process and were obtained from Aldrich Chemical Company Ltd. (Gillingham, UK) to a stated purity of 99 - 97%. The protein bovine insulin (M.W. = 5733.5 Da) was obtained from Aldrich Chemical Company Ltd. (Gillingham, UK) to a stated purity of 99.5 %.

Transmission data was obtained using ATI Unicam Ltd. (Cambridge, UK) UV3-200 and UV-5625 spectrophotometers, having a wavelength resolution was 1.5 nm, that is, much less than the width of the observed features. Samples for transmission measurements were either solid sublimed films deposited on fused silica substrates, as described in §3.5, or matrix solutions contained in fused silica cuvettes and using solvents appropriate for each compound (§3.3).

Details of the time-of-flight (TOF) mass spectrometer and pulsed UV lasers are found in §3.2.

4.3 Absorption Spectra

The measured absorption spectra of the various MALDI matrix films are shown in fig. 4.1 (a-f) for the 200 - 500 nm wavelength range. The magnitude of the absorption coefficient, α, was derived from the sample transmission, T, using

$$\alpha = -\frac{2.303 \log_{10} T}{d} \qquad 4.1$$

where d is the sample thickness in cm. The absorbance ($A = -\log_{10} T$) term was recorded directly by the spectrophotometer. It should be noted that by measuring A relative to the uncoated fused silica substrate, surface reflection losses from the sublimed films are corrected for provided that the refractive index of the deposited layer, n_f, does not differ significantly from that of the substrate, n_s. Measurement of the Brewster angle (θ_B) of a coumarin 120 deposited layer ($\theta_B = 58.7°$) using a polarised He-Ne laser beam gave $n_f \sim 1.64 \pm 0.04$ (at 632.8 nm). This value is relatively close to $n_s = 1.458$ (at 589.29 nm - sodium D line) so the above assumption appears to be reasonable. The error in α corresponding to this level of index mismatch would be no more than 3 %, even for the thinnest films used.

Absorption spectra of matrix solutions are shown in fig. 4.2 (a-f) with the molar extinction coefficient, ε, being calculated from spectrophotometry data by

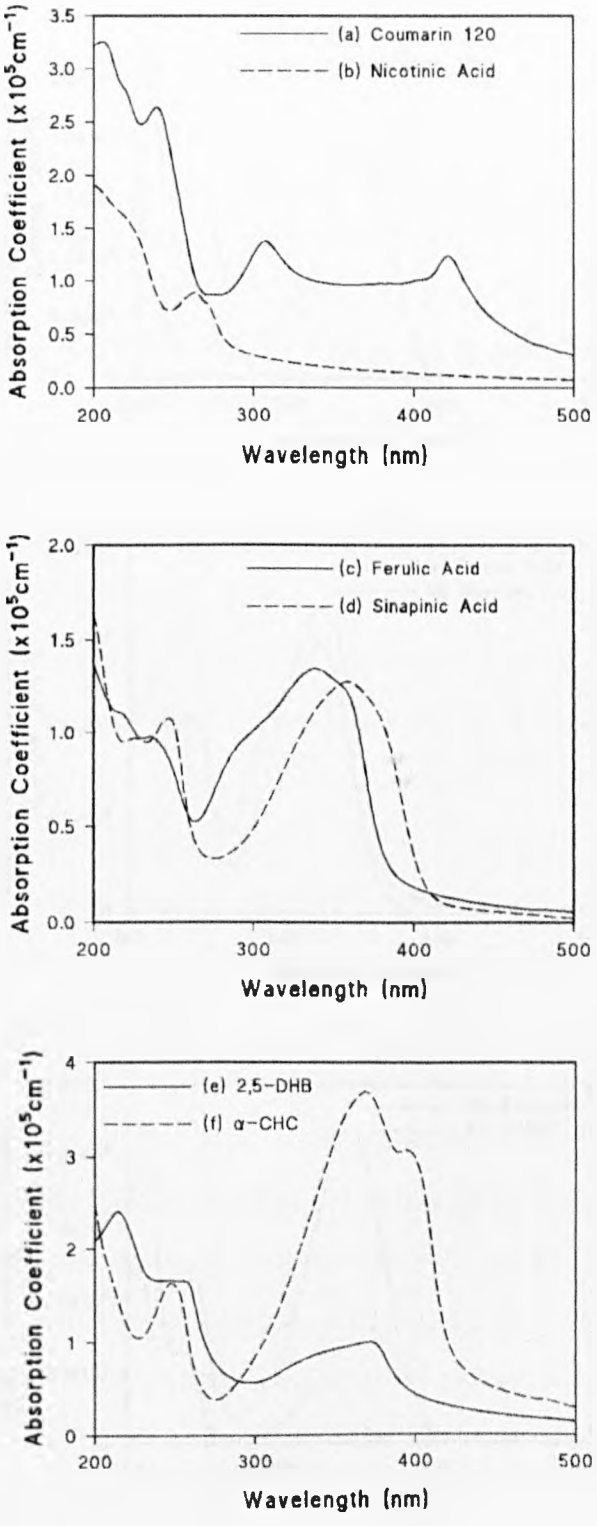

Figure 4.1. Sublimed thin film absorption spectra of several MALDI matrices.

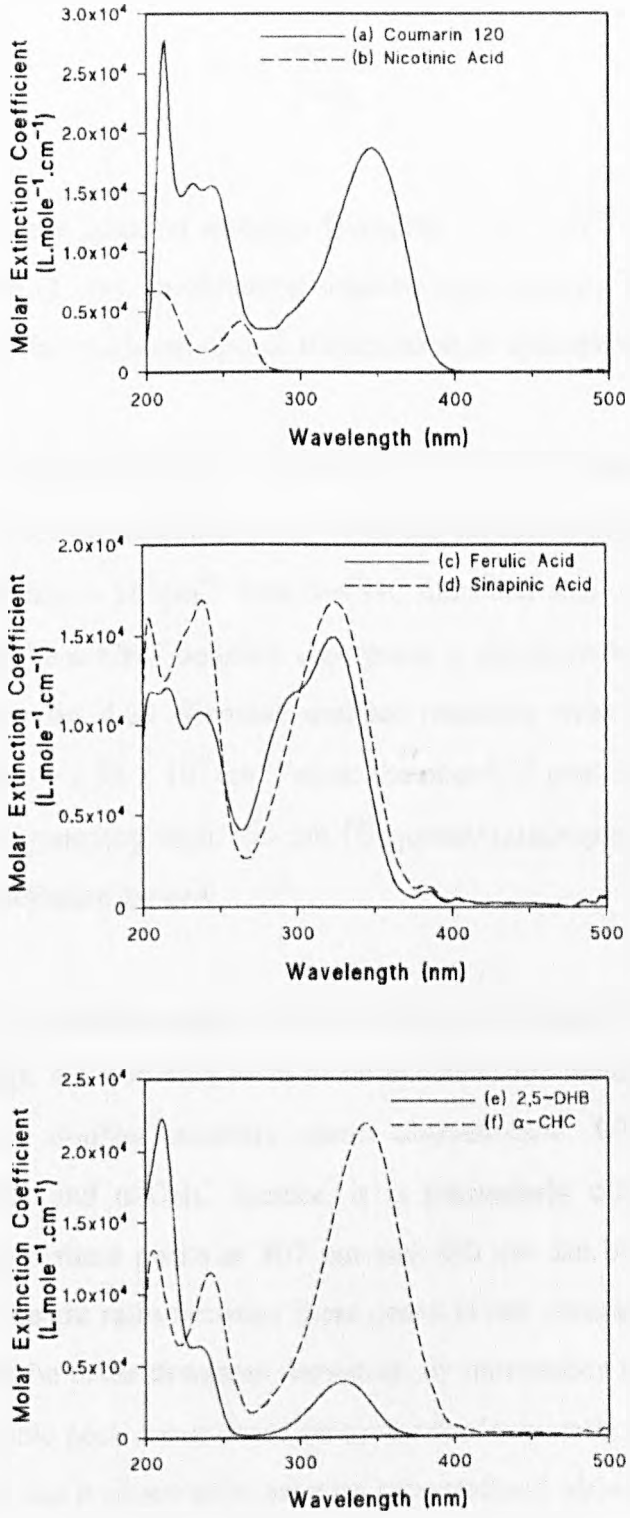

Figure 4.2. Solution phase absorption spectra of several MALDI matrices.

$$\varepsilon = -\frac{\log_{10} T}{[M]l_c} \qquad 4.2$$

where *[M]* is the solution molarity (typically ~ 5 × 10^{-5} Molar) and l_c is the internal cuvette width (1 cm). In obtaining solution phase spectra of matrices, baseline data was provided by the measured optical transmission of appropriate solvents.

The values of the absorption coefficient at 337 nm (N_2 laser wavelength), α_{337}, are noted in table 4.1 for the sublimed films. With the exception of α-CHC and nicotinic acid, the films all had $\alpha_{337} \sim 10^5$ cm^{-1}. That α–CHC films had $\alpha_{337} \sim 2.2 \times 10^5$ cm^{-1} is not surprising given that the α-CHC solution absorption is significantly greater than that of other matrix solutions (fig. 4.2). Nicotinic acid has relatively weak absorption at the N_2 laser wavelength ($\alpha_{337} \sim 2.32 \times 10^4$ cm^{-1}) since the near-UV peak is at 263 nm, thereby suiting this matrix to pumping with 266 nm (frequency-quadrupled Nd-YAG laser) or 248 nm (KrF laser) radiation instead.

The near-UV absorption peaks for the solids are consistently broader than in the case of solutions (figs. 4.1 and 4.2), as is to be expected for molecular crystals, and in fact in many cases a doublet structure seems characteristic. While this structure is apparent in 2,5-DHB and α-CHC spectra, it is particularly evident in the case of coumarin 120 where distinct peaks at 307 nm and 420 nm can be seen, although it is noted that the peak height ratio between these peaks is not constant. It was found that the 420 nm peak can be made dominant, however, by momentary heating of the film to near 100°C. The double peak is not observed in standard coumarin 120 solutions used in dye lasers [237] nor was it observed in samples recrystallised (dried) from solutions. An additional observation is that the doublet structure seen in absorption spectra from sublimed films is not found in spectra from either a redissolved film or dissolved vapour-source material after use; these revert to normal solution absorption spectra. Nevertheless, with the exception of the 100°C annealed samples, the strongest absorption of the coumarin 120 sublimed films was at 307 nm.

MATRIX	337 nm	MAXIMA	
	α_{film} (cm^{-1})	σ_{film} (cm^2)	σ_{soln} (cm^2)
Coumarin 120	9.69×10^{4}	3.91×10^{-17}	7.16×10^{-17}
Ferulic Acid	1.16×10^{5}	3.46×10^{-17}	6.10×10^{-17}
Sinapinic Acid	1.10×10^{5}	4.34×10^{-17}	6.85×10^{-17}
α-CHC	2.18×10^{5}	1.04×10^{-16}	8.24×10^{-17}
2,5-DHB	7.95×10^{4}	1.98×10^{-17}	1.46×10^{-17}
Nicotinic Acid *	$\alpha_{248}=7.35 \times 10^{4}$ $\alpha_{266}=8.71 \times 10^{4}$	1.67×10^{-17}	1.76×10^{-17}

* Note that α_{film} at 248 nm and 266 nm is given for nicotinic acid instead of at 337 nm as the absorption is very weak at this wavelength.

Table 4.1. Absorption coefficients of sublimed matrix films, α_{film}, at 337 nm and maximum absorption cross-sections of sublimed films, σ_{film}, and solutions, σ_{soln}, in the near-UV.

Coumarin 120 is well known to form dimers under high intensity illumination [238] and displays transient radical attachment [239,240] although under the low irradiance conditions of optical spectrophotometry, the stable dimerisation of two coumarin 120 molecules upon crystallisation seems the more probable explanation of doublet structure in the absorption spectrum. Dimer formation can cause splitting of the degenerate monomer electronic states leading to a doublet absorption band structure centred about the monomer absorption maximum [117]. However, no specific chemical alteration of the coumarin monomers would be expected to occur, consistent with the observed replication of solution absorption spectra by dissolving either the sublimed films or the heated sample material.

The maximum optical cross-sections of the near-UV peak derived from thin film (σ_{film}) and solution (σ_{soln}) absorption spectra are also given in table 4.1. The cross-sections for the solids are calculated assuming a film density of 1.1 g.cm^{-3} and by using the relationship

$$\sigma = \frac{\alpha}{n} \qquad 4.3$$

where n is the number density of the absorbing molecule, i.e. the matrix. Solution phase cross-sections can be derived from eqns. 4.1 - 4.3 and

$$[M] = \frac{10^3 n}{N_A} \qquad 4.4$$

to give

$$\sigma = \frac{2.3 \times 10^3 \varepsilon}{N_A} \qquad 4.5$$

where N_A is Avogadro's number.

The maximum near-UV optical cross-sections of the films (σ_{film}) are of the same order as those for dissolved molecules (σ_{soln}), with the ratio σ_{film} / σ_{soln} lying between ~ 0.55 and 1.36 for the different matrices studied. This suggests that, in general, the solution data can only be relied upon to within a factor of ~ 2 to provide data for modelling the solid matrices.

4.4 Matrix Absorption in MALDI

As part of a previous study to assess the suitability of different molecules as MALDI matrices, the compounds 2,3-DHB, 2,4-DHB, 2,5-DHB and THB (fig. 4.3) received ratings that varied from 'poor' to 'excellent' [138]. This assessment was carried out using N_2 laser radiation (337 nm) although it was noted that the threshold fluence for ion production varies with the irradiating wavelength for benzoic acid derivatives [112,113], presumably due to changes in absorption. It would appear reasonable, therefore, that investigation into why different matrix ratings are apparent for chemically similar molecules commence with an assessment of their absorption strengths.

The thin film absorption spectra of the compounds studied were determined in exactly the same manner as those in §4.3 and are shown in fig. 4.4. The values of α at 308 nm (α_{308}) and at 337 nm (α_{337}) are listed in table 4.2, together with the previous ratings of the molecules as MALDI matrices using a desorbing wavelength of 337 nm [138]. The order of molecules in ascending order of α_{337}, THB, 2,3-DHB, 2,4-DHB and 2,5-DHB, corresponds with the matrix performance ratings of 'poor' for THB, 'fair' for 2,3-DHB and 2,4-DHB, and 'excellent' for 2,5-DHB. It is interesting to note that despite the large (~ ×2) difference in α_{337} for 2,3-DHB and 2,4-DHB, both have been rated, broadly, as having a like efficiency for the generation of analyte ions. Although the matrix classifications are somewhat qualitative and subjective in nature, it is likely that different matrix molecules have photophysical properties further to α that differ and consequently affect their performance in MALDI, e.g., solid densities or ionisation energies.

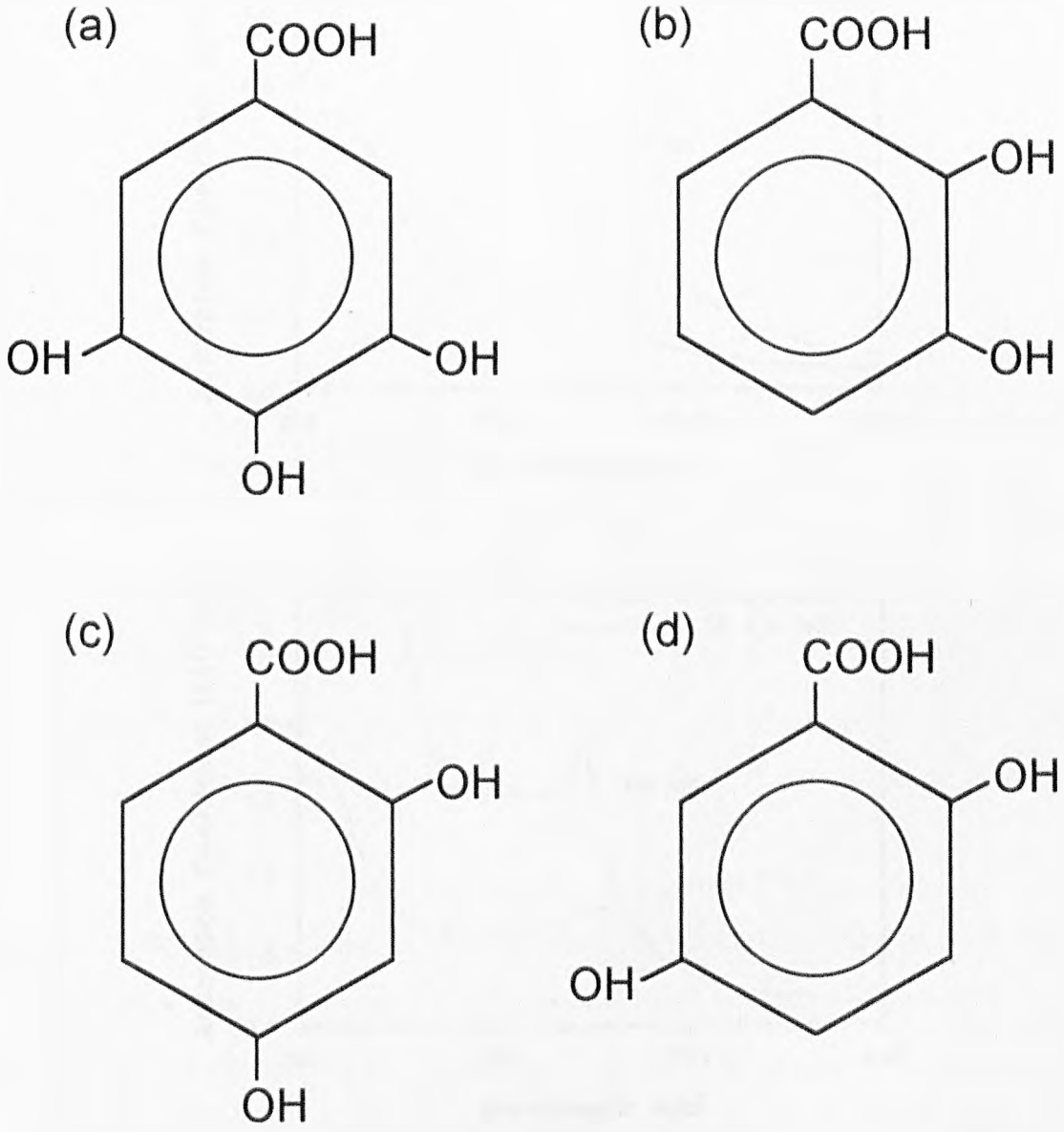

Figure 4.3. Chemical structure of (a) 3,4,5-trihydroxybenzoic acid, (b) 2,3-dihydroxybenzoic acid (2,3-DHB), (c) 2,4-DHB and (d) 2,5-DHB.

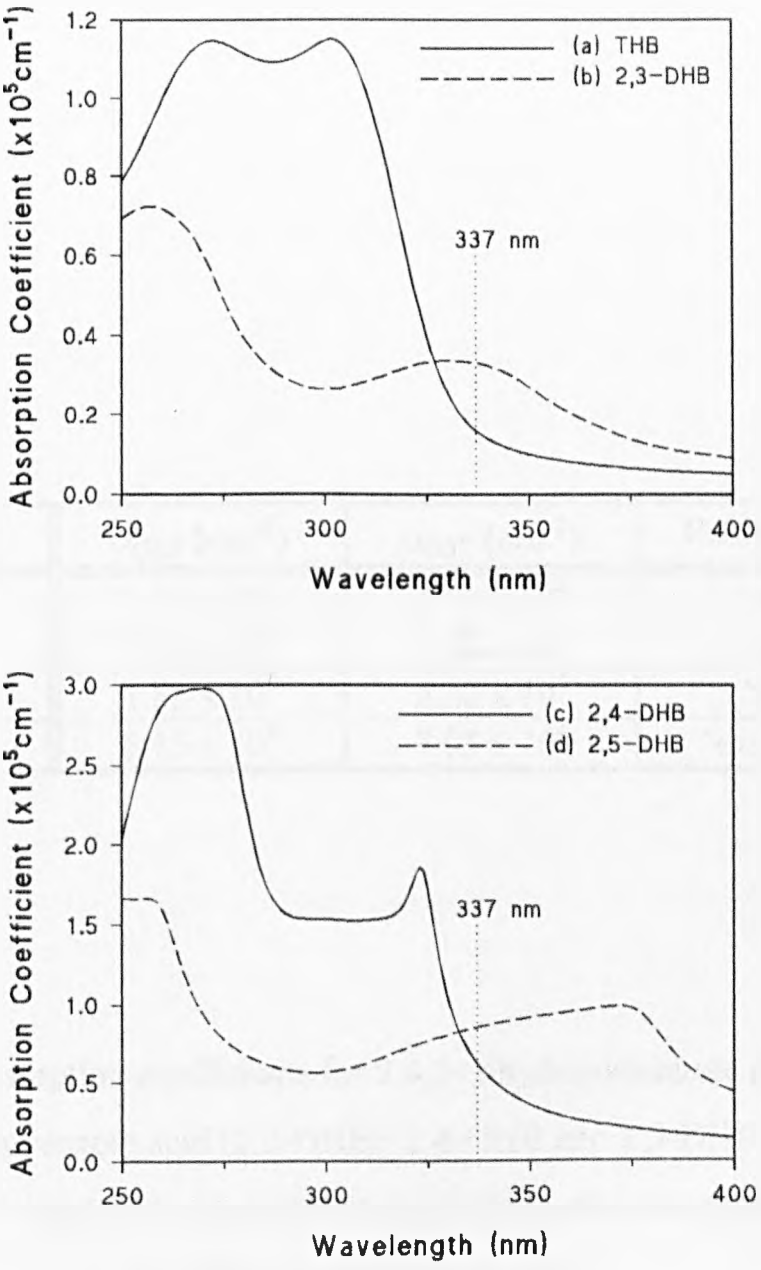

Figure 4.4. Sublimed thin film absorption spectra of hydroxy-substituted benzoic acid derivatives.

MATRIX	α_{308} (cm^{-1})	α_{337} (cm^{-1})	Rating [138]
THB	1.05×10^5	1.66×10^4	'poor'
2,3-DHB	2.76×10^4	3.29×10^4	'fair'
2,4-DHB	1.55×10^5	6.22×10^4	'fair'
2,5-DHB	6.15×10^4	7.95×10^4	'excellent'

Table 4.2. Absorption coefficients for 3,4,5-trihydroxybenzoic acid (THB), 2,3-dihydroxybenzoic acid (2,3-DHB), 2,4-DHB and 2,5-DHB at 308 nm (α_{308}) and 337 nm (α_{337}). Also indicated are the matrix ratings attributed to the different compounds [138].

From fig. 4.4 it is clear that although 2,3-DHB and 2,5-DHB are very close to their peak absorptivity at 337 nm, 2,4-DHB and THB become greatly more absorptive when the wavelength of the light is reduced slightly, reaching peak α values of 1.93×10^5 cm^{-1} at 324 nm and of 1.10×10^5 cm^{-1} at 303 nm, respectively. 337 nm TOF mass spectrometry of THB and bovine insulin dried-droplet samples (see §3.3 for preparation details) failed to yield a detectable analyte ion signal at fluences up to ~ 70 $mJ.cm^{-2}$; indeed, it was unusual to even observe a matrix ion peak. However, by changing the desorbing wavelength from 337 nm to 308 nm with a corresponding increase in α from 1.66×10^4 cm^{-1} to 1.05×10^5 cm^{-1}, insulin ions could be detected at modest fluences. For example, fig. 4.5 shows singly ($[M+H]^+$) and doubly ($[M+2H]^{2+}$) charged insulin ion peaks obtained from a THB matrix irradiated with a fluence of ~ 20 $mJ.cm^{-2}$. Figure 4.5 represents the average of spectra acquired from 10 successive laser pulses incident upon the same sample region. That the singly charged insulin ion peak in fig. 4.5 displays such a large signal-to-noise ratio demonstrates the effectiveness of irradiating MALDI samples with a laser wavelength that corresponds to a near maximum in matrix absorptivity, as also described in refs. 112 and 113. However, by demonstrating a direct correlation between a molecule's suitability as a MALDI matrix with its optical absorptivity at the irradiating wavelength the importance of α within MALDI is shown more clearly than before.

4.5 Matrix Ion Yield

In order to further investigate the influence of α on the MALDI process, the TOF mass spectrometer was used to determine the integrated matrix ion yield, Y, from 2,5-DHB sublimed films as a function of fluence, F. This was accomplished using both N_2 (337 nm, 3 ns FWHM) and XeCl (308 nm, 10 ns FWHM) lasers. In the solid phase, α for 2,5-DHB falls from $\alpha = 7.95 \times 10^4$ cm^{-1} at 337 nm to $\alpha = 6.15 \times 10^4$ cm^{-1} at 308 nm (table 4.2). However, since gas-phase spectra would generally be expected to be spectrally narrower than their solid phase equivalents, the difference in absorptivity of 2,5-DHB at these wavelengths may become more marked in a desorbed plume.

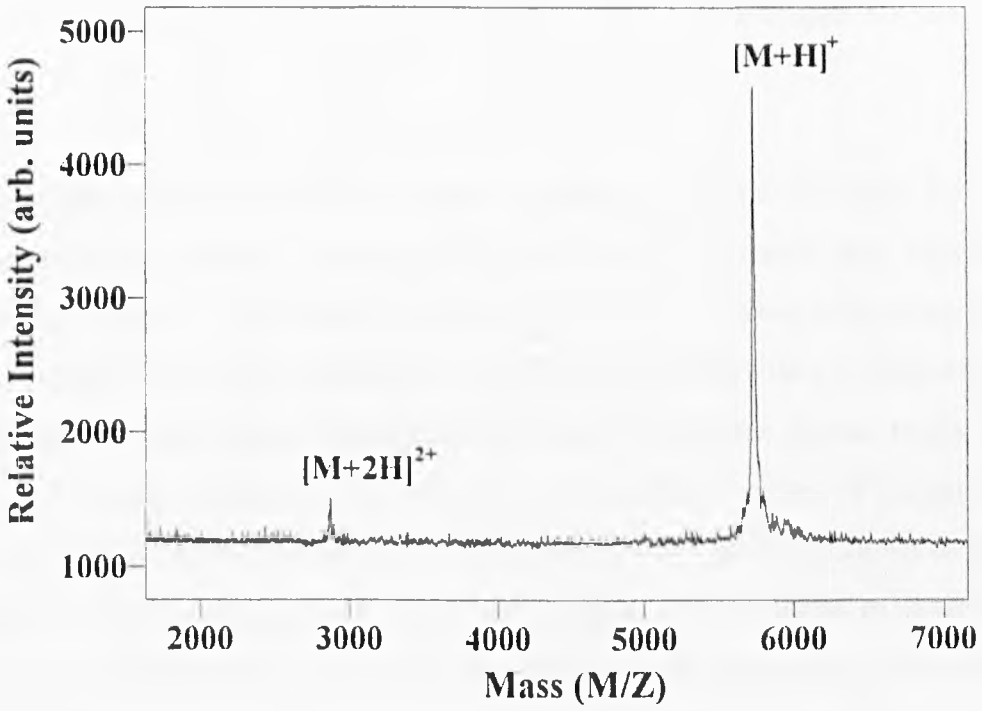

Figure 4.5. Positive ion time-of-flight mass spectrum of bovine insulin from a 3,4,5-trihydroxybenzoic acid matrix, irradiated with ~ 20 $mJ.cm^{-2}$ 308 nm radiation. The peaks shown correspond to the singly charged ($[M+H]^+$) and doubly charged ($[M+2H]^{2+}$) insulin monomer ions.

An identical optical path was used for each laser, passing through an aperture to ensure that the laser spot sizes on the sample were of approximately equal dimensions (~ 1 mm × 600 μm ellipse). 10 samples of thickness > 1 μm were used for each laser wavelength and data was obtained from each sample by averaging the spectra resulting from 10 consecutive laser pulses at a given fluence. During data acquisition, the mass spectrometer sample pins were constantly rotated in the laser beam in an attempt to sample from as wide a region as possible. The integrated signals of the m^+, $[m+H]^+$ and $[m+2H]^+$ matrix ion peaks (where *m* is the matrix) were then averaged for the 10 samples.

The resulting integrated matrix ion signals are shown in fig. 4.6. The error bars in fig. 4.6 represent one standard deviation for each data point which was between 15 - 50 % of the mean for XeCl irradiation and up to 67 % of the mean when using the N_2 laser. Despite this, it is clearly seen that for the N_2 laser 2,5-DHB ions are observed at significantly lower fluences than with the XeCl laser and that, in the fluence region of ~ 20 $mJ.cm^{-2}$, ion signals using the 337 nm laser are more than 3 orders of magnitude greater than for the 308 nm wavelength. Linear regression fits to the data (shown on fig. 4.6) highlight the strong dependence of the matrix ion signal on the fluence, as observed previously [125,145,154] (§3.4.3). However, the strength of this dependence differs for the two wavelengths used with Y varying as $\sim F^{10}$ and $\sim F^{8}$ for the N_2 and XeCl lasers, respectively.

As there are experimental differences in optical absorption, photon energy and laser pulse length for the two sets of data, they should be analysed in these terms. The larger photon energy of the 308 nm radiation (~ 4.0 eV) compared with that of 337 nm radiation (~ 3.7 eV) will lead to a larger degree of matrix heating per absorbed photon, although this will be compensated for by the increased number of photons within a pulse of longer wavelength (assuming equal pulse energies). The absorption of two photons of 308 nm wavelength will cause the excited matrix molecule to be closer to the ionisation potential than if 337 nm radiation is used (see Chapter 6), leading to a lower ionisation efficiency for the case of (stepwise) photoionisation. However, Chapters 6 and 7 discuss an alternative ionisation mechanism to photoionisation in which higher energy photons actually enhance matrix ionisation. The effect of laser pulse length is largely unknown at

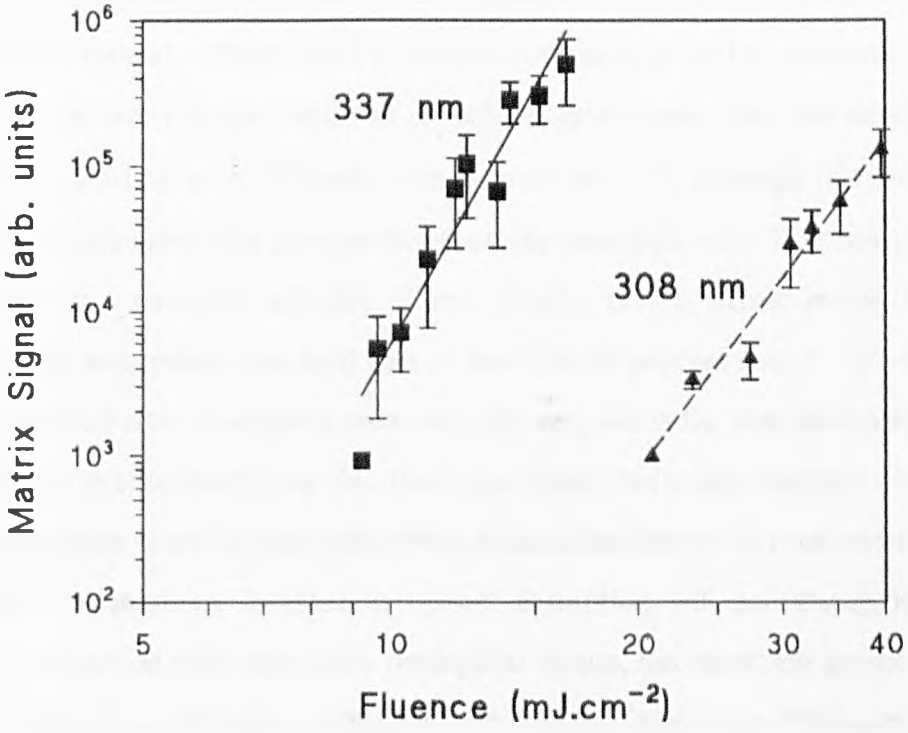

Figure 4.6. Observed TOF-MS integrated 2,5-DHB ion yield as a function of fluence using N_2 (337 nm) and XeCl (308 nm) lasers.

present, although two studies are discussed in §2.3.3 [118,154]. The lower temporal irradiance in longer pulses may be compensated for by an increased temperature during the laser pulse due to non-radiative relaxation of excited matrix molecules, again, Chapters 6 and 7 discuss this further.

The drop in Y for the XeCl laser should, therefore, be discussed most strongly in terms of absorption. The scale of the difference in Y for the two laser wavelengths (3 orders of magnitude at ~ 20 mJ.cm^{-2}) is perhaps surprising given the comparatively small difference in the two relevant values of α. Indeed, given these data, the dependence of the matrix ion yield on α would need to be as great as ~ α^{26}, although this assumes that α is the only parameter that changes between the two data sets. This can perhaps be explained by two mutually inclusive effects. Firstly, that a strong matrix ion signal dependence on absorptivity is indeed part of the MALDI process (i.e. $Y \sim \sigma^{l}$, where σ is the matrix ground state absorption cross-section) and, secondly, that absorption of laser energy occurs predominantly in desorbed gas-phase molecules thereby accentuating spectral differences in solid-phase absorption, as described above. It is counterintuitive to assume that a continuing increase in optical absorption will necessarily lead to an increase in desorption yield since once desorption occurs, the absorbing gas-phase plume is likely to shield the solid-phase molecules from further illumination. Photoionisation can be assumed to possess an approximately linear dependence on ground state absorption and so does not meet the $Y \sim \sigma^{l}$ requirement either. However, the alternative ionisation mechanism discussed in Chapters 6 and 7 provides a possible explanation for the matrix ion yield's strong dependence on optical absorption, outlined above (see, particularly, §7.3). The modelled matrix ion yield does, indeed, display a very strong dependence on σ although, to produce a consistent description of the results, the ratio of the gas-phase absorption cross-sections at 337 nm and 308 nm for 2,5-DHB is still required to be greater than for the solid phase.

4.6 Conclusions

Quantitative values for the solid-phase absorption coefficient, α, of several common MALDI matrices have been determined by transmission measurements on thin

(50 - 600 nm) sublimed films. For common laser wavelengths used in MALDI, $\alpha \sim 10^5\ cm^{-1}$ is typical. Comparison with absorption cross-sections estimated from solution measurements suggests that solution-based values are accurate only to within a factor of ~ 2.

The influence of absorption on MALDI has been investigated in two ways. Firstly, for chemically similar compounds, a direct correlation was found between α and a molecule's effectiveness as a MALDI matrix. Indeed, 3,4,5-trihydroxybenzoic acid (THB), rated as a 'poor' matrix for 337 nm (N_2) laser irradiation [138], has been shown to support the production of bovine insulin ions in MALDI when using a 308 nm laser (XeCl) where THB displays much stronger optical coupling. Secondly, the effect of changing laser wavelength on the matrix ion yield - laser fluence characteristics shows ion production to be strongly dependent on the absorption strength of the matrix. This could be due to matrix ionisation being strongly dependent on absorption of the laser energy and that this absorption takes place predominantly in the gas-phase where a spectrally narrower absorption band may be relevant as compared to the solid-phase.

5 MATRIX FLUORESCENCE

5.1 Introduction

In attempting to elucidate photoexcitation mechanisms, the study of fluorescence has great potential. The fluorescence of MALDI samples has been reported previously including: lifetime and quantum efficiency measurements on matrices [109,118,241,242], fluorescence intensity as a function of incident fluence [118,242], spatial imaging of desorbed plumes [132] and for viewing the effect of heavy-atom substitution into matrices [121]. Despite this, there is still a lack of energetic and mechanistic data that fluorescence experiments could yield. The study described here attempts to remedy this deficiency by obtaining the solid and solution phase fluorescence spectra of several common MALDI matrices. Analysis of these, together with previously obtained absorption data, give estimates of the vibrationless (0-0) ground-singlet (S_0-S_1) energy, ε, fluorescence quantum efficiency, ϕ_{qe}, fluorescence and non-radiative decay rates, k_f and k_{nr} respectively, and the average fluorescence wavelength, $\bar{\lambda}_f$. Furthermore, an analysis of previously published data [118] allows an estimate of the excited singlet-singlet interaction parameter, k_{SS}, to be made. These parameters are valuable both in modelling the role of matrix molecules within MALDI and in ascertaining matrix characteristics beneficial to the MALDI process.

5.2 Theory

There exist several texts (for example, refs. 117,243,244) that describe the photoexcited mechanisms of aromatic molecules both phenomenologically and mathematically, from which the following brief explanation is derived.

Of fundamental importance are the fluorescence decay rate, or radiative transition probability, k_f, and the non-radiative decay rate, k_{nr}, that describe decay from the lowest excited singlet state (S_1) to the ground state (S_0) via radiative and non-radiative (internal conversion) mechanisms respectively. The total S_1-S_0 decay rate, k_1, can therefore be expressed as

$$k_1 = k_f + k_{nr} \qquad 5.1$$

The radiative lifetime, τ_f, can be written as

$$\tau_f = \frac{1}{k_f} \qquad 5.2$$

and the total S_1 decay lifetime, τ_1, as

$$\tau_1 = \frac{1}{k_1} \qquad 5.3$$

which corresponds to the time for the population in state S_1 to fall to e^{-1} by decay to the ground state. The fluorescence quantum efficiency, ϕ_{qe}, is defined as the number of photons radiatively emitted from the S_1 state divided by the total number of photons absorbed. If collisional quenching, excited state interactions, self-absorption and intersystem crossing to the triplet manifold are ignored, ϕ_{qe} may be calculated as

$$\phi_{qe} = \frac{k_f}{k_1} \qquad 5.4$$

The spectral quantum efficiency, $F(\nu)$, can now be defined by

$$\phi_{qe} = \int_0^\infty F(\nu)d\nu \qquad 5.5$$

Molecular absorption and fluorescence are examples of *vibronic* transitions where both the electronic and vibrational coordinates of the molecule may change. For example, such a transition may involve changes in the electronic and vibrational coordinates of $k \rightarrow l$ and $m \rightarrow n$ respectively, the overall transition may then be described as $km \rightarrow ln$. For solutions and solids, τ_1 is usually sufficiently long to allow the excess

vibrational energy from an absorption transition to be thermalised by collisions and lattice interactions before fluorescence takes place. Fluorescence transitions are, therefore, predominantly of the form $10 \rightarrow 0n$ (see fig. 5.1), or more generally $k0 \rightarrow ln$, i.e. from the lowest available vibrational level within the excited electronic state. The Einstein A coefficient describing this transition is given by

$$A_{k0\rightarrow ln} = 8\pi h\nu^{3}_{k0\rightarrow ln} n^{3} c^{-3} B_{k0\rightarrow ln} \qquad 5.6$$

where h is Planck's constant, $\nu_{k0\rightarrow ln}$ is the frequency of the vibronic transition, n is the refractive index of the medium, c is the speed of light in vacuum and $B_{k0\rightarrow ln}$ is the Einstein B coefficient of the transition. $A_{k0\rightarrow ln}$ also has the relation

$$A_{k0\rightarrow ln} \propto \int_{\nu_{k0\rightarrow ln}} F(\nu)d\nu \qquad 5.7$$

Approximating vibrational wavefunctions with equal vibrational but different electronic coordinates to be the same (i.e. $\Phi_{kn} = \Phi_{ln}$), it can be shown that

$$B_{k0\rightarrow ln} = B_{l0\rightarrow kn} \qquad 5.8$$

where one side of the equation represents absorption and the other fluorescence. Note that eqn. 5.8 describes transitions of unequal energies and is different to the more common (Einstein) relation describing equi-energetic transitions

$$B_{kn\rightarrow lm} = B_{lm\rightarrow kn} \qquad 5.9$$

Since $\int F(\nu)d\nu$ varies linearly with $B_{k0\rightarrow ln}$ (eqns. 5.6 and 5.7), eqn. 5.8 describes what is known as the *mirror symmetry relation* between absorption and fluorescence spectra. This is seen as a mirror symmetry in the **normalised** absorption and fluorescence spectra about a certain symmetry-point frequency, ν_0, at energies $h(\nu_0 + \Delta\nu)$ and $h(\nu_0 - \Delta\nu)$

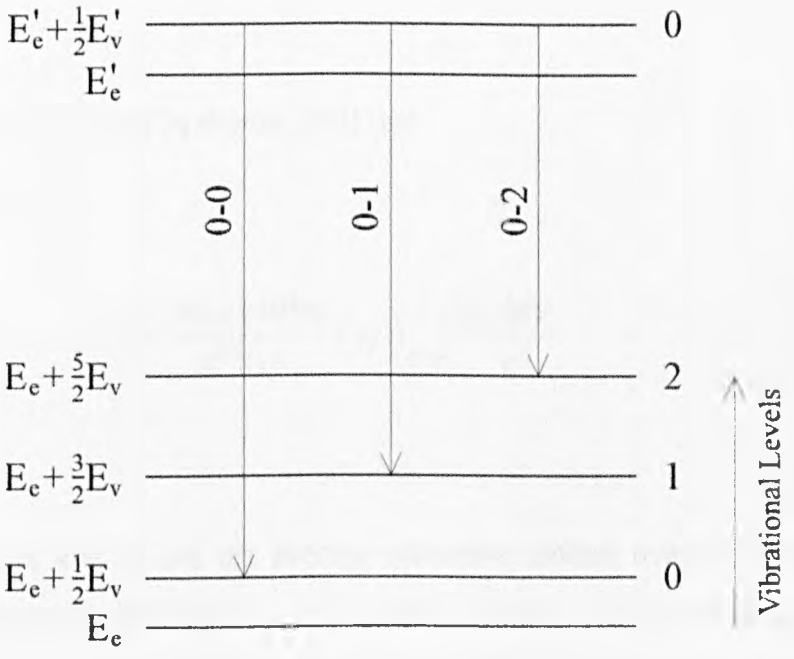

Figure 5.1. Vibronic fluorescence transitions [243].

respectively (eqn. 5.8; see fig. 5.2), where $\Delta\nu$ represents a small change in frequency. The (vibrationless or 0-0) transition of frequency ν_0 is described by $k0 \rightarrow l0$ (see fig. 5.1).

Now, k_f is equal to the sum of $A_{k0\rightarrow ln}$ over all fluorescence transitions

$$k_f = \sum_n A_{k0\rightarrow ln} \qquad 5.10$$

from which it can be shown [243] that

$$k_f = \frac{8\pi \times 2303 n_f^3}{c^2 N_A n_a} \left\langle \nu_f^{-3} \right\rangle_{AV}^{-1} \int \frac{\varepsilon(\nu) d\nu}{\nu} \qquad 5.11$$

where n_f and n_a are the average refractive indices over the fluorescence and absorption bands respectively, N_A is Avogadro's number, $\varepsilon(\nu)$ is the frequency dependent molar extinction coefficient of the absorption band, ν_f represents fluorescence band frequencies and $\left\langle \nu_f^{-3} \right\rangle_{AV}^{-1}$ is the reciprocal intensity weighted average of ν_f^{-3} given by

$$\left\langle \nu_f^{-3} \right\rangle_{AV}^{-1} = \frac{\int F(\nu) d\nu}{\int \frac{F(\nu) d\nu}{\nu^3}} \qquad 5.12$$

Equation 5.11 can be written in terms of absorption cross-section, $\sigma(\nu)$,

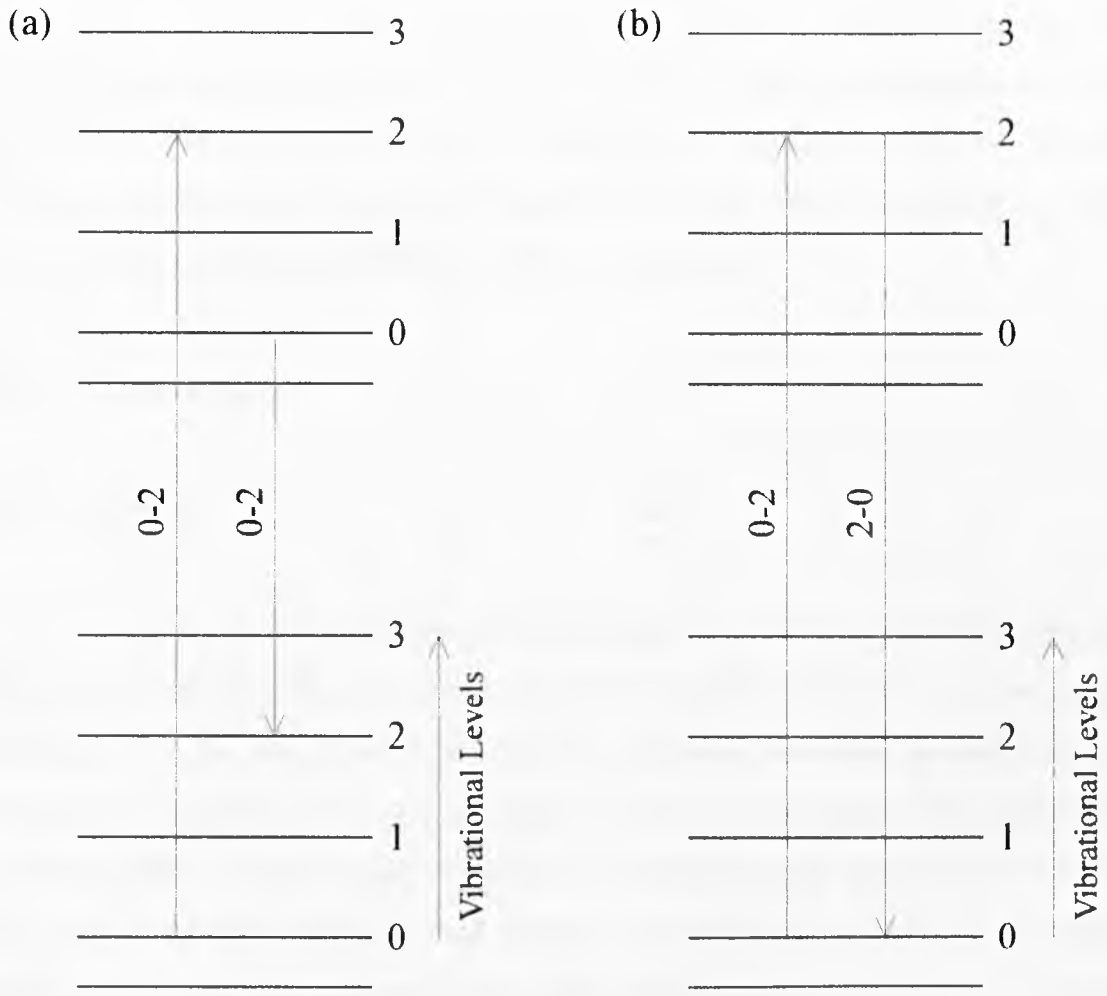

Figure 5.2. Vibronic transitions of equal transition probability:

(a) mirror symmetry (eqn. 5.8) and (b) Einstein relation (eqn. 5.9).

$$k_f = \frac{8\pi n_f^3}{c^2 n_a} \left\langle \nu_f^{-3} \right\rangle_{AV}^{-1} \int \frac{\sigma(\nu) d\nu}{\nu} \qquad 5.13$$

There exists, therefore, a means of estimating k_f using absorption and fluorescence spectral data without having to resort to direct measurement methods. However, the technique is based upon the assumption that the mirror symmetry relation, and hence the vibrational wavefunction approximation ($\Phi_{kn}=\Phi_{ln}$), is valid and therefore has a varying degree of applicability for different molecules.

5.3 Experimental

5.3.1 Method

Several texts comprehensively describe standard methodologies for fluorescence spectrometry of solutions (for example, refs. 245 and 246). One of the recommended techniques for the measurement of ϕ_{qe} is to calibrate detection apparatus with a fluorescence standard [245] over a range of solution absorbances for geometrical correction [246]. Despite several fluorescence standards being proposed in literature [247,248], quinine bisulfate (empirical formula $C_{20}O_2N_2H_{19}$) in 1.0 N (0.5 M) sulphuric acid [247,248] was chosen since it has a well defined quantum yield for $\lambda < 350$ nm excitation (0.546 ± 5% at 25°C) with a well defined temperature dependence (-0.25% / °C), exhibits little or no impurity quenching and has an emission region similar to those of the compounds to be measured (400 - 500 nm).

The experimental arrangement for the measurement of solution phase fluorescence is shown in fig. 5.3. Briefly, PC based software (AMKO MuLTIray, AMKO GmbH, Tornesch bei Hamburg, Germany) externally triggered a home-built N_2 laser (3 ns FWHM). The laser output was attenuated with glass microscope slides and spatially filtered with a circular aperture (~11 mm diameter) before being slightly focussed onto the fused silica sample cuvette with a 76.2 mm focal length plano-convex fused silica lens. Beam attenuation was increased as the concentration of solutions

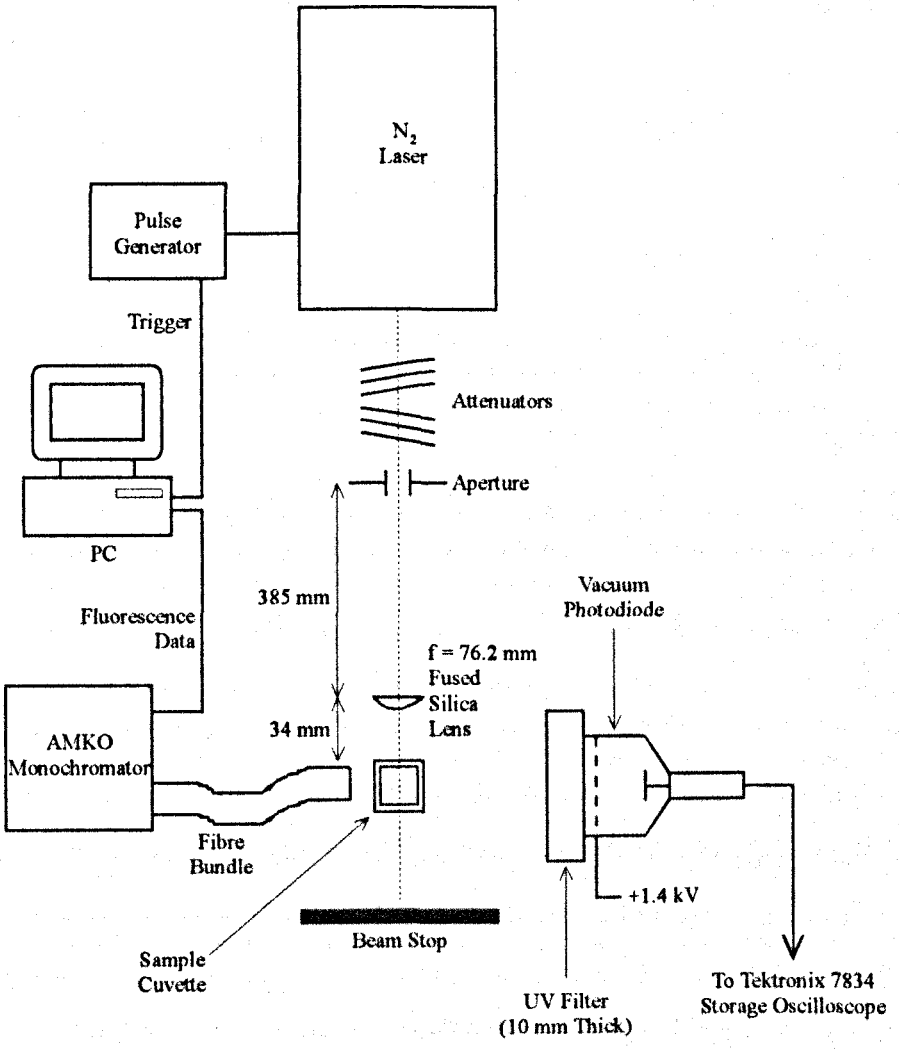

Figure 5.3. Schematic diagram of experimental arrangement for the measurement of fluorescence from solutions.

increased to reduce the likelihood of lasing in the excited solution (e.g. coumarin 120). Incident laser energies (40 - 150 μJ) were monitored immediately following the measurement of fluorescence from each solution. In order to reduce noise due to scattering, fluorescence signals were detected orthogonally to the laser beam direction.

The temporal behaviour of the fluorescence was observed by using a Photek S20 vacuum photodiode (sub-nanosecond risetime; Photek Limited, East Sussex, UK) connected to a Tektronix 7834 Storage Oscilloscope (400 MHz; Tektronix Inc., Beaverton, Oregon, USA) using a 7A19 50Ω plug-in amplifier and a 7B85 plug-in timebase. Instrument response times were not included in decay time calculations. A polymethylmethacrylate (PMMA) UV filter was placed over the front of the vacuum photodiode to ensure that the visible fluorescence, and not scattered laser radiation, was being detected. Fluorescence was also captured using a fibre bundle (circular-to-rectangular array of 20 × 1.4 mm diameter UV grade fibre optics) and analysed on an 01-001A AMKO grating monochromator (300 lines/mm; 500 nm blaze wavelength) to give the emission spectrum of the analyte solution. Within the monochromator, an approximately 1 mm slit at the termination of the fibre bundle was imaged using the grating and two concave mirrors onto a CCD detector array (1024 elements) to give a spectral resolution of 5 nm (FWHM; λ = 632.8 nm). The CCD array was gated 'open' for 10 ms by the PC software triggering the N_2 laser and the detected signal read into the computer for analysis. Furthermore, the software allowed the summation of spectra from consecutive laser pulses thus improving the signal-to-noise ratio. The monochromator was calibrated using scattered N_2 (337.1 nm) and He-Ne (632.8 nm) laser light which fell at points towards the two extremes of the spectral range measured.

The arrangement for detection of fluorescence from solid films is shown in fig. 5.4. Again, the N_2 laser is triggered from the PC but the aperture is now imaged onto the sample to give a spot roughly 6 mm in diameter. Incident laser energies of 200 - 300 μJ therefore gave fluences of between 0.7 and 1.0 $mJ.cm^{-2}$, i.e. below the desorption threshold. Detected signals were obtained at approximately 45° to the incident laser pulse direction, both with the fibre bundle and the vacuum photodiode. A 3 cm focal length plano-convex fused silica lens was used prior to the vacuum photodiode to

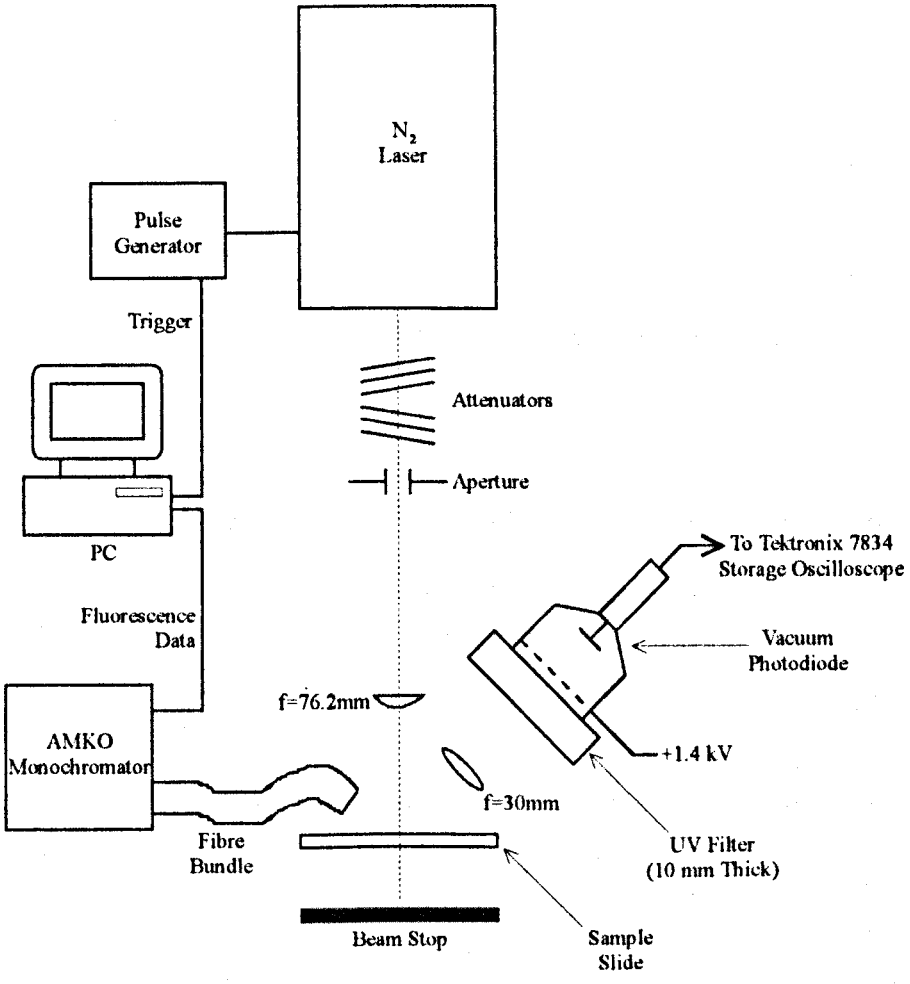

Figure 5.4. Schematic diagram of experimental arrangement for the measurement of fluorescence from solid films.

capture a greater amount of emitted light. Otherwise, data acquisition was identical to that described above for solutions.

5.3.2 Chemicals

All MALDI matrices measured were obtained from the sources described in Chapter 3 and were used without further purification. Matrices were dissolved in solvents deemed as 'standard' for MALDI preparation (see Chapter 3) unless otherwise stated. Quinine bisulphate was obtained from Aldrich Chemical Company Ltd. (Gillingham, UK) to a stated purity of 90 % (remainder hydroquinine sulphate monohydrate). Solid samples were obtained by sublimation deposition onto glass microscope slides, as described in Chapter 3. With the exception of α-cyano-4-hydroxycinnamic acid (α-CHC), films were grown to a thickness of > 1 μm (estimated by inspection) in order to completely absorb low-intensity 337 nm laser radiation. α-CHC films could not be grown to such a thickness without undue time being spent in deposition; absorption measurements of such samples were therefore made in order to establish the amount of energy deposited into the sample by each incident laser pulse.

5.4 Results and Analysis

5.4.1 Fluorescence Spectra

Before meaningful fluorescence measurements could be made, an estimate of the molar extinction coefficient of quinine bisulfate in 1.0 N sulphuric acid was required in order to calculate the amount of energy absorbed from each laser pulse. The absorption spectrum of 10 mg.litre^{-1} (1.31×10^{-4} Molar) and 100 mg.litre^{-1} (1.31×10^{-3} Molar) quinine bisulphate solutions (fig. 5.5) was obtained by spectrophotometry (see Chapter 4 for details). The molar extinction coefficient at 337 nm, ε_{337}, was calculated as 1.0×10^4 litre.mole^{-1}.cm^{-1} (cf. $\varepsilon_{337} = 9.7 \times 10^3$ litre.mole^{-1}.cm^{-1} [246]). Fluorescence spectra from either 200 or 400 laser pulses were then obtained (fig. 5.5) for solution concentrations of between 5×10^{-6} and 1×10^{-2} Molar, corresponding to absorbances ($-\log_{10}$[transmission] = $\varepsilon_{337} \times$ molarity, $[M]$, $\times$ cuvette length, l_c) of between 0.05 and 100. The solution

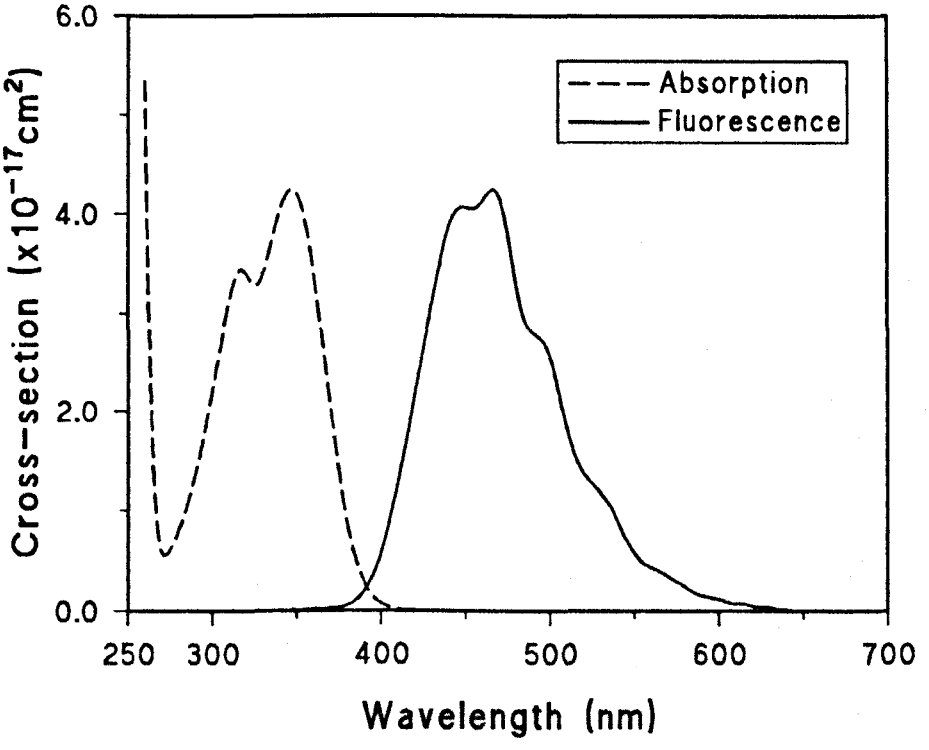

Figure 5.5. Absorption cross-section (1.3×10^{-4} Molar) and fluorescence (arb. units; 2×10^{-5} Molar; 400 pulses) spectra of quinine bisulfate solutions.

temperature was measured to be 16°C and hence ϕ_{qe} was assumed to be 0.558 (see §5.3.1). Monochromator sensitivity, S, was determined by

$$S = \frac{\int f(\lambda)d\lambda}{\frac{E_{tot}}{E_{337}}\left\{1-\exp\left(-\varepsilon_{337}[M]l_c\right)\right\}.\phi_{qe}} \qquad 5.14$$

where $f(\lambda)$ is the fluorescence signal, λ is the wavelength, E_{tot} is the incident laser energy and E_{337} the laser photon energy. The denominator of eqn. 5.14 represents the number of photons absorbed and the numerator the **relative** number of photons emitted; the dependence of $f(\lambda)$ on photon wavelength is ignored since the quinine bisulfate fluorescence spectrum falls in approximately the same spectral region as those of MALDI matrices. Once S was calculated, ϕ_{qe} could be determined for other solutions by rearrangement of eqn. 5.14. No marked variation of sensitivity with solution absorbance was observed, despite the contrary observations in the literature [246]. This was probably due to employing the fibre bundle collection system with a wider spatial sampling region than that available with the more usual method of directly illuminating the monochromator entrance slit.

Before investigating matrices in solvents typically used in MALDI sample preparation, verification of S was provided by estimating ϕ_{qe} for a previously measured solution. Coumarin 120 in ethanol was selected for this, having ϕ_{qe} = 0.75 [249]. Spectrophotometry (see Chapter 4 for details) on a 5×10^{-5} Molar solution gave $\varepsilon_{337} = 1.52 \times 10^4$ litre.mole^{-1}.cm^{-1} (fig. 5.6). Fluorescence spectra (e.g. fig. 5.6) comprising either 200 or 400 laser pulses were collected from 11 solutions within a concentration range of 5×10^{-7} to 1×10^{-3} Molar, corresponding to absorbances of 7.6×10^{-3} and 15.2 respectively. ϕ_{qe} was calculated to be 0.74 ± 0.03 (eqn. 5.14), where the estimated error represents one standard deviation in the data. With this value of ϕ_{qe} lying close to that given in literature, fluorescence measurements of MALDI matrices in other solutions could proceed with a greater degree of confidence.

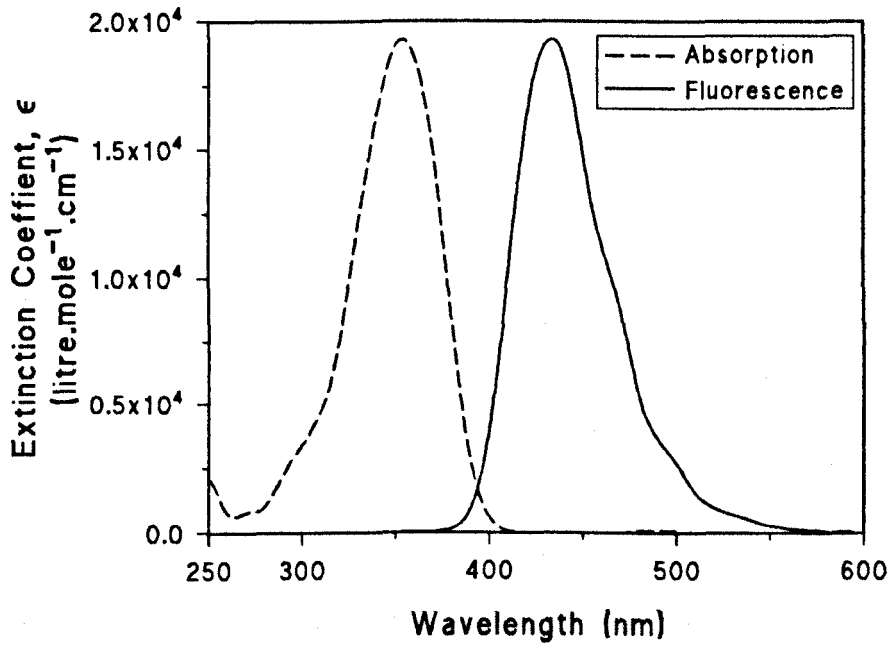

Figure 5.6. Absorption and fluorescence (arb. units; 200 pulses) spectra of coumarin 120 in ethanol (5×10^{-5} Molar).

Spectra from coumarin 120 in 50:50 methanol:acetonitrile + 0.1 % trifluoroacetic acid (TFA) were collected over a concentration range of 2×10^{-6} to 1×10^{-3} Molar (fig. 5.7a). ε_{337} for coumarin 120 in the methanol/acetonitrile solvent was taken from the literature [186] whereas the values for all other matrix solutions are listed in Chapter 4. ϕ_{qe} for coumarin 120 was estimated as 0.82 (see table 5.1) and τ_l was measured with the vacuum photodiode to be 3.3 ns ± 10% (compare fig. 5.8a incident N_2 laser pulse and fig. 5.8b coumarin 120 solution fluorescence), to give $k_l = 3.0 \times 10^8$ s^{-1} (eqn. 5.3) and $k_f = 2.0 \times 10^8$ s^{-1} (eqn. 5.4). The fluorescence spectra of 2,5-dihydroxybenzoic acid (2,5-DHB; 600 pulse spectra; 5 solutions in range 5×10^{-5} to 5×10^{-3} Molar), ferulic acid (1000 pulse spectra; 5×10^{-3} and 2×10^{-4} Molar) and sinapinic acid (1000 pulse spectrum; 5×10^{-3} Molar) were also collected (fig. 5.7b-d respectively). However, decay lifetimes were so short as to be difficult to interpret from the vacuum photodiode since the exponential decay envelope fell within the 3 ns (FWHM) excitation pulse. Estimates of the decay rates had to be made, therefore, by using the mirror symmetry relation.

In performing mirror symmetry calculations (eqn. 5.13), both the absorption and fluorescence spectra are integrated, albeit in different forms. Although this was straightforward for fluorescence spectra, higher energy absorption bands overlapped with the low wavelength side of the S_0-S_1 absorption band rendering accurate integration impossible. This was avoided by 'creating' absorption spectra by reflecting (in the frequency domain) a solution's fluorescence spectrum about ν_0 and normalising the reflected maxima to the maximum solution phase absorption cross-section. This method, therefore, produced perfectly symmetrical spectra which, although 'ideal' in theory, were presumably an increasingly large source of error as the degree of observed (real) symmetry decreased. Values of n_a and n_f (eqn. 5.13) were estimated using wavelength dependent data of the solvent components [250].

Using this technique, k_f for coumarin 120 (in methanol/acetonitrile) was calculated using the mirror symmetry relation to be 2.2×10^8 s^{-1}, i.e. within 10 % of the directly measured value. This similarity of k_f for coumarin 120 using the two methods described suggested that mirror symmetry analysis of optical spectra for the other solutions would be feasible, although these spectra are inherently less symmetrical (by

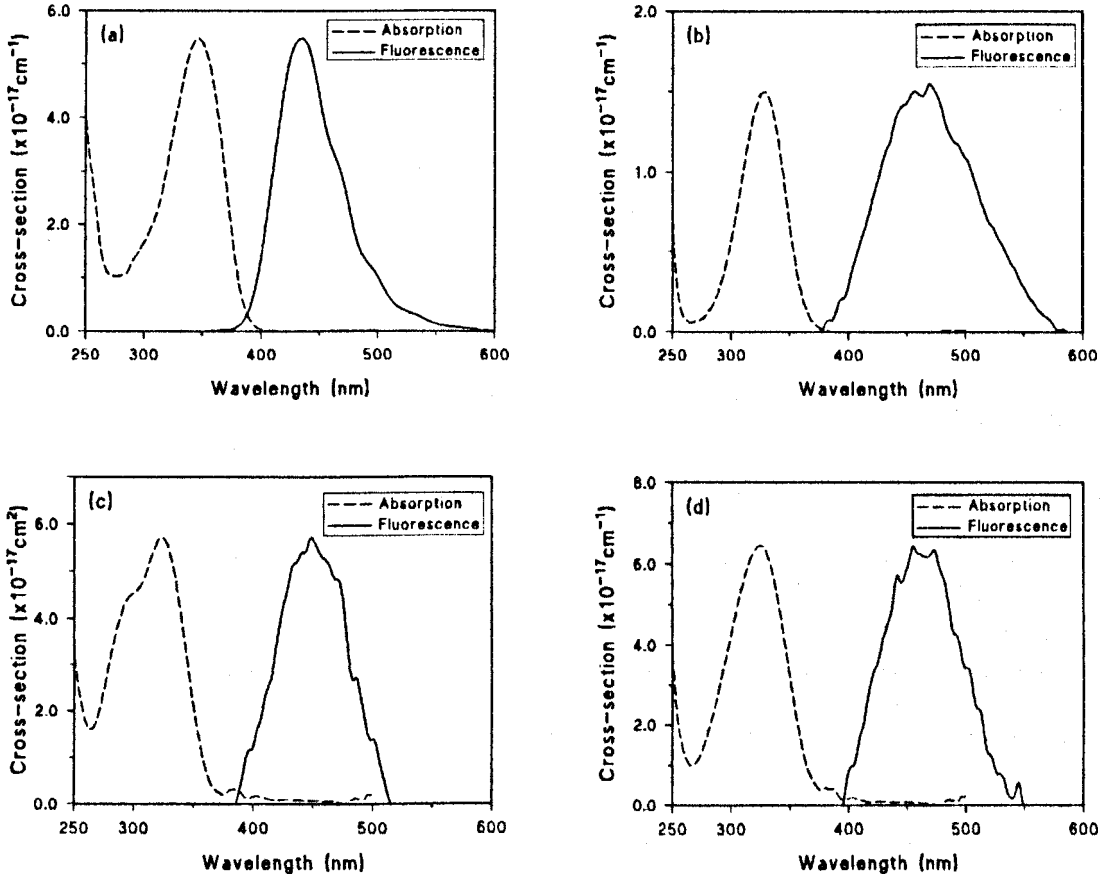

Figure 5.7. Solution phase absorption cross-section and fluorescence (arb. units) spectra of (a) coumarin 120 (50:50 MetOH:ACN), (b) 2,5-DHB, (c) ferulic acid and (d) sinapinic acid.

MATERIAL:	Fluorescence Quantum Efficiency, ϕ_{qe}	Fluorescence Decay Rate, k_f (s^{-1})	Total Decay Rate, k_1 (s^{-1})	Non-radiative Decay Rate, k_{nr} (s^{-1})
SOLUTIONS				
Coumarin 120	0.82	2.4×10^8	3.0×10^8	6.3×10^7
Ferulic Acid	2.2×10^{-3}	2.5×10^8	1.1×10^{11}	1.1×10^{11}
2,5-DHB	0.017	8.9×10^7	5.2×10^9	5.1×10^8
Sinapinic Acid	1.9×10^{-3}	2.4×10^8	1.3×10^{11}	1.3×10^{11}
FILMS				
Coumarin 120	0.46	2.2×10^8	4.8×10^8	2.6×10^8
Ferulic Acid	0.31	2.0×10^8	6.6×10^8	4.6×10^8
2,5-DHB	0.59	7.7×10^7	1.3×10^8	5.4×10^7
α-CHC	0.082	4.2×10^8	5.1×10^9	4.7×10^9

Table 5.1. Relaxation data for common MALDI matrices.

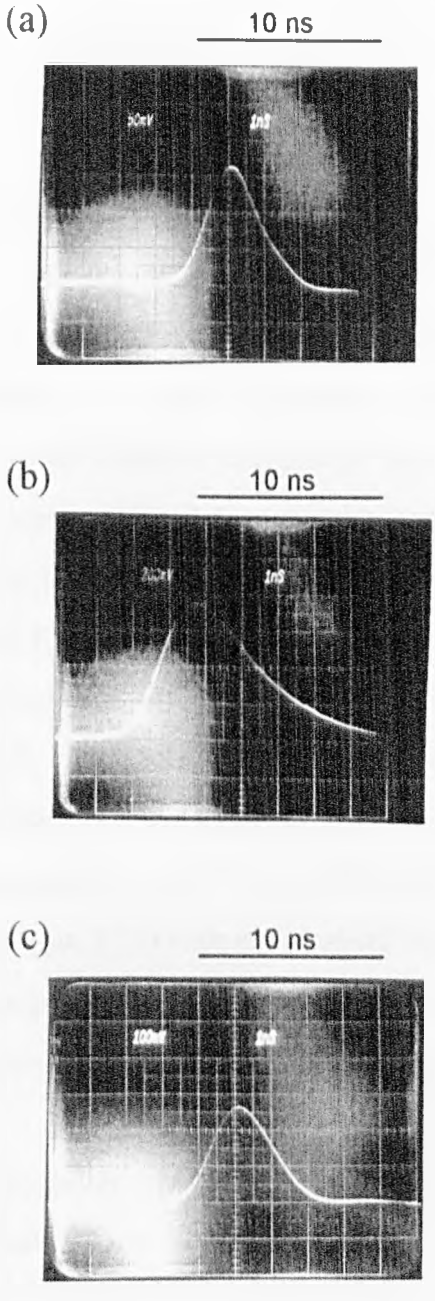

Figure 5.8. Temporal Pulse Shapes of (a) N_2 Laser, (b) Coumarin 120 Solution Fluorescence and (c) Ferulic Acid Film Fluorescence

inspection) than those for coumarin 120. k_f was, therefore, calculated by mirror symmetry analysis (eqn. 5.13) and ϕ_{qe} by eqn. 5.14, the combination of which gave estimates of k_{nr} and k_l (eqns. 5.1 and 5.4), summarised in table 5.1.

Fluorescence spectra, each comprising the sum of data from 600 laser pulses, were also collected from sublimated solid films of ferulic acid, α-CHC (estimated thickness 150 nm), 2,5-DHB and coumarin 120 (fig. 5.9). Fluorescence from sinapinic acid films could not be detected. Short fluorescence lifetimes for the solid films precluded accurate determination of τ_l and only estimates could be made. Despite this, ferulic acid was selected as the calibrant compound since its characteristic optical absorption and emission spectra exhibited a reasonable degree of symmetry (see fig. 5.9a). In order to minimise the error in measuring τ_l directly, a computer simulation was used to generate the expected FWHM of a fluorescence signal as a function of k_l for a 3 ns (FWHM) Gaussian excitation pulse (fig. 5.10). The model assumed a simple two level system composing S_0 and S_1. Fig. 5.8c shows a trace obtained with the vacuum photodiode for a ferulic acid film. This had a measured FWHM of 3.85 ns ± 10% (cf. 3.0 ns for the laser pulse), corresponding to τ_l = 1.5 ns ± 20% or $k_l = 6.6 \times 10^8$ s^{-1}. By using the mirror symmetry relation (eqn. 5.13) with an 'idealised' absorption spectrum, a value of $k_f = 2.0 \times 10^8$ s^{-1} was estimated; hence $k_{nr} = 4.6 \times 10^8$ s^{-1} and $\phi_{qe} = 0.31$ (eqns. 5.1 and 5.4) allowing the monochromator/detectors to be calibrated (eqn. 5.14).

The fluorescence properties for other matrices were estimated by firstly calculating ϕ_{qe} (eqn. 5.14) and k_f (eqn. 5.13, 'idealised' mirror symmetry method) and then k_l and k_{nr} (eqns. 5.4 and 5.1 respectively). In the absence of any other suitable data, the refractive indices in eqn. 5.13 were assumed to be $n_f = n_a = 1.64$, based on previous Brewster angle measurements (§4.3). The fluorescence parameters estimated in this way are summarised in table 5.1. Note that for the case of coumarin 120, for which the absorption spectrum develops a severe doublet structure (as discussed in Chapter 4), the maximum absorption cross-section of the reflected fluorescence spectrum was taken as twice that of the actual value as there are two absorption peaks (fig. 5.9d); also, in calculating ν_0, the wavelength of maximum absorption was taken as the average value of the two absorption peaks. This procedure gave $k_l = 4.8 \times 10^8$ s^{-1} for coumarin 120,

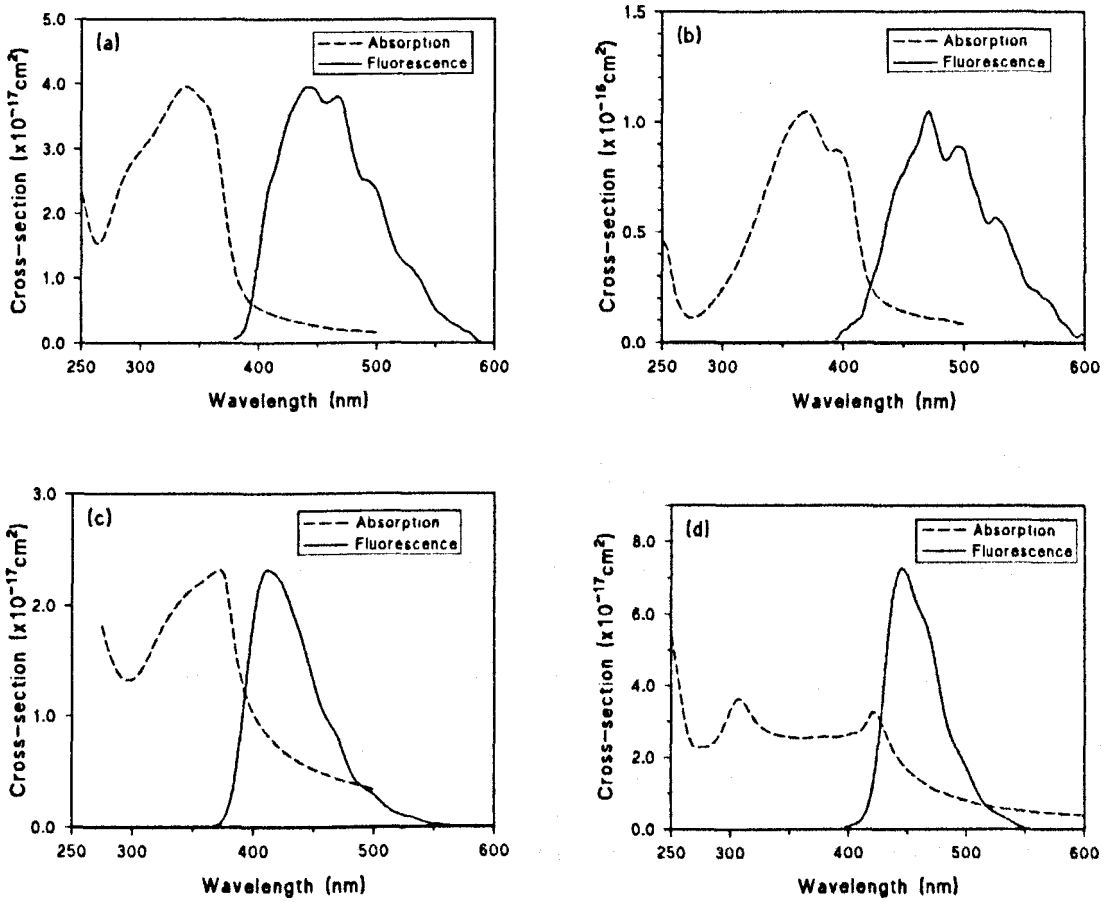

Figure 5.9. Solid phase absorption cross-section and fluorescence (arb. units) spectra of (a) ferulic acid, (b) α-CHC, (c) 2,5-DHB and (d) coumarin 120.

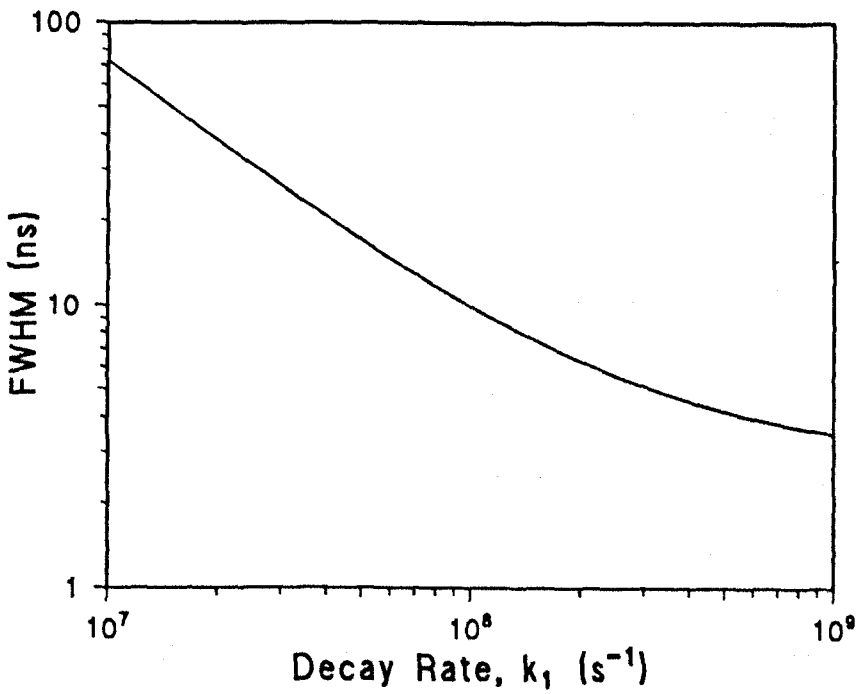

Figure 5.10. Calculated FWHM of fluorescence emission as a function of decay rate, k_1 (s^{-1}), using a 3 ns (FWHM) gaussian excitation.

compared to 5.5×10^8 s^{-1} based on the measured vacuum photodiode signal FWHM of 4.05 ns ± 10%.

In assessing the accuracy of these values, it may be assumed that an error of less than ± 5% applies to the solution ϕ_{qe} measurements (given the agreement with the literature value for coumarin 120 in ethanol). The other measurements are subject to larger error beacause of the assumption of mirror symmetry. As the symmetry between a molecule's absorption and fluorescence spectra decreases, so the inaccuracy of values calculated using the mirror symmetry relation will increase. For molecules possessing a good degree of spectral symmetry, an error of ± 10% may be assumed (from coumarin 120 in methanol/acetonitrile) but for those with significant asymmetry, e.g. 2,5-DHB, the uncertainty may be much greater. However, the similarity of the directly measured and 'idealised' mirror symmetry values of k_l for coumarin 120 films lends confidence to the values calculated. The differing physical nature of the matrix films could be another source of inaccuracy since different absorption lengths and optical scattering coefficients may cause the emission collection efficiency to vary from matrix to matrix.

Previous measurements on solid samples crystallised from solution have given values of τ_l = 5 ns ($k_1 = 2.0 \times 10^8$ s^{-1}) and $\phi_{qe} \leq 0.2$ for 2,5-DHB [109,118], $\tau_l \leq 3$ ns ($k_l \geq 3.3 \times 10^8$ s^{-1}) and $\phi_{qe} = 0.11$ for ferulic acid [118], and $\tau_f \leq 30$ ns ($k_f \geq 3.3 \times 10^7$ s^{-1}) for sinapinic acid single crystals [109], although the method for determining ϕ_{qe} is not made clear. Furthermore, there exist problems with experimenting on 'dried-droplet' samples in terms of accurately determining the absorbed laser energy (see Chapters 3 and 4). It is clear, however, that fluorescence quantum efficiencies presented here for solid films (table 5.1) are larger than those previously reported by a factor of 2-3. The possible inaccuracies with measurements from dried-droplet samples should be compared with those outlined above for the present method in order to determine which values are more appropriate. Also of note in table 5.1 is the relatively low ϕ_{qe} and high k_l for solid α-CHC compared with other matrices implying a rapid and efficient thermalisation of absorbed energy; this inference is consistent with the relatively low fluence threshold of α-CHC desorption/ionisation (see Chapter 3) and fragmentation [163]. The values presented here show matrices in solution to have similar values of k_f but k_{nr} spanning

over three orders of magnitude; this, obviously, leads to ϕ_{qe} for solutions having a similar spread of values. A comparison of values obtained for solutions and solids shows that despite the large variations in k_{nr} between different phases, there is a degree of consistency for k_f. This should be expected as k_f is an inherent property of a molecule and remains relatively insensitive to the molecule's environment, whereas k_{nr} can be greatly affected by oxygen and other impurities that enhance internal conversion to the S_0 state [243,244] or intersystem crossing to the triplet manifold [242].

In using the mirror symmetry relation to obtain k_I, it is necessary to calculate ν_0. This was accomplished in two ways: firstly, by graphically determining the cross-over wavelength of normalised absorption and fluorescence spectra and, secondly, by assuming symmetry in the spectra and averaging the photon energies of the absorption and fluorescence maxima. Once ν_0 is established, it is simple to find the 0-0 transition energy, ε. The values of ε, arrived at using the two methods described above, are summarised in table 5.2 for solutions and solid films. ε is generally lower in the solid phase than in solution and has a range of between 2.9 and 3.3 eV for the matrices studied.

Also of interest for modelling is the average fluorescence wavelength, $\bar{\lambda}_f$, and the associated average fluorescence energy, $\bar{\varepsilon}_f$. Fluorescence transitions from the lowest vibrational level of S_1 will, on average, cause a heating of the molecule due to a remnant energy given by $(\varepsilon - \bar{\varepsilon}_f)$. $\bar{\lambda}_f$ was calculated by integrating the fluorescence bands according to

$$\bar{\lambda}_f = \frac{\int \lambda f(\lambda) d\lambda}{\int f(\lambda) d\lambda} \qquad 5.15$$

and is summarised for the different matrices studied in table 5.3. $\bar{\lambda}_f$ ranges between approximately 430 and 490 nm which corresponds to 2.9 and 2.5 eV. In comparing the value $(\varepsilon - \bar{\varepsilon}_f)$ for various matrices, it is clear that in fluorescence transitions there exists between 0.2 and 0.4 eV of thermalisation.

MATERIAL:	ε (eV; Graphical Intersection)	ε (eV; Assumed Symmetry)
SOLUTIONS		
Coumarin 120	3.18	3.20
Ferulic Acid	3.20	3.30
2,5-DHB	3.29	3.25
Sinapinic Acid	3.13	3.24
FILMS		
Coumarin 120	2.86	2.86
Ferulic Acid	3.12	3.19
2,5-DHB	3.12	3.15
α-CHC	2.91	2.92

Table 5.2. 0-0 ground-singlet transition energies of common MALDI matrices.

MATERIAL:	Average Fluorescence Wavelength, $\bar{\lambda}_f$ (nm)
SOLUTIONS	
Coumarin 120	445
Ferulic Acid	442
2,5-DHB	471
Sinapinic Acid	456
FILMS	
Coumarin 120	457
Ferulic Acid	458
2,5-DHB	430
α-CHC	485

Table 5.3. Average fluorescence wavelengths of common MALDI matrices.

5.4.2 Excited State Interactions

Figure 5.11 shows a graph presented in ref. 118 that describes a study of matrix luminescence intensity to fluence ratio. Evidently, luminescence in solid samples becomes increasingly quenched as the fluence increases. This was qualitatively attributed to excited state interactions of the form [118]:

$$S_1 + S_1 \xrightarrow{1} S_p + S_0 \xrightarrow{2} S_1 + S_0 \qquad 5.16$$

where S_p represents some higher lying singlet state (i.e. $p > 1$). It is noted [118] that stage 2 of the process in eqn. 5.16 will lead to heating of the matrix molecules.

Singlet-singlet interactions of this form have been observed to cause photoconductivity [251-253] and fluorescence quenching [254-256] in anthracene crystals and solutions. Calculated values for anthracene of the single-singlet interaction rate constant, k_{SS}, range from 4×10^{-8} $cm^3.s^{-1}$ (for excitation) to 0.9×10^{-12} $cm^3.s^{-1}$ (for ionisation).

A simple numerical model was used to determine k_{SS} for 2,5-DHB at 300 K from the experimental results shown in fig. 5.11. A four level system is assumed, with a molecule being in either the ground (S_0), S_1, S'_p or S_p state, with population densities n_0, n_1, n'_p and n_p respectively. Here, S'_p is at an energy ε above S_1 and is populated by excited state interactions, whereas S_p lies above S_1 by an energy $h\nu$, the energy of one photon, and is populated by photoexcitation. Both S'_p and S_p are, however, assumed to relax at the same rate, k_p. If stimulated emission is neglected, the rate equations governing the population densities of states are:

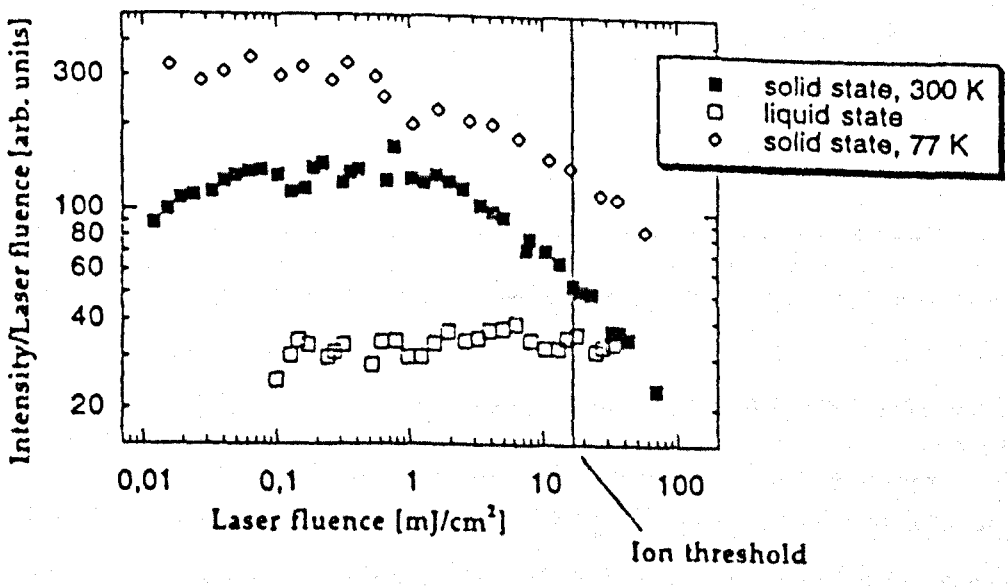

Figure 5.11. Relative luminescence yield of 2,5-DHB as a function of incident (355 nm) fluence [118].

$$\left.\begin{aligned}
\frac{dn_0}{dt} &= n_1 k_1 - n_0 \sigma_0 \frac{I}{h\nu} + \frac{1}{2} k_{SS} n_1^2 \\
\frac{dn_1}{dt} &= n_0 \sigma_0 \frac{I}{h\nu} - n_1 \sigma_1 \frac{I}{h\nu} - n_1 k_1 + k_p \left(n_p' + n_p\right) - k_{SS} n_1^2 \\
\frac{dn_p'}{dt} &= \frac{1}{2} k_{SS} n_1^2 - n_p' k_p \\
\frac{dn_p}{dt} &= n_1 \sigma_1 \frac{I}{h\nu} - n_p k_p
\end{aligned}\right\} \quad 5.17$$

where σ_0 and σ_1 represent the ground and S_1 state absorption cross-sections respectively, and I is the laser irradiance (square temporal pulse shape). Equation 5.17 therefore includes the effects of both second photon absorption and singlet-singlet interaction as mechanisms for fluorescence quenching. Temperature effects on fluorescence are ignored since the rate of fluorescence quenching is very similar for solid samples initially at 77 K and 300 K (fig. 5.11). If the fluorescence quenching coefficient, Q, is defined as the ratio of the number of $S_1 \rightarrow S_0$ relaxation transitions to the total number of absorption transitions (Q = 1.0 for no fluorescence quenching), then comparison of the modelled Q with the observed value (fig. 5.11) allows an estimate of k_{SS} to be arrived at by iteration. The values used in the model were a photon energy $h\nu$ = 3.5 eV (laser wavelength λ = 350 nm), a laser FWHM of 6 ns, $k_1 = 7.7 \times 10^8$ s^{-1} or 1.7×10^8 s^{-1} (corresponding to data presented above and elsewhere [118] respectively), $k_p = 10^{12}$ s^{-1} (prompt relaxation), $\sigma_0 = 2.0 \times 10^{-17}$ cm^2 or 7.0×10^{-17} cm^2, $\sigma_1 = 1.0 \times 10^{-17}$ cm^2 and a total (gas-phase) population density n_T (= $n_0 + n_1 + n_p$) = 3.0×10^{19} cm^{-3}, although k_{SS} is independent of n_T. These values are based upon experimental conditions [118] and upon data used in more detailed modelling (see Chapter 6).

From the data shown for 2,5-DHB at 300 K in fig. 5.11, it is estimated that Q varies between 0.87 to 0.60 within the fluence range 4 - 10 mJ.cm^{-2}. Using the values given above, k_{SS} varies between 2.8×10^{-11} cm^3.s^{-1} to 8.6×10^{-10} cm^3.s^{-1}. More specifically, using the values of $\sigma_0 = 7 \times 10^{-17}$ cm^2 and $k_1 = 7.7 \times 10^8$ s^{-1}, as used in ionisation modelling (see Chapters 6 and 7), and for 10 mJ.cm^{-2} fluence, $k_{SS} = 2.7 \times 10^{-10}$ cm^3.s^{-1}. This appears to be a reasonable range of values for k_{SS} given that for anthracene, described above. A reasonable estimate of k_{SS} for MALDI matrices, based upon measurements made on 2,5-DHB, would perhaps be 2×10^{-10} cm^3.s^{-1} since this exists in

the mid-point of the overall calculated range and is close to the value obtained for the specific case detailed.

5.5 Conclusions

Collection of solution and solid phase fluorescence spectra has allowed estimates to be made of fluorescence quantum efficiencies (ϕ_{qe}) S_1 decay rates, 0-0 ground-singlet transition energies (ε) and average emission wavelength ($\bar{\lambda}_f$) for several common MALDI matrices. Calculated values of ϕ_{qe} for solid samples were a factor of 2-3 times higher than previously measured. The low ϕ_{qe} and high decay rate for α-CHC are suggested as contributory reasons for the molecule's relatively low desorption/ionisation threshold fluence and high degree of fragmentation compared with other matrices. The increase of a molecule's vibrational energy following a fluorescence transition is estimated to be between 0.2 and 0.4 eV. Furthermore, analysis of previous fluorescence data [118] has allowed an estimate of the singlet-singlet annihilation rate constant, k_{SS} = 2.0×10^{-10} $cm^3.s^{-1}$, to be made. These parameters are valuable both in quantitative modelling and to the general understanding of the role of matrices in MALDI.

6 IONISATION MODELLING I

6.1 Introduction

Section §2.3.3 summarises the current understanding of desorption and ionisation mechanisms in MALDI. Briefly, all significant ionisation is thought to occur in the gas-phase desorbed plume [138,141] with analyte molecules being ionised by collisional charge transfer reactions with matrix species [90,146,147]. The charge-donating matrix in these reactions for UV-MALDI is presumed to be either the protonated $[m+H]^+$ ion [109,138,148] or a photoexcited molecule, m^* [121,147,149,150]. For the former scheme, the radical matrix molecular ion, m^+, is often thought to be a precursor to the formation of $[m+H]^+$ ions [138,109,148], their formation taking place during the laser pulse [118]. If such a mechanism dominates matrix ionisation in MALDI, then a full description of m^+ ion generation will be a necessary and fundamental first step in understanding all subsequent ionisation reactions.

This chapter lays down the foundations for quantitative modelling of matrix ionisation by assuming that gas-phase photoexcited matrix molecules are ionised to form m^+ ions by coupling of their vibrational and excited electronic states. Therefore, despite many collisions being necessary to maintain a thermal distribution of vibrational energy, ionisation proceeds within such an environment as a unimolecular reaction. Such a scheme bears some similarity with thermionic emission, the reservoir of vibrational energy within the molecule resembling that of the 'solid' in thermionic emission. More direct analogies include the detachment of electrons from negative ions [257] and *inverse electronic relaxation*, proposed to account for excited electronic states in molecules resulting from multiple infrared photon absorption [258-260]. Several molecular processes, at this stage, are omitted for reasons of simplicity but are included in a broader assessment of the model in Chapter 7.

6.2 Basic Model

6.2.1 Analysis

Matrix ionisation is assumed to occur in the desorbed gas-phase plume, during the laser pulse, with no molecular energy lost due to the solid-gas phase change. Molecules are taken to be colliding sufficiently frequently that a Boltzmann distribution amongst the matrix molecule vibrational states is maintained, as observed for laser desorbed fullerenes [261].

A simple energy level system is used to describe matrices under photoexcitation (fig. 6.1), and rate equations used to determine the population of states within the laser pulse duration. All molecules are initially assumed to be in the electronic ground state, S_0 (initial fractional population density $n_0 = 1$), until the absorption of a photon of energy $h\nu$, whereupon excitation to the first excited singlet state, S_1 (fractional population density n_1), occurs, followed by rapid thermal relaxation (by energy $\Delta = h\nu - \varepsilon$, where ε is the S_0-S_1 vibrationless transition energy) to the lower vibrational levels of S_1. Depopulation of the S_1 state may proceed either by decay across the energy gap ε to the ground state at a rate k_1 (governed by both radiative and non-radiative decay) or by photoexcitation to a higher energy singlet state, S_p (fractional population density n_p). Intersystem crossing to the triplet manifold is, at this stage, neglected. Loss from the S_p state is taken to be by rapid internal conversion to S_1 with a rate k_p. Assuming that stimulated emission is negligible at the irradiances considered, the rate equations governing the change in state populations are as follows:

$$\left.\begin{aligned} \frac{dn_0}{dt} &= k_1 n_1 - A n_0 \\ \frac{dn_1}{dt} &= A n_0 - B n_1 - k_1 n_1 + k_p n_p \\ \frac{dn_p}{dt} &= B n_1 - k_p n_p \approx 0 \end{aligned}\right\} \qquad 6.1$$

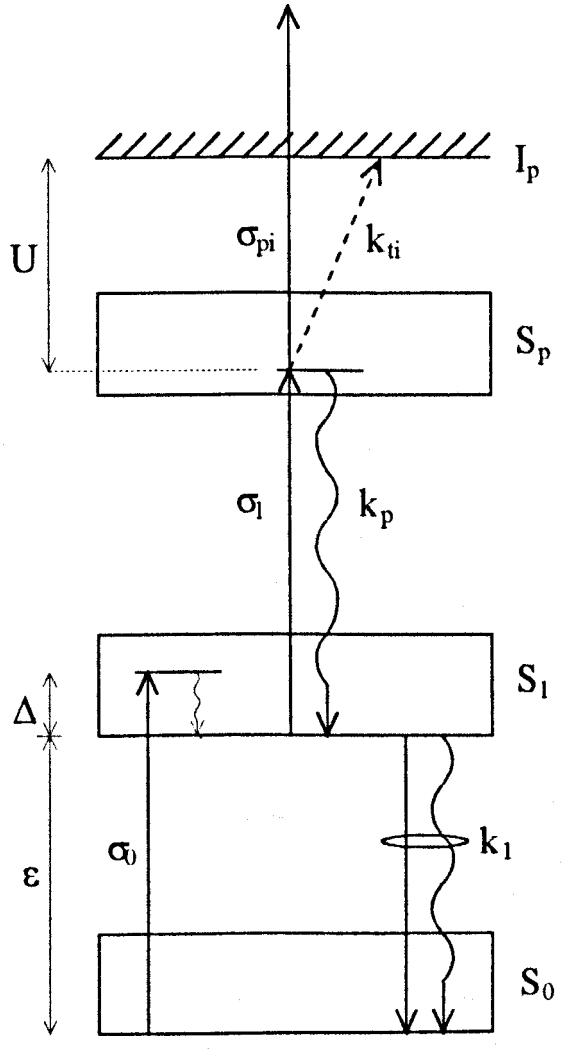

Figure 6.1. Energy level diagram of matrix molecules.

where $A = \sigma_0 I(t)/(h\nu)$, $B = \sigma_1 I(t)/(h\nu)$, σ_0 and σ_1 are the photoexcitation cross-sections from the S_0 and S_1 states, respectively, and $I(t)$ is the laser irradiance.

The average vibrational energy per molecule, E, is found using:

$$\frac{dE}{dt} = An_0\Delta + k_1 n_1 \varepsilon(1-f) + k_p n_p h\nu \qquad 6.2$$

where f is the fluorescence quantum efficiency of S_1 and k is Boltzmann's constant.

Subject to the constraint $n_0 + n_1 + n_p = 1$, and for a laser pulse of duration τ and constant irradiance I (i.e. 'top-hat' temporal pulse shape, $I(t)=I$ for $0 \le t < \tau$), eqns. 6.1 and 6.2 can be integrated to give:

$$n_1 = \frac{A}{C}\left(1-e^{-Ct}\right) \qquad 0 \le t < \tau \qquad 6.3$$

$$n_p = \frac{n_1 B}{k_p} \qquad 0 \le t < \tau \qquad 6.4$$

and

$$E = \frac{AD}{C}\left(t + \frac{e^{-Ct}}{C}\right) + \Delta A t - \frac{AD}{C^2} \qquad 0 \le t < \tau \qquad 6.5$$

where $D = ([1-f]k_1\varepsilon + Bh\nu - A\Delta - BA\Delta/k_p)$ and $C = (A + AB/k_p + k_1)$. The matrix temperature, T, can now be found from:

$$T = T_0 + \frac{2E}{sk} \qquad 6.6$$

where T_0 is the initial temperature of the system (293 K) and s is the number of degrees of freedom available to the molecule.

Ionisation is now assumed to proceed from state S_p at an effective ionisation potential U ($= I_p + \Delta - 2h\nu$, see fig. 6.1), either as unimolecular thermal ionisation or by absorption of a third photon (photoionisation). For the former process of excited-state thermal ionisation (ESTI), calculation of the rate constant, k_{ti}, is shown in Appendix B and is estimated to be given by:

$$k_{ti} \approx 1.2 \times 10^{16} \exp\left(-\frac{U}{kT}\right) \quad (s^{-1}) \qquad 6.7$$

where U is the effective ionisation energy of a photoexcited molecule in the S_p state (see fig. 6.1). The value of the scaling constant (or frequency factor) in this Arrhenius-type equation ($a = 1.2 \times 10^{16}$ s^{-1}) compares well with that used for describing thermionic emission from the ground state of desorbed fullerenes ($a = 1.6 \times 10^{16}$) [261], derived using a quantum mechanical hard-sphere model [262].

For comparison, the rate constant for direct photoionisation of S_p, k_{pi}, can be written as:

$$k_{pi} = \sigma_{pi}\left(\frac{I}{h\nu}\right) \qquad 6.8$$

where the photoionisation cross-section, σ_{pi}, can be estimated using the hydrogenic model [263] as:

$$\sigma_{pi} = 1.58 \times 10^{-17}\left(\frac{U}{h\nu}\right)^3 \quad (cm^2) \qquad 6.9$$

The ion fractions formed by excited-state thermal ionisation, n_{ti}, and photoionisation, n_{pi}, are now calculated numerically from the rate equations by:

$$\left.\begin{aligned}\frac{dn_{ti}}{dt} &= k_{ti} n_p \\ \frac{dn_{pi}}{dt} &= k_{pi} n_p\end{aligned}\right\} \qquad 6.10$$

respectively. In order to allow eqns. 6.3 - 6.5 to remain valid as analytical expressions, the approximation that $k_p >> k_{ti} \sim k_{pi}$ is made such that ionisation from S_p represents a negligible perturbation compared with the number of neutral molecules (i.e. $n_0 + n_1 + n_p = 1$ remains valid throughout).

Once electrons are removed from matrix molecules, they may either escape from the desorbed plume, attach to neutral molecules to form negative ions or recombine with positive m^+ ions. The latter mechanism is described by:

$$\left(\frac{d\rho_e}{dt}\right)_{recomb} = -\gamma \rho_e \rho_i \qquad 6.11$$

where ρ_e and ρ_i are the electron and ion number densities, respectively, and γ is the recombination coefficient, given by:

$$\gamma = \pi r_c^2 v_e = \pi r_c^2 \sqrt{3kT_e/m_e} \qquad 6.12$$

where r_c is the electron capture radius, v_e is the electron velocity, T_e is the free electron temperature and m_e is the free electron mass. Additionally, r_c is defined by:

$$r_c = \frac{e^2}{6\pi\varepsilon_0 kT_e} \qquad 6.13$$

where e is the charge on an electron and ε_0 is the permittivity of free space. From eqn. 6.12, $T_e \geq 0.1$ eV gives $\gamma \leq 6.7 \times 10^{-5}$ cm^3.s^{-1} and for $n_i \leq 10^{-5}$ and a total neutral number density, $\rho_T \leq 3 \times 10^{19}$ cm^{-3} the recombination time-constant is $t_r = (\gamma\rho_i)^{-1} \geq 50$ ps.

Electron attachment to neutral matrix molecules is described by:

$$\left(\frac{d\rho_e}{dt}\right)_{attachment} = -k_A \rho_e \qquad 6.14$$

where k_A is the rate of the attachment. $k_A \geq 10^7$ $s^{-1}.torr^{-1}$ is representative for aromatic molecules [257] which gives a value for the neutral-attachment time-constant, $t_A = (Pressure \times k_A)^{-1} \leq 28$ ps, assuming $\rho_T = 3 \times 10^{19}$ cm^{-3}. The average electron loss distance, $v_e t_A$, is < 10 μm for $T_e \sim 0.1$ eV, i.e., less than typical spot-size dimensions, although electron escape from the desorbed plume might be expected for low plasma densities if the electron velocity is directed away from the substrate. The dominant loss mechanism of free electrons is, however, expected to be by attachment to gas-phase neutral matrix molecules, although, as ion fractions increase, recombination will become more prevalent.

6.2.2 Results and Discussion

The model is evaluated using the data shown in table 6.1. Briefly, 337 nm (N_2 laser) pulses with $\tau = 3$ ns and of constant irradiance are assumed. Measured solid-phase absorption coefficients (see Chapter 4) provide a reasonable means of estimating the typical ground state vapour-phase absorption cross-section as $\sigma_0 = 7 \times 10^{-17}$ cm^2. However, the value of $\sigma_1 = 1 \times 10^{-17}$ cm^2 for excited state absorption is a cautious estimate and one used in the absence of any suitable data. Relaxation rates are chosen as $k_1 = 1.0 \times 10^9$ s^{-1} and $k_p = 1.0 \times 10^{-12}$ s^{-1}, based on representative data from the literature [117]. The ionisation energy of aromatic molecules typically lies between 7.5 and 10 eV [243], $I_p = 8.5$ eV being chosen as a representative value which, together with $\varepsilon = 3.0$ eV, gives values of $\Delta = 0.68$ eV and $U = 1.82$ eV. For typical matrix molecules, s is dominated by vibration and a fixed value of $s = 60$ is used, which corresponds to ~ 70 % of vibrational modes being classically populated in a 15-atom molecule. For simplicity, S_1-S_0 fluorescence is neglected at present ($f = 0$).

λ (nm)	337
τ (ns)	3.0
I_p (eV)	8.5
ε (eV)	3.0
σ_0 (cm^2)	7.0×10^{-17}
σ_1 (cm^2)	1.0×10^{-17}
k_1 (s^{-1})	1.0×10^{9}
k_p (s^{-1})	1.0×10^{12}
s	60
f	0.0

Table 6.1. Values of several parameters used in estimating the ion yield of a 'generic' MALDI matrix.

In fig. 6.2a the fractional ionisations n_{ti} and n_{pi} are shown as a function of laser fluence, F. Ionisation arising from excited-state thermal ionisation (ESTI) shows a strong dependence on fluence, varying as $\sim F^{12}$ in the vicinity of 15 mJ.cm^{-2}. Furthermore, fractional ion yields of $n_{ti} \sim 5 \times 10^{-6}$ at 10 mJ.cm^{-2} and approaching 10^{-2} at 20 mJ.cm^{-2} compare well with the experimentally determined minimum ion fraction of $\sim 10^{-5}$ [125]. This is despite only modest plume temperatures being reached, e.g. ~ 1300 K at 10 mJ.cm^{-2} fluence (fig. 6.2b). In contrast, the photoionisation yield varies as $\sim F^{2.7}$, consistent with a stepwise three-photon absorption process. However, n_{pi} does not even approach 10^{-5} in the fluence range modelled and so is unlikely to be of any consequence.

Results from Dreisewerd *et al* [145] for 3 ns (FWHM) 337 nm radiation show that the threshold for observation of 2,5-dihydroxybenzoic acid (2,5-DHB) matrix ions occurs in a region where the number of neutral molecules desorbed approaches a maximum, the latter displaying a power law that reduces from $\sim F^6$ near threshold to less than unity. Thus, within the useful fluence range for the observation of ions, the underlying desorption yield can, to a good approximation, be taken to be constant and the ion yield vs. fluence scaling of $n_i \sim F^{10.5}$ representative of the *ionisation* processes near threshold. The calculated ESTI yield thus not only produces the ion fractions necessary for successful MALDI signal acquisition but also shows good agreement with the experimentally determined ion yield vs. fluence power dependence within the appropriate fluence range. The $\sim F^{2.7}$ dependence that the modelled photoionisation exhibits is much weaker than that observed experimentally, again indicating ionisation probably follows an alternative route, such as ESTI.

6.3 Numerical Model

6.3.1 Analysis

Building upon the encouraging agreement with experiments displayed by the semi-analytical ESTI model (§6.2), it was extended to a fully numerical calculation to allow a greater level of flexibility in terms of experimental conditions and (matrix) molecular processes. This flexibility was tested by including electron removal and

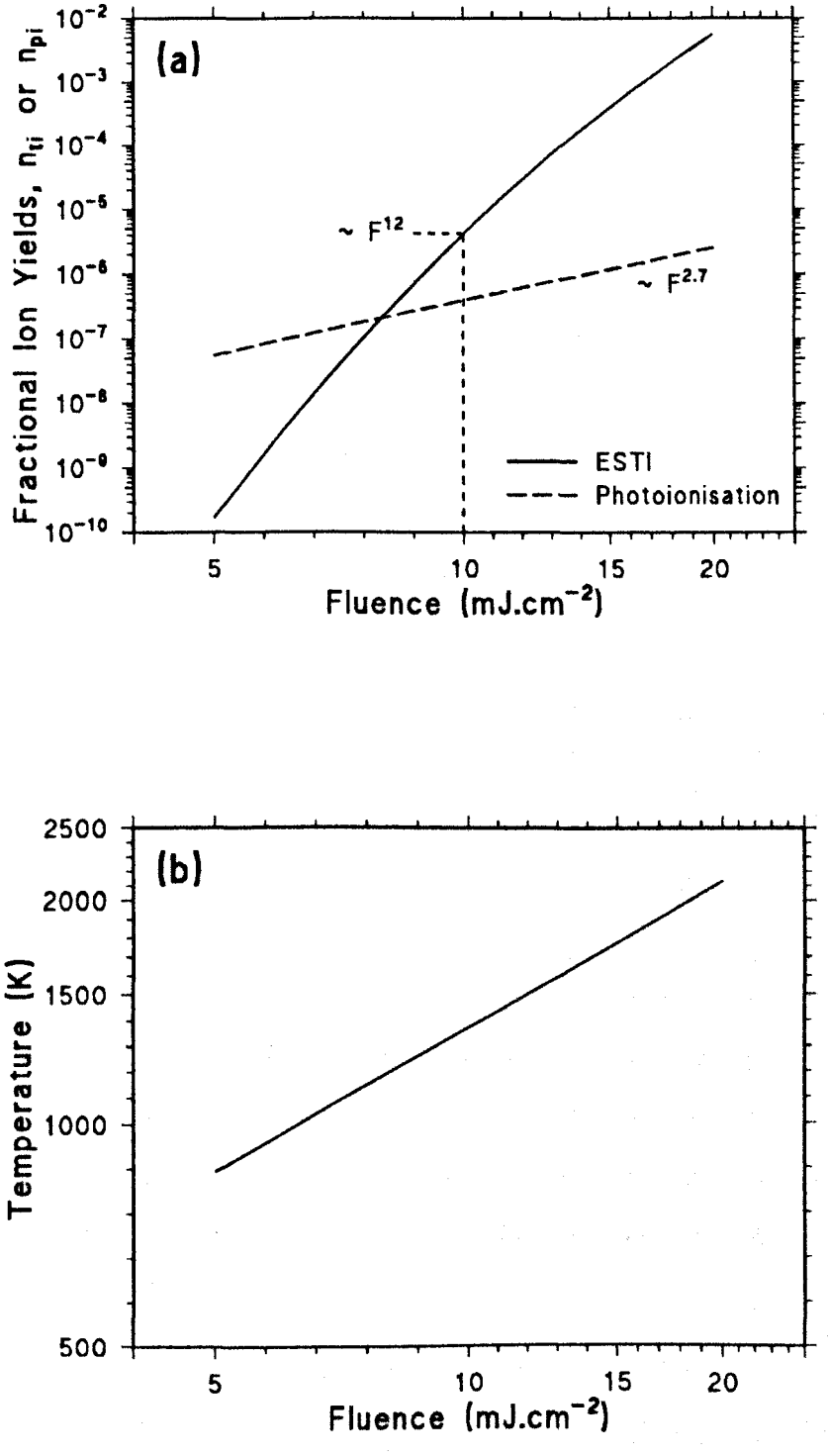

Figure 6.2. (a) Calculated matrix fractional ion yields for ESTI, n_{ti}, and photoionisation, n_{pi}, versus laser fluence and (b) matrix vibrational temperature versus laser fluence.

subsequent attachment to matrix molecules as neutral loss mechanisms and by modelling ionisation using more realistic temporal laser pulse-shapes than the constant irradiance pulse previously assumed.

Assuming that electron-neutral attachment occurs solely with ground state molecules, the rate equations 6.1 governing population of the singlet states are modified to become:

$$\left.\begin{aligned}
\frac{dn_0}{dt} &= k_1 n_1 - A n_0 - k_i n_p \\
\frac{dn_1}{dt} &= A n_0 - B n_1 - k_1 n_1 + k_p n_p \\
\frac{dn_p}{dt} &= B n_1 - k_p n_p - k_i n_p \\
\frac{dn_i}{dt} &= \frac{dn_-}{dt} = k_i n_p
\end{aligned}\right\} \qquad 6.15$$

where n_i and n_- represent the positive and negative ion fractional number densities respectively, and k_i represents the sum of the rates k_{ti} and k_{pi}. Note that the condition $n_0 + n_1 + n_p = 1$ is no longer valid and ion number densities must also be included. Furthermore, E is now calculated numerically using eqn. 6.2 rather than by the analytical expression given in eqn. 6.5.

Four temporal laser pulse shapes were investigated, each being characterised principally by pulse length, τ, and fluence, F. To provide a useful format for numerical modelling, all laser pulses were calculated in terms of temporal irradiance, $I(t)$.

The 'top-hat' laser pulse is identical to that used in the semi-analytical model (§6.2) in that it describes a constant temporal irradiance of duration τ (fig. 6.3a), described in terms of fluence simply by:

$$I(t) = \frac{F}{\tau} \qquad 6.16$$

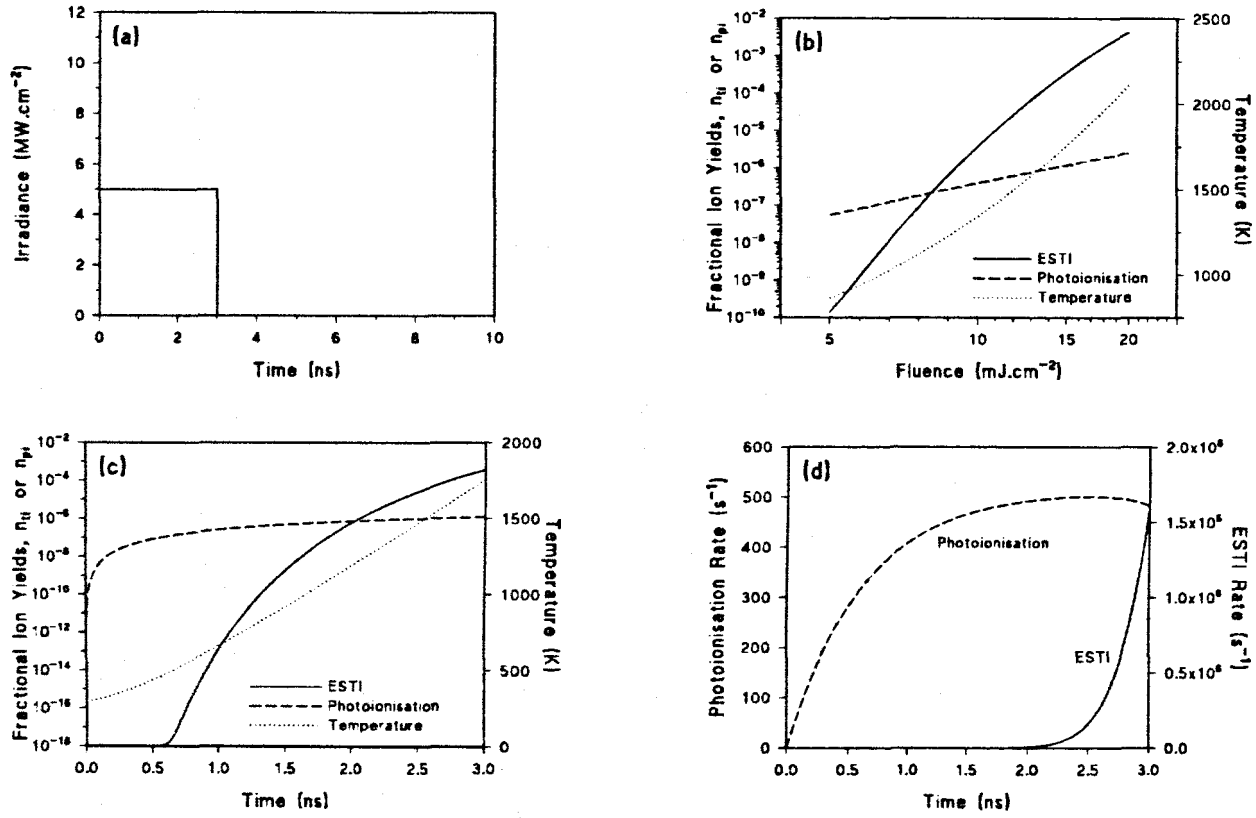

Figure 6.3. (a) Temporal irradiance profile of a 15 mJ.cm^{-2} 3 ns constant irradiance laser pulse. (b) Excited state thermal ionisation (ESTI, n_{ti}) and photoionisation (n_{pi}) ion yields and matrix vapour temperature as a function of fluence. (c) Temporal evolution of n_{ti}, n_{pi} and temperature at a fluence of 15 mJ.cm^{-2}. (d) Variation of ESTI and photoionisation rates within a 15 mJ.cm^{-2} laser pulse. See table 6.1 for parameter values.

Laser pulses approximated by a triangular temporal irradiance possess a maximum irradiance, I_{max}, and were defined by τ, F, the time of maximum irradiance, t_{max}, and the pulse termination time, t_{end}, (see fig. 6.4a for $t_{max} = \frac{1}{2} t_{end}$) to give:

$$I_{max} = \frac{2F}{t_{end}} \qquad 6.17$$

$$I(t) = I_{max} \frac{t}{t_{max}} \qquad (0 < t \leq t_{max}) \qquad 6.18$$

$$I(t) = I_{max} \left(\frac{t_{end} - t}{t_{end} - t_{max}} \right) \qquad (t_{max} < t \leq t_{end}) \qquad 6.19$$

Gaussian laser pulses, with the time constant, τ, governing the full width at half maximum (FWHM) time, were defined to start ($t = 0$) and finish ($t = t_{end}$) when $I(t)$ was 10^{-3} of the peak irradiance, $I(t_{max}) = I_{max}$. The irradiance between these limits was described by (see fig. 6.5a):

$$I(t) = I_{max} \exp\left[-\frac{(t - t_{max})^2}{\tau^2} \right] \quad (0 \leq t \leq t_{end}) \qquad 6.20$$

which provides:

$$\tau = \frac{FWHM}{2\sqrt{\ln 2}} \qquad 6.21$$

$$t_{end} = 2t_{max} = 2\tau\sqrt{\ln 10^3} \qquad 6.22$$

and can be integrated to give:

$$I_{max} = \frac{F}{\tau\sqrt{\pi}} \qquad 6.23$$

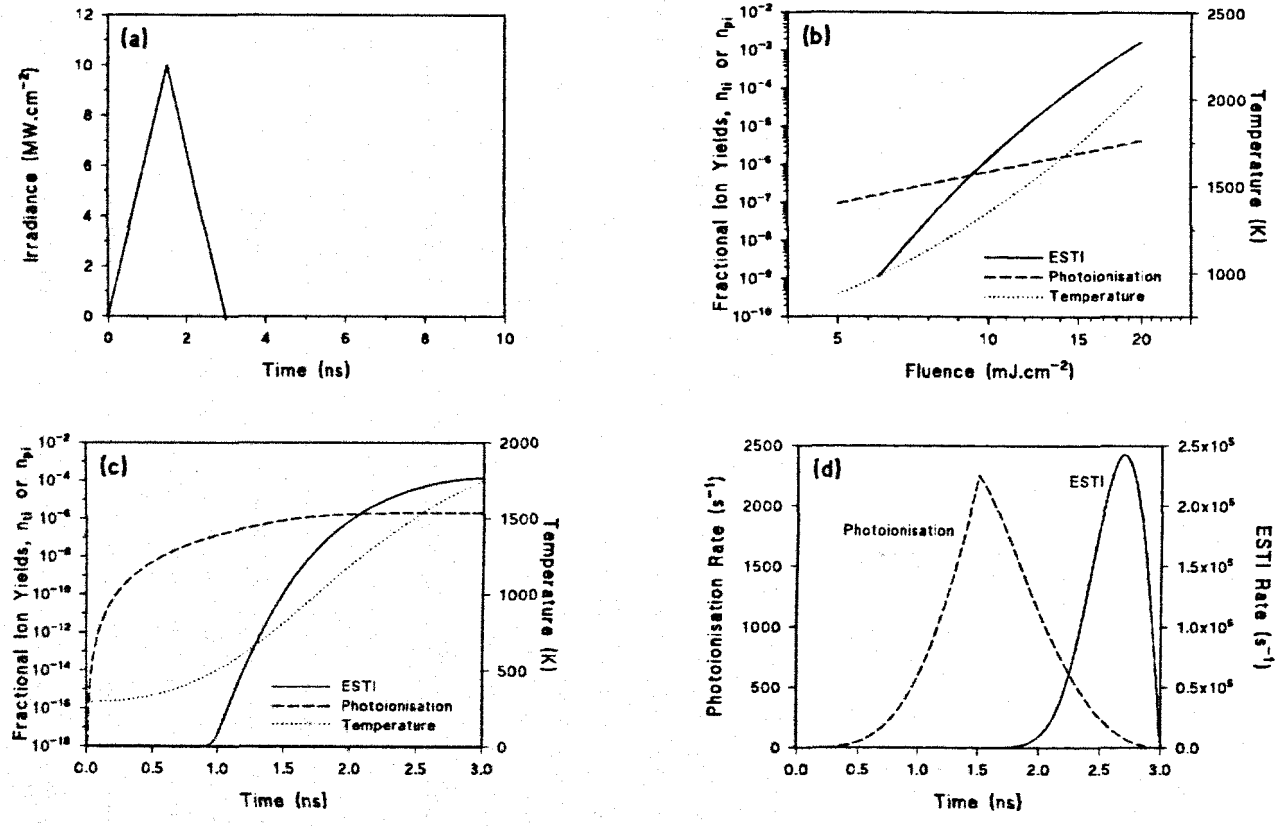

Figure 6.4. (a) Temporal irradiance profile of a 15 mJ.cm^{-2} 3 ns triangular laser pulse. (b) Excited state thermal ionisation (ESTI, n_{ti}) and photoionisation (n_{pi}) ion yields and matrix vapour temperature as a function of fluence. (c) Temporal evolution of n_{ti}, n_{pi} and temperature at a fluence of 15 mJ.cm^{-2}. (d) Variation of ESTI and photoionisation rates within a 15 mJ.cm^{-2} laser pulse. See table 6.1 for parameter values.

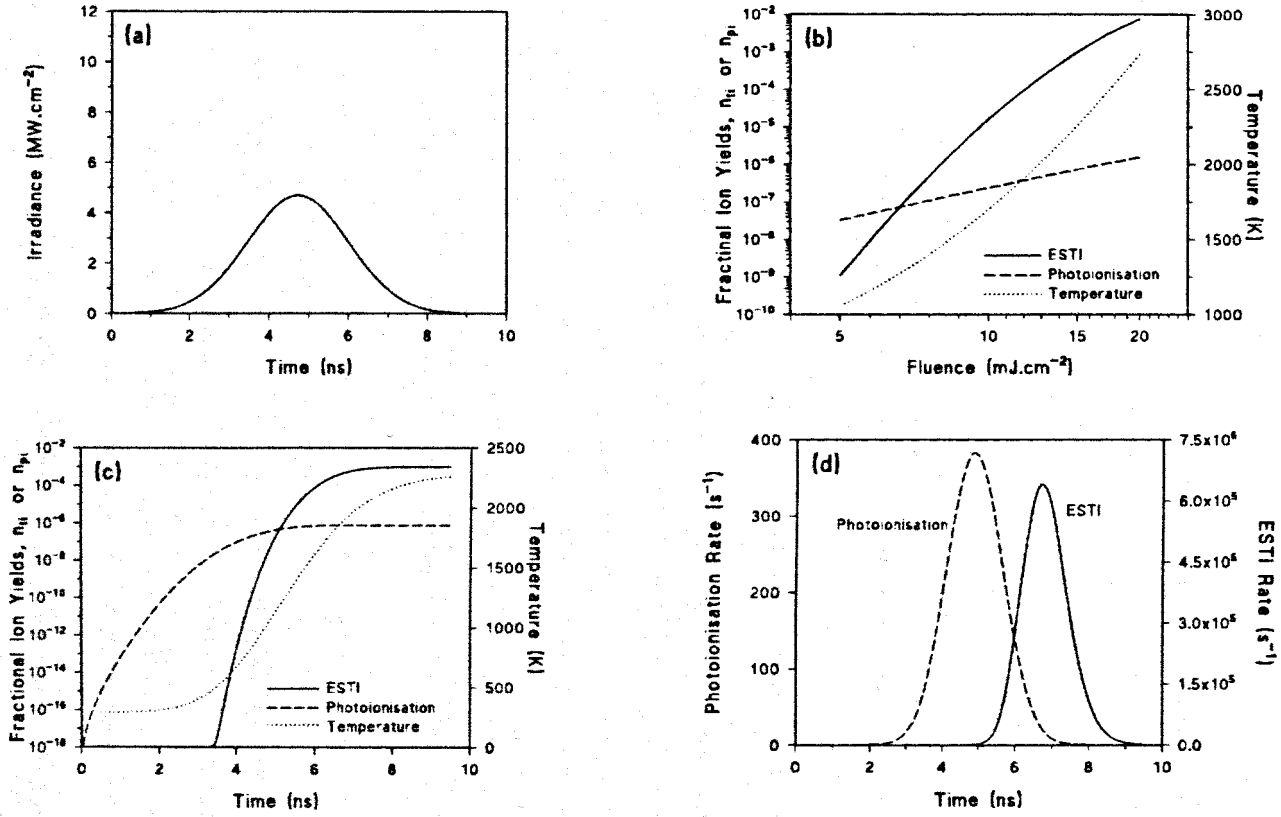

Figure 6.5. (a) Temporal irradiance profile of a 15 mJ.cm^{-2} 3 ns full width at half maximum (FWHM) Gaussian laser pulse. (b) Excited state thermal ionisation (ESTI, n_{ti}) and photoionisation (n_{pi}) ion yields and matrix vapour temperature as a function of fluence. (c) Temporal evolution of n_{ti}, n_{pi} and temperature at a fluence of 15 mJ.cm^{-2}. (d) Variation of ESTI and photoionisation rates within a 15 mJ.cm^{-2} laser pulse. See table 6.1 for parameter values.

Temporal laser pulse shapes characteristic of those emitted by excimer lasers wth unequal rise and fall times can be described by [264] (fig. 6.6a):

$$I(t) = F\frac{p(p+q)}{q}e^{-pt}\left(1-e^{-qt}\right) \qquad (0 < t \leq t_{end}) \quad 6.24$$

where p and q are pulse-defining parameters and t_{end} is defined by $I(t_{end}) = 10^{-3} \times I_{max}$, approximated by:

$$t_{end} = \frac{\ln\left(10^3\right)}{p} \qquad 6.25$$

6.3.2 Results and Discussion

Figures 6.3 b-d shows the modelled ion yield and temperature vs. fluence, the temporal evolution of ionisation and temperature within a 15 mJ.cm^{-2} laser pulse and ESTI and photoionisation rates within a 15 mJ.cm^{-2} laser pulse, respectively, for a top-hat temporal laser pulse shape. Figures 6.4 - 6.6 replicate this data for triangular (t_{end} = 3 ns), Gaussian (FWHM = 3 ns) and excimer ($p = 1 \times 10^9$ s^{-1} and $q = 2 \times 10^8$ s^{-1}) temporal laser pulse shapes, respectively.

The fluence-dependent characteristics (figs. 6.3b - 6.6b) are very similar to those determined semi-analytically (fig. 6.2), with ion fractions approaching 10^{-2} for ESTI but never reaching greater than 10^{-6} for photoionisation for the fluence range modelled. ESTI retains the strong dependence on fluence, e.g. for the Gaussian (3 ns FWHM) laser pulse (fig. 6.5b), n_{ti} varied approximately as $F^{11.6}$, $F^{8.5}$ and $F^{5.9}$ at fluences of 10, 15 and 20 mJ.cm^{-2}, respectively. Comparison of fig. 6.3b with fig. 6.2, in which identical laser pulses are considered, shows both ion yields to be almost identical. The matrix temperatures shown in figs. 6.5b and 6.6b are higher than in figs. 6.3b and 6.4b due to both the former cases having an extended laser pulse tail. This allows excited matrix molecules more time to relax to the ground state, thus heating the matrix system. Top-

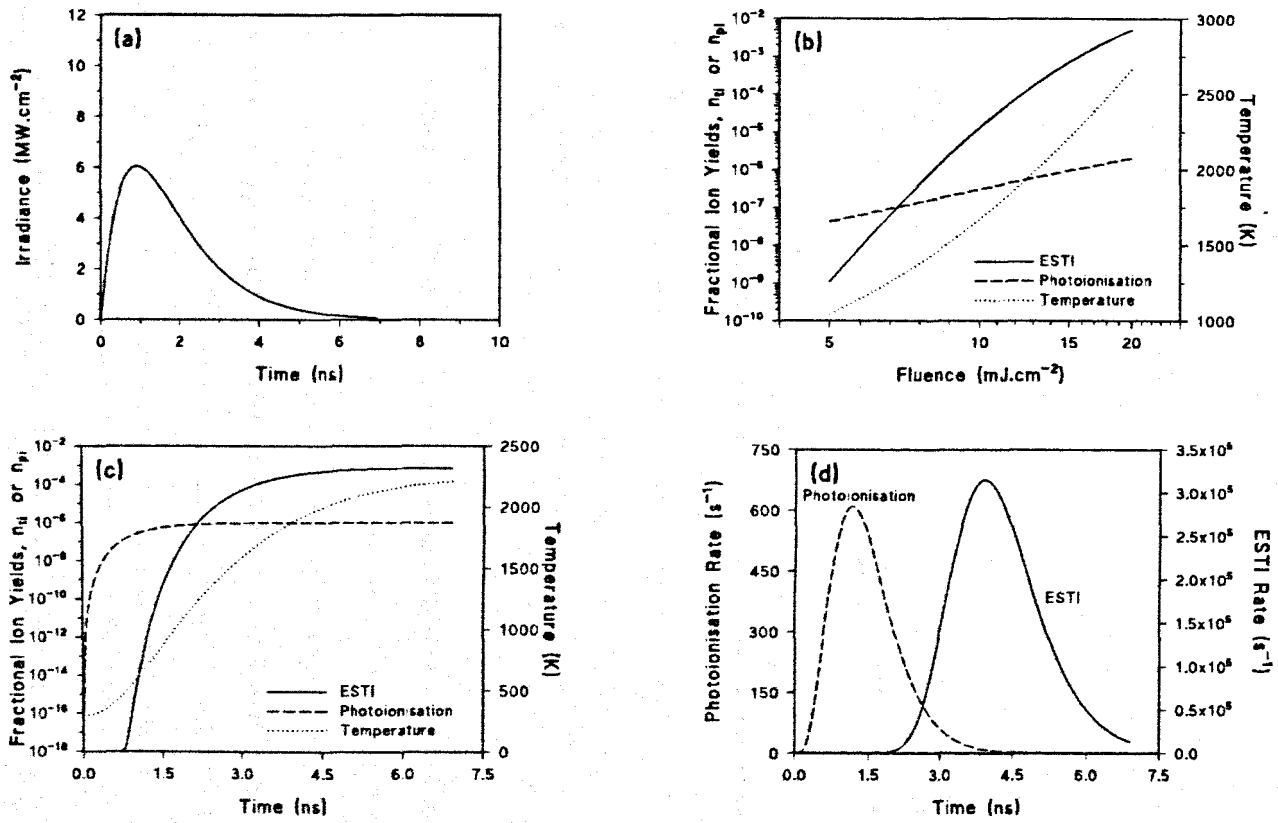

Figure 6.6. (a) Temporal irradiance profile of a 15 mJ.cm^{-2} excimer laser pulse. (b) Excited state thermal ionisation (ESTI, n_{ti}) and photoionisation (n_{pi}) ion yields and matrix vapour temperature as a function of fluence. (c) Temporal evolution of n_{ti}, n_{pi} and temperature at a fluence of 15 mJ.cm^{-2}. (d) Variation of ESTI and photoionisation rates within a 15 mJ.cm^{-2} laser pulse. See table 6.1 for parameter values.

hat and triangular laser pulses have a more well defined cut off point at which time there will still be a significant fraction of excited matrix species. Figures 6.3c - 6.6c show that whereas photoionisation may proceed from the early parts of the laser pulse, ESTI relies on an increase in matrix temperature before becoming significant. Of the ionisation rates shown (figs. 6.3d - 6.6d) perhaps that resulting from (3 ns FWHM) Gaussian shape laser excitation (fig. 6.5d) is most easily understood. Here, as expected, photoionisation is seen to follow approximately the instantaneous laser irradiance (photoionisation FWHM $\approx$ 1.8 ns), whereas ESTI proceeds in the later stages of the laser pulse, i.e. beyond the peak irradiance. It is in this time-window that the temperature of the matrix starts to increase due to the non-radiative relaxation of photoexcited molecules; n_{ti} rises rapidly but reaches a maximum value and then decays owing to the diminishing photon flux and subsequent decrease in n_p. Despite the temperature continuing to increase, the temporal shape of the ESTI rate displays a FWHM of only ~ 1.5 ns due to the decrease in n_p. Since ESTI occurs over a shorter time than that of the laser pulse, it will not limit the resolution of MALDI analysis. Furthermore, such a short timescale event is consistent with experimental observations of m^+ ions being observed to be formed within the laser pulse [118].

6.4 Conclusions

Modelling of excited-state thermal ionisation (ESTI) in the desorbed plume suggests the process to be a plausible matrix ionisation route in MALDI. Several simplifications are made, e.g. neglect of triplet states, but numerical modelling allows more realistic laser pulse shapes to be considered than would otherwise be possible. ESTI exhibits an ion yield vs. fluence relationship that is in good agreement with experiment. No fundamentally new processes are necessary but rather the conjunction of existing known mechanisms. For a 3 ns FWHM Gaussian laser pulse, positive ions are created within a 1.5 ns FWHM envelope, suggesting that the mass resolution of the resultant spectra will not be significantly limited by this ionisation route. The primary loss of electrons is proposed to be through attachment to neutral molecules, leading to an equal number of positively and negatively charged matrix ions being produced.

Formation of protonated matrix ions and analyte ions is then possible through gas-phase proton or charge transfer reactions, as is commonly discussed [109,121,141].

7 IONISATION MODELLING II

7.1 Introduction

In Chapter 6 a model of excited state thermal ionisation (ESTI) of gas-phase matrix molecules in matrix-assisted laser desorption/ionisation (MALDI) was shown to successfully predict certain experimental observations. However, several processes were neglected for reasons of simplicity. This chapter develops ESTI to take into account pertinent mechanisms, previously omitted, and investigates their effect. Furthermore, the influence of several important molecular parameters on MALDI is explored and comparisons with experiment, further to those described in Chapter 6, are made.

7.2 Additional Processes

The values of basic parameters used here are the same as those used in Chapter 6, listed in table 6.1, and 3 ns top-hat (constant irradiance within pulse duration) laser excitation is assumed throughout. Each of the following mechanisms are considered in isolation, i.e. their effects are analysed individually with reference to the results in Chapter 6 and not cumulatively, although excited state interactions and electron-ion recombination are considered alongside triplet states by necessity. However, the mechanisms are required to be incorporated into the basic model, as given in Chapter 6. As such, all rate equations given henceforth that govern population changes are combined with those in eqn. 6.15 whilst those describing changes in molecular internal energy, E, are included within eqn. 6.2.

7.2.1 Temperature-dependent Heat Capacity

Until now, the calculation of matrix temperature from the average excess energy per molecule has been approximated by assuming a fixed number of vibrational degrees of freedom. Although this has previously been justifiable within the context of investigating the plausibility of an ESTI mechanism, further refinements to the model

must address the issue more carefully, particularly considering the strong influence that temperature is likely to have on ion formation within ESTI. An alternative, and more accurate, method of calculation regards each vibrational mode of a (gas-phase) matrix molecule as contributing towards the heat capacity by an extent dependent on the frequency of the mode and on the matrix temperature itself.

Bowley and Sanchéz [265] provide a statistical mechanics treatment of harmonic oscillators. Essentially, the allowable energies, ε_n, of a one dimensional harmonic oscillator of angular frequency ω are given by:

$$\varepsilon_n = \hbar\omega\left(n+\frac{1}{2}\right) \qquad n = 0,1,2,3,... \qquad 7.1$$

from which the partition function, Z, is defined as:

$$\left.\begin{aligned} Z &= \sum_{n=0}^{\infty} e^{-\hbar\omega\left(n+1/2\right)/kT} \\ &= e^{-\hbar\omega/2kT} + e^{-3\hbar\omega/2kT} + e^{-5\hbar\omega/2kT} + ... \\ &= \frac{e^{-\hbar\omega/2kT}}{1-e^{-\hbar\omega/kT}} \end{aligned}\right\} \qquad 7.2$$

where the exact expression for a geometric progression is used and T is the system temperature. The Hemholtz free energy, F, may then be calculated as:

$$F = -kT\ln(Z) = \frac{\hbar\omega}{2} + kT\ln\left(1-e^{-\hbar\omega/kT}\right) \qquad 7.3$$

from which the entropy, S, can be shown to be:

$$S = -\frac{\partial F}{\partial T} = -k\ln\left(1-e^{-\hbar\omega/kT}\right) + \frac{\left(\frac{\hbar\omega}{kT}\right)}{\left(e^{\hbar\omega/kT}-1\right)^2} \qquad 7.4$$

and the heat capacity of the harmonic oscillator, C':

$$C' = T\left(\frac{\partial S}{\partial T}\right) = \frac{\hbar^2\omega^2}{kT^2}\frac{e^{\hbar\omega/kT}}{\left(e^{\hbar\omega/kT}-1\right)^2} \qquad 7.5$$

Now, assuming that the vibrational modes of a polyatomic matrix molecule may be regarded as the sum of several 1-D harmonic oscillators, the total vibrational heat capacity, C_{vib}, is now expressed as the sum of C' for all i molecular vibrations of angular frequency ω_i:

$$C_{vib} = \sum_i C'_i = \sum_i \frac{\hbar^2\omega_i^2}{kT^2}\frac{e^{\hbar\omega_i/kT}}{\left(e^{\hbar\omega_i/kT}-1\right)^2} \qquad 7.6$$

Assuming that rotational degrees of freedom are saturated at the temperatures involved (room temperature), the 3 translational and 3 rotational degrees of freedom will each contribute ½k towards the total heat capacity, C, i.e.:

$$C = C_{vib} + 3k = \sum_i \frac{\hbar^2\omega_i^2}{kT^2}\frac{e^{\hbar\omega_i/kT}}{\left(e^{\hbar\omega_i/kT}-1\right)^2} + 3k \qquad 7.7$$

The change in energy, E, between temperatures T_1 and T_2 is found by integrating eqn. 7.7 to provide:

$$E = \int_{T_1}^{T_2} C\,dT = \left(3kT_2 + \sum_i \frac{\hbar\omega_i}{\exp\left(\frac{\hbar\omega}{kT_2}\right)-1}\right) - \left(3kT_1 + \sum_i \frac{\hbar\omega_i}{\exp\left(\frac{\hbar\omega}{kT_1}\right)-1}\right) \qquad 7.8$$

The 45 vibrational frequencies of the 17-atom MALDI matrix 2,5-dihydroxybenzoic acid (2,5-DHB) have been determined previously [266] and allow eqn. 7.7 to be calculated (fig. 7.1) and temperature ($T \equiv T_2$) to be plotted as a function of

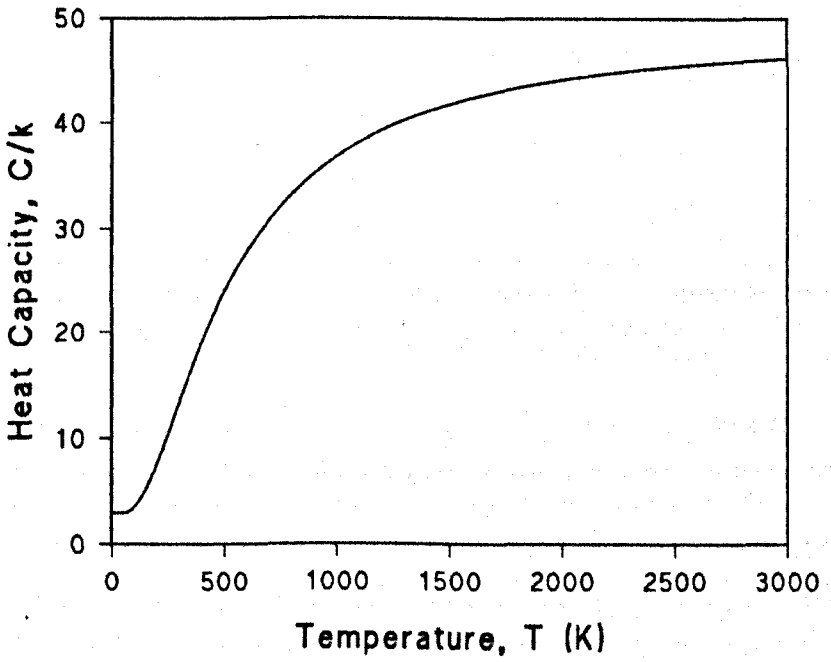

Figure 7.1. Heat capacity of vapour phase 2,5-dihydroxybenzoic acid as a function of temperature, calculated from molecular vibrational frequencies.

E (using eqn. 7.8), assuming a fixed value of T_l = 293 K (fig. 7.2). A 6th order polynomial fit to the data shown in fig. 7.2 then allows the temperature to be calculated as a function of E, the polynomial coefficients being listed in table 7.1. Also shown in fig. 7.2 is the temperature of the matrix plume as determined using eqn. 6.6 assuming a constant contribution from a fixed number of degrees of freedom. This linear relationship describes the temperature reasonably well up to $E \sim 3$ eV, above which it increasingly overestimates temperature compared with that calculated using the temperature-dependent method, detailed above.

The effect of temperature-dependent heat capacity on the modelling of MALDI matrix ionisation by ESTI is shown in fig. 7.3. Clearly the lower final matrix temperatures at fluences greater than 7 mJ.cm^{-2} with a variable heat capacity compared to the simplified, fixed heat capacity (fig. 7.3b) leads to the concomitant difference in the ESTI fractional ion yield, n_{ti}, at fluences greater than 10 mJ.cm^{-2} (fig. 7.3a). For example, at 20 mJ.cm^{-2} the temperature is over 300 K lower using the variable rather than fixed heat capacity model, and n_{ti} is reduced by a factor of more than 3 for the former case.

7.2.2 Triplets

A modified energy structure is necessary compared to that used previously in order to include triplet states, as shown in fig. 7.4. Essentially, there are four additional parameters that govern triplet state populations. The lowest triplet state, T_1 (fractional population density n_{t1}), is found at an energy ε_{isc} below the first excited singlet state S_1 (fractional population density n_1; energy above ground (S_0) state ε). Population transfer between these two states is governed primarily by the inter-system crossing rate constant, k_{isc}. Rate equations are again used to describe inter-system crossing, both from S_1 to T_1 and from T_1 to S_1 where the energy barrier ε_{isc} must also be overcome (leading to 'E-type' fluorescence [243]):

$$\left(\frac{dn_{t1}}{dt}\right)_{isc} = -\left(\frac{dn_1}{dt}\right)_{isc} = n_1 k_{isc} - n_{t1} k_{isc} \exp\left(-\frac{\varepsilon_{isc}}{kT}\right) \qquad 7.9$$

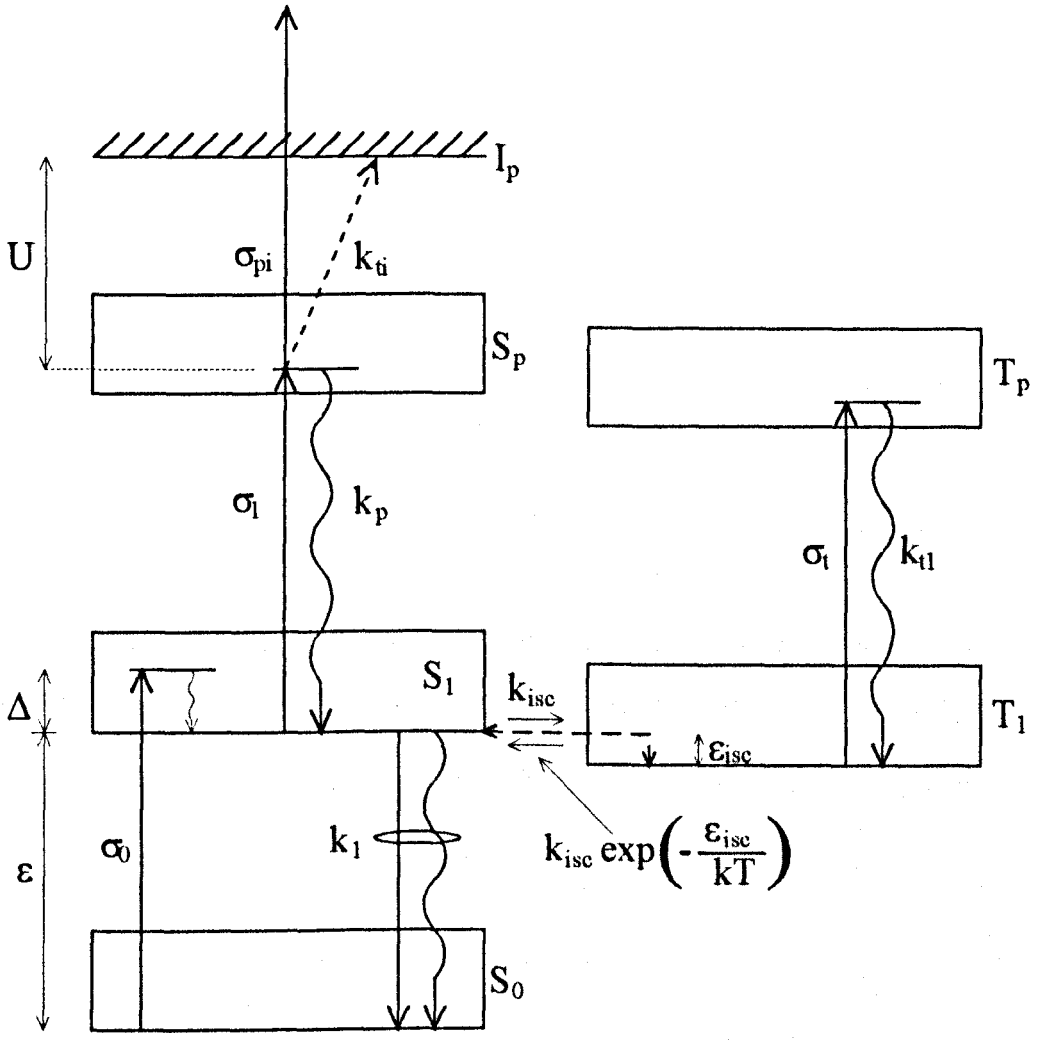

Figure 7.4. Energy level diagram of matrix molecules including triplet states.

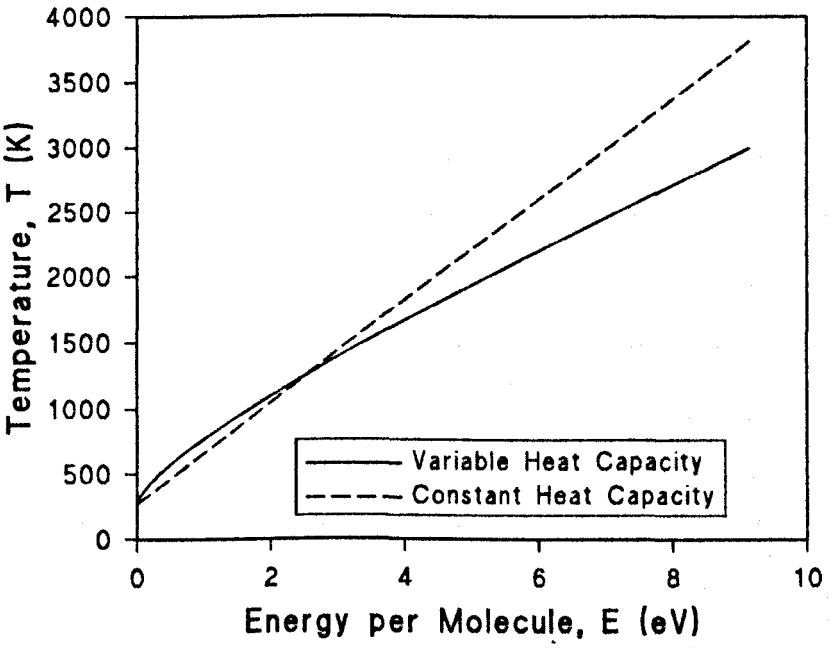

Figure 7.2. Calculated temperature of vapour phase 2,5-dihydroxybenzoic acid as a function of molecular internal energy.

A_0	293.0
A_1	645.5783
A_2	- 221.8611
A_3	69.8133
A_4	- 11.7505
A_5	0.988426
A_6	- 0.03263

Table 7.1. Values of polynomial coefficients used to fit matrix temperature, *T*, to excess energy per molecule, *E*, based on the vibrational frequencies of 2,5-dihydroxybenzoic acid [266].

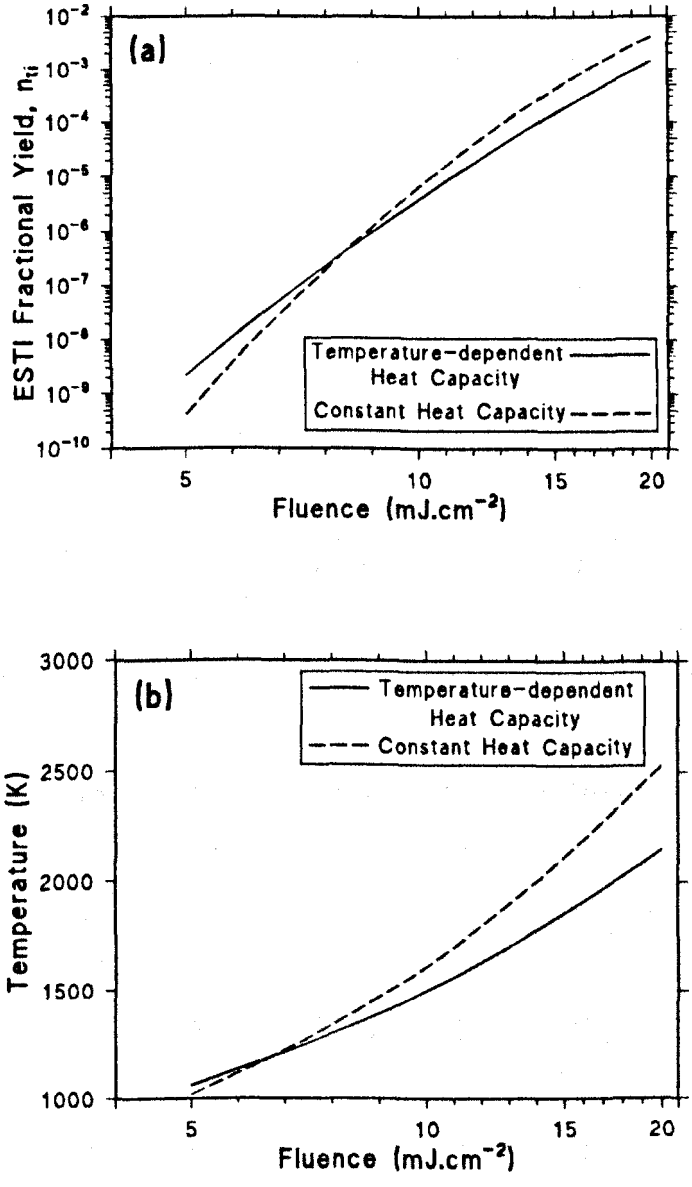

Figure 7.3. (a) ESTI yield and (b) temperature of matrices using constant and temperature-dependent heat capacities.

Obviously, the S_1-T_1 transition will increase a molecule's vibrational energy by ε_{isc} whereas the T_1-S_1 transition will require energy ε_{isc} to be lost from a molecule.

Molecules in the T_1 state may be excited to a higher lying triplet state T_p (fractional population density n_{tp}) by the absorption of a UV photon (see fig. 7.4) with an absorption cross-section σ_t. From state T_p molecules will relax non-radiatively by internal conversion back to T_1 at a rate k_{tp}, leading to heating of the matrix molecule by an amount $h\nu$. The rate equations describing these transitions are:

$$\left(\frac{dn_{tp}}{dt}\right)_{abs} = -\left(\frac{dn_{t1}}{dt}\right)_{abs} = \sigma_t\left(\frac{I}{h\nu}\right)n_{t1} - n_{tp}k_{tp} \qquad 7.10$$

where I is the instantaneous laser irradiance and $h\nu$ is the photon energy. Fukumura and Masuhara attributed UV laser induced polymer heating to cyclic T_1-T_p absorption and relaxation [119], a process which may be relevant to ESTI.

Ionisation from state T_p is neglected, as are T_1-S_0 (ground state) transitions since the relaxation rate is typically of the order of microseconds [243].

Typical triplet rate parameters for laser dyes and other aromatic molecules [117,243] were used to provide $k_{isc} = 1 \times 10^8$ s^{-1}, $\varepsilon_{isc} = 0.75$ eV, $\sigma_t = 1.0 \times 10^{-17}$ cm^2 and $k_{tp} = 1.0 \times 10^{12}$ s^{-1} (σ_t and k_{tp} are estimated by analogy with the equivalent singlet parameters given in §6.2.2). Variation of k_{isc} around a value of $k_{isc} = 1 \times 10^8$ s^{-1} changes the final values of n_{ti} and temperature, T (fig. 7.5). As k_{isc} increases, and hence the relative population of triplet states, both n_{ti} and T decrease. The inclusion of triplet states causes singlet state populations to decrease with two main effects: firstly, matrix heating by non-radiative S_1-S_0 relaxation is reduced (fig. 7.5) since the transition occurs less frequently, and, secondly, fewer molecules reach the highly excited S_p singlet state from which ionisation may take place. Both of these effects contribute to the decrease in n_{ti} seen in fig. 7.5. Taking a value of $k_{isc} = 1 \times 10^8$ s^{-1} as a representative rate for inter-system crossing, ESTI is reduced by a factor of more than 2 when triplet states are

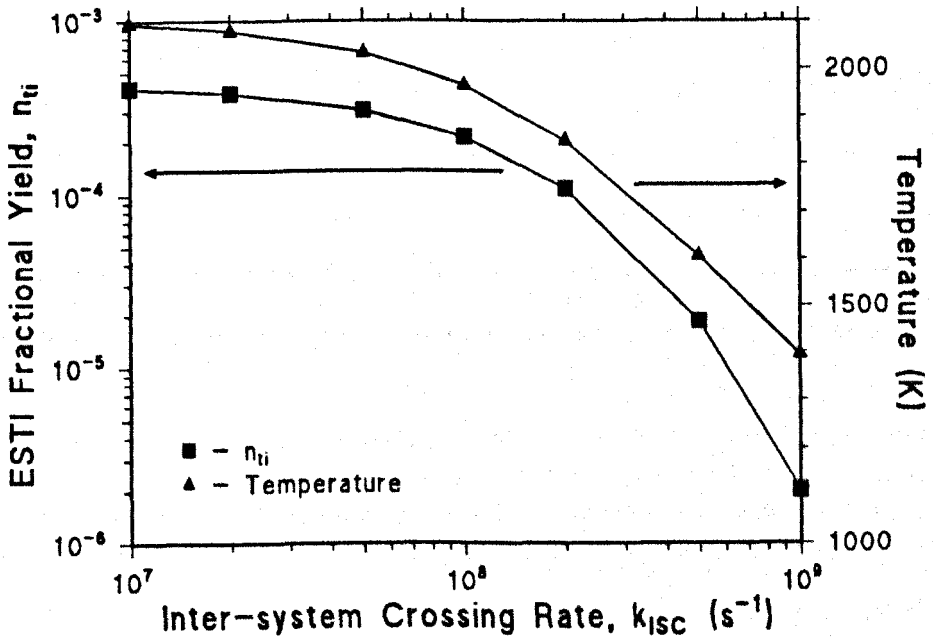

Figure 7.5. ESTI yield and matrix temperature versus the intersystem crossing rate, k_{isc}, for a 15 mJ.cm^{-2} N_2 (337 nm) laser pulse.

included in the modelling. Furthermore, over the range k_{isc} = 1 × 10^7 s^{-1} - 1 × 10^9 s^{-1} the final value of n_{ti} is reduced by approximately two orders of magnitude.

Increasing ε_{isc} or σ_t both marginally increase matrix heating leading to a small increase in n_{ti}.

7.2.3 Excited State Interactions

§5.4.2 provides a brief description of excited state interactions between singlet state molecules and estimates the singlet-singlet interaction rate parameter, k_{SS} ~ 2 × 10^{-10} $cm^3.s^{-1}$. Equation 5.16 describes singlet-singlet interactions and introduces another excited state, S'_p (fractional population density n'_p), lying at an energy double that of the lowest vibrational level of S_1, i.e. 2ε. Triplet-triplet interaction processes which result in two singlet state molecules are known to occur [243], e.g.

$$T_1 + T_1 \xrightarrow{1} S_0 + S''_p \xrightarrow{2} S_0 + S_1 \qquad 7.11$$

where S''_p (fractional population density n''_p) is a high-lying singlet state, but these and singlet-triplet interactions are usually negligibly small in number due to the low S_0 - T_1 transition moment [243]. Ionisation from S'_p can be neglected since the energy gap to the ionisation energy, I_p, is larger compared with the photoexcited S_p state. Relaxation from S'_p to S_1 at a rate k_p (= 10^{12} s^{-1}) will, however, cause matrix heating by an amount ε.

For the purposes of modelling, and because S'_p - S_1 relaxation is assumed to be rapid, the excited states arising from singlet-singlet interactions are taken to immediately populate the S_1 state, with matrix heating also occurring instantaneously due to the assumed relaxation. The rate equation expressions due to excited state interactions (esi) are, therefore:

$$\left.\begin{aligned}\left(\frac{dn_0}{dt}\right)_{esi} &= \frac{1}{2}n_1^2 k_{SS} \\ \left(\frac{dn_1}{dt}\right)_{esi} &= -\frac{1}{2}n_1^2 k_{SS} \\ \left(\frac{dE}{dt}\right)_{esi} &= \frac{1}{2}n_1^2 k_{SS}\varepsilon\end{aligned}\right\} \qquad 7.12$$

where the population terms and energy term are considered additionally to those in eqn. 6.15 and eqn. 6.2, respectively, as has already been explained. Figure 7.6 shows plots of n_{ti} and T as functions of k_{SS} for a fluence of 15 mJ.cm^{-2}. Over the two orders of magnitude variation in k_{SS}, T increases by ~ 600 K. This in turn causes the observed increase in n_{ti}, varying by almost an order of magnitude over the same range. More specifically, the matrix heating due to excited state interactions leads to an increase in n_{ti} by a factor of ~ 5 for $k_{SS} = 2 \times 10^{-10}$ cm^3.s^{-1} and a fluence of 15 mJ.cm^{-2}.

7.2.4 Electron-ion Recombination

Electron-ion recombination may act as a competing process to electron-neutral attachment in the loss of free electrons and, if significant, will lower the efficiency of ion production. Equations 6.20 - 6.22 provide the mathematical descriptions of the electron loss processes. Once ionised, the ratio of neutral attachment to ion recombination rates will determine what fraction of ions will remain in their charged state and a corresponding negative ion formed. Having recombined with positive ions, electrons are expected to be in either the S_1 or T_1 state [244], populating the T_1 state three times as often as in the S_1 state due to the three-fold degeneracy of triplet states. Furthermore, a significant degree of matrix heating will occur upon recombination, equal to (I_p - ε) or (I_p - ε + ε_{isc}) for the resulting neutral molecule being in the singlet or triplet manifold, respectively. In deducting molecules from the neutral population for electron-neutral attachment, it is assumed the neutral molecule is in the ground (S_0) state. Heating due to electron-neutral attachment is ignored.

Using the values given in §6.2.1, a plot of the final fraction of ions produced with and without electron-ion recombination being included is shown in fig. 7.7. Clearly, it is

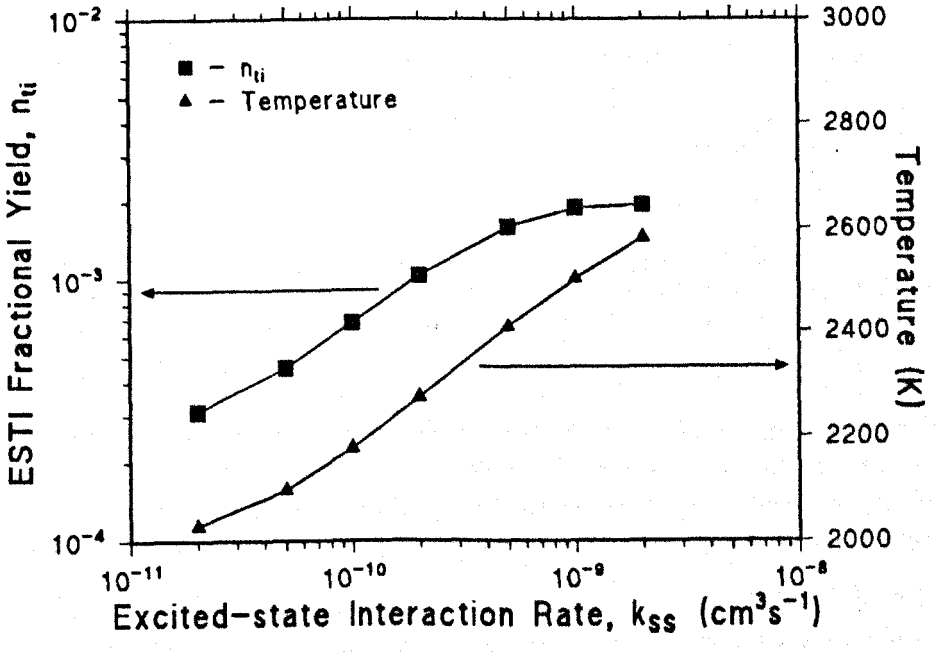

Figure 7.6. ESTI yield and matrix temperature versus the excited-state interaction rate constant, k_{SS}, for a 15 mJ.cm^{-2} N_2 (337 nm) laser pulse.

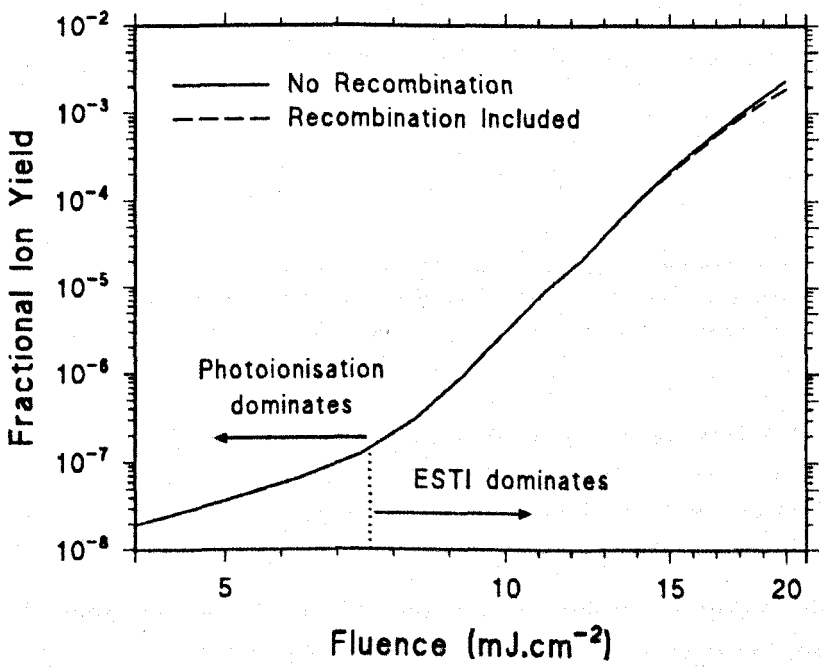

Figure 7.7. Matrix ion yield as a function of laser fluence with and without electron-ion recombination being included.

only at the highest fluences, where ion fractions reach in excess of 10^{-3}, that electron-ion recombination noticeably affects the number of ions. Even in this region, however, including recombination into the modelling only reduces the matrix ionisation by a factor of 2.

7.2.5 Thermionic Cooling

When a molecule becomes thermally ionised, vibrational energy is expended in the transition. For example, cooling of gas-phase desorbed fullerenes has previously been attributed to thermionic emission from the ground state [267]. The reduction in energy for a thermal ionisation from the S_p state will be $U = I_p - \varepsilon - h\nu$. However, when such a term was added into the ionisation model, a negligibly small difference in ESTI was observed (< 1 % for up to 20 mJ.cm^{-2} fluence).

7.2.6 Fluorescence Heating

The majority of S_1 - S_0 fluorescence transitions are at energies lower than ε, the remainder of the energy becoming thermalised collisionally. For example, the average fluorescence wavelengths, $\bar{\lambda}_f$, determined for solid matrix films (table 5.3) of between 430 nm - 485 nm correspond to photon energies between 2.88 eV - 2.56 eV, compared with values of ε (table 5.2) of between 2.86 eV and 3.19 eV.

Introducing fluorescence has the effect of reducing the matrix temperature since the number of non-radiative transitions is decreased. For example, at 15 mJ.cm^{-2} the final matrix temperature drops from 1755 K to 1449 K when the fluorescence quantum efficiency, f, is increased from 0.0 to 0.3, leading to a decrease in ESTI from $n_{ti} \sim 3.6 \times 10^{-4}$ to $n_{ti} \sim 2.6 \times 10^{-5}$. Allowing for heating due to remnant vibrational energy following a fluorescence transition reduces the change in vibrational energy to give a final temperature of 1480 K, yielding $n_{ti} \sim 3.6 \times 10^{-5}$ for $\bar{\lambda}_f = 460$ nm, $f = 0.3$ and 15 mJ.cm^{-2} fluence. Thus, although this 'fluorescence heating' is not of primary importance, its influence is to compensate slightly for the loss of energy through radiative emission.

7.3 Influence of Experimental Parameters

Observation of how ESTI varies with different molecular parameters may help in the understanding of the related processes and provide a platform for experimental verification of the proposed ionisation mechanism. Here, the influence of various parameters are investigated using the fully numerical ionisation model described in §6.3 with all of the additional processes discussed in §7.2 included. A 3 ns full width at half maximum (FWHM) Gaussian laser pulse at 337 nm (N_2 laser) is assumed throughout. Table 7.2 lists all of the other standard parameter values used. Note that representative data for S_1 - S_0 decay rate, k_1, fluorescence quantum efficiency, f, 0-0 S_0 - S_1 transition energy, ε, and average fluorescence wavelength, $\bar{\lambda}_f$, were taken rom the results described in Chapter 5. The effect of varying each of the parameters was considered in isolation to any other changes, the standard values listed in table 7.2 being reverted to after investigation of a specific mechanism.

Perhaps the most obvious of the molecular properties to investigate is the absorption of laser light, characterised by the ground state absorption cross-section, σ_0 (see Chapter 4). n_{ti} is shown as a function of laser fluence for several different values of σ_0 in fig. 7.8. The strength of the dependence of ESTI on σ_0 is remarkable with n_{ti} increasing by over eleven orders of magnitude at a fluence of 15 mJ.cm^{-2} for a change in σ_0 of only one order of magnitude. The power law dependence of n_{ti} changes with σ_0, for example, $n_{ti} \sim \sigma_0^{13}$ for $\sigma_0 = 2 \times 10^{-17}$ cm^2 and $n_{ti} \sim \sigma_0^{5}$ for $\sigma_0 = 7 \times 10^{-17}$ cm^2. As investigated experimentally (Chapter 4), this strong dependence underlines the primary importance that ground state absorption of laser energy plays in MALDI, since population of the S_1 state is responsible for both the resultant heating of matrix molecules and ensuring that population of S_p is possible, from which ionisation may take place. Also, absorption is perhaps one of the more easily altered experimental conditions and so the matrix ion dependence on σ_0 one of the more easily verified relationships (see §4.5).

λ (nm)	337
τ (ns)	3.0
I_p (eV)	8.5
ε (eV)	3.0
σ_0 (cm^2)	7.0×10^{-17}
σ_1 (cm^2)	1.0×10^{-17}
k_1 (s^{-1})	7.0×10^{8}
k_p (s^{-1})	1.0×10^{12}
f	0.3
k_{isc} (s^{-1})	1.0×10^{8}
ε_{isc} (eV)	0.75
σ_t (cm^2)	1.0×10^{-17}
k_{tp} (s^{-1})	1.0×10^{12}
$\bar{\lambda}_f$ (nm)	460
k_{SS} ($cm^3.s^{-1}$)	2.0×10^{10}

Table 7.2. Values of parameters used in estimating the ESTI yield of a 'generic' MALDI matrix, based on experimental data where available.

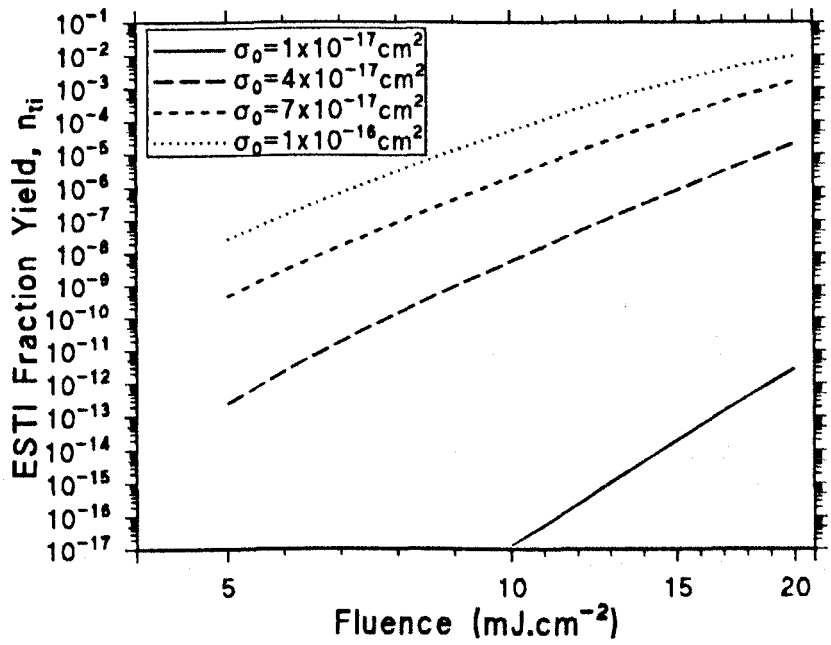

Figure 7.8. ESTI yield as a function of laser fluence for several different values of the matrix ground-state optical absorption cross-section, σ_0.

Figure 7.9 shows the variation in n_{ti} as a function of fluence for different values of the excited (S_1) state absorption cross-section, σ_1. Across an order of magnitude variation in σ_1, n_{ti} varies by approximately three orders of magnitude over the fluence range investigated. Although this dependency is not as marked as that in fig. 7.8 for σ_0, the relationship is still very strong indeed, since providing increased excitation to S_p again allows greater matrix heating due to internal conversion back to S_1 and a greater number of molecules amenable to thermal ionisation.

In contrast to these large changes with absorption cross-sections, the singlet-ground relaxation rate, k_1, causes very little alteration in the level of ESTI. Figure 7.10 again shows n_{ti} as a function of fluence, but this time for various values of k_1. n_{ti} changes by, at most, a factor of two for a change in k_1 of two orders of magnitude. Although this might appear surprising at first, the value of k_1 controls the balance between two processes, both of which contribute towards an increased rate of ESTI. If k_1 is low, then the population of S_1 will build up causing more molecules to be excited to the S_p state, from where ionisation can take place. An increase in k_1 infers a greater degree of non-radiative relaxation to S_0 and the corresponding increase in matrix temperature appears to offset the lower S_p population.

Figure 7.11 shows the n_{ti} vs. fluence characteristics for three close-lying wavelengths corresponding to XeCl (308 nm), N_2 (337 nm) and frequency-tripled Nd:YAG (355 nm) lasers, assuming σ_0 is constant throughout. Despite these small differences in wavelength, n_{ti} spans two orders of magnitude at a fluence of 15 $mJ.cm^{-2}$. Differences in matrix heating between the different wavelengths are likely to be minimal since the greater heating per photon of shorter wavelength radiation will be offset by the greater number of long wavelength photons, assuming an equal fluence. However, the effective ionisation potential, U, will be smaller for higher energy photons ($U = I_p - \varepsilon - h\nu$) leading to more efficient thermal ionisation (eqn. 6.16). This factor alone appears to explain the stark differences in ESTI for the different laser wavelengths, variations in matrix heating and excited state populations making a negligible contribution. Similarly, changing ε or I_p directly affects the value of U leading to

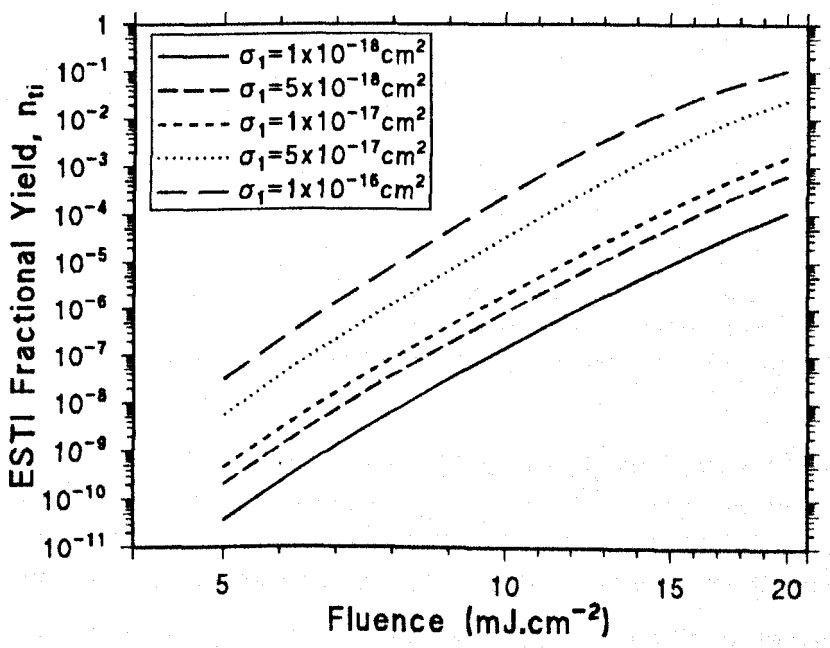

Figure 7.9. ESTI yield as a function of laser fluence for several different values of the matrix excited-state (S_1) optical absorption cross-section, σ_1.

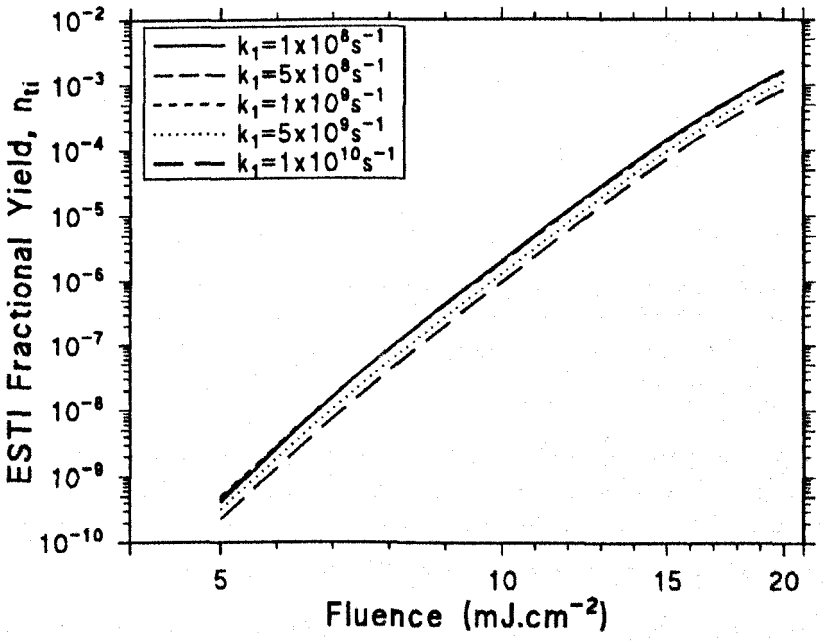

Figure 7.10. ESTI yield as a function of laser fluence for several different values of the matrix singlet-ground relaxation rate, k_1.

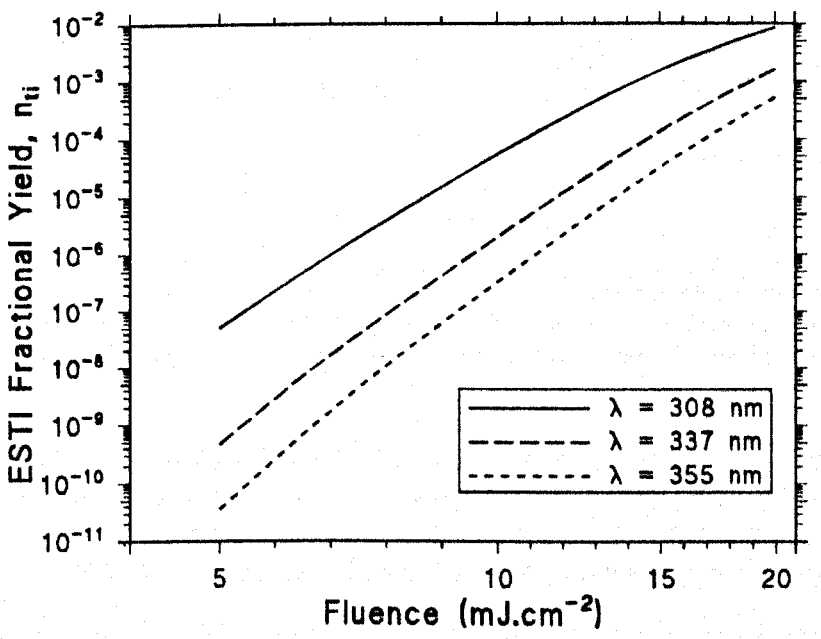

Figure 7.11. ESTI yield as a function of laser fluence for different wavelengths corresponding to XeCl (308 nm), N_2 (337 nm) and frequency-tripled Nd:YAG (355 nm) lasers.

dramatic changes in ESTI. For example, changes in ε of approximately 7 % or less can cause order of magnitude changes in n_{ti} (fig. 7.12).

Figure 7.13 shows n_{ti} and the fractional photoionisation, n_{pi}, at a fluence of 15 mJ.cm^{-2} for laser pulse lengths between 1 ps - 30 ns. As is expected, photoionisation dominates for short pulse lengths, where the irradiance is higher, and decreases in magnitude as the pulse lengths are extended. Note, however, that stimulated emission, whilst not considered here, may limit the amount of matrix ionisation for short pulse lengths by depopulating S_1. At a pulse length of ~ 0.5 ns, ESTI becomes the more significant matrix ionisation process and continues to increase until a maximum is reached at a pulse length of ~ 10 ns. The increase in ESTI up to this point can be understood in terms of excited state matrix molecules being allowed a greater time to relax within the laser pulse and contribute to the matrix heating. Such heating within the laser pulse is important since thermal ionisation must take place whilst there exists sufficient laser irradiance to maintain a reasonable S_p population. As laser pulse lengths increase beyond 10 ns, matrix relaxation within the laser pulse duration is already almost 100 % efficient meaning that the reduction in the S_p state population within the increasingly lower irradiance pulses will limit matrix ionisation.

7.4 Comparisons with Experiment

Although the model of ESTI provides good agreement with the power law dependence shown by matrix ions on laser fluence (see refs. 125 and 145, and §3.4.3), further comparisons with experiment may serve as verification of the proposed ionisation mechanism.

As discussed in §2.3.3, the threshold fluences for the observation of analyte ions using 560 fs (FWHM; 248 nm wavelength) and 3 ns (FWHM; 337 nm wavelength) lasers were very similar [160], the authors proposing that the total energy deposited in samples by the laser is of greater importance than irradiance. However, the ion scalings with fluence appear to be very different for the two lasers, the ion signal using the 560 fs laser increasing much more slowly than with the 3 ns laser. This may indicate that different

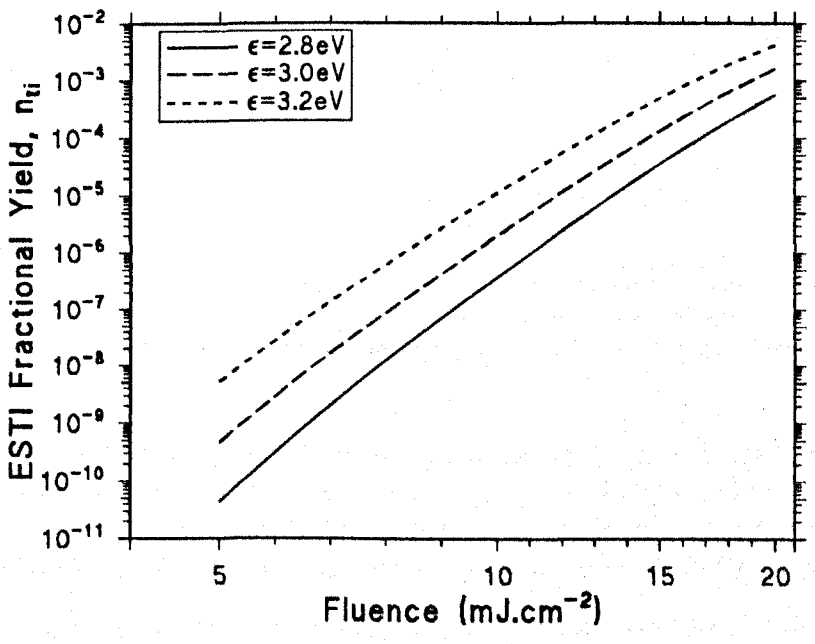

Figure 7.12. ESTI yield as a function of laser fluence for different values of the 0-0 ground-singlet transition energy, ε.

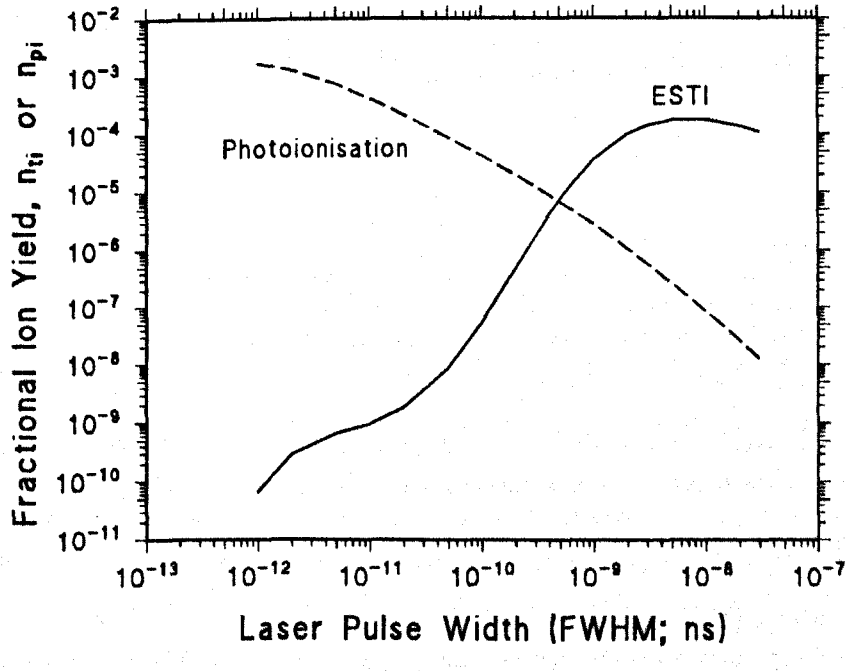

Figure 7.13. ESTI and photoionisation yields (n_{ti} and n_{pi}, respectively) as a function of laser pulse width (FWHM) for a Gaussian-shaped temporal 15 mJ.cm^{-2} N_2 laser (337 nm) incident pulse.

matrix ionisation mechanisms are applicable for the two lasers, assuming that matrix ionisation is a pre-requisite for analyte ionisation. The rapid rise in ion signal with the 3 ns laser is in agreement with other experimental observations (refs. 125 and 145, and §3.4.3) and with ESTI modelling, whilst the slow increase in ion signal using the 560 fs laser may be indicative of matrix photoionisation, perhaps including instantaneous multiphoton absorption at such short pulse lengths. Certainly, the modelling here suggests this to be a likely ionisation route for such short pulse lengths (see §7.3), particularly as the photon energy (~ 5 eV) is such that absorption of only two photons is sufficient. However, if this is the dominant mechanism for such short pulses, the experimental results in ref. 160 suggest that modelling of photoionisation here may have overestimated its significance since fig. 7.13 shows photoionisation for picosecond laser pulses to be over an order of magnitude greater than ESTI with nanosecond pulses.

The data discussed in Chapter 6 from Dreisewerd *et al* [145] were obtained using a 3 ns (FWHM) N_2 laser and the experiment was subsequently repeated using a 0.55 ns (FWHM) N_2 laser [154]. The authors expressed surprise at matrix ions actually appearing at higher fluences with the shorter pulse length laser when the irradiance was almost six times higher than for the earlier experiments. However, fig. 7.13 suggests that this is to be expected if ESTI is the dominant matrix ionisation mechanism, with n_{ti} decreasing when moving from a 3 ns to a 0.55 ns laser pulse. If threshold fluences, F_{th}, from the experimental data are assumed to be at the point at which matrix ions are first observed, this gives values of $F_{th} \sim 7$ mJ.cm^{-2} and $F_{th} \sim 9$ mJ.cm^{-2} when using the 3 ns and 0.55 ns lasers, respectively. Figure 7.14 shows plots of n_{ti} determined using the standard matrix parameters listed in table 7.2 but with laser pulse lengths of 3 ns and 0.55 ns (FWHM) in order to replicate the experimental conditions. It can be seen that the predicted ion yield threshold fluence for the 0.55 ns laser is higher than for the 3 ns laser. If the value of n_{ti} at 7.0 mJ.cm^{-2} for the 3 ns laser ($n_{ti} = 3.4 \times 10^{-8}$) is assumed to be the threshold ionisation level for matrix detection, then the intersection of the 0.55 ns laser ion yield with this value provides an estimate of $F_{th} \sim 9.0$ mJ.cm^{-2} for the shorter pulse length laser. This is in excellent agreement with experiment, although it should be borne in mind that the assumption is made that the neutral desorption yield is constant in both cases, as discussed in §6.2.2.

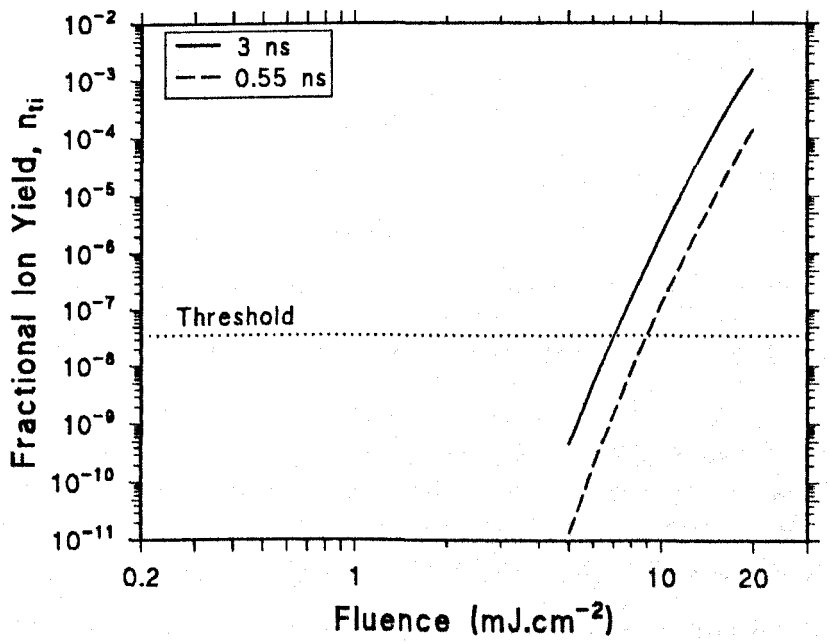

Figure 7.14. ESTI yield as a function of laser fluence for temporal laser pulse widths of 3 ns and 0.55 ns.

Tang *et al* [161] showed that an optimum delay time (≤ 10 ns) exists between the incidence of two collinear laser pulses for the formation of analyte ions. This is most easily explained by ESTI of matrix molecules, the ionised matrices providing the charge for all subsequent ions. Within this scheme, the delay between the laser pulses ensures that a significant fraction of excited molecules due to the first laser pulse will have relaxed before the second laser pulse arrives, thus 'pre-heating' the matrix. This matrix pre-heating will then allow ESTI to proceed more efficiently within the second laser pulse to give an ion yield greater than if both laser pulses had arrived simultaneously.

Finally, the investigation described in §4.5 of the 2,5-DHB ion yield, Y, dependence on fluence for lasers of different wavelength can be discussed in terms of the ESTI model. Data appropriate to the N_2 (3 ns FWHM; 337 nm) and XeCl (10 ns FWHM; 308 nm) lasers used experimentally were included in the modelling and values of $k_1 = 1.8 \times 10^8$ s^{-1} and $f = 0.59$ were obtained using data from Chapter 5. However, even assuming that $\sigma_0 = 7 \times 10^{-17}$ cm^2 at 337 nm, it is unclear from the absorption data (§4.3) what value to ascribe to σ_0 at 308 nm since gas phase, rather than solid phase, absorption is likely to dominate, thus altering the relative values. Nevertheless, fig. 7.15 shows plots of n_{ti} as a function of fluence, F, assuming $\sigma_0 = 2 \times 10^{-17}$ cm^2 at 308 nm. For the N_2 laser, agreement with experiment is excellent with $n_{ti} \sim F^{10.2}$ over the relevant fluence range (cf. §4.5 and fig. 4.6: $Y \sim F^{10.1}$). For the XeCl laser the agreement is poorer, with $n_{ti} \sim F^{9.4}$ predicted compared with $Y \sim F^{7.6}$ obtained experimentally over the 20 - 40 mJ.cm^{-2} range (§4.5 and fig. 4.6). Furthermore, the relative value of n_{ti} for the XeCl laser compared with that for the N_2 laser appears to be slightly too large considering the ion yields observed experimentally (fig. 4.6). Despite these discrepancies, ESTI describes the matrix ion yield using lasers of different pulse length and wavelength to a satisfying extent.

7.5 Conclusions

Consideration of previously neglected processes relevant to the modelling of excited state thermal ionisation (ESTI) of matrix molecules in MALDI shows their influence on matrix ion generation to be sufficiently large to warrant their inclusion. In

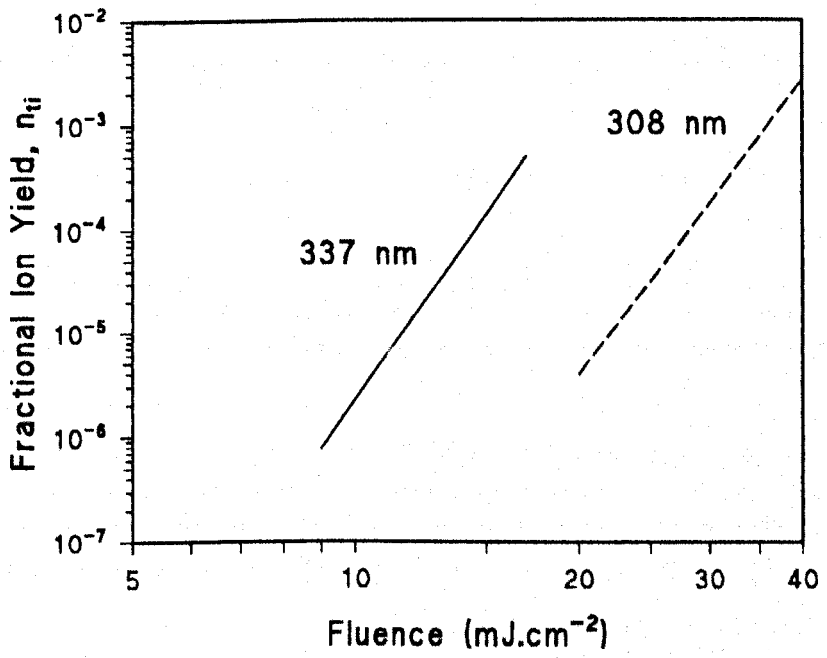

Figure 7.15. Modelled ESTI yield of 2,5-dihydroxybenzoic acid as a function of laser fluence using N_2 (337 nm) and XeCl (308 nm) laser radiation.

particular, a temperature-dependent heat capacity, based on the vibrational modes of matrix molecules, and the inclusion of triplet states reduce ESTI whereas interactions between photoexcited matrix molecules act to increase this. Thermionic cooling has little influence on ESTI and electron-ion recombination only marginally reduces the number of matrix ions at high laser fluences (15 - 20 $mJ.cm^{-2}$). 'Fluorescence heating' has little direct effect but does partly offset the energy loss through radiative S_1 - S_0 relaxation.

Investigations of the influence of experimental parameters on ESTI indicated that a strong dependence on the absorption of laser photons is likely, particularly ground state absorption. Surprisingly, variation by two orders of magnitude in the S_1-S_0 decay rate has little effect on ESTI of matrices; a fast decay rate results in a lower population of an upper excited state, S_p, from where ionisation may proceed but this is compensated for by the higher matrix temperature due to an increased number of non-radiative relaxation transitions. For slow decay rates, the opposite is true. Changes in laser wavelength, 0-0 ground-singlet transition energy and ionisation potential are all, ultimately, responsible for changes in the effective ionisation potential that is presented following the absorption by a molecule of a second photon. Small changes in these experimental parameters, therefore, will have a marked influence on the number of ions produced. Photoionisation becomes increasingly prevalent for short laser pulse lengths whereas ESTI increases with longer pulse lengths until a maximum is reached at a pulse length of ~ 10 ns (FWHM). This maximum is apparent since matrix heating within the laser pulse due to non-radiative transitions is already highly efficient whereas the reduced laser irradiance of long pulse lengths causes the population of S_p to become increasingly diminished, thus reducing the level of ionisation. That there is a maximum also indicates that neither laser fluence or irradiance solely determines the level of matrix ionisation, but rather that sufficient energy in a sufficiently short laser pulse is requred for significant ionisation, as proposed by Beavis [116].

The excited state thermal ionisation model thus provides a plausible route for matrix ionisation within MALDI. Predictions made using the model show good agreement with experimental observations of the dependence of matrix ion yield on laser fluence, wavelength and, in particular, pulse length.

8 CONCLUSIONS

In summarising the major features of this experimental and theoretical investigation of molecules commonly used as matrices in matrix-assisted laser desorption/ionisation (MALDI) mass spectrometry, it is important to note the sequential nature of the work performed.

Improved sample uniformity has been achieved with film thicknesses of 12 - 60 μm by mechanically crushing MALDI samples. The degree of uniformity displayed depends on the crushing and substrate materials used and on the amount of sample present. This has led to a reduction in the threshold fluence for the observation of matrix ions by up to ~ 15 % in certain cases. However, more significant improvements in sample preparation have been made by the vacuum sublimation-deposition of matrices to form films of controllable thickness (> 50 nm). Importantly, these films covered a wide substrate area (several cm^2) and could be deposited on glass or fused silica allowing quantitative optical spectra of matrix molecules to be obtained. Ground state absorption coefficients (α, typically $\alpha \sim 10^5$ cm^{-1} at laser wavelengths used), fluorescence decay rates, fluorescence quantum efficiencies, 0-0 (vibrationless) ground-singlet energies and average fluorescence wavelengths have been determined for typical matrix molecules. Furthermore, analysis of data obtained by others [118] has allowed an excited state singlet-singlet interaction rate to be estimated for the MALDI matrix 2,5-dihydroxybenzoic acid (2,5-DHB). The experimental significance of α has been demonstrated by its correlation with the different matrix ratings attributed to four chemically similar molecules. One molecule, which had previously been assigned a 'poor' rating as a matrix, has been shown to support the formation of insulin ions when using a laser wavelength at which α is increased by almost an order of magnitude from that upon which the matrix rating was based. This critical dependence of matrix ion yield on the absorption coefficient is further evidenced by the observation that 2,5-DHB ions appear at markedly lower fluences when using 337 nm (N_2 laser) rather than 308 nm (XeCl laser) radiation. This is largely due to a slight difference in (solid-phase) α at these two wavelengths, a difference that is possibly accentuated in a desorbed gas-phase environment.

By drawing upon these experimentally determined parameters, a basic model of excited-state thermal ionisation (ESTI) for matrices has been proposed whereby a matrix molecule becomes excited by the (stepwise) absorption of two (UV) photons before undergoing vibronic coupling to become electronically ionised. This is assumed to occur within the laser desorbed gas-phase plume, where rapid (~ps) thermalisation of the vibrational modes may occur. The encouraging initial results obtained from ESTI modelling prompted its extension to include other effects and processes, most notably temperature-dependent heat capacity, triplet states, excited state interactions and the consideration of 'realistic' temporal laser pulse shapes, e.g. Gaussian. Theoretical predictions based on this modelling show good agreement with experimental observations of the matrix ion yield - fluence relationship and the total fractional ion yield. Further verification of ESTI is provided by comparison with other experiments. For example, Dreisewerd *et al.* [154] show 2,5-DHB ion yields to be lowered by reducing a N_2 laser pulse length (FWHM) from 3 ns to 0.55 ns. Although this may at first appear somewhat counterintuitive, the ESTI model predicts this effect with surprising accuracy.

It is hoped that in investigating one aspect of MALDI, this work will ultimately aid the improvement and implementation of the process as a whole. However, it remains to be seen whether, or if at all, this occurs by the provision of useful experimental data, by the promotion of further theoretical treatment of MALDI (that may or may not agree with the findings herein) or simply by removing some of the mystique with which MALDI has previously been regarded. However, this work might best be drawn upon in understanding more fully the role of the matrix and the nature of matrix-analyte interactions. To expand briefly, the ESTI modelling could be used as the basis for investigation of matrix-matrix and matrix-analyte gas-phase charge transfer reactions, although the mechanisms involved will be inherently different to the unimolecular reactions assumed within ESTI. Any improved understanding of MALDI that this gives may then suggest desirable features of a potential matrix molecule or instrumental modifications. Otherwise, an extension of the ESTI modelling to include the temporal effects of desorption and subsequent plume expansion may be particularly informative, especially if gas-phase matrix absorption cross-sections can also be determined. This

could lead to an increase in the amount of data that MALDI could provide. For example, such work might allow highly spatially resolved analysis of a spatially non-uniform sample (e.g. a chromatogram or even real tissue) without the significant decrease in signal that is currently observed.

Great improvements have been made in the understanding of MALDI during the ten years since its introduction as an analytical technique. However, there still remains much to be discovered over the next ten years, and perhaps beyond.

APPENDIX A CLUSTERING

A.1 Introduction

In the MALDI analysis of mixtures of high mass molecules, the phenomenon of analyte clustering to form multimeric molecules needs to be recognised in order not to falsely assign observed ion peaks. Furthermore, an improved understanding of analyte clustering can only improve the quality of such analysis. As described in §2.3.5, matrix properties [182], laser fluence [180] and analyte concentration [182] are all known to affect the degree to which analyte clustering is observed, although it is unclear as to whether clustering occurs in solution, upon crystallisation of MALDI samples or in the laser desorbed gas-phase plume. This appendix highlights the commonality with which protein-protein clustering is observed, particularly between different types of protein molecule, and reports investigations of the influence of experimental conditions on such aggregations.

A.2 Sample Preparation

The matrices used in MALDI analysis were ferulic acid, sinapinic acid, 2,5-dihydroxybenzoic acid (2,5-DHB) and coumarin 120 (see §3.3 for details of suppliers). The proteins bovine insulin (M.W. 5 733.5 Da), chicken egg lysozyme (M.W. 14 306 Da), β-lactoglobulin (M.W. ~ 18 300 Da), bovine serum albumin (BSA; M.W. ~ 67 kDa) and bovine immunoglobulin G (IgG; M.W. ~ 150 kDa) were obtained from Sigma Chemical Co. Ltd. (Dorset, UK) to a stated purity of 97 - 99.5 %. Samples were prepared by the *dried-droplet* technique (§3.3) by mixing 1.5 μlitre each of both matrix and analyte solutions on a time-of-flight (TOF) mass spectrometer pin substrate and allowing them to dry. Matrix solutions were prepared using the appropriate standard solvents (§3.3) to a concentration of 10 g.litre^{-1}. Protein solutions were prepared with a 30 % acetonitrile (ACN; aq) + 0.1 % trifluoroacetic acid (TFA) solvent, if using ferulic acid or sinapinic acid as a matrix, or else H_2O + 0.1 % TFA. For mono-analyte clustering, protein solution concentrations ranged between 0.05 - 5 g.litre^{-1}, with

1 g.litre^{-1} solutions being used for investigations of laser fluence on clustering. Multi-analyte samples were prepared by mixing equal volumes of appropriate equi-molar protein solutions, e.g. 0.775 g.litre^{-1} lysozyme and 1.0 g.litre^{-1} β–lactoglobulin. This mixed solution was then deposited with a 1.5 μlitre volume of matrix solution onto a substrate, in the usual manner. All samples prepared for quantitative analysis contained ferulic acid as the matrix and were recrystallised by the application of 1 μlitre of 30 % ACN (aq) + 0.1 % TFA.

Analysis of samples was performed on the Vestec Reseachtec TOF mass spectrometer, as described in §3.2, using a N_2 laser (337 nm) for sample desorption and ionisation.

A.3 Initial Observations

Clustering of protein molecules from mono-analyte samples is commonly observed within MALDI (see §2.3.5). For example, the mass spectrum in fig. A.1 was obtained from a ferulic acid/lysozyme sample using a laser fluence approximately three times that of the threshold for observation of lysozyme ions. In this spectrum, the most intense peak (M^+) represents the singly charged monomer of lysozyme. In higher mass regions, where peaks correspond to successively larger analyte aggregations, up to the 18-mer ($18M^+$) lysozyme cluster is visible (M/z ~ 257 800 Da), representing an increase in the largest lysozyme cluster observed from the 15-mer ion reported previously [181].

Clustering could also be readily observed from multi-analyte samples. For example, fig. A.2 shows a mass spectrum of lysozyme (M) and β-lactoglobulin (m) obtained using a ferulic acid matrix and a laser fluence approximately three times that required to observe lysozyme ions. The usual monomer ion peaks are present (M^+ and m^+) as well as peaks corresponding to cluster ions containing just one protein (homo-multimers) up to the hexamer of lysozyme ($6M^+$) and the pentamer of β-lactoglobulin ($5m^+$). Interestingly, however, several mixed molecular cluster ions (hetero-multimers) are also observed up to the lysozyme pentamer combined with a β-lactoglobulin molecular ion, $[5M+m]^+$.

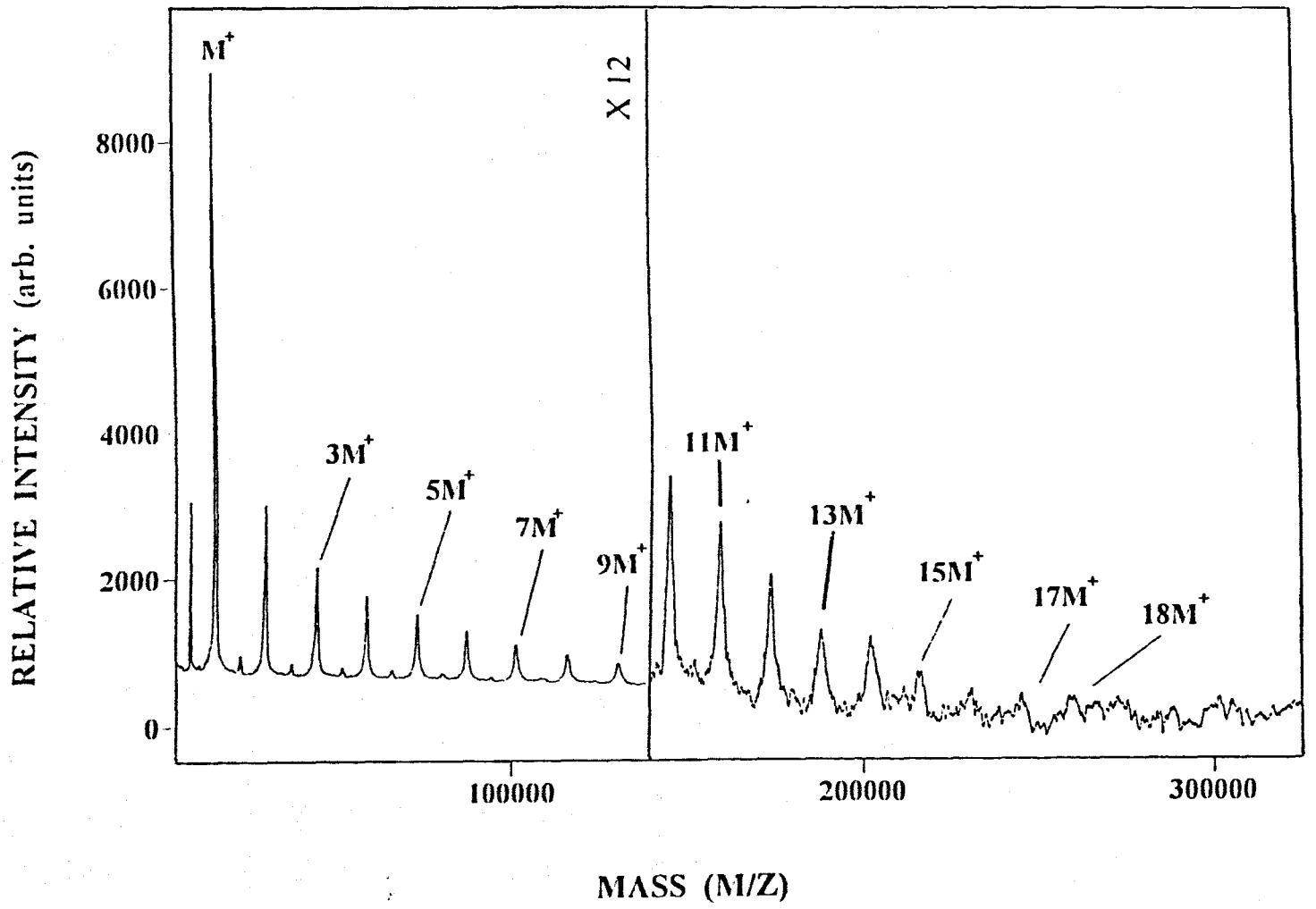

Figure A.1. Positive ion time-of-flight mass spectrum of chicken egg lysozyme from a ferulic acid matrix, illustrating the detection of up to the 18-mer ($18M^+$) of lysozyme.

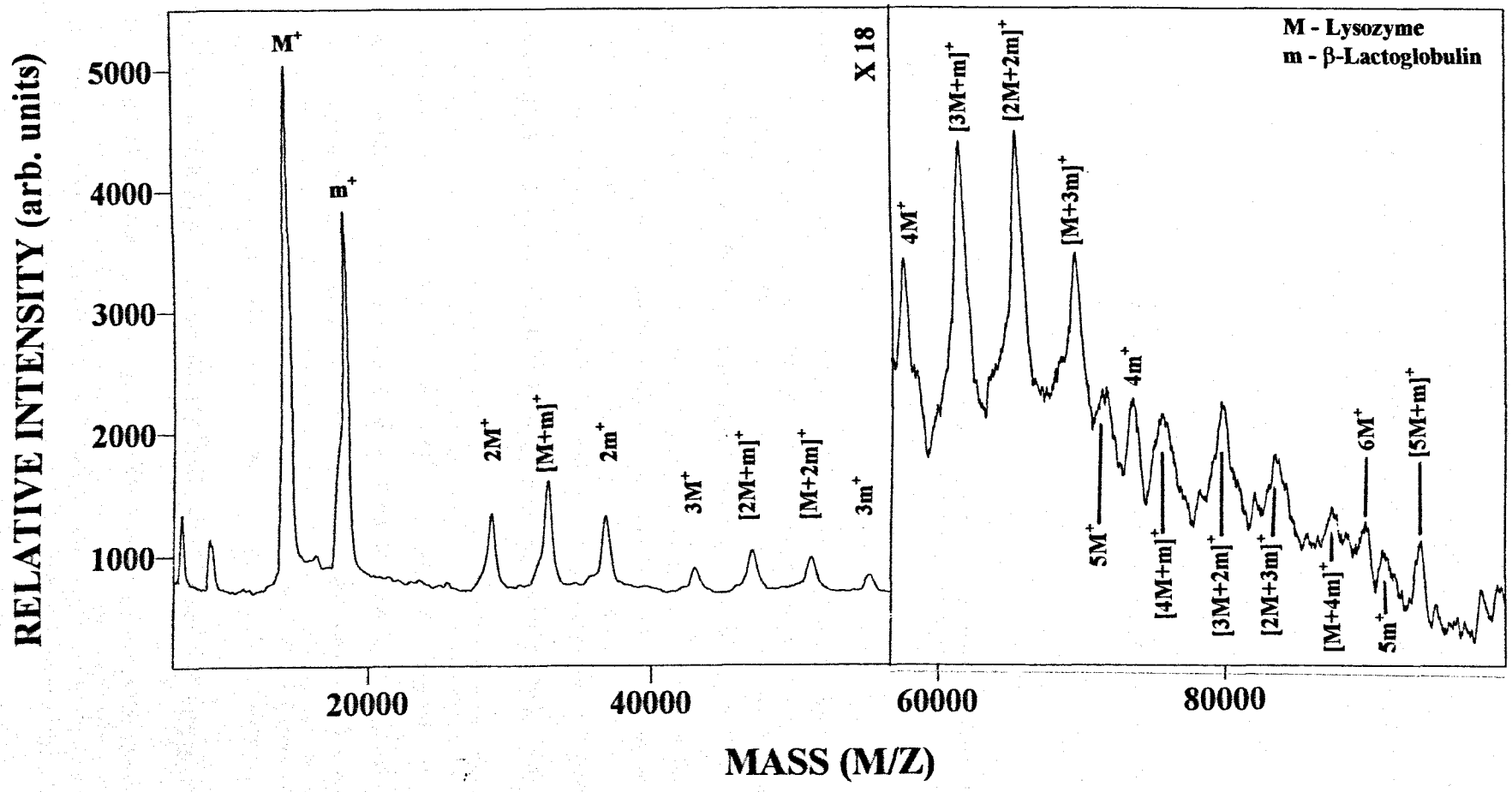

Figure A.2. Mass spectrum of an equimolar mixture of chicken egg lysozyme andβ-lactoglobulin from a ferulic acid matrix. Several homo and hetero-cluster ions are visible, where M and m denote lysozyme and lactoglobulin constituents, respectively.

Similar observations were made when using other matrices. Figure A.3 also shows a mass spectrum of lysozyme (M) and β-lactoglobulin (m) but this time from a 2,5-DHB matrix. Although only up to the dimer of β-lactoglobulin is observed, several hetero-multimers are clearly visible, again up to the $[5M+m]^+$ ion. The use of sinapinic acid and coumarin 120 as matrices yielded broadly similar results, although the range of both homo- and hetero-multimers observed was substantially reduced.

Hetero-multimerisation was also commonly observed for proteins of higher mass. Figure A.4 shows a mass spectrum obtained from a ferulic acid sample containing lysozyme (M) and BSA (m). In addition to the singly and double charged molecular ions of lysozyme (M^+ and M^{2+}) and BSA (m^+ and m^{2+}), lysozyme ions formed by Na adduction are also observed ($[M+Na]^+$), causing an apparent splitting of the lysozyme molecular ion peak. Several cluster ions are observed up to the trimer of lysozyme ($3M^+$), the dimer of BSA ($2m^+$) and including the hetero-multimer ions $[M+m]^+$ and $[M+2m]^+$, the latter peak displaying a mass of approximately 150 kDa. The mass spectrum in fig. A.5, again obtained from a ferulic acid matrix, shows the clustering of bovine IgG (M) and bovine insulin (m). The attachment of successive insulin molecules to the IgG protein, up to [M+4m], is clearly seen for both singly and doubly charged ions. At higher masses still, the hetero-multimer ion $[M+m]^+$ is observed in fig. A.6 from a ferulic acid matrix crystal containing IgG (M) and BSA (m), and corresponds to a mass of ~ 217 kDa.

The clustering of more than two protein molecules in MALDI can also be observed, although analysis becomes more complicated and careful assignment of peaks is necessary. Figure A.7 shows a mass spectrum of bovine insulin (M_1), chicken egg lysozyme (M_2) and β-lactoglobulin (M_3) and fig. A.8 one of chicken egg lysozyme (M_2), β-lactoglobulin (M_3) and BSA (M_4), both obtained using ferulic acid as a matrix. In both spectra, although a wide variety of different hetero-multimers are observed, the cluster containing all three proteins can be determined, $[M_1+M_2+M_3]^+$ in fig. A.7 and $[M_2+M_3+M_4]^+$ in fig. A.8.

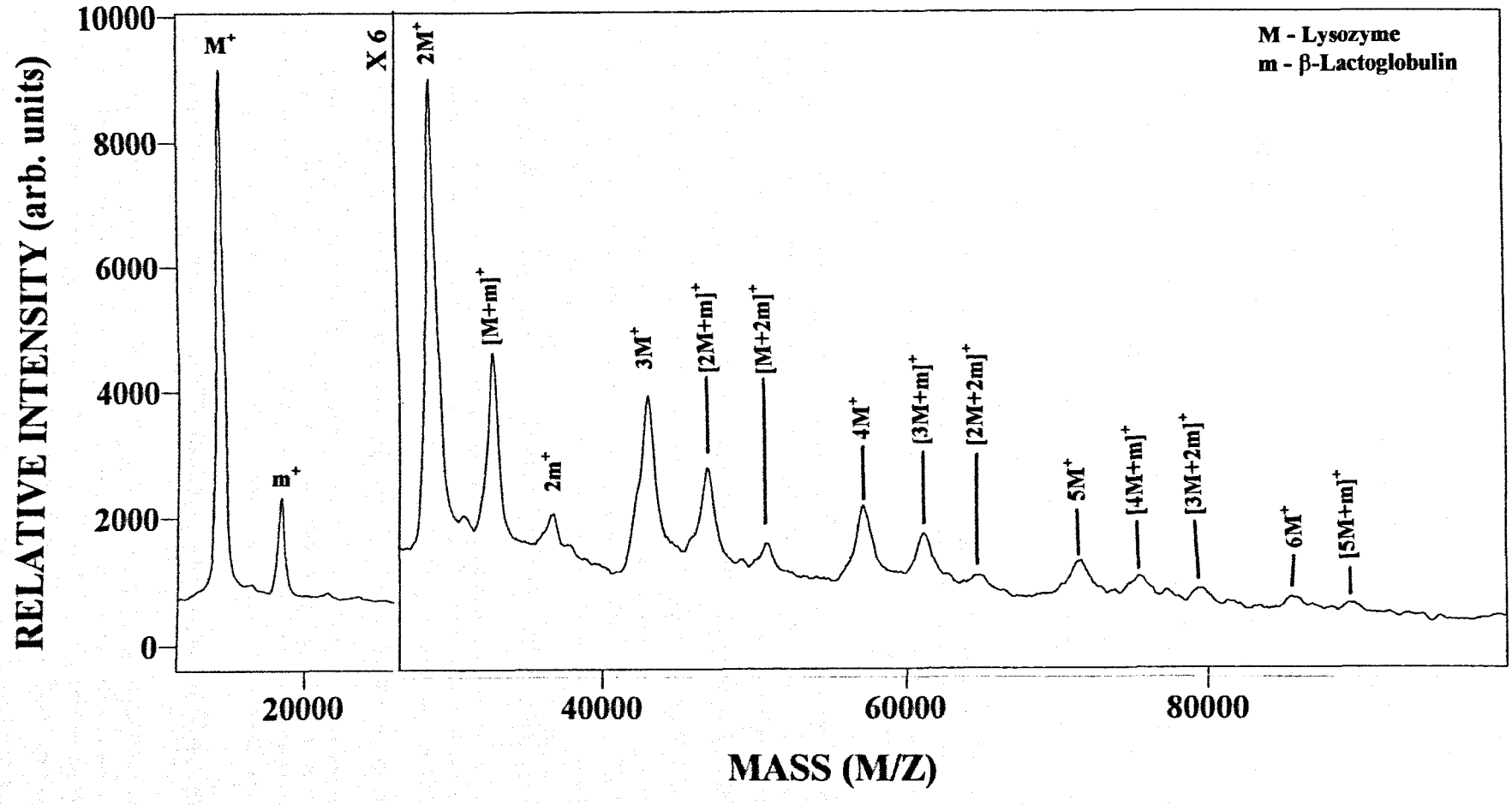

Figure A.3. Mass spectrum of an equimolar mixture of chicken egg lysozyme andβ-lactoglobulin from a 2,5-DHB matrix. Several homo and hetero-cluster ions are visible, where M and m denote lysozyme and lactoglobulin constituents, respectively.

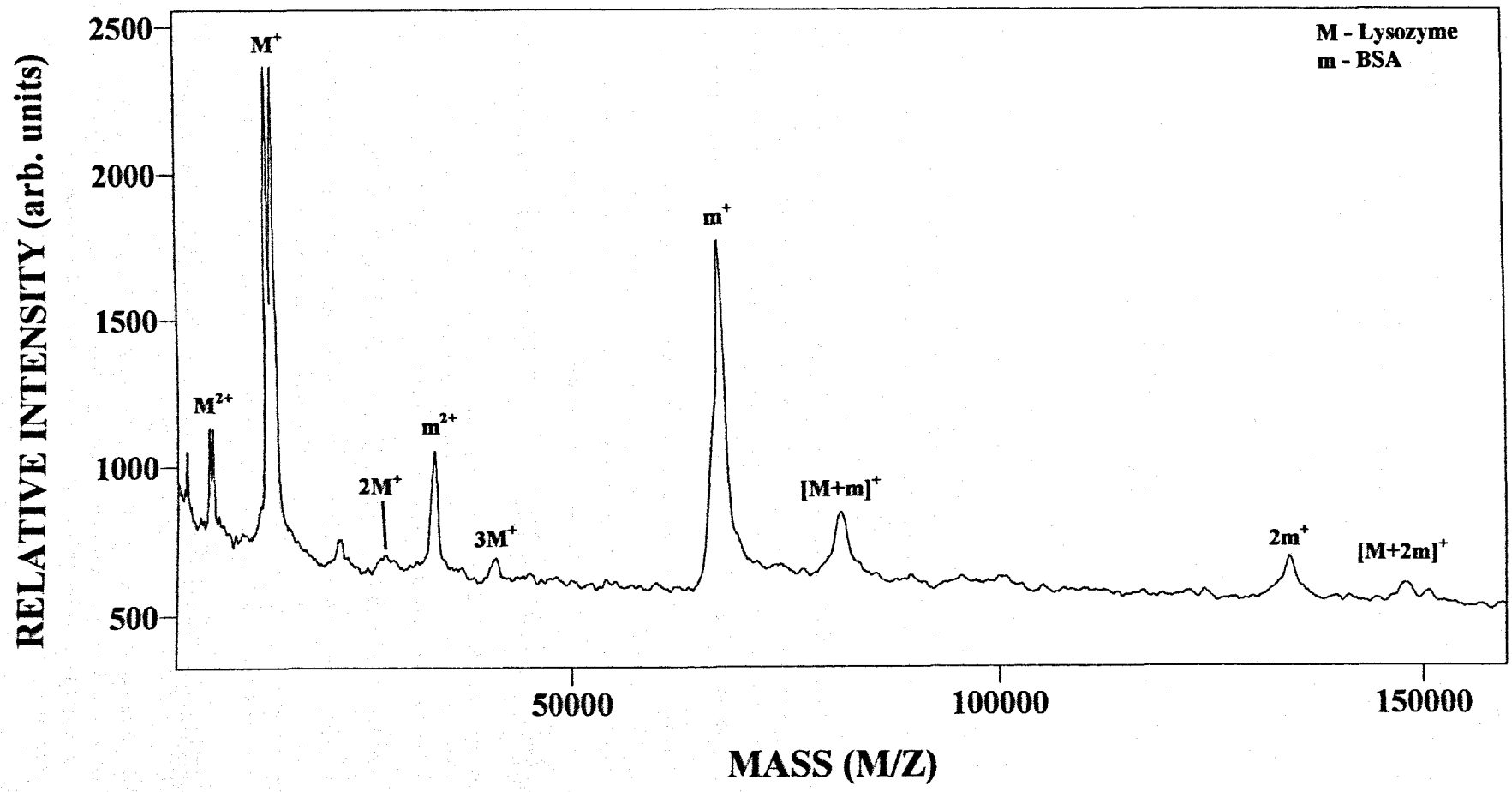

Figure A.4. Mass spectrum of an equimolar mixture of chicken egg lysozyme and bovine serum albumin (BSA) from a ferulic acid matrix. For the homo and hetero-cluster ions visible, M and m denote lysozyme and BSA constituents, respectively.

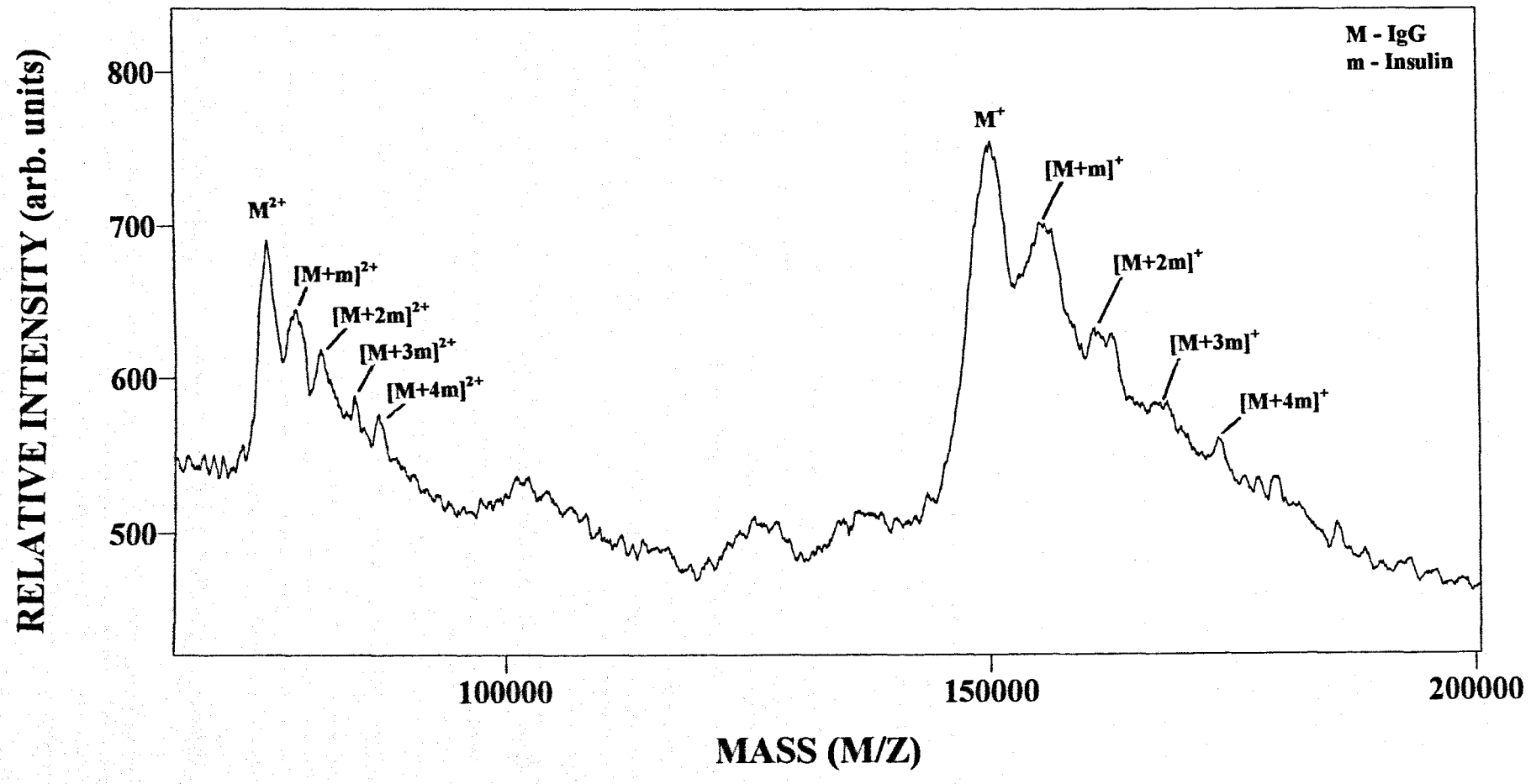

Figure A.5. Mass spectrum of an equimolar mixture of bovine immunoglobulin G (IgG) and bovine insulin from a ferulic acid matrix. For the cluster ions visible, M and m denote IgG and insulin constituents, respectively.

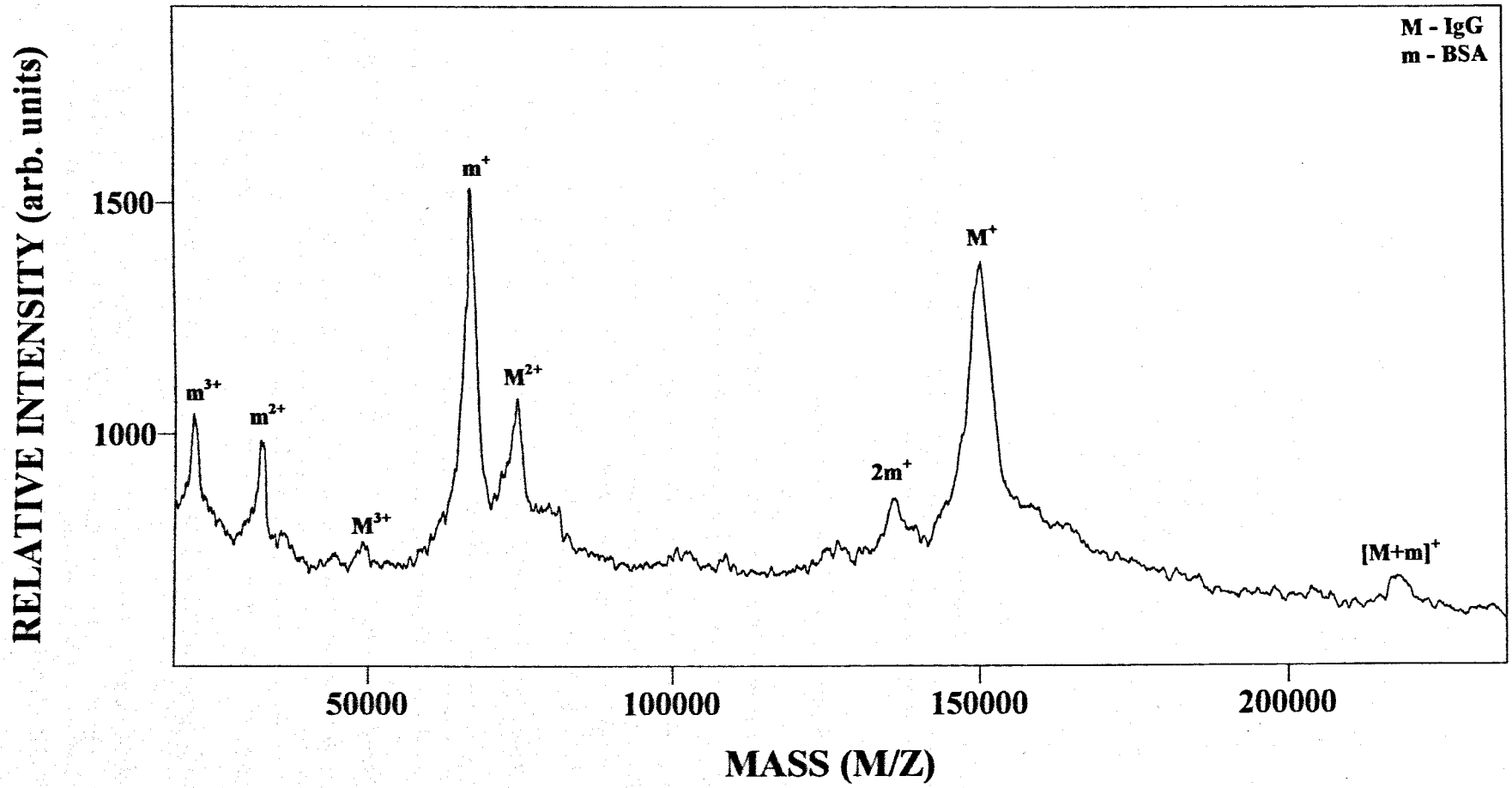

Figure A.6. Mass spectrum of an equimolar mixture of bovine immunoglobulin G (IgG) and bovine serum albumin (BSA) from a ferulic acid matrix. For the homo and hetero-cluster ions visible, M and m denote IgG and BSA constituents, respectively.

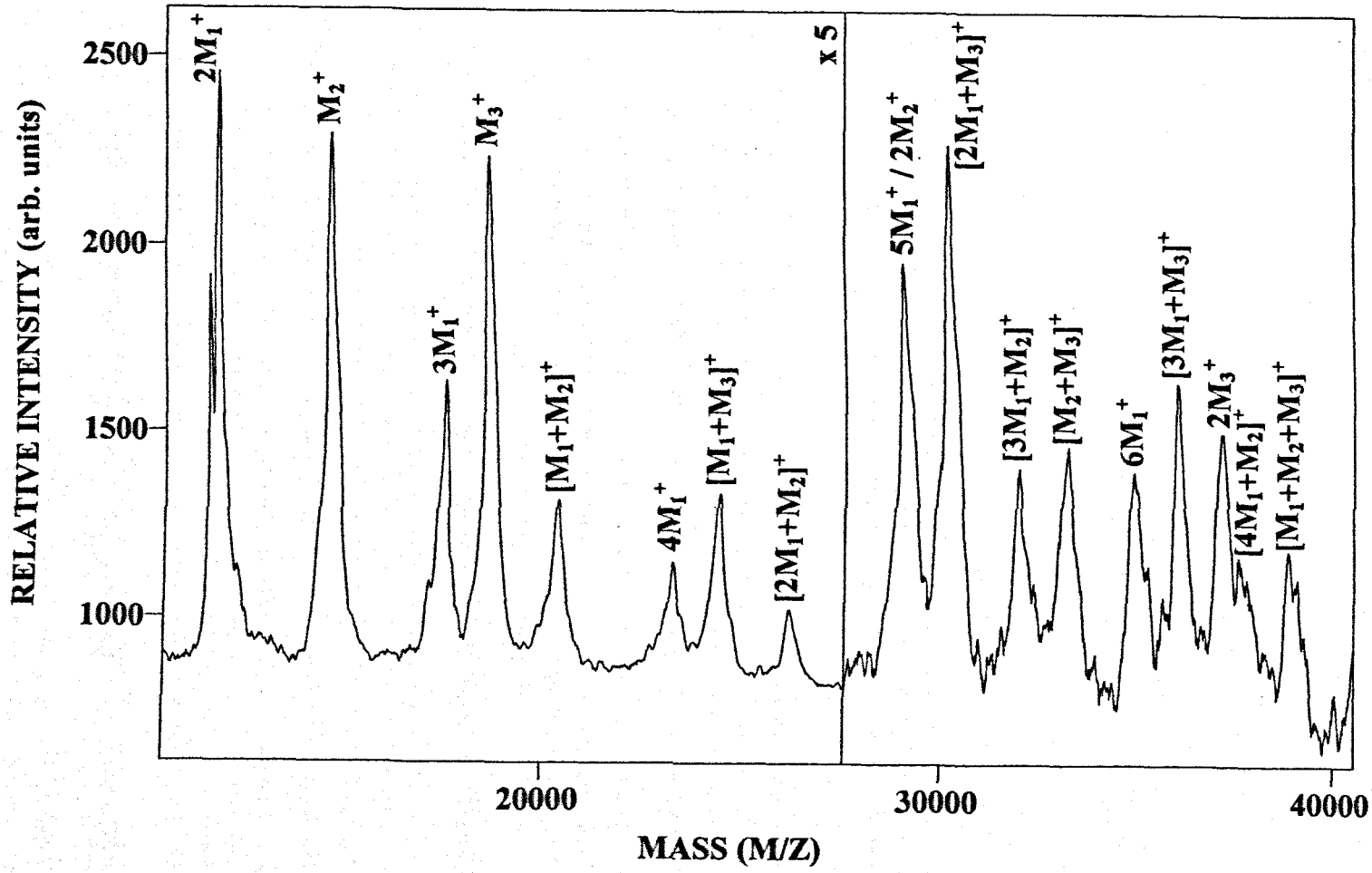

Figure A.7. Mass spectrum of an equimolar mixture of bovine insulin (M_1), chicken egg lysozyme (M_2) and β-lactoglobulin (M_3) using ferulic acid as a matrix. Several homo and hetero-cluster peaks are visible, including that which corresponds to the aggregation of all three proteins present in the sample ($[M_1+M_2+M_3]^+$).

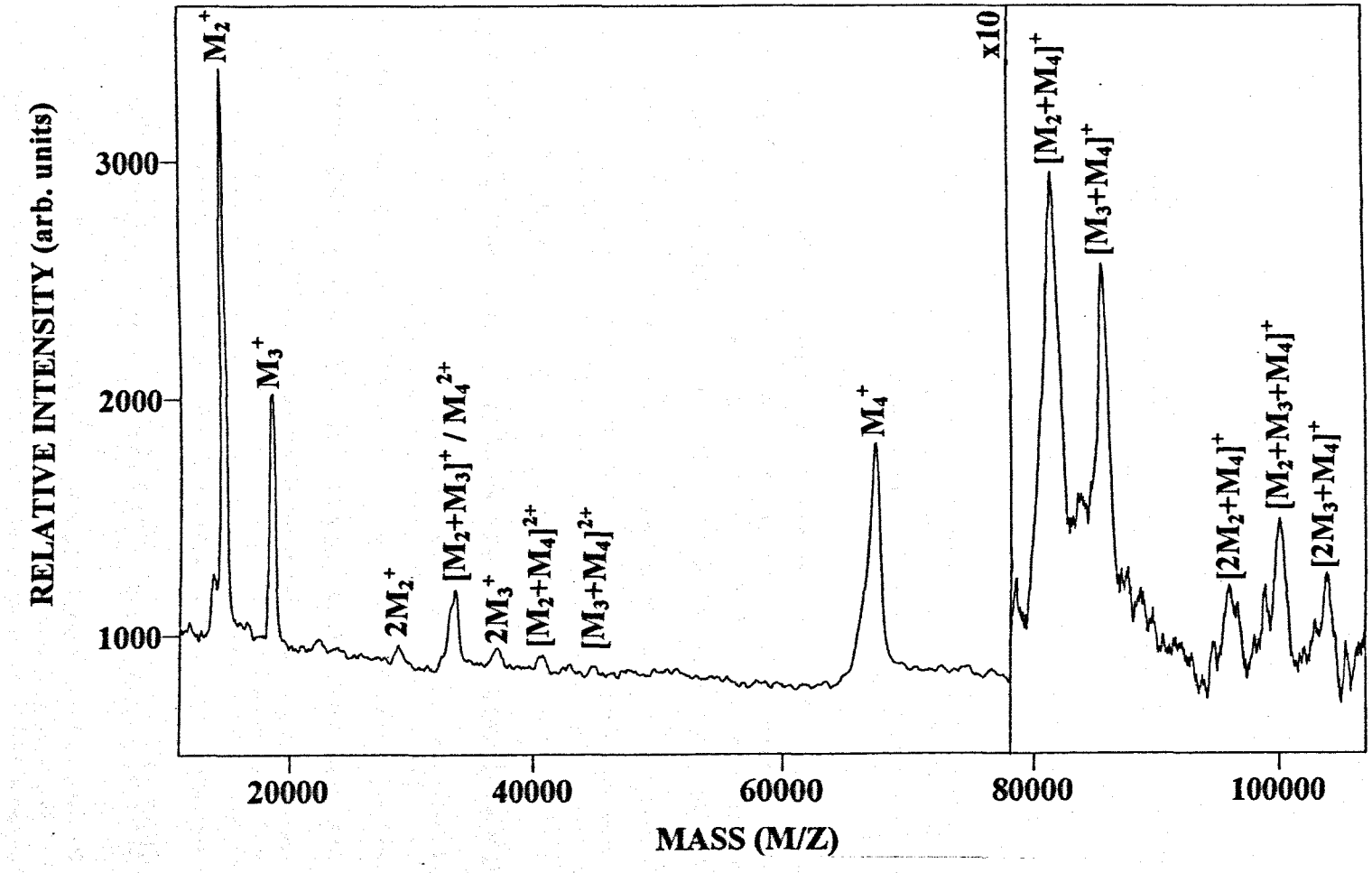

Figure A.8. Mass spectrum of an equimolar mixture of chicken egg lysozyme (M_2), β-lactoglobulin (M_3) and bovine serum albumin (M_4) using ferulic acid as a matrix. Several homo and hetero-cluster peaks are visible, including that which corresponds to the aggregation of all three proteins present in the sample ($[M_2+M_3+M_4]^+$).

A.4 Analysis

In MALDI-TOF mass spectrometry, the high mass (> 10 kDa) ions incident upon multichannel plate detectors sputter secondary ions in preference to causing electron emission [224]. The efficiency of ion detection also falls with mass, which can, for example, cause misrepresentation of polymer distributions in TOF mass spectrometry [268]. In the current mass analysis of protein clusters, the detected signal intensity is assumed to be proportional to the velocity of an incident ion, and hence to the inverse of the square root of the ion mass. A modifying factor is, therefore, applied to integrated ion peak signals, equal to the square root of the mass - charge ratio of the multimer ion. For mono-analyte (chicken egg lysozyme) samples, this allows the multimer ion fraction, F, to be defined as

$$F = \frac{\sum_{i=2}\sum_{z=1}\left(I_{iMz}\left\{\frac{iM}{z}\right\}^{1/2}\right)}{\sum_{i=1}\sum_{z=1}\left(I_{iMz}\left\{\frac{iM}{z}\right\}^{1/2}\right)} \qquad \text{A.1}$$

where M is the monomer molecular weight, i is the degree of protein clustering (monomer: i=1, dimer: i=2, trimer: i=3), z is the number of charges on an ion and I_{iMz} is the integrated signal intensity of the i^{th} cluster of the monomer with mass M and charge z. The numerator in eqn. A.1 represents the total integrated multimer ion signal and the denominator represents the total integrated signal for all analyte ion species. F = 0, therefore, signifies a total absence of protein clustering whereas F = 1 indicates a mass spectrum consisting entirely of multimer analyte ions and no monomers. Similarly, individual multimer ion fractions, F_r, may be represented by

$$F_r = \frac{\sum_{z=1}\left(I_{rMz}\left\{\frac{rM}{z}\right\}^{1/2}\right)}{\sum_{i=1}\sum_{z=1}\left(I_{iMz}\left\{\frac{iM}{z}\right\}^{1/2}\right)} \qquad \text{A.2}$$

to allow analysis of the separate cluster ion signals, e.g., dimers (r=i=2) or trimers (r=i=3).

For samples containing two proteins, namely chicken egg lysozyme (mass M) and β-lactoglobulin (mass m), eqn. A.1 is developed to give the total homo-multimer ion fraction, F_{aa}, as

$$F_{aa} = \frac{\sum_{i=2}\sum_{z=1}\left(I_{iMz}\left\{\frac{iM}{z}\right\}^{1/2}\right) + \sum_{j=2}\sum_{z=1}\left(I_{jmz}\left\{\frac{jm}{z}\right\}^{1/2}\right)}{\sum_{i=0}\sum_{j=0}\sum_{z=1}\left(I_{(iM+jm)z}\left\{\frac{iM+jm}{z}\right\}^{1/2}\right)} \qquad \text{A.3}$$

and the hetero-multimer ion fraction, F_{ab}, as

$$F_{ab} = \frac{\sum_{i=1}\sum_{j=1}\sum_{z=1}\left(I_{(iM+jm)z}\left\{\frac{iM+jm}{z}\right\}^{1/2}\right)}{\sum_{i=0}\sum_{j=0}\sum_{z=1}\left(I_{(iM+jm)z}\left\{\frac{iM+jm}{z}\right\}^{1/2}\right)} \qquad \text{A.4}$$

where i and j refer to the number of lysozyme and β-lactoglobulin molecules in a cluster, respectively, and $I_{(iM+jm)z}$ represents the integrated signal intensity of the $[iM + jm]^{z+}$ ion. It should be noted that in the above analysis, no correction is made for doubly charged protein clusters that coincide on mass spectra with smaller, singly charged clusters.

A.4.1 Analyte Concentration

Samples prepared from ferulic acid and 0.05 - 5 g.litre^{-1} chicken egg lysozyme solutions were investigated for protein clustering using an incident laser fluence of ~ 40 mJ.cm^{-2}. Figure A.9 displays spectra obtained using lysozyme solution concentrations of (a) 1.4×10^{-5} Molar (0.2 g.litre^{-1}) , (b) 7.0×10^{-5} Molar (1.0 g.litre^{-1}) and (c) 2.1×10^{-4}

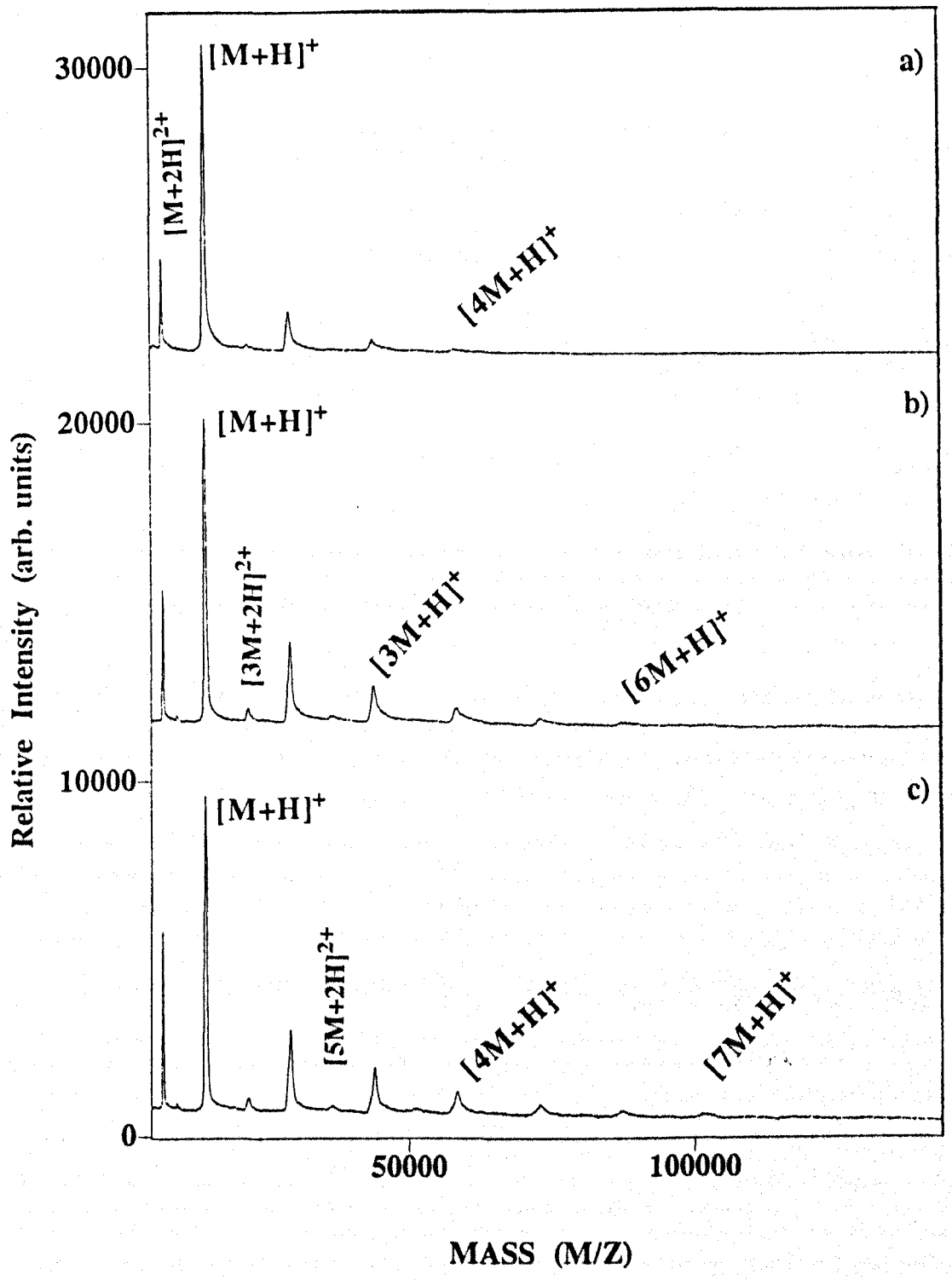

Figure A.9. Positive ion time-of-flight mass spectra of chicken egg lysozyme at initial concentrations of (a) 1.4×10^{-5} Molar, (b) 7.0×10^{-5} Molar and (c) 2.1×10^{-4} Molar, using ferulic acid as the matrix and a fluence of ~ 40 mJ.cm^{-2}.

Molar (3.0 g.litre^{-1}). Most notably, an increase in the size of the largest lysozyme cluster detected is observed, increasing from the tetramer ($[4M+H]^+$) in fig. A.9a, through the hexamer ($[6M+H]^+$) in fig. A.9b to the pentamer ($[7M+H]^+$) in fig. A.9c. However, at higher analyte concentrations (3.5×10^{-4} Molar or 3.5 g.litre^{-1}), the largest analyte cluster that could be detected was the pentamer ($[5M+H]^+$).

More detailed analysis was allowed by obtaining 5 - 10 mass spectra, each representing the average of 10 laser pulses, from 2 samples for each analyte concentration and applying the data to eqns. A.1 and A.2. The variation of the multimer ion fraction, F, with analyte concentration is shown in fig. A.10, where the error bars represent 1 standard deviation in the data. Figure A.10 shows good agreement with the observations highlighted above. For low analyte concentrations, F increases very quickly before reaching a maximum value at $\sim 1.8 \times 10^{-4}$ Molar (estimated) and decreasing at higher concentrations still. A similar behaviour was observed in the individual multimer ion fractions, F_2 (dimers), F_3 (trimers) and F_4 (tetramers), shown in fig. A.11. F_2 and F_3 reach a maximum at analyte concentrations of approximately 1.0×10^{-4} Molar and 2.0×10^{-4} Molar, respectively, above which a gradual decline is seen. However, F_4 appears to increase continuously over the analyte concentration range studied, although, based on the maxima seen in F_2 and F_3, it may be postulated that F_4 will reach a maximum at a higher analyte concentration.

These results, however, do not indicate where protein clustering takes place. If analyte clusters can be present in matrix crystals, formed either in solution or upon crystallisation, then an increase in analyte concentration will presumably lead to a greater number of clusters being formed. As the analyte concentration increases, however, the matrix will become increasingly diluted and the desorption process less efficient (see §2.3.3), affecting higher mass clusters to a greater extent than the monomeric signal. Alternatively, if clusters are formed in the gas-phase then the observations made here may be explained by the previously reported monomer ion signal dependence on analyte concentration [157]. As the analyte concentration increases initially, the number of analyte molecules desorbed will also increase, leading to a greater number of gas-phase clusters forming. However, as the matrix:analyte ratio in the crystals decreases further,

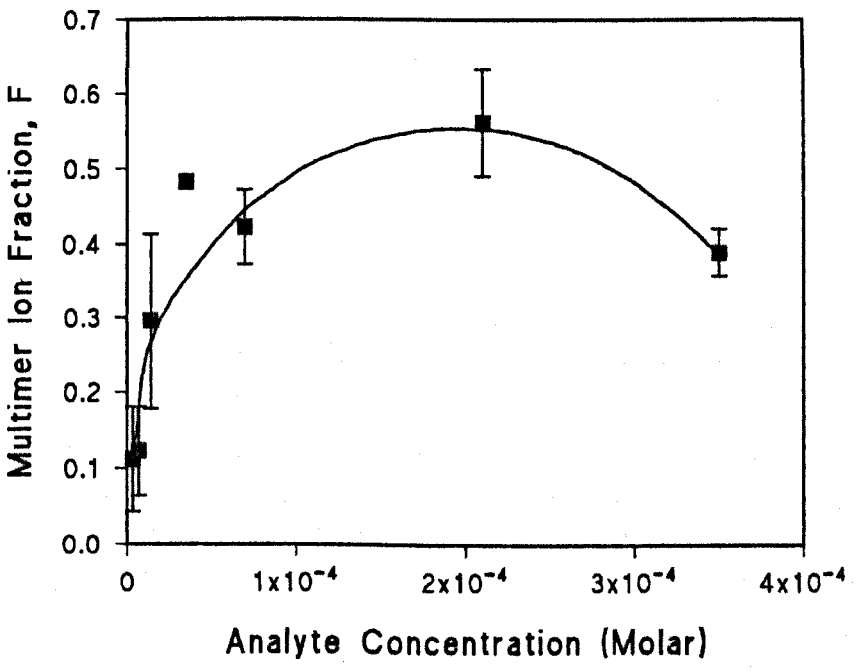

Figure A.10. Multimer ion fraction *F* as a function of analyte concentration for chicken egg lysozyme in a ferulic acid matrix, irradiated with ~ 40 mJ.cm^{-2} fluence.

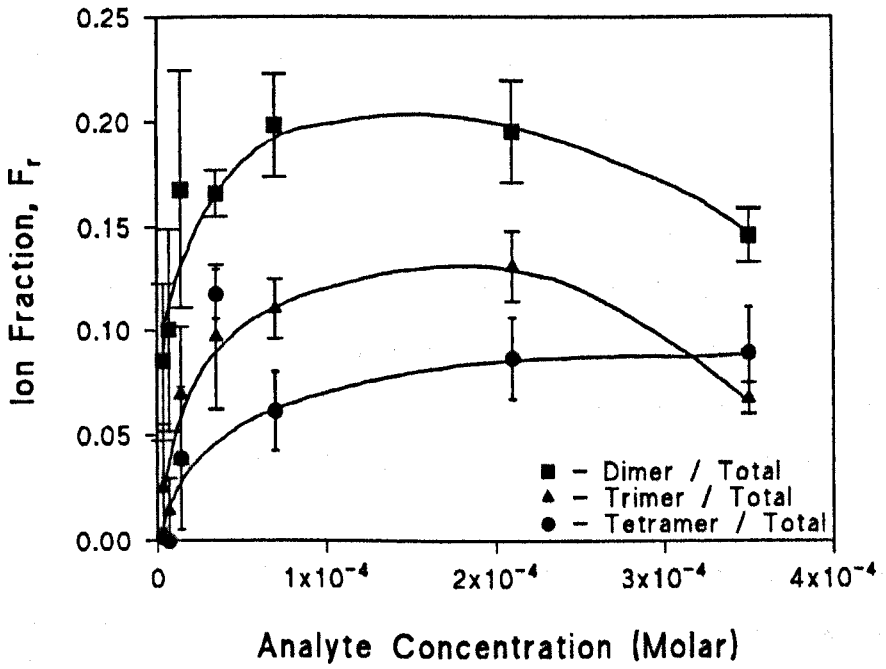

Figure A.11. Individual multimer ion fraction F_r (dimer, $r = 2$; trimer, $r = 3$; tetramer, $r = 4$) as a function of analyte concentration for chicken egg lysozyme in a ferulic acid matrix, irradiated with ~ 40 mJ.cm^{-2} fluence.

the desorption process will become less efficient, as mentioned above, and the resultant decrease in desorbed gas-phase protein molecules will in turn lead less clustering.

A.4.2 Fluence

Mass spectra obtained from ferulic acid/chicken egg lysozyme samples (fig. A.12) indicate that protein clustering increases with fluence. The largest observed cluster ion at fluences of 25 $mJ.cm^{-2}$ (fig. A.12a), 30 $mJ.cm^{-2}$ (fig. A.12b) and 40 $mJ.cm^{-2}$ (fig. A.12c) ranged from the dimer, the tetramer to the hexamer, respectively.

Statistical analysis of the clustering dependence on laser fluence proceeded in exactly the manner described in §A.4.1 above. The multimer ion fraction, F, increases linearly from a threshold fluence value of about 22.5 $mJ.cm^{-2}$ (fig. A.13). However, as the fluence approaches 40 $mJ.cm^{-2}$, F tends to saturate. By analysing the data using the individual multimer ion fraction, F_r, (eqn. A.2) threshold fluences for the appearance of each cluster species is observed (fig. A.14), estimated to be approximately 22.5 $mJ.cm^{-2}$ for dimers, 26.0 $mJ.cm^{-2}$ for trimers and 29.0 $mJ.cm^{-2}$ for tetramers. Furthermore, F_r tends to saturate at just above 40 $mJ.cm^{-2}$ for each of the ion fractions analysed.

Again, the variation of analyte clustering with fluence may be discussed in terms of cluster formation in solution, upon crystallisation or in the gas-phase. If protein clusters are present in matrix crystals, formed either in solution or upon crystallisation, then, by analogy with increasing threshold fluences for proteins of increasing molecular weight [156], the threshold fluence for observation of the larger mass clusters will be greater than for the monomer. If, however, analyte clustering occurs in the gas-phase, the observations described here may simply be explained in terms of an increase in the number of desorbed gas-phase protein monomers with fluence until a saturation limit is reached.

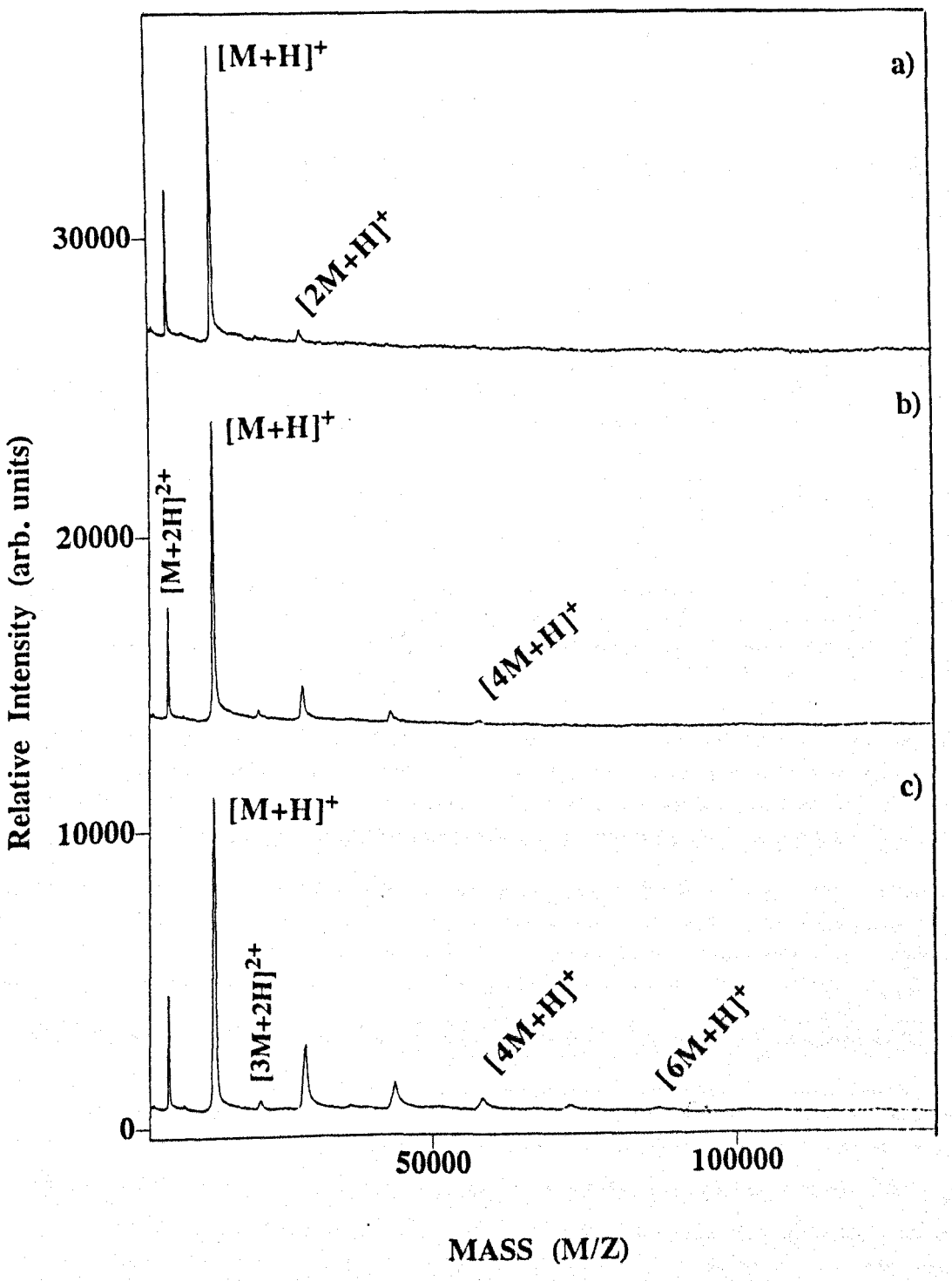

Figure A.12. Positive ion time-of-flight mass spectra of chicken egg lysozyme at laser fluences of (a) 25, (b) 30 and (c) 40 $mJ.cm^{-2}$, using ferulic acid as the matrix and an initial analyte concentration of 1 $g.litre^{-1}$.

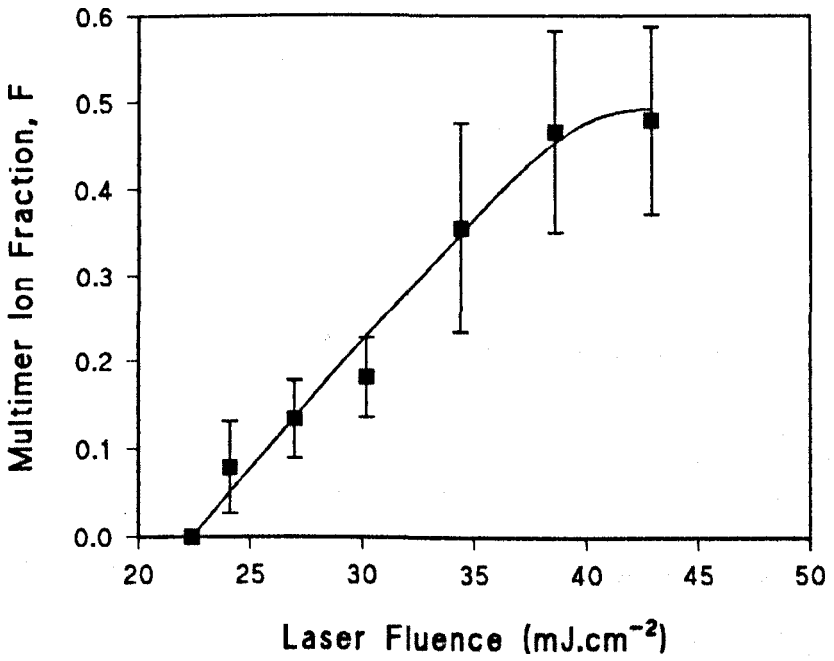

Figure A.13. Multimer ion fraction F of chicken egg lysozyme (1 g.litre^{-1}) as a function of laser fluence using ferulic acid as a matrix.

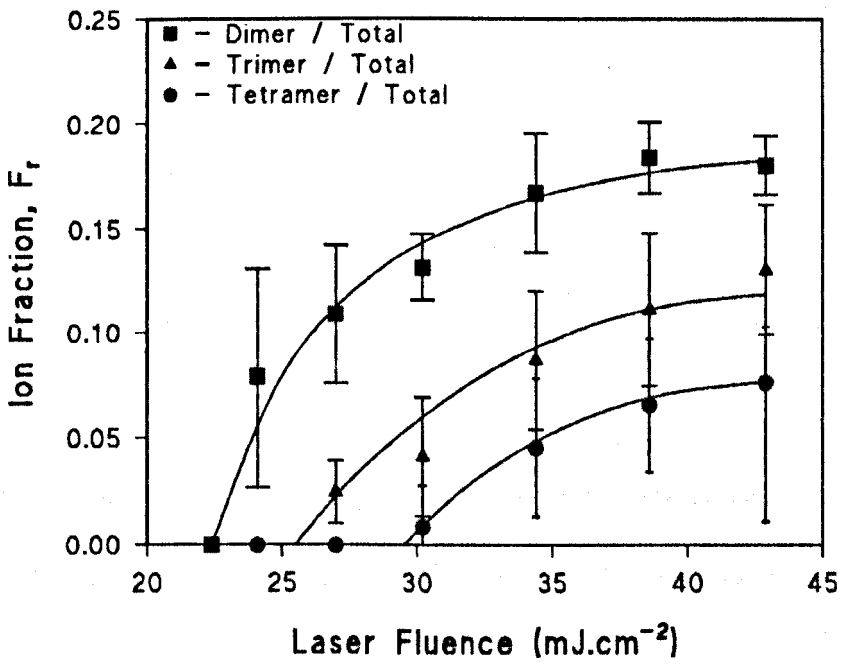

Figure A.14. Individual multimer ion fraction F_r (dimer, $r = 2$; trimer, $r = 3$, tetramer, $r = 4$) of chicken egg lysozyme (1 g.litre^{-1}) as a function of laser fluence using ferulic acid as a matrix.

A.4.3 Hetero-clustering

Data on the effect of fluence on mixed molecular clustering was accumulated by analysing 10 mass spectra for each value of fluence, each spectrum representing the average of spectra arising from 10 laser pulses. The variation of the homo- and hetero-multimer ion fractions, F_{aa} and F_{ab}, with fluence is shown in fig. A.15, the error bars again representing one standard deviation in the data. The threshold fluence for observation of either homo- or hetero-clusters is similar, at about 27 $mJ.cm^{-2}$, but both F_{aa} and F_{ab} saturate at approximately 35 $mJ.cm^{-2}$. The hetero-multimer signal is, however, generally greater than that for homo-clusters.

A.5 Conclusions

There are three main conclusions that can be drawn from the above study. Firstly, the regularity with which hetero-multimer ions are observed for a wide variety of proteins serves as a warning for the analysis of more complex mixtures. Not only might hetero-clustering peaks be wrongly assigned as separate species in their own right but might also obscure attempts to analyse protein reactions in solution. Secondly, protein clustering reaches a maximum at some optimum analyte solution concentration and, thirdly, each cluster component appears at some threshold fluence before saturating at a higher fluence. However, it remains unclear during which step in MALDI that analyte clusters form.

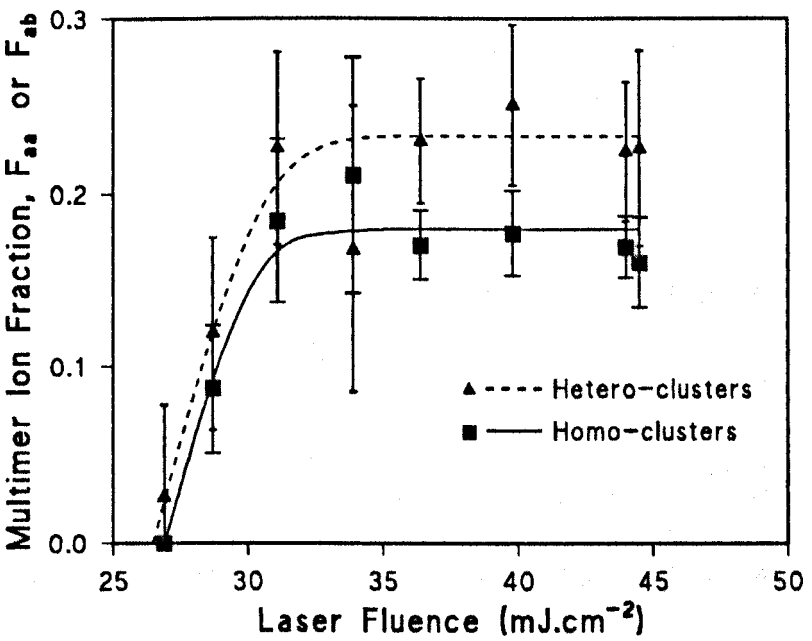

Figure A.15. Homo (F_{aa}) and hetero (F_{ab}) multimer ion fractions from an equimolar mixture of chicken egg lysozyme and β-lactoglobulin as a function of laser fluence. Ferulic acid was used as the matrix throughout.

APPENDIX B ESTIMATION OF ESTI RATE CONSTANT

B.1 Introduction

Chapter 6 discusses the possibility of excited-state thermal ionisation (ESTI) of matrix molecules as the main route of matrix ion formation within matrix-assisted laser desorption/ionisation (MALDI). This includes quantitative modelling of matrix ionisation within a laser pulse which requires a reasonable estimate of the ESTI ionisation rate, k_{ti}.

B.2 Analysis

The energy structure shown in fig. 6.1 is assumed, with ionisation commencing from an upper lying singlet state.

The ESTI reaction constant, k_{ion}, may be estimated by analogy with the detailed balance treatment of electron detachment from negative ions [257] to give:

$$k_{ion} = \frac{\rho^{+}}{\rho^{0}} v_e \sigma_r \qquad \text{B.1}$$

where $\rho^{+} = \rho^{ion}\rho^{e}$ is the combined number of states available to the molecular ion (ρ^{ion}, units J^{-1}) and free electron (ρ^{e}, units m^{-3}) per unit energy per unit volume, ρ^{0} is the number of states available to the excited-state molecule per unit energy, v_e is the electron velocity and σ_r the recombination cross-section. The density of states of the free electron is assumed to be a continuum of states, approximated by:

$$\rho^{e} = \frac{m_e^2 v_e}{\pi^2 \hbar^3} \Sigma \qquad \text{B.2}$$

where m_e is the free electron mass and Σ is the free electron kinetic energy. Using the classical treatment of vibrational states, molecular density of states have the general form [257]:

$$\rho = \frac{(E_{mol} - E_0)^{s-1}}{\prod_{i=1}^{s} \hbar\omega_i} \qquad \text{B.3}$$

where ω_i represent the molecular vibrational angular frequencies, $E_0 = \frac{1}{2}\sum_{i=1}^{s} \hbar\omega_i$ is the vibrational zero-point energy and E_{mol} represents the total molecular vibrational energy. By ignoring E_0, ρ^0 and ρ^{ion} may now be represented by:

$$\frac{\rho^{ion}}{\rho^0} = \left(\frac{E-U}{E}\right)^{s-1} \qquad \text{B.4}$$

where E is the average vibrational energy per molecule and U is the energy difference between the molecular state from which the ion is formed and the ground state of the ion (i.e. the effective ionisation energy of the photoexcited state; see fig. 6.1). This equation has the same form as that used elsewhere for density of states ratios of ground and excited state molecules [259,269]. By substituting eqns. B.2 and B.4 into eqn. B.1, k_{ion} becomes:

$$k_{ion} = \left(\frac{E-U}{E}\right)^{s-1} \frac{m_e^2 v_e}{\pi^2 \hbar^3} v_e \sigma_r \Sigma \qquad \text{B.5}$$

The classical expression for the fraction of molecules with internal energy within the range E to $E+\delta E$, $f_{E\to E+\delta E}$, is [269]:

$$f_{E\to E+\delta E} = \left(\frac{E}{kT}\right)^{s-1} \exp\left(-\frac{E}{kT}\right) \frac{1}{(s-1)!} \frac{dE}{kT} \qquad \text{B.6}$$

Multiplying eqns. B.5 and B.6 gives the thermal ionisation rate constant, k_{ti}, for an ensemble of molecules at a temperature T as:

$$k_{ti} = \frac{m_e^2 v_e}{\pi^2 \hbar^3}(v_e \sigma_r \Sigma)\int_0^{\infty}\left(\frac{E-U}{E}\right)^{s-1}\left(\frac{E}{kT}\right)^{s-1}\exp\left(-\frac{E}{kT}\right)\frac{1}{(s-1)!}\frac{dE}{kT} \qquad \text{B.7}$$

Equation B.7 integrates to [269]:

$$k_{ti} = \frac{m_e^2 v_e}{\pi^2 \hbar^3}(v_e \sigma_r \Sigma)\exp\left(-\frac{U}{kT}\right) \qquad \text{B.8}$$

which becomes:

$$k_{ti} = \frac{2m_e}{\pi^2 \hbar^3}(\sigma_r \Sigma^2)\exp\left(-\frac{U}{kT}\right) \qquad \text{B.9}$$

noting that $m_e v_e^2 = 2\Sigma$. Now, assuming that the electron recombination cross-section is given by:

$$\sigma_r = \pi r_c^2 = \pi\left(\frac{e^2}{6\pi\varepsilon_0 kT_e}\right)^2 \qquad \text{B.10}$$

where r_c is the electron capture radius, e is the charge on an electron, ε_0 is the permittivity of free space and T_e the free electron temperature, substituting into eqn. B.9 yields:

$$k_{ti} = \frac{16 m_e e^4}{36\varepsilon_0^2 h^3}\exp\left(-\frac{U}{kT}\right) \qquad \text{B.11}$$

which provides:

$$k_{ti} \approx 1.2 \times 10^{16}\exp\left(-\frac{U}{kT}\right) \quad (s^{-1}) \qquad \text{B.12}$$

APPENDIX C PUBLICATIONS

The following list details the journal and conference papers resulting from the work described in this thesis:

"Observation of Mixed Molecular Cluster Ions in Matrix Assisted UV Laser Desorption/Ionization of High Mass Protein Mixtures"
I. K. Perera, D. Allwood, P. E. Dyer and G. A. Oldershaw, *Int. J. Mass Spectrom. Ion Proc.*, **145** (1995) L9-16.

"Formation of Homo and Hetero Multimeric Ions of Large Proteins in Matrix Assisted UV Laser Desorption/Ionization"
I. K. Perera, D. Allwood, P. E. Dyer and G. A. Oldershaw, Special Issue of *J. Mass Spectrom. and Rapid Comm. Mass Spectrom.*, (1995) S3 and *Proc. 3rd Intl. Symp. on Applications of Mass Spectrometry in the Health and Life Sciences, Barcelona, 9 -13 July 1995.*

"Effects of Sample Homogeneity on the Analysis of High Mass Proteins by Matrix Assisted Laser Desorption/Ionization Mass Spectrometry"
D. Allwood, I. K. Perera, J. Perkins, P. E. Dyer and G. A. Oldershaw, *Oral Presenation at 21st BMSS Annual Meeting, Manchester, UK, 3 - 6 September 1995*;

"Preparation of 'Near' Homogeneous Samples for the Analysis of Matrix-assisted Laser Desorption/Ionization Processes"
D.A. Allwood, I. K. Perera, J. Perkins, P. E. Dyer and G. A. Oldershaw, *Appl. Surf. Sci.*, **103** (1996) 231.

"UV Optical Absorption of Matrices Used for Matrix-assisted Laser Desorption/Ionization"
D.A. Allwood, R.W. Dreyfus, I.K. Perera and P.E. Dyer, *Rapid Commun. Mass Spectrom.*, **10** (1996) 1575.

"Optical Absorption of Matrix Compounds for Laser-induced Desorption and Ionization (MALDI)"

D.A. Allwood, R.W. Dreyfus, I.K. Perera and P.E. Dyer, presented at *E-MRS Spring Meeting, Strasbourg, 4 - 7 June, 1996* and published as *Appl. Surf. Sci.*, **109/110** (1997) 154.

"Plasma Modelling of Matrix Assisted UV Laser Desorption Ionisation (MALDI)"

D.A. Allwood, P.E. Dyer, R.W. Dreyfus and I.K. Perera, presented at *E-MRS Spring Meeting, Strasbourg, 4 - 7 June, 1996* and published as *Appl. Surf. Sci.*, **109/110** (1997) 616.

"Ionization Modelling of Matrix Molecules in Ultraviolet Matrix-assisted Laser Desorption/Ionization"

D.A. Allwood, P.E. Dyer and R.W. Dreyfus, *Rapid Commun. Mass Spectrom.*, **11** (1997) 499.

"Characterisation and Modelling of Matrix Molecules in UV-MALDI Mass Spectrometry"

D.A. Allwood, P.E. Dyer, R.W. Dreyfus and I.K. Perera, presented at *Highlights of Physics Research, Rutherford Appleton Laboratory, Oxfordshire, 2 October 1997*

REFERENCES

[1] M. Karas and F. Hillenkamp, *Anal. Chem.*, **60** (1988) 2299.

[2] K. Tanaka, H. Waki, Y. Ido, S. Akita, Y. Yoshida and T. Yoshida, *Rapid Commun. Mass Spectrom.*, **2** (1988) 151.

[3] F. Hillenkamp, M. Karas, R.C. Beavis and B.T. Chait, *Anal. Chem.*, **63** (1991) 1193A.

[4] M. Salehpour, I.K. Perera, J. Kjellberg, A. Hedin, M.A. Islamian, P. Håkansson and B.U.R. Sundqvist, *Rapid Commun. Mass Spectrom.*, **3** (1989) 529.

[5] M. Karas, U. Bahr and F. Hillenkamp, *Int. J. Mass Spectrom. Ion Proc.*, **92** (1989) 231.

[6] R.C. Beavis and B.T. Chait, *Rapid Commun. Mass Spectrom.*, **3** (1989) 233.

[7] P. Juhasz, C.E. Costello and K. Biemann, *J. Am. Soc. Mass Spectrom.*, **4** (1993) 399.

[8] R.C. Beavis and B.T. Chait, *Anal. Chem.*, **62** (1990) 1836.

[9] R.C. Beavis and B.T. Chait, *Rapid Commun. Mass Spectrom.*, **12** (1989) 436.

[10] R.C. Beavis and B.T. Chait, *Rapid Commun. Mass Spectrom.*, **12** (1989) 432.

[11] R.C. Beavis, Y. Chaudhary and B.T. Chait, *Org. Mass Spectrom.*, **27**(1992) 156.

[12] K. Strupat, M. Karas and F. Hillenkamp, *Int. J. Mass Spectrom. Ion Proc.*, **111** (1991) 89.

[13] R.S. Bordoli, K. Howes, R.G. Vickers, R.H. Bateman and D.J. Harvey, *Rapid Commun. Mass Spectrom.*, **8** (1994) 585.

[14] V.S.K. Kolli and R. Orlando, *Anal. Chem.*, **69** (1997) 327.` nb

[15] V.M. Doroshenko and R.J. Cotter, *AIP Laser Ablation: Mechanisms and Applications II - 2nd International Conference, Knoxville, TN, April 1993*, Ch 6, p459 (1993) AIP Press (New York).

[16] Y. Li and R.T. McIver, Jr., *Rapid Commun. Mass Spectrom.*, **8** (1994) 743.

[17] J.A. Castro, C. Köster and C. Wilkins, *Rapid Commun. Mass Spectrom.*, **6** (1992) 239.

[18] R.T. McIver Jr., Y. Li and R.L. Hunter, *Int. J. Mass Spectrom. Ion Proc.*, **132** (1994) L1.

[19] L. Pasa-Tolic, Y. Huang, S. Guan, H.Y. Kim and A.G. Marshall, *J. Mass Spectrom.*, **30** (1995) 825.

[20] J.A. Castoro and C.L. Wilkins, *Anal. Chem.*, **65** (1993) 2621.

[21] L.-S. Sheng, J.E. Covey, S.L. Shaw, B.E. Winger and J.E. Campana, *Rapid Commun. Mass Spectrom.*, **8** (1994) 498.

[22] R.M. Major, G.F. Healey and K.N. Cheng, *21st BMSS Annual Meeting, Manchester, UK, 3 - 6 Sept 1995.*

[23] Y. Li and R.T. Hunter, Jr., *Rapid Commun. Mass Spectrom.*, **8** (1994) 743.

[24] T. Solouki, K.J. Gillig and D.H. Russell, *Rapid Commun. Mass Spectrom.*, **8** (1994) 26.

[25] Y. Li, R.T. McIver, Jr. and R.L. Hunter, *Anal. Chem.*, **66** (1994) 2077.

[26] S.J. Gaskell, *J. Mass Spectrom.*, **32** (1997) 677.

[27] *Electrospray Ionization Mass Spectrometry*, R.B. Cole (Ed.), John Wiley and Sons (1997).

[28] M.H. Allen, D.J. Grindstaff, M.L. Vestal and R.W. Nelson, *Biochem. Soc. Trans.*, **19** (1991) 954.

[29] S. Jesperson, W.M.A. Niesson, U.R. Tjaden, J. van der Greef, E. Litborn, U. Lindberg and J. Roeraade. *Rapid Commun. Mass Spectrom.*, **8** (1994) 581.

[30] R.W. Nelson, D. Droguel and P. Williams, *Rapid Commun. Mass Spectrom.*, **8** (1994) 627.

[31] R.W. Nelson, D. Droguel and P. Williams, *Rapid Commun. Mass Spectrom.*, **9** (1995) 625.

[32] O.N. Jensenm A, Podtelejnikov and M. Mann, *Rapid Commun. Mass Spectrom.*, **10** (1996) 1371.

[33] M.L. Vestal, P. Juhasz and S.A. Martin, *Rapid Commun. Mass Spectrom.*, **9** (1995) 1044.

[34] R. Lidgard and M.W. Duncan, *Rapid Commun. Mass Spectrom.*, **9** (1995) 128.

[35] G. Talbo and M. Mann, *Rapid Commun. Mass Spectrom.*, **10** (1996) 100.

[36] F. Kanda, S. Yoshida, T. Okumura and T. Takamatsu, **9** (1995) 1095.

[37] K. Tang, S.L. Allman and C.H. Chen, *AIP Laser Ablation: Mechanisms and Applications II, 2nd International Conference, Knoxville TN, April 1993.*

[38] N.I. Taranenko, K. Tang, S.L. Allman, L.-Y. Ch'ang and C.H. Chen, *Rapid Commun. Mass Spectrom.*, **8** (1994) 1001.

[39] K.J. Wu, A. Steding and C.H. Becker, *Rapid Commun. Mass Spectrom.*, **7** (1993) 142.

[40] E. Nordhoff, A. Ingedoh, R. Cramer, A. Overberg, B. Stahl, M. Karas, F. Hillenkamp and P.F. Crain, *Rapid Commun. Mass Spectrom.*, **6** (1992) 771.

[41] E. Nordhoff, M. Karas, R. Cramer, S. Hahner, F. Hillenkamp, F. Kirpekar, A. Lezius, J. Muth, C. Meier and J.W. Engels, *J. Mass Spectrom.*, **30** (1995) 99.

[42] W.H. Benner, D. Horn, J. Katz and J. Jaklevic, *Rapid Commun. Mass Spectrom.*, **9** (1995) 537.

[43] K. Tang, S.L. Allman, C.H. Chen, L.Y. Chang and M. Schell, *Rapid Commun. Mass Spectrom.*, **8** (1994) 183.

[44] T.A. Stahler, Y. Tan, J.N. Wickham, K.J. Wu and C.H. Becker, *Rapid Commun. Mass Spectrom.*, **9** (1995) 942.

[45] G.J. Currie and J.R. Yates III, *J. Am. Soc. Mass Spectrom.*, **4** (1993) 955.

[46] N.I. Taranenko, C.N. Chung, Y.F. Zhu, S.L. Allman, V.V. Golovlev, N.R. Isola, S.A. Martin, L.A. Haff and C.H. Chen, *Rapid Commun. Mass Spectrom.*, **11** (1997) 386.

[47] E. Nordhoff, M. Karas, R. Cramer, S. Hahner, F. Hillenkamp, F. Kirpekar, A. Lezius, J. Muths, C. Meier and J.W. Engels, *J. Mass Spectrom.*, **30** (1995) 99.

[48] M.C. Fitzgerald, L. Zhu and L.M. Smith, *Rapid Commun. Mass Spectrom.*, **7** (1993) 895.

[49] K. Tang, N.L. Taranenko, S.L. Allman, C.H. Chen, L.Y. Chang and K.B. Jacobson, *Rapid Commun. Mass Spectrom.*, **8** (1994) 673.

[50] F. Kipekar, E. Nordhoff, K. Kristiansen, P. Roepstorff, S. Hahner and F. Hillenkamp, *Rapid Commun. Mass Spectrom.*, **9** (1995) 525.

[51] G. Montaudo, M.S. Montaudo, C. Puglisi and F. Samperi, *Rapid Commun. Mass Spectrom.*, **8** (1994) 1011.

[52] D.R. Maloney, K.H. Hunt, P.M. Lloyd, A.V.G. Muir, S.N. Richards, P.J. Derrick and D.M. Haddleton, *J. Chem. Soc., Chem. Commun.*, (1995) 561.

[53] G. Monatudo, M.S. Montaudo, C. Puglisi and F. Samperi, *Anal. Chem.*, **66** (1994) 4366.

[54] G. Monatudo, M.S. Montaudo, C. Puglisi and F. Samperi, *Rapid Commun. Mass Spectrom.*, **8** (1994) 981.

[55] G. Monatudo, M.S. Montaudo, C. Puglisi and F. Samperi, *Rapid Commun. Mass Spectrom.*, **9** (1995) 453.

[56] J.S. Cottrell, M. Koerner and R. Gerhards, *Rapid Commun. Mass Spectrom.*, **9** (1995) 1562.

[57] P.M. Lloyd, K.G. Suddaby, J.E. Varney, E. Scrivener, P.J. Derrick and D.M. Haddleton, *Eur. Mass Spectrom.*, **1** (1995) 293.

[58] S. Weidner, G. Kühn and U. Just, *Rapid Commun. Mass Spectrom.*, **9** (1995) 697.

[59] G. Monatudo, M.S. Montaudo, C. Puglisi and F. Samperi, *Rapid Commun. Mass Spectrom.*, **9** (1995) 1158.

[60] D. Droguel, R.W. Nelson and P. Williams, *Rapid Commun. Mass Spectrom.*, **10** (1996) 801.

[61] I.A. Mowat, R.J. Donovan and R.R.J. Maier, *Rapid Commun. Mass Spectrom.*, **11** (1997) 89.

[62] J.P. Barry, W.J. Carton, K.M. Pesci, R.T. Anselmo, D.R. Radtke and J.V. Evans, *Rapid Commun. Mass Spectrom.*, **11** (1997) 437.

[63] B. Guo, H. Chen, H. Rachidzadeh and X. Liu, *Rapid Commun. Mass Spectrom.*, **11** (1997) 781.

[64] A.A. Herod, C.-Z. Li, J.E. Parker, P. John, C.A.F. Johnson, G.P. Smith, P. Humphrey, J.R. Chapman and R. Kandiyoti, *Rapid Commun. Mass Spectrom.*, **8** (1994) 808.

[65] A.A. Herod, C.-Z. Li, B. Xu, J.E. Parker, C.A.F. Johnson, P. John, G.P. Smith, P. Humphrey, J.R. Chapman and R. Kandiyoti, *Rapid Commun. Mass Spectrom.*, **8** (1994) 815.

[66] C.-Z. Li, A.A. Herod, P. John, C.A.F. Johnson, J.E. Parker, G.P. Smith, P. Humphrey, J.R. Chapman, M. Rahman, R.R.F. Kinghorn and R. Kandiyoti, *Rapid Commun. Mass Spectrom.*, **8** (1994) 823.

[67] P. John, C.A.F. Johnson, J.E. Parker, G.P. Smith, A.A. Herod, C.-Z. Li and R. Kandiyoti, *Rapid Commun. Mass Spectrom.*, **7** (1993) 795.

[68] S. Weidner, A. Höllander and G. Kühn, *Rapid Commun. Mass Spectrom.*, **11** (1997) 447.

[69] G.R. Kinsel, L.M. Preston and D.H. Russell, *Biol. Mass Spectrom.*, **23** (1994) 205.

[70] D.J. Harvey, *Rapid Commun. Mass Spectrom.*, **7** (1993) 614.

[71] D.J. Harvey, T.J.P. Naven, B. Küster, R.H. Bateman, M.R. Green and G. Critchley, *Rapid Commun. Mass Spectrom.*, **9** (1995) 1556.

[72] D. Garrozzo, G. Impallomeni, A. Spina, L. Sturiale and F. Zanetti, *Rapid Commun. Mass Spectrom.*, **9** (1995) 937.

[73] D.J. Harvey, *Rapid Commun. Mass Spectrom.*, **7** (1993) 614.

[74] M.G.Bartlett, K.L. Busch, C.A. Wells and K.L. Schey, *J. Mass Spectrom.*, **31** (1996) 275.

[75] M.G. Bartlett, K.L. Busch, C.A. Wells and K.L. Schey, *J. Mass Spectrom.*, **31** (1996) 275.

[76] R.S. Youngquist, G.R. Fuentes, M.P. Lacey and T. Keough, *Rapid Commun. Mass Spectrom.*, **8** (1994) 77.

[77] M.D. Knierman, J.E. Coligan and K.C. Parker, *Rapid Commun. Mass Spectrom.*, **8** (1994) 1007.

[78] P.R. Griffin, M.J. MacCoss, J.K. Eng, R.A. Blevins, J.S. Aaronson and J.R. Yates III, *Rapid Commun. Mass Spectrom.*, **9** (1995) 1546.

[79] I.K. Perera, J.M. Candy, P. Håkansson, A.E. Oakley, G. Brinkmalm and B.U.R. Sundqvist, *Rapid Commun. Mass Spectrom.*, **4** (1990) 527. (1990) 527.

[80] I.K. Perera, E. Uzcategui, P. Håkansson, G. Brinkmalm, G. Petterson, G. Johansson and B.U.R Sundqvist, *Rapid Commun. Mass Spectrom.*, **4** (1990) 285.

[81] J.C. Blais, P.Nagnan-Le-Meillour, G. Bolbach and J.C. Tabet, *Rapid Commun. Mass Spectrom.*, **10** (1996) 1.

[82] M. Karas, U. Bahr, K. Strupat, F. Hillenkamp, A. Tsarbopoulos and B.N. Pramanik, *Anal. Chem.*, **67** (1995).

[83] R.C. Beavis and B.T. Chait, *Proc. Natl. Acad. Sci., U.S.A.*, **87** (1990) 6873.

[84] J. Bai, X. Liang, Y.-H. Liu, Y. Zhu and D.M. Lubman, *Rapid Commun. Mass Spectrom.*, **10** (1996) 839.

[85] R. Marsilio, S. Catinella, R. Seraglia and P. Traldi, *Rapid Commun. Mass Spectrom.*, **9** (1995) 550.

[86] T.C. Cain, D.M. Lubman, and W.J. Weber, Jr., *Rapid Commun. Mass Spectrom.*, **8** (1994) 1026.

[87] M.K. Khurana, I.K. Perera, P.J. Large, P. Bagga, D. Verma and P.E. Dyer, *21st BMSS Annual Meeting, Swansea, UK, Sept 1996.*

[88] P.A. van Veelen, C.R. Jiménez, K.W. Li, W.C. Wildering, W.P.M. Geraerts, U.R. Tjaden and J. van der Greef, *Org. Mass Spectrom.*, **28** (1993) 1542.

[89] B.H. Wang, U. Bahr, M. Karas and F. Hillenkamp, *Int. J. Mass Spectrom. Ion Proc.*, **92** (1989) 321.

[90] T.-W.D. Chan, A.W. Colburn, P.J. Derrick, D.J. Gardiner and M. Bowden, *Org. Mass Spectrom.*, **27** (1992) 188.

[91] J. Bai, Y.-H. Liu, D.M. Lubman and D. Siemieniak, *Rapid Commun. Mass Spectrom.*, **8** (1994) 687.

[92] J. Baim Y.-H. Liu, T.C. Cain and D.M. Lubman, *Anal. Chem.*, **66** (1994) 3423.

[93] K.O. Börnsen, M.D. Mohr and H.M. Widmer, *Rapid Commun. Mass Spectrom.*, **9** (1995) 1031.

[94] H. Zhang and R.M. Caprioli, *J. Mass Spectrom.*, **31** (1996) 690.

[95] K.O. Börnsen, M.A.S. Gass, G.J.M. Bruin, J.H.M. von Adrichem, M.C. Biro, G.M. Kresbach and M. Ehrat, *Rapid Commun. Mass Spectrom.*, **11** (1997) 603.

[96] I.K. Perera, J. Perkins and S. Kantartzoglou, *Rapid Commun. Mass Spectrom.*, **9** (1995) 180.

[97] F. Xiang and R.C. Beavis, *Org. Mass Spectrom.*, **28** (1993) 1424.

[98] T. Huth-Fehre and C.H. Becker, *Rapid Commun. Mass Spectrom.*, **5** (1991) 378.

[99] J. Axelsson, A.-M. Hoberg, C. Waterson, P. Myatt, G.L. Shield, J. Varney, D.M. Haddleton and P.J. Derrick, *Rapid Commun. Mass Spectrom.*, **11** (1997) 209.

[100] G.S. McLeod, J. Axelsson, R. Self and P.J. Derrick, *Rapid Commun. Mass Spectrom.*, **11** (1997) 214.

[101] O. Vorm, P. Roepstorff and M. Mann, *Anal. Chem.*, **66** (1994) 3281.

[102] F. Xiang and R.C. Beavis, *Rapid Commun. Mass Spectrom.*, **8** (1994) 199.

[103] R. Milberg, in *Proceedings of the 44th ASMS Conference on Mass Spectrometry and Allied Topics* (1996).

[104] K.K. Murray and D.H. Russell, *AIP Laser Ablation: Mechanisms and Applications II, 2nd International Conference, Knoxville TN, April 1993.*

[105] K.K. Murray, T.M. Lewis, M.D. Beeson and D.H. Russell, *Anal. Chem.*, **66** (1994) 1601.

[106] D.H. Russell and M.D. Beeson, *J. Mass Spectrom.*, **31** (1996) 295.

[107] P.-C. Liao and J. Allison, *J. Mass Spectrom.*, **30** (1995) 763.

[108] R.C. Beavis and J.N. Bridson, *J. Phys. D.*, **26** (1993) 442.

[109] V. Bökelmann, B. Spengler and R. Kaufmann, *Eur. Mass Spectrom.*, **1** (1995) 81.

[110] M. Karas, H. Ehring, E. Nordhoff, B. Stahi, K. Strupat, F. Hillenkamp, M. Grehl and B. Krebs, *Org. Mass Spectrom.*, **28** (1993) 1476.

[111] S.J. Doktycz, P.J. Savickas and D.A. Krueger, *Rapid Commun. Mass Spectrom.*, **5** (1991) 145.

[112] K. Tang, S.L. Allman, R.B. Jones, C.H. Chen and S. Araghi, *Rapid Commun. Mass Spectrom.*, **7** (1993) 435.

[113] K. Tang, PhD Thesis, Vanderbilt University, Nashville, TN (1994).

[114] R.S. Brown and J. Feng, in *Proceedings of the 44th ASMS Conference on Mass Spectrometry and Allied Topics* (1996).

[115] A. Vertes, R. Gijbels and R.D. Levine, *Rapid Commun. Mass Spectrom.*, **4** (1990) 228.

[116] R.C. Beavis, *Org. Mass Spectrom.*, **27** (1992) 864.

[117] *Dye Lasers, 2nd Ed.*, F.P. Schäfer, Springer-Verlag, 1977, p22.

[118] H. Ehring and B.U.R. Sundqvist, *J. Mass Spectrom.*, **30** (1995) 1303.

[119] H. Fukumura and H. Masuhara, *Chem. Phys. Lett.*, **221** (1994) 373.

[120] M. Sadeghi, Z. Olumee, X. Tang, A. Vertes, Z.-X. Jiang, A.J. Henderson, H.S. Lee and C.R. Prasad, *Rapid Commun. Mass Spectrom.*, **11** (1997) 393.

[121] L.M. Preston-Schaffter, G.R. Kinsel and D.H. Russell, *J. Am. Soc. Mass Spectrom.*, **5** (1994) 800.

[122] R.C. Beavis, *Org. Mass Spectrom.*, **27** (1992) 653.

[123] M. Karas and F. Hillenkamp, *AIP Laser Ablation: Mechanisms and Applications II, 2nd International Conference, Knoxville TN, April 1993.*

[124] R.C Beavis and B.T. Chait, *Chem. Phys. Lett.*, **181** (1991) 479.

[125] W. Ens, Y. Mao, F. Mayer and K.G. Standing, *Rapid Commun. Mass Spectrom.*, **5** (1991) 117.

[126] R.C. Beavis and B.T. Chait, in *Methods and Mechanisms for Producing Ions from Large Molecules*, K.G. Standing and W. Ens (Eds.), Plenum Press, New York (1991).

[127] P.T.A Reilly and J.P. Reilly, *Rapid Commun. Mass Spectrom.*, **8** (1994) 731.

[128] A.P. Quist, T. Huth-Fehre and B.U.R. Sundqvist, *Rapid Commun. Mass Spectrom.*, **8** (1994) 149.

[129] P. Juhasz, M.L. Vestal and S.A. Martin, *J. Am. Soc. Mass Spectrom.*, **8** (1997) 209.

[130] B. Winter, R. Mitzner, C. Kusch, E.E.B. Campbell and I.V. Hertel, *J. Chem. Phys.*, **104** (1996) 9179.

[131] F. Aksouh, P. Chaurand, C. Deprun, S. Della-Negra, J. Hoyes, Y. Le Beyec, R.R. Pinho, *Rapid Commun. Mass Spectrom.*, **9** (1995) 515.

[132] T.W. Heise and E.S. Yeung, *Anal. Chem.*, **66** (1996) 355.

[133] A. Vertes and R. Gijbels, in *Laser Ionization Mass Analysis*, A. Vertes, R. Gijbels and F. Adams (Eds.), John Wiley & Sons, Inc., (1993) p127.

[134] A. Bencsura, V. Navale, M. Sadeghi and A. Vertes, *Rapid Commun. Mass Spectrom.*, **11** (1997) 679.

[135] R.E. Johnson, *Int. J. Mass Spectrom. Ion Proc.*, **139** (1994) 25.

[136] L.V. Zhigilei, P.B.S. Kodali and B.J. Garrison, *J. Phys. Chem.* (submitted).

[137] A. Bencsura and A. Vertes, *Chem. Phys. Lett.*, **247** (1995) 142.

[138] H. Ehring, M. Karas and F. Hillenkamp, *Org. Mass Spectrom.*, **27** (1992) 472.

[139] P. Juhasz and C.E. Costello, *Rapid Commun. Mass Spectrom.*, **7** (1993) 343.

[140] W. Tang, C.M. Nelson, L. Zhu and L.M. Smith, *J. Am. Soc. Mass Spectrom.*, **8** (1997) 218.

[141] B.H. Wang, K. Dreisewerd, U. Bahr, M. Karas and F. Hillenkamp, *J. Am. Soc. Mass Spectrom.*, **4** (1993) 393.

[142] Y.F. Zhu, K.L. Lee, K. Tang, S.L. Allman, N.I. Taranenko and C.H.Chen, *Rapid Commun. Mass Spectrom.*, **9** (1995) 1315.

[143] C.K.L. Wong and T.-W. D. Chan, *Rapid Commun. Mass Spectrom.*, **11** (1997) 513.

[144] E. Lehmann, R. Knochenmuss and R. Zenobi, *Rapid Commun. Mass Spectrom.*, **11** (1997) 1483.

[145] K. Dreisewerd, M. Schürenberg, M. Karas and F. Hillenkamp, *Int. J. Mass Spectrom. Ion Proc.*, **141** (1995) 127.

[146] J.D. Haywood, P.Y. Yui and P.J. Derrick, *20th BMSS Annual Meeting, 1993.*

[147] R. Knochenmuss, F. Dubois, M.J. Dale and R. Zenobi, *Rapid Commun. Mass Spectrom.*, **10** (1996) 871.

[148] P.-C. Liao and J. Allison, *J. Mass Spectrom.*, **30** (1995) 408.

[149] M.E. Gimon, L.M. Preston, T. Solouki, M.A. White and D.H. Russell, *Org. Mass Spectrom.*, **27** (1992) 827.

[150] R.D. Burton, C.H. Watson, J.R. Eyler, G.L. Lang, D.H. Powell and M.Y. Avery, *Rapid Commun. Mass Spectrom.*, **11** (1997) 443.

[151] T. Kosaka, T. Kinoshita and M. Takayama, *Rapid Commun. Mass Spectrom.*, **10** (1996) 405.

[152] H. Ehring, C. Costa, P.A. Demirev and B.U.R. Sundqvist, *Rapid Commun. Mass Spectrom.*, **10** (1996) 821.

[153] C.D. Mowry and M.V. Johnston, *Rapid Commun. Mass Spectrom.*, **7** (1993) 569.

[154] K. Dreisewerd, M. Schürenberg, M. Karas and F. Hillenkamp, *Int. J. Mass Spectrom. Ion Proc.*, **154** (1996) 171.

[155] K. Riahi, G. Bolbach, A. Brunot, F. Breton, M. Spiro and J.-C. Blais, *Rapid Commun. Mass Spectrom.*, **8** (1994) 242.

[156] A. Westman, T. Huth-Fehre, P. Demirev, J. Bielawski, N. Medina and B.U.R. Sundqvist, *Rapid Commun. Mass Spectrom.*, **8** (1994) 388.

[157] N. Medina, T. Huth-Fehre, A. Westman and B.U.R. Sundqvist, *Org. Mass Spectrom.*, **29** (1994) 207.

[158] A. Westman, P. Demirev, T. Huth-Fehre and B.U.R Sundqvist, *Int. J. Mass Spectrom. Ion Proc.*, **130** (1994) 107.

[159] P.Y. Yau, T.-W.D. Chan, P.G. Cullis, A.W. Colburn and P.J. Derrick, *Chem. Phys. Lett.*, **202** (1993) 93.

[160] P. Demirev, A. Westman, C.T. Reimann, P. Håkansson, D. Barofsky, B.U.R. Sundqvist, Y.D. Cheng, W. Seibt and K. Siegbahn, *Rapid Commun. Mass Spectrom.*, **6** (1992) 187.

[161] X. Tang, M. Sadeghi, A. Olumee and A. Vertes, *Rapid Commun. Mass Spectrom.*, **11** (1997) 484.

[162] G.R. Kinsel, L.M. Preston and D.H. Russell, *Biol. Mass Spectrom.*, **23** (1994) 205.

[163] F. Hillenkamp, *Plenary Lecture, 21st BMSS Annual Meeting, Manchester, UK, 3 - 6 Sept 1995.*

[164] T.J.D. Jorgensen, T. Vilius and G. Bojesen, *13th International Mass Spectrometry Conference, Budapest, Hungary , 29 August - 2 September 1994.*

[165] L.W. Summer, Y. Huang and D.H. Russell, in *Proceedings of the 44th ASMS Conference on Mass Spectrometry and Allied Topics* (1996).

[166] H.-C. Luedemann, J. Stahl-Zeng and F. Hillenkamp, in *Proceedings of the 44th ASMS Conference on Mass Spectrometry and Allied Topics* (1996).

[167] R. Kaufmann, B. Spengler and F. Lützenkirchen, *Rapid Commun. Mass Spectrom.*, **7** (1993) 902.

[168] B. Spengler, *J. Mass Spectrom.*, **32** (1997) 1019.

[169] T.J.P. Naven, D.J. Harvey, J. Brown and G. Critchley, *Rapid Commun. Mass Spectrom.*, **11** (1997) 1681.

[170] P.-C. Liao, Z.-H. Huang and J. Allison, *J. Am. Soc. Mass Spectrom.*, **8** (1997) 501.

[171] S.T. Fountain, H. Lee and D.M. Lubman, *Rapid Commun. Mass Spectrom.*, **8** (1994) 407.

[172] T. Kosaka, T. Ishikawa and T. Kinoshita, *Rapid Commun. Mass Spectrom.*, **9** (1995) 1342.

[173] D.J. Harvey, R.H. Bateman and M.R. Green, *J. Mass Spectrom.*, **32** (1997) 167.

[174] T.J. Cornish and R. Cotter, *AIP Laser Ablation: Mechanisms and Applications II - 2nd International Conference, Knoxville, TN, April 1993*, Ch 6, p459 (1993) AIP Press (New York).

[175] R.J. Cotter and T.J. Cornish, *Rapid Commun. Mass Spectrom.*, **8** (1994) 339.

[176] K.F. Medzihradszky, D.A. Maltby, Y. Qui, Z. Yu, S.C. Hall, Y. Chen and A.L. Burlingame, *Int. J. Mass Spectrom. Ion Proc.*, **160** (1997) 357.

[177] *Techniques in Protein Chemistry III*, M.J.-F. Suter, W.T. Moore, T.B. Farmer, J.S. Cottrell and R.M. Caprioli, Academic Press, p447 (1992).

[178] M. Dey and J. Grotemeyer, *Eur. Mass Spectrom.*, **1** (1995) 95.

[179] L.R.H. Cohen, K. Strupat and F. Hillenkamp, in *Proceedings of the 44th ASMS Conference on Mass Spectrometry and Allied Topics* (1996).

[180] I.K. Perera, S. Kantartzoglou and P.E. Dyer, *Int. J. Mass Spectrom. Ion Proc.*, **156** (1996) 151.

[181] T.-W.D. Chan, A.W. Colburn and P.J. Derrick, *Org. Mass Spectrom.*, **27** (1992) 53.

[182] F. Zhong and S. Zhao, *Rapid Commun. Mass Spectrom.*, **9** (1995) 570.

[183] L.W. Summer, B.P. Wolf and D.H. Russell, in *Proceedings of the 44th ASMS Conference on Mass Spectrometry and Allied Topics* (1996).

[184] M.C. Fitzgerald, G.R. Parr and L.M. Smith, *Anal. Chem.*, **65** (1993) 3204.

[185] I.K. Perera, S. Kantartzoglou and P.E. Dyer, *Int. J. Mass Spectrom. Ion Proc.*, **137** (1994) 151.

[186] K. Tang, S.L. Allman, R.B. Jones and C.H. Chen, *Org. Mass Spectrom.*, **27** (1992) 1389.

[187] H.M.D. Lu and U.P. Schlunegger, **10** (1996) 483.

[188] J.J. Gorman, B.L. Ferguson and T.B. Nguyen, *Rapid Commun. Mass Spectrom.*, **10** (1996) 529.

[189] J. Krause, M. Stoeckli and U.P. Schlunegger, *Rapid Commun. Mass Spectrom.*, **10** (1996) 1927.

[190] A. Overberg, M. Karas, U. Bahr, R. Kaufmann and F. Hillenkamp, *Rapid Commun. Mass Spectrom.*, **4** (1990) 293

[191] A.I. Gusev, W.R. Wilkinson, A. Proctor and D.M. Hercules, *Anal. Chem.*, **67** (1995) 1034.

[192] B. Rosinke, K. Strupat, F. Hillenkamp, J. Rosenbach, N. Dencher, U. Krüger and H.-J. Galla, *J. Mass Spectrom.*, **30** (1995) 1462.

[193] Y.F. Zhu, C.N. Chung, N.I. Taranenko, S.L. Allman, S.A. Martin, L. Haff and C.H. Chen, *Rapid Commun. Mass Spectrom.*, **10** (1996) 383.

[194] M. Dale, R. Knochenmuss and R. Zenobi, *Rapid Commun. Mass Spectrom.*, **11** (1997) 136.

[195] T.A. Simmons and P.A. Limbach, *Rapid Commun. Mass Spectrom.*, **11** (1997) 567.

[196] R.T. McIver, Jr., Y. Li, R.L. Hunter, *Proc. Natl. Acad. Sci. USA*, **91** (1994) 4801.

[197] A. Overberg, M. Karas and F. Hillenkamp, *Rapid Commun. Mass Spectrom.*, **5** (1991) 128.

[198] R. Cramer, F. Hillenkamp and R.F. Haglund, Jr., *J. Am. Soc. Mass Spectrom.*, **7** (1996) 1187.

[199] R.J. Cotter, *Anal. Chem.*, **64** (1992) 1027A.

[200] C.C. Vera, R. Zubarev, H. Ehring, P. Håkansson and B.U.R. Sundqvist, *Rapid Commun. Mass Spectrom.*, **10** (1996) 1429.

[201] G.R. Kinsel, R.D. Edmondson and D.H. Russell, *J. Mass Spectrom.*, **32** (1997) 714.

[202] G.R. Kinsel, J.M. Grundwuermer and J. Grotemeyer, *J. Am. Soc. Mass Spectrom.*, **4** (1994) 2.

[203] S.M. Colby, T.B. King and J.P. Reilly, *Rapid Commun. Mass Spectrom.*, **8** (1994) 865.

[204] R.S. Brown and J.J. Lennon, *Anal. Chem.*, **67** (1995) 1998.

[205] T.B. King, S.M. Colby and J.P. Reilly, *Int. J. Mass Spectrom. Ion Proc.*, **145** (1995) L1.

[206] M. Karas, *J. Mass Spectrom.*, **32** (1997) 1.

[207] R.M. Whittal, L.M. Russon, S.R. Weinberger and L. Li, *Anal. Chem.*, **69** (1997) 2147.

[208] J. Franzen, *Int. J. Mass Spectrom. Ion Proc.*, **164** (1997) 19.

[209] U. Bahr, J. Stahl-Zeng, E. Gleitsmann and M. Karas, *J. Mass Spectrom.*, **32** (1997) 1111.

[210] Y. Zhu, L. He, J.R. Srinivasan and D.M. Lubman, *Rapid Commun. Mass Spectrom.*, **11** (1997) 987.

[211] R.S. Brown and N.L. Gilfrich, *Rapid Commun. Mass Spectrom.*, **6** (1992) 697.

[212] C.L. Just and C.D. Hanson, *Rapid Commun. Mass Spectrom.*, **7** (1993) 502.

[213] B. Spengler, D. Kirsch, R. Kaufmann and E. Jaeger, *Rapid Commun. Mass Spectrom.*, **6** (1992) 105.

[214] T.J. Cornish and R.J. Cotter, *Rapid Commun. Mass Spectrom.*, **8** (1994) 781.

[215] W. Ens, V. Spicer, K.G. Standing and J. Zhou, *Org. Mass Spectrom.*, **28** (1993) 1430.

[216] C.A. Flory, R.C. Taber and G.E. Yefchak, *Int. J. Mass Spectrom. Ion Proc.*, **152** (1996) 177.

[217] C.A. Flory, R.C. Taber and G.E. Yefchak, *Int. J. Mass Spectrom. Ion Proc.*, **152** (1996) 169.

[218] A.A. Makarov, E.N. Raptakis and P.J. Derrick, *Int. J. Mass Spectrom. Ion Proc.*, **146/147** (1995) 165.

[219] H. Lee and D.B. Lubman, *Anal. Chem.*, **67** (1995) 1400.

[220] B.M. Chien, S.M. Michael and D.M. Lubman, *Rapid Commun. Mass Spectrom.*, **7** (1993) 837.

[221] S.T. Fountain, H. Lee and D.M. Lubman, *Rapid Commun. Mass Spectrom.*, **8** (1994) 487.

[222] P. Kofel, M. Stöckli, J. Krause and U.P. Schlunegger, *Rapid Commun. Mass Spectrom.*, **10** (1996) 658.

[223] R.J. Cotter, *AIP Laser Ablation: Mechanisms and Applications II - 2nd International Conference, Knoxville, TN, April 1993*, Ch 6, p459 (1993) AIP Press (New York).

[224] B. Spengler, D. Kirsch, R. Kaufmann, M. Karas, F. Hillenkamp and U. Giessmann, *Rapid Commun. Mass Spectrom.*, **4** (1990) 301.

[225] T.B. Farmer and R.M. Caprioli, *J. Mass Spectrom.*, **30** (1995) 1245.

[226] R.S. Brown and N.L. Gilfrich, *Rapid Commun. Mass Spectrom.*, **6** (1992) 690.

[227] J. Axelsson, E.S. Parilis, C.T. Reimann, P. Sullivan and B.U.R. Sundqvist, *Nucl. Inst. and Methods in Phys. Research B*, **101** (1995) 343.

[228] J. Axelsson, E. Scrivener and P.J. Derrick, *21st BMSS Annual Meeting, Manchester, UK, 3 - 6 Sept 1995.*

[229] M.W. Duncan, G. Matanovic and A. Cerpa-Poljak, *Rapid Commun. Mass Spectrom.*, **7** (1993) 1090.

[230] S. Jespersen, W.M.A Niessen, U.R. Tjaden and J. van der Greef, *J. Mass Spectrom.*, **30** (1995) 357.

[231] D.C. Imrie, J.M. Pentney and J.S. Cottrell, *Rapid Commun. Mass Spectrom.*, **9** (1995) 1293.

[232] U. Bahr, U. Röhling, C. Lautz, K. Strupat, M. Schürenberg and F. Hillenkamp, *Int. J. Mass Spectrom. Ion Proc.*, **153** (1996) 9.

[233] M.A. Park and J.H. Callahan, *Rapid Commun. Mass Spectrom.*, **8** (1994) 317.

[234] W.H. Benner, D.M. Horn, J.M. Jaklevic, M. Frank, C. Mears, S. Labov and A.T. Barfknecht, *J. Am. Soc. Mass Spectrom.*, **8** (1997) 1094.

[235] A. Westman, T. Huth-Fehre, P. Demirev and B.U.R. Sundqvist, *J. Mass Spectrom.*, **30** (1995) 206.

[236] *Principles of Optics, 4th Ed.*, M. Born and E. Wolf, Pergamon, Oxford, (1970).

[237] *Kodak Laser Dyes*, Publication JJ-169, Eastman Kodak Co. Inc., Rochester, NY 14650, USA.

[238] R. Srinivasan, R. von Gutfeld, C. Angadiyavar and R.W. Dreyfus, *Chem. Phys. Lett.*, **25** (1974) 537.

[239] *Fluorescence and Phosphorescence*, P. Prinsheim (Ed.), Wiley Interscience, New York (1965) p. 353ff and references therein.

[240] A. Dienes, C. Shank and R. Kohn, *IEEE J. Quant. Elec.*, **QE-9** (1973) 833.

[241] H. Ehring and B.U.R. Sundqvist, *13th International Mass Spectrometry Conference, 29 August - 2 September (1994) Budapest, Hungary.*

[242] H. Ehring and B.U.R. Sundqvist, *Appl. Surf. Sci.*, **96-98** (1996) 577.

[243] *Photophysics of Aromatic Molecules*, J.B. Birks, John Wiley & Sons, Ltd. (1970).

[244] *Organic Molecular Photophysics, Vol 1*, J.B. Birks (Ed.), John Wiley & Sons, Ltd. (1973).

[245] *Standards in Fluorescence Spectrometry*, J.N. Miller (Ed.), Ultraviolet Spectrometry Group, Chapman and Hall (1981).

[246] *Handbook of Fluorescence Spectra of Aromatic Molecules*, 2nd Ed., I.B. Berlman, Academic Press (1971).

[247] J.N. Demas and G.A. Crosby, *J. Phys. Chem.*, **75** (1971) 991.

[248] W.H. Melshuish, *J. Phys. Chem.*, **65** (1961) 229.

[249] G.A. Reynolds and K.H. Drexhage, *Optics Commun.*, **13** (1975) 222.

[250] *CRC Handbook of Chemistry and Physics, 46th Ed.*, R.C. Weast (Ed. in Chief), The Chemical Rubber Co. (1965).

[251] S. Choi and S.A. Rice, *Phys. Rev. Lett.*, **8** (1962) 410.

[252] M. Silver, D. Olness, M. Swicord and R.C. Jarnagin, *Phys. Rev. Lett.*, **10** (1963) 12.

[253] C.L. Braun, *Phys. Rev. Lett.*, **21** (1968) 215.

[254] A. Bergman, M. Levine and J. Jortner, *Phys. Rev. Lett.*, **18** (1967) 593.

[255] S.D. Babenko, V.A. Benderskii, V.I. Goldanskii, A.G. Lavrushko and V.P. Tychinskii, *Chem. Phys. Lett.*, **8** (1971) 598.

[256] S.D. Babenko, V.A. Benderskii, V.I. Goldanskii, A.G. Lavrushko and V.P. Tychinskii, *Phys. Stat. Sol. (b)*, **45** (1971) 91.

[257] L.G. Christophorou, *Adv. Electron. Electron Phys.*, **46** (1978) 55.

[258] *Multiple Photon Infrared Laser Photophysics and Photochemistry*, V.N. Bragratashvili, V.S. Letochov, A.A. Makarov and E.A. Ryabov, Hatwood, Amsterdam (1985).

[259] A. Nitzan and J. Jortner, *Chem. Phys. Lett.*, **60** (1978) 1.

[260] A. Nitzan and J. Jortner, *J. Chem. Phys.*, **71** (1979) 3524.

[261] R. Mitzner and E.E.B. Campbell, *J. Chem. Phys.*, **103** (1995) 2445.

[262] C.E. Klots, *Chem. Phys. Lett.*, **186** (1991) 73.

[263] *Physics of Shock Waves and High Temperature Hydrodynamic Phenomena, Vol 1*, Y.B. Zeldovich and Y.P. Raizer, Academic Press, New York (1968).

[264] P.E. Dyer, in *Laser-Tissue Interaction*, SPIE Vol. 1202 (1990).

[265] *Introductory Statistical Mechanics*, R. Bowley and M. Sánchez, Oxford University Press (1996).

[266] *Assignments for Vibrational Spectra of Seven Hundred Benzene Derivatives, Vols 1 and 2*, G. Várssay, Adam Hilger (Publ.), London (1974).

[267] K. Hansen and E.E.B. Campbell, *J. Chem. Phys.*, **104** (1996) 5012.

[268] J. Axelsson, E. Scrivener and P.J. Derrick, *21st BMSS Annual Meeting, Manchester, UK, 3 - 6 Sept 1995.*

[269] *Unimolecular Reactions, 2nd Ed.*, K.A. Holbrook, M.J. Pilling and S.H. Robertson, John Wiley and Sons (1996).